



DETERMINATION OF THE FATIGUE PROPERTIES OF Ti6Al4V (ELI) PARTS BUILT BY A DIRECT METAL LASER SINTERING SYSTEM WITH STANDARD PROCESS PARAMETERS FOLLOWED BY POST-PROCESSING TREATMENTS

LERATA BOTSANE MALEFANE

Dissertation submitted in fulfilment of the requirements for the degree

MASTER OF ENGINEERING IN MECHANICAL ENGINEERING

in the

Department of Mechanical and Mechatronics Engineering
Faculty of Engineering, Built Environment and Information Technology

at the

Central University of Technology, Free State

Supervisor: Prof W B du Preez, PhD

Co-supervisor: Dr M Maringa, PhD

BLOEMFONTEIN
February 2019

DECLARATION

DECLARATION WITH REGARD TO INDEPENDENT WORK

I, LERATA BOTSANE MALEFANE, passport number _____ and student number _____, do hereby declare that this research project submitted to the Central University of Technology, Free State for the Degree MASTER OF ENGINEERING IN MECHANICAL ENGINEERING, is my own independent work; and complies with the Code of Academic Integrity, as well as other relevant policies, procedures, rules and regulations of the Central University of Technology, Free State; and has not been submitted before to any institution by myself or any other person in fulfilment of the requirements for the attainment of any qualification.



17 October 2018

SIGNATURE OF STUDENT

DATE

ACKNOWLEDGEMENTS

The author passes all the praise and gratitude to the all mighty Tlatlamacholo, Jere mojari oa lits'ito tsa rona batho. The author would also like to thank the people who aided in the compilation of this Master of Engineering in Mechanical Engineering dissertation; in particular, Professor Willie du Preez and Doctor Maina Maringa from Central University of Technology, Free State, for their exceptional supervision and guidance through the entire project. This project would not have been possible without the support received from:

- The author's spouse; Makhiba Masingoaneng Malefane, for her motivation, support and understanding.
- The author's parents; Tanki Malefane and Mamokhethi Malefane, for their guidance and support.
- Professor Anton du Plessis; for showing interest and support on the project.
- Doctor Thywill Dzogbewu; for his guidance and assistance towards the completion of this project.
- JB Marks Education Trust Fund; for their financial support.
- DST; for their financial support through the Collaborative Program in Additive Manufacturing.

The author also thanks the staff from the Department of Mechanical and Mechatronic Engineering at Central University of Technology, Free State.

TABLE OF CONTENTS

DECLARATION	i
ACKNOWLEDGEMENTS	ii
TABLE OF CONTENTS	iii
LIST OF TABLES.....	vii
LIST OF FIGURES	ix
SYMBOLS, ABBREVIATIONS AND ACRONYMS.....	xviii
NOMENCLATURE.....	xx
SUMMARY	xxi
PUBLICATIONS EMANATING FROM THE RESEARCH	xxiii
Chapter 1 INTRODUCTION	1
1.1 Background.....	1
1.2 Problem Statement	2
1.3 Aim of the Project	3
1.4 Objectives.....	3
1.5 Research Methodology	3
1.6 Overview of the Dissertation	5
Chapter 2 LITERATURE REVIEW.....	6
2.1 Introduction.....	6
2.2 Additive Manufacturing	6

2.3	Direct Metal Laser Sintering (DMLS)	8
2.4	Titanium and Titanium alloys	9
2.5	Ti6Al4V (ELI)	12
2.6	DMLS of Ti6Al4V (ELI).....	15
2.6.1	Ti6Al4V (ELI) acicular α' martensite transformation during DMLS	15
2.6.2.	Residual stresses induced during DMLS	16
2.6.3	Porosity in DMLS	18
2.7	Heat Treatment of DMLS Ti6Al4V (ELI).....	19
2.7.1.	Single stage high temperature annealing of conventionally produced Ti6Al4V (ELI) to a bi-modal microstructure.....	20
2.7.2.	Single stage high temperature annealing of DMLS Ti6Al4V (ELI) to a bi-modal microstructure	22
2.8	Fatigue.....	24
2.8.1	Stages of fatigue.....	24
2.8.2	Categories of Fatigue	28
2.8.3	S-N curve.....	29
2.8.4	Fatigue fracture surface	31
2.8.5.	Linear elastic fracture mechanics	32
2.9	Summary	34
Chapter 3	METHODOLOGY	35
3.1	Introduction.....	35
3.2	DMLS Building of the Specimens	35
3.3	Calculation of Density	37

3.4	Ultrasonic Testing for Homogeneity and Orthotropy	38
3.5	Post Heat Treatment.....	38
3.6	Machining of Tensile and Fatigue Test Specimens	40
3.7	Micro-CT Scanning of High Temperature Annealed Specimens.....	40
3.8	Tensile Testing	41
3.9	Fatigue Testing	41
3.10	Metallographic Analysis	42
3.11	Fractography.....	45
Chapter 4	RESULTS AND DISCUSSIONS	46
4.1	Introduction.....	46
4.2	Density.....	46
4.3	Ultrasonic Longitudinal Test Results.....	47
4.3.1	Orthotropy in the X-, Y- and Z-built as-built DMLS Ti6Al4V (ELI) specimens	47
4.3.2	Homogeneity in the X-, Y- and Z-built as-built DMLS Ti6Al4V (ELI) specimens	52
4.4	Microstructural Analysis of DMLS Ti6Al4V (ELI) Specimens	56
4.4.1	As-built DMLS Ti6Al4V (ELI).....	56
4.4.2	Stress relieved and high temperature annealed DMLS Ti6Al4V (ELI)	58
4.5	Tensile Properties.....	63
4.6	Fatigue Properties	70
4.6.1	Introduction.....	70

4.6.2	Fatigue test results for the as-built fatigue specimens	71
4.6.3	Fatigue test results of stress relieved and HTA treated fatigue specimens.....	104
4.6.4	Summary	142
4.7	Comparison of the DMLS Ti6Al4V fatigue endurance limits	147
CHAPTER 5 CONCLUSIONS AND FUTURE WORK.....		151
5.1	Introduction.....	151
5.2	Conclusions.....	151
5.3	Future Work.....	153
REFERENCES		154
APPENDIX A- Tensile and Fatigue test specimen		163
APPENDIX B– Crack Initiation Sites		164

LIST OF TABLES

Table 2.1: Stabilizer composition of Ti6Al4V and Ti6Al4V (ELI) [4][27][28].....	12
Table 3.1: Standard process parameters of the EOSINT M 280 DMLS machine	35
Table 3.2: Tension-tension fatigue test criteria	41
Table 3.3: The recommended grinding and polishing procedure for the Struers Tegramin-25	43
Table 4.1: Calculated values of densities of the specimens tested for various build orientations	46
Table 4.2: x-, y- and z- axis average values of C_L for X-built specimens	47
Table 4.3: x-, y- and z-direction average values of C_L for Y-built specimens	49
Table 4.4: x-, y- and z-direction average values of C_L for Z-built specimens	50
Table 4.5: Average values of longitudinal velocity (C_L) in the y- and z-axis directions of the X-built specimens.....	52
Table 4.6: Average values of longitudinal velocity (C_L) in the x- and z-axis directions of the Y-built specimens.....	53
Table 4.7: Average values of longitudinal velocity (C_L) in the x- and y-axis directions of the Z-built specimens.....	55
Table 4.8: Tensile properties of stress relieved and HTA treated X-, Y- and Z-built Ti6Al4V (ELI) specimens.....	64
Table 4.9: The sums of DMLS process related pore areas projected in the x-y planes (perpendicular to the load axis) on the fracture planes and cross sections above and below the fracture planes of the tensile specimens	65
Table 4.10: Dimensions of DMLS process related initiation pores for fatigue failure cracks and their stress intensity ranges for selected load stress data.....	72

Table 4.11: Dimensions of DMLS process related initiation pores for fatigue failure cracks and their stress intensity ranges for selected load stress data of X-built as-built DMLS Ti6Al4V (ELI) specimens.....	82
Table 4.12: Dimensions of DMLS process related initiation pores for fatigue failure cracks and their stress intensity ranges and selected load stress data of Y-built as-built DMLS Ti6Al4V (ELI) specimens.....	89
Table 4.13: Dimensions of DMLS process related initiation pores for fatigue failure cracks and their stress intensity ranges for selected load stress data of X-built stress relieved plus HTA DMLS Ti6Al4V (ELI) specimens	105
Table 4.14: Dimensions of DMLS process related initiation pores for fatigue failure cracks and their stress intensity ranges for selected load stress data of Y-built stress relieved plus HTA DMLS Ti6Al4V (ELI) specimens.	116
Table 4.15: Dimensions of DMLS process related initiation pores for fatigue failure cracks and their stress intensity ranges for selected load stress data of Z-built the stress relieved plus HTA DMLS Ti6Al4V (ELI) specimens	124
Table 4.16: Comparison of the fatigue strengths at 10^4 load cycles and the fatigue endurance limits between the as-built and stress relieved plus HTA DMLS Ti6Al4V (ELI) specimens	146
Table 4.17: DMLS process parameters used in the production of specimens and the resulting material and fatigue features	147

LIST OF FIGURES

Figure 1.1: Schematic diagram of the research methodology	4
Figure 2.1: Schematic illustration of the DMLS process [20].....	8
Figure 2.2: 3D phase diagram representing the weight percentage alloying of Ti with Al and V [23] 10	
Figure 2.3: Hcp (a) and bcc (b) crystal lattice structures [26].....	10
Figure 2.4: Four different Ti6Al4V (ELI) microstructural morphologies: (a) martensitic grain structure, (b) fully lamellar grain structure, (c) equiaxed grain structure and (d) bimodal grain structure [7].....	13
Figure 2.5: Schematic of the state of stress of a layer during heating and during cooling [43].....	16
Figure 2.6: Residual stress profile of parts removed from a build plate [46].....	17
Figure 2.7: The orientation of pores due to localised lack of fusion with reference to the DMLS build direction [50]	18
Figure 2.8: Ti6Al4V phase diagram representing 30% and 80% volume fraction of α_p [33].....	21
Figure 2.9: Ti6Al4V cooling rates showing the different transformations of β from the β phase field [40].....	22
Figure 2.10: Different stages of fatigue life [15].....	24
Figure 2.11: Stages in the development of a crack along a slip plane [65]	25
Figure 2.12: (a) Zigzag crack propagation along grain boundaries; (b) fractograph showing fatigue striations [71]	27
Figure 2.13: S-N curve showing low-cycle fatigue and high-cycle fatigue and corresponding N, σ_y represents the tensile yield strength [72]	28
Figure 2.14: Typical fatigue stress cycles	30
Figure 2.15: Schematic representation of a typical HCF fracture surface.....	31
Figure 2.16: An internal crack of a denoted area within an infinitely large body [82].....	33
Figure 3.1: CAD model of 45 bar specimens on the DMLS build platform	36

Figure 3.2: Layer-upon-layer laser scan strategy, (a) layer one showing strips with the back and forth laser scan strategy, (b) layer two showing an angle shift of the direction of the strips, (c) the layer hatch spacing and overlap of the melt pool..... 37

Figure 3.3: (a) Stress-relieving heat treatment parameters and (b) high-temperature annealing heat treatment parameters..... 39

Figure 3.4: (a) Citopress-1 and (b) Struers Tegramin-25 machines..... 43

Figure 3.5: (a) Ultrasonic cleaner and (b) ESCO fume hood..... 44

Figure 3.6 ZEISS Axio Scope A1 optical microscope 44

Figure 3.7: JOEL JSM-7800 SEM..... 45

Figure 4.1: Average values of C_L in the x-, y- and z-axis directions for the X-built specimens..... 48

Figure 4.2: Average values of C_L in the x-, y- and z-axis directions for the Y-built specimens..... 49

Figure 4.3: Average values of C_L in the x-, y- and z-axis directions for the Z-built specimens 51

Figure 4.4: Ultrasonic longitudinal average velocities in the y- and z-axis directions of the X-built bars 53

Figure 4.5: Ultrasonic longitudinal average velocities in the x- and z-axis directions of the Y-built bars 54

Figure 4.6: Ultrasonic longitudinal average velocities in the x- and y-axis directions of the Z-built bars 55

Figure 4.7: Micrograph of as-built DMLS Ti6Al4V (ELI) sectioned in the x, y plane (a) and micrograph of as-built DMLS Ti6Al4V (ELI) sectioned in the x, z plane (b)..... 57

Figure 4.8: Micrograph of an X-built specimen after stress relieving..... 58

Figure 4.9: Micrographs of DMLS Ti6Al4V (ELI) stress relieved, followed by HTA at 950 °C for 2 h and furnace cooled (a) X-built specimen and (b) Y-built specimen 60

Figure 4.10: Micrograph of DMLS Ti6Al4V (ELI) stress relieved followed by HTA at 950 °C for 2 h and furnace cooled, for Z-built specimens 62

Figure 4.11: Stress–strain graph of the stress-relieved and HTA DMLS Ti6Al4V (ELI) 63

Figure 4.12: (a) Overall fractograph of specimen X-2 (b) a magnified micrograph of the transverse crack propagation area (c) further magnification of the transverse crack propagation area around a pore (d) high magnification of the transverse crack propagation area around a pore (e) high magnification of the shear lip area 66

Figure 4.13: (a) Overall fractograph of specimen Y-2 (b) a magnified micrograph of the transverse crack propagation area (c) further magnification of the transverse crack propagation area around a pore (d) high magnification of the transverse crack propagation area around a pore (e) a micrograph of the shear lip area 67

Figure 4.14: (a) Overall fractograph of specimen Z-2 (b) a magnified micrograph of the transverse crack propagation area (c) further magnification of the transverse crack propagation area (d) and (e) high magnifications of the shear lip areas around semi-melted areas 68

Figure 4.15: Semi–log₁₀ S-N curve for as-built X-built specimens..... 73

Figure 4.16: (a) Overall fractograph of specimen X-2 (b) a magnified area around the crack initiation site (c) further magnification of the area around the crack initiation site (d) high magnification of the path of crack propagation showing fatigue striations (e) a magnified area of crack propagation with DMLS process-related pores 75

Figure 4.17: (a) Overall fractograph of specimen X-4 (b) a magnified area around the crack initiation site (c) further magnification of the area around the crack initiation site (d) high magnification of the area of stable crack propagation around a DMLS process-related pore (e) a magnified unstable crack propagation area 77

Figure 4.18: (a) Overall fractograph of specimen X-4 (b) a magnified area around the crack initiation site (c) further magnification around the crack initiation site (d) high magnification of fatigue striations in an area of stable crack propagation (e) micrograph showing shallow dimples in an area of unstable crack propagation 79

Figure 4.19: (a) Overall fractograph of specimen X-9 (b) a magnified area around the crack initiation site (c) further magnification around the crack initiation site.....	80
Figure 4.20: Semi- \log_{10} S-N curve for as-built Y-built specimens.....	82
Figure 4.21: (a) Overall fractograph of specimen Y-19 (b) high magnification of an area around the crack initiation site (c) and (d) high magnification of DMLS process-related pores on a stable crack propagation area and (e) high magnification of a DMLS process-related pore on an unstable crack propagation area.....	84
Figure 4.22: (a) Overall fractograph of specimen Y-14 (b) increased magnification of an area around the crack initiation area and (c) high magnification of the crack initiation area.....	86
Figure 4.23: (a) Overall fractograph of specimen Y-18 and (b) high magnification of crack initiation site (c) high magnification of the area of stable crack propagation and (c) higher magnification of the area of stable crack propagation, indicating fatigue striations.....	87
Figure 4.24: (a) Overall fractograph of specimen Y-13 (b) a magnified area around the crack initiation site (c) further magnification around the crack initiation site	88
Figure 4.25: Semi- \log_{10} S-N curve for as-built Z-built specimens.....	90
Figure 4.26: (a) Overall fractograph of the specimen Z-29 (b) high magnification of an area around the crack initiation site and (c) high magnification on a tear ridge showing fatigue striations.....	91
Figure 4.27: Fractograph of specimen Z-23 in the area of stable propagation of a crack and (b) high magnification of an area around the site for initiation of a crack	92
Figure 4.28: Overall fractograph of specimen Z-25 and (b) high magnification of an area around the site of crack initiation (c) high magnification of the area of stable propagation of a crack around a pore and (d) high magnification of the area of stable propagation of a crack, showing fatigue striations	93
Figure 4.29: Schematic of a fracture surface with the line X-X indicating the section line of cut for metallographic preparation	94

Figure 4.30: A stitched micrograph of specimen X-1 showing propagation of the fatigue failure crack 96

Figure 4.31: (a) A micrograph of specimen X-1 around the enclosed area labelled I in Figure 54 and
(b) a micrograph of specimen X-1 around the enclosed area labelled II in Figure 54 97

Figure 4.32: (a) A micrograph of specimen X-1 around the enclosed area labelled III in Figure 54 and
(b) a micrograph of specimen X-1 around the enclosed area labelled IV in Figure 54 98

Figure 4.33: A stitched micrograph of specimen Z-22 showing crack propagation 100

Figure 4.34: (a) A micrograph of specimen Z-22 around the enclosed area labelled I in Figure 57 and
(b) a micrograph of specimen Z-22 around the enclosed area labelled II 101

Figure 4.35: (a) A micrograph of specimen Z-22 around the enclosed area labelled III in Figure 57
and (b) a micrograph of specimen Z-22 around the enclosed area labelled IV 102

Figure 4.36: Semi-log S-N curves for stress-relieved plus HTA DMLS Ti6Al4V (ELI) X-built
specimens..... 106

Figure 4.37: (a) Overall fractograph of specimen X-3; (b) a magnified area around the area of
initiation of the fatigue failure crack; (c) high magnification of the site of initiation of the fatigue failure
crack, with the crack initiation pore encircled; (d) high magnification of the area of stable propagation
of the fatigue failure crack, showing fatigue striations; (e) high magnification of the area of unstable
propagation of the fatigue failure crack, showing shallow dimples and (f) high magnification of the
final area of fracture, showing shallow dimples..... 108

Figure 4.38: (a) Overall micro-CT scan image of specimen X-3 showing porosity at ± 2 mm off the
plane of fracture and (b) high magnification of the micro-CT scan image around the crack initiation
pore..... 109

Figure 4.39: (a) Overall fractograph of specimen X-5; (d) magnified area around the crack initiation
site; (c) high magnification of the crack initiation site showing an area with facets; (d) high

magnification of the area of stable crack propagation showing fatigue striations and (e) high magnification of the area of unstable crack propagation showing fine shallow dimples 111

Figure 4.40: Overall micro-CT scan image of specimen X-5 showing porosity at ± 2 mm off the plane of fracture 112

Figure 4.41: Overall fractograph of specimen X-9; (b) a magnified area around the area of initiation of the fatigue failure crack ; (c) high magnification of the site of initiation of the fatigue failure crack with the crack initiation pore encircled; (d) high magnification of the area of stable propagation of the fatigue failure crack, showing fatigue striations; (e) high magnification of the area of unstable propagation of the fatigue failure crack, showing shallow fine dimples and (f) high magnification of the area of final fracture, showing shallow dimples 114

Figure 4.42: (a) Overall micro-CT scan image of specimen X-9 showing porosity at ± 2 mm off the plane of fracture and (b) high magnification of the micro-CT scan image around the crack initiation pore 115

Figure 4.43: Semi-log S-N curve for stress-relieved plus HTA DMLS Ti6Al4V (ELI) Y-built specimens 117

Figure 4.44: (a) Overall fractograph of specimen Y-11; (b) magnified area of around the site of initiation of the fatigue failure crack showing; (c) high magnification of the site of initiation of the fatigue failure crack, showing an area with facets; (d) high magnification of the area of stable propagation of the fatigue failure crack, showing fatigue striations and (e) high magnification of the area of unstable propagation of the fatigue failure crack, fine shallow dimples 119

Figure 4.45: Overall micro-CT scan image of specimen Y-11 showing porosity at ± 2 mm off the plane of fracture and (b) high magnification of the micro-CT scan image around the crack initiation pore 120

Figure 4.46: (a) Overall fractograph of specimen Y-8; (b) magnification around an internal site of the initiation of a fatigue failure crack, showing a fisheye morphology; (c) higher magnification around

the site of initiation of a fatigue failure crack, showing facets on α lath grains; (d) high magnification showing the site of initiation of faceted cracks ; (e) high magnification of the area of stable propagation of the fatigue failure crack and (f) high magnification of the area of unstable propagation of the fatigue failure crack 122

Figure 4.47: Overall micro-CT scan image of specimen Y-8 showing porosity at ± 2 mm off the plane of fracture 123

Figure 4.48: Semi-log S-N diagram for stress-relieved plus HTA DMLS Ti6Al4V (ELI) Z-built specimens 125

Figure 4.49: (a) Overall fractograph of specimen Z-7; (b) a magnified area around the site of initiation of the fatigue failure crack; (c) high magnification of the site of initiation of the fatigue failure crack, with the crack initiation pore encircled; (d) high magnification of the area of stable propagation of the fatigue failure crack, showing fatigue striations; (e) high magnification of the area of unstable propagation of the fatigue failure crack, showing shallow dimples and (f) high magnification of the area of final fracture, showing shallow dimples 126

Figure 4.50: Overall micro-CT scan image of specimen Z-7 showing porosity at ± 2 mm off the plane of fracture 127

Figure 4.51: Overall fractograph of specimen Z-3; (b) magnified and (c) high magnification areas around the site of initiation of fatigue failure crack, showing facets at α laths 128

Figure 4.52: (a) Overall fractograph of specimen X-12; (b) a magnified area around the site of the fatigue failure crack initiation with the crack initiation pore encircled; (c) high magnification of the area stable crack propagation showing fatigue striations with the arrow indicating the direction of the fatigue crack propagation; (d) high magnification of the area of unstable crack propagation showing a shallow dimpled fracture mode (e) high magnification of the area of the shear lip showing a dimpled fracture mode 130

Figure 4.53: Micro-CT scan image on the plane of fracture for specimen X-12, with the crack initiation pore marked with a cross 131

Figure 4.54: (a) High magnification fractograph of specimen Y-12 around the area of stable crack propagation; (b) a high magnification of the site of the fatigue crack initiation with the crack initiation pore encircled; (c), (d) and (e) high magnification of the area of stable crack propagation around DMLS process-related pores and (f) high magnification of the area of unstable crack propagation showing shallow dimples 132

Figure 4.55: Micro-CT scan image on the plane of fracture for specimen Y-12, with the crack initiation pore marked with a cross 133

Figure 4.56: A magnified fractograph of specimen Z-12 around the crack initiation pore; (b) high magnification around the site with the crack initiation pore encircled 134

Figure 4.57: Micro-CT scan image on the plane of fracture for specimen Z-12, with the crack initiation pore marked with a cross 134

Figure 4.58: (a) A stitched micrograph of HTA specimen X-12 showing the fatigue failure propagated crack 136

Figure 4.59: (a) A micrograph of specimen X-12 around the enclosed area labelled I in Figure 82 and (b) a micrograph of specimen X-12 around the enclosed area labelled II, (c) a micrograph of specimen X-12 around the enclosed area labelled III in Figure 82 and (d) a micrograph of specimen X-12 around the enclosed area labelled IV in Figure 82 137

Figure 4.60: A stitched micrograph of specimen Y-12 showing the fatigue failure propagated crack 138

Figure 4.61: (a) A micrograph of specimen Y-12 around the enclosed area labelled I in Figure 84 and (b) a micrograph of specimen Y-12 around the enclosed area labelled II in Figure 84, (c) a micrograph of specimen Y-12 around the enclosed area labelled III in Figure 84 and (d) a micrograph of specimen Y-12 around the enclosed area labelled IV in Figure 84 139

Figure 4.62: A stitched micrograph of specimen Z-12 showing the fatigue failure propagated crack 140

Figure 4.63: (a) A micrograph of specimen Z-12 around the enclosed area labelled I in Figure 86 and (b) a micrograph of specimen Z-12 around the enclosed area labelled II in Figure 86, (c) a micrograph of specimen Z-12 around the enclosed area labelled III in Figure 86 and (d) a micrograph of specimen Z-12 around the enclosed area labelled IV in Figure 86 141

Figure 4.64: Semi-log₁₀ HCF S-N curves for as-built DMLS Ti6Al4V (ELI) specimens oriented in the X-Y- and Z-directions 143

Figure 4.65: Semi-log₁₀ HCF S-N curves for stress-relieved plus HTA DMLS Ti6Al4V (ELI) specimens built in the X-Y- and Z-directions 144

Figure 4.66: Semi-log₁₀ HCF S-N curves for as-built and stress-relieved plus HTA DMLS Ti6Al4V (ELI) specimens built in the X-Y- and Z-direction 145

Figure 4.67: Comparison of the values of fatigue endurance limits presented in Table 22 149

Figure A.1: Tensile and fatigue specimen dimensions 163

Figure B.1: Crack initiation sites of as-built X-build direction specimens indicated by arrows 164

Figure B.2: Crack initiation sites of as-built Y-build direction specimens indicated by arrows 165

Figure B.3: Crack initiation sites of as-built Z-build direction specimens indicated by arrows 166

Figure B.4: Crack initiation sites of HTA X-build direction specimens indicated by arrows 167

Figure B.5: Crack initiation sites of HTA Y-build direction specimens indicated by arrows 168

Figure B.6: Crack initiation sites of HTA Z-build direction specimens indicated by arrows 169

SYMBOLS, ABBREVIATIONS AND ACRONYMS

α	Hexagonal close packed phase in titanium and titanium alloys
α'	Hexagonal close packed martensitic phase in titanium and titanium alloys
$\alpha_{g,b}$	Hexagonal close packed grain boundary
α_p	Hexagonal close packed primary grain
β	Body centred cubic phase in titanium and titanium alloys
σ	Stress
σ_a	Stress amplitude
σ_m	Mean stress
σ_{max}	Maximum stress
σ_{min}	Minimum stress
$\Delta\sigma$	Change in stress
ΔK	Change in stress intensity
ΔK_{th}	Change in stress intensity threshold
$\frac{da}{dN}$	Crack growth rate
\sqrt{area}	Square root of the projected area for crack initiation flaws
a_c	Critical crack length
C	Murakami's constant of the position of a crack initiation flaw on the specimen
C_l	Ultrasonic longitudinal velocity
C_t	Ultrasonic transverse velocity
E	Elastic modulus
G	Shear modulus
K	Stress intensity factor
K_{IC}	Critical stress intensity factor
K_t	Stress concentration factor
m	Gradient of a linear curve
N	Number of load cycles
N_i	Number crack initiation load cycles
N_p	Number of crack propagation load cycles
v	Poisson's ratio

2D	Two-Dimensional
3D	Three-Dimensional
AM	Additive Manufacturing
ASTM	American Society for Testing of Materials
bcc	Body- centred cubic crystal structure
CAD	Computer Aided Design
CRPM	Centre for Rapid Prototyping and Manufacturing
CV	Coefficient of variance
DMLS	Direct Metal Laser Sintering
DST	Department of Science and Technology
E	Young's modulus of elasticity
ELI	Extra low interstitial
EOS	Electro Optical Systems GmbH
FDM	Fused deposition modelling
G	Shear modulus of elasticity
ISO	International organization for standardization
HCF	High cycle fatigue
HEF	High endurance fatigue
hcp	Hexagonal close packed crystal structure
HTA	High temperature anneal
LCF	Low cycle fatigue
LEF	Low endurance fatigue
LEFM	Linear elastic fracture mechanics
NRF	National Research Foundation
PSB	Persistent slip bands
S	Stress load
SEM	Scanning electron microscope
SEI	Secondary electron imaging
THRIP	Technology and Human Resources for Industry Programme
UTS	Ultimate tensile stress
UV	Ultraviolet

NOMANTLATURE

as-built specimens	Machined specimens without any post DMLS heat treatment
HTA specimens	High temperature annealed and Machined test specimens
Stress relieve heat treatment	Post DMLS anneal treatment of the specimens before cutting them from DMLS built platform that alleviates internal residual stresses
X-built specimen	Specimen built with its longitudinal axis aligned with the X-axis of the DMLS machine
Y-built specimen	Specimen built with its longitudinal axis aligned with the Y-axis of the DMLS machine
YS	Yield stress at 0.2% offset
Z-built specimen	Specimen built with its longitudinal axis aligned with the Z-axis of the DMLS machine

SUMMARY

Design of hard tissue medical prostheses is typically based on the mechanical properties of the materials used. However, apart from non-loadbearing implants, medical prostheses in use are exposed to various forms of dynamic loading. Therefore, to eventually deliver qualified medical prostheses produced through additive manufacturing (AM), it is necessary to develop a data bank on both their static and dynamic properties. This is done here with reference to the fatigue properties of Direct Metal Laser Sintering (DMLS) of Ti6Al4V (ELI) parts, produced at the Centre for Rapid Prototyping and Manufacturing (CRPM) of Central University of Technology, Free State. The effect of flaws inherent in DMLS-produced specimens and their microstructure on the mechanical properties for as-built and high-temperature annealed specimens is investigated here.

From literature, orthotropy in DMLS Ti6Al4V (ELI) specimens, with reference to the three mutually orthogonal DMLS build directions, has been reported. It was attributed to the presence and orientation of the DMLS process-related pores within DMLS Ti6Al4V (ELI) specimens to their loading axis, the presence and direction of the residual stresses within the DMLS Ti6Al4V (ELI) specimens to their loading axis, and the direction of the prior beta (β) grains of DMLS Ti6Al4V (ELI) specimens to the loading axis. These are all factors of growth of the layers of the DMLS process in relation to the three mutually orthogonal DMLS build directions. Therefore, in this project the first step was the non-destructive testing of DMLS Ti6Al4V (ELI) specimens for the presence or lack of orthotropy. It was done by the ultrasonic testing of rectangular bars of as-built Ti6Al4V (ELI) of dimensions 60 x 11 x 11 mm built to align with X-, Y- and Z-axes of the DMLS machine, where Z is the build direction and X is the direction of movement of the recoater blade. From the data obtained, the tested DMLS Ti6Al4V (ELI) specimens showed to be both homogeneous and isotropic.

The high-cycle fatigue (HCF) properties of as-built and high-temperature annealed (HTA) DMLS Ti6Al4V (ELI) machined and polished specimens built to align with the three mutually orthogonal machine axes were investigated. This was carried out by cycling the specimens under load control, in a tension–tension fatigue testing machine. From the data collected, semi-log graphs of maximum stress (S) against life (N) of the specimens produced along the respective three build directions were plotted, and the displayed endurance limits compared. The as-built specimens aligned with the Y- and Z-axes showed the same endurance limit of 485 MPa and it was slightly higher than the 450

MPa endurance limit of the specimens aligned with the X-axis. Whereas the HTA specimens aligned with the X- and Y-axes showed the same endurance limit of 450 MPa, the specimens aligned with the Z-axis showed a slightly higher endurance limit of 486 MPa. Optical and scanning electron microscopy of the fracture surfaces were used to compare and analyse the crack initiation and propagation characteristics of the specimens. These showed that the dominating crack initiators were DMLS process-related pores. The HTA DMLS Ti6Al4V (ELI) specimens were micro-CT scanned in an attempt to relate the pores in the specimens with their fatigue properties. The micro-CT pore information from suspected crack initiation pores on the surfaces of eventually fractured specimens was used to calculate stress intensity factors, which correlated well with the decreasing cycles to failure of the fatigue test specimens for all three build directions. Three representative specimens were analysed and the “killer pore” identified in each micro-CT scan and fractographs, all which were proximal to the surface of the specimen.

PUBLICATIONS EMANATING FROM THE RESEARCH

1.0 Peer Reviewed Journals

1. L. B. Malefane, W. B. du Preez, M. Maringa, “High Cycle Fatigue Properties of As-Built Ti6Al4V (ELI) Produced by Direct Metal Laser Sintering”, *South African Journal of Industrial Engineering*, November 2017 Vol 28(3) Special Edition, pp 188–199, ISSN 2224-7890, <http://dx.doi.org/10.7166/28-3-1861>.
2. L. B. Malefane, W. B. du Preez, M. Maringa and A du Plessis “Tensile and High Cycle Fatigue Properties of Annealed Ti6Al4V (ELI) Specimens Produced by Direct Metal Laser Sintering”, *South African Journal of Industrial Engineering*, November 2018 Vol 29(3) Special Edition, pp 299-311, <http://dx.doi.org/10.7166/29-3-2077>.

2.0 Peer Reviewed Conference Proceedings

1. L. B. Malefane, W. B. du Preez, M. Maringa, “Testing for homogeneity and orthotropy of Ti6Al4V (ELI) parts built by Direct Metal Laser Sintering”, Rapid Product Development Association of South African (RAPDASA) 17th Annual International Conference, Pre-conference Seminar on Additive Manufacturing of Titanium Parts, VUT Southern Gauteng Technology and Science Park, Vanderbijpark, South Africa, 2–4 November 2016, ISBN 978-0-620-72061-8, <http://conferences.sun.ac.za/index.php/rapdasa17/rapdasa17>.

CHAPTER 1 INTRODUCTION

1.1 Background

Central University of Technology, Free State (CUT), with the financial assistance of the Department of Science and Technology (DST), the National Research Foundation (NRF) and the Technology and Human Resources for Industry Programme (THRIP) and various industrial partners, have developed a financially self-sustainable programme known as the Centre for Rapid Prototyping and Manufacturing (CRPM). The centre was established in 1997 and employs additive manufacturing (AM) technologies for rapid prototyping, rapid manufacturing, rapid tooling and medical product development using either metal or polymer powders. The ASTM F2792-12a standard defines AM as 'A process of joining materials to make objects from three-dimensional (3D) model data, usually layer upon layer, as opposed to subtractive manufacturing methodologies' [1].

The Direct Metal Laser Sintering (DMLS) technology has over the years gained use in the medical field for the manufacture of medical implants from Ti6Al4V extra low interstitial (ELI) powder due to its ability to manufacture complex parts with customised geometries at minimum or absolutely no waste of material as opposed to conventional subtractive manufacturing methods [2]. DMLS also allows the manufacture of porous hard tissue prostheses which allows for bone ingrowth with ease [3]. Design of porous hard tissue prostheses also helps bring down the Young's modulus of parts to values close to that of bone [3]. Ti6Al4V (ELI) is the material of choice for medical implants because it is biocompatible, has a good strength to density ratio (specific strength), and a good resistance to corrosion [4]. The Ti6Al4V (ELI) powder is processed into medical implants at the CRPM in an Electro Optical Systems (EOS) EOSINT M 280 machine, with a 200 W fibre laser that scans at a typical speed of 1 m/s and which has a focal diameter of 80 μm [5].

Although DMLS medical implants are expected to have the mechanical properties of the medical implants manufactured from wrought Ti6Al4V (ELI), Ti6Al4V (ELI) parts as-built through DMLS show lower ductility and reduced fatigue properties partly as a result of the martensitic microstructure and tensile residual stresses arising from the process [6]. Medical implants include those that are static, for instance, a skull plate implant, and those that are dynamic, an example being a hip joint. As opposed to static implants, dynamic implants experience cyclic loading. For example, a hip joint implant is exposed to the patient's weight while walking, running and impact forces due to jumping,

or when the patient falls: hence, the need to know the fatigue properties of dynamic implants because fatigue failure occurs at stresses well below the ultimate tensile stress (UTS). This means that the dynamic implants have to be designed with knowledge of the fatigue limit stress (σ_f) and manufactured with the necessary caution in order for them not to fail during operational life. Such failure can cause trauma to the patient and unnecessary cost of removing the broken implant and manufacturing and implanting a new one. Determination of the fatigue properties of implants produced through DMLS of Ti6Al4V (ELI) powder, as intended in this study, is therefore of crucial importance.

1.2 Problem Statement

The mechanical properties of parts are influenced by their microstructure, which is determined by the grain morphology, grain size and grain orientation that result from their manufacturing process and post-heat-treatment processes. Ti6Al4V (ELI) can exist in either a martensitic, lamellar, equiaxed or bi-modal microstructural morphology, each of which has its own distinctive dynamic and static mechanical properties [7]. Thus far, the research on DMLS Ti6Al4V (ELI) at the CRPM has been primarily focused on static tensile properties of strength, yield, elongation, stiffness and hardness prior to and after stress-relieving heat treatment and post-processing heat treatment, which were found to comply with set standards for medical prostheses [6]. While testing of static properties serves to confirm performance under static loads, it however is not sufficient when it comes to dynamically loaded prostheses like hip joints.

The failure of dynamically loaded components is a result of fatigue, for which the stress-limiting value is well below the UTS. Research has proven that increasing the tensile properties of parts does not guarantee an increase in the fatigue strength, meaning that the microstructures that give rise to high UTS do not necessarily give high fatigue strength [6]. Therefore, in order to design and successfully manufacture dynamically loaded DMLS Ti6Al4V (ELI) medical implants, the fatigue properties of such parts, with different grain structure and orientation resulting from the respective manufacturing and heat treatment processes, need to be investigated and compared with standard specified fatigue properties for hard tissue prostheses.

1.3 Aim of the Project

The research study is aimed at determining the fatigue properties of DMLS Ti6Al4V (ELI) parts and their level of conformity to the internationally accepted specifications for such parts produced through conventional manufacturing routes.

1.4 Objectives

- Plot and compare the semi-log₁₀ S-N curves of as-built and post-process heat-treated DMLS Ti6Al4V (ELI) to identify the significance of this heat treatment on the fatigue properties of the alloy.
- Through fractography, the points of the crack initiation and the areas of crack propagation and final fracture will be identified, and their dependence on microstructure studied.
- The fatigue properties thus obtained will be compared with standard properties of dynamically loaded conventionally manufactured Ti6Al4V (ELI) test specimens in order to determine the suitability of DMLS Ti6Al4V (ELI) parts for possible use as medical implants.

1.5 Research Methodology

The research study is aimed at determining the fatigue properties of DMLS Ti6Al4V (ELI) parts and their level of conformity to the internationally accepted specifications for such specimens produced through conventional manufacturing routes. This will be done by testing of machined as-built DMLS Ti6Al4V (ELI) (no post-DMLS heat treatment applied) and post-DMLS high-temperature annealed Ti6Al4V (ELI) fatigue test specimens. Machined and polished fatigue test specimens negate the influence of surface roughness on the fatigue properties and are considered as a reference on which fatigue limits of any designed structures are based [8]. The methodological approach to achieve the objectives of this research project is outlined in the schematic in Figure 1.1.

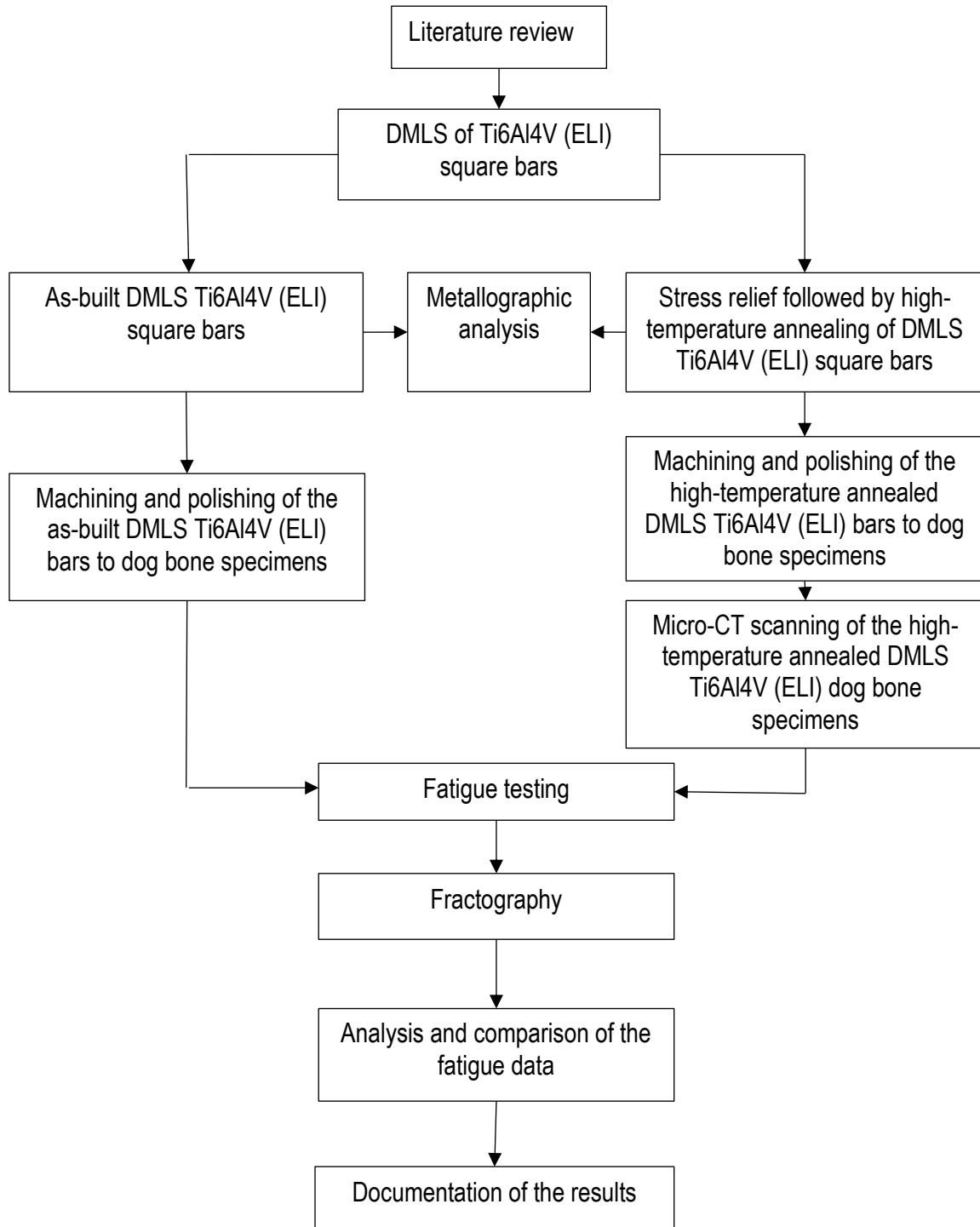


Figure 1.1: Schematic diagram of the research methodology

1.6 Overview of the Dissertation

The dissertation is divided into five chapters. The first chapter contains background on the research project which includes the statement of the problem that led to this research project, its aim, objectives and the methodological approach for resolving the problem.

Chapter 2 contains a background literature review on the high-cycle fatigue (HCF) of DMLS Ti6Al4V (ELI). This was done by first discussing the additive manufacturing (AM) process with emphasis on direct metal laser sintering (DMLS) followed by a brief description of titanium (Ti) and its alloys. The details of DMLS of Ti6Al4V (ELI) and the resultant microstructure and inherent process-related features are discussed next. Material on stress relieving and high-temperature annealing of Ti6Al4V (ELI) is then presented and the theory of HCF properties of Ti and its alloys is discussed. Information and results gathered from publications that include the HCF properties of SLM/DMLS Ti6Al4V are presented and discussed in the final section of this chapter and serves as the basis of comparison in Chapter 4 with the results obtained in the present study.

Chapter 3 outlines the experimental methodology used in this research project. This includes the building, machining and polishing of the specimens to ASTM standards. In this chapter, the procedures for testing for homogeneity and orthotropy in DMLS-processed parts, fatigue testing, stress relieving and annealing and the methods for preparing metallographic specimens for inspection of microstructures and presentation of fractographs, are also discussed.

The results obtained from the experiments are presented and discussed in Chapter 4.

Chapter 5 contains the conclusions drawn from the study and recommendations for further work.

CHAPTER 2 LITERATURE REVIEW

2.1 Introduction

This chapter presents the information gathered from literature on the HCF properties of DMLS Ti6Al4V (ELI) with emphasis on the influence of the DMLS process on the fatigue strength of Ti6Al4V (ELI) specimens. It aims at providing a basis of understanding of the existing knowledge of the field and the context of the research conducted in this project. A brief description of the AM categories followed by a detailed elaboration on DMLS is covered. The crystallographic morphology of titanium and its alloys is also covered in this chapter. The chemical composition, crystallographic morphology and the amenability to heat treatment of Ti6Al4V (ELI), the alloy which is being investigated, is discussed and followed by a discussion of the relevant considerations when manufacturing parts from this alloy through the DMLS technology. The principles of fatigue are also covered here.

2.2 Additive Manufacturing

The AM technology was invented in the 1980s and has over the years been modified into a variety of processes that use different materials. These different AM processes can be divided into three categories which depend on the status of the material used to create parts [9]. These categories are liquid-based-, solid-based- and powder-based AM processes [9]. All the aforementioned AM categories use the principle of slicing solid 3D CAD models into multiple layers and using a heat source to build up parts layer upon layer [2]. The materials processed by this technology include various metals, plastics and ceramics [10].

Liquid-based additive manufacturing processes – This AM category is divided into stereolithographic and extrusion fused deposition modelling (FDM) processes and the building material is in a liquid state [9]. The more widely used process in this category is stereolithography. In stereolithography, the parts are built by curing a photocurable liquid resin, layer by layer [11]. When the build platform of the stereolithography machine is at the top of its trajectory, an ultraviolet (UV) laser irradiates the resin along the areas of the particular two-dimensional (2D) slice of the CAD model forming a thin hardened layer [12]. When curing of the 2D layer of irradiated photocurable liquid resin is complete, the build platform is lowered to allow the next layer of liquid resin to be

applied over the previous one and the curing process is repeated to form the next layer over the first one and fuse the layers together. This continues until the entire 3D part is formed.

FDM builds polymer parts layer upon layer from a supply of a filament of polymer. When the build platform of the FDM machine is at the top of its trajectory, the filament is fed to a nozzle head where it is heated to a molten paste state [13][14]. The nozzle then deposits the molten polymer paste on the build platform in the x-y plane to build the bottom layer of the part. After completion of this layer, the build platform descends a distance equal to a layer thickness for the extrusion and build-up of the next layer to proceed. The molten polymer paste fuses with the previously built layer and solidifies [13][14]. The process is repeated until the 3D part build-up is complete. The extrusion pressure of the polymer paste and the speed of the nozzle in the x-y plane are kept constant for the entirety of the build-up of the part.

Solid-based additive manufacturing processes – In this AM category, the building material consists of sheets of solid material bonded together layer upon layer. These processes include ultrasonic additive manufacturing (UAM) and laminated object manufacturing (LOM) [9]. In UAM, the sheets are welded together by ultrasound [15]. Each sheet represents one layer and after each sheet is welded onto the preceding layer, profiles are then cut off in accordance with the particular 2D slice [15]. The process is repeated until the 3D part is complete. In LOM, a layer is formed by a laser which cuts out the profiles from a continuous sheet roll according to the sliced 2D data layers from the 3D CAD model [16]. To form the next layer, the sheet is rolled over the previously cut layer and bonded by a heat-activated resin after which the profiles are cut off with the laser according to the detail of the successive 2D data slice [16]. The process is repeated until a 3D part is complete.

Powder-based additive manufacturing processes – The building material in this AM category is powder. These processes include the sintering, melting and binding of the powder in a layer upon layer format to form a 3D part [9]. In the sintering powder-based AM process, fusion of the powder particles is achieved by heating the powder to temperatures below their melt temperatures, whereas the melting of the powder particles is required in the melting powder-based AM process. In the binding powder-based AM process, a binding agent is added to fuse the powder particles. These three powder fusion AM processes can be executed through either powder bed fusion or a direct energy deposition process [17]. In powder bed fusion-based AM processes, the thermal energy provided by a laser or an electron beam, selectively fuses the powder along the layer profile on the

powder bed [17]. In the direct energy deposition process, the thermal energy of the laser or electron beam fuses the powder as it is deposited from a nozzle [17].

2.3 Direct Metal Laser Sintering (DMLS)

This project deals with the manufacture of metallic prostheses for the replacement of hard tissue in the human body. Most metallic parts in AM are fabricated through powder-based AM processes [18]. Effective manufacturing through AM processes requires part build-up with minimum or no rigid supports (rigid supports form waste material) [19]. The AM fabrication of metallic parts with a minimum number of rigid supports is possible through powder bed fusion AM processes because the unprinted powder that surrounds the printed part acts as support [18]. CRPM manufactures hard tissue prostheses using an EOSINT M280 DMLS machine, which is a laser powder bed fusion (PBF) machine.

The DMLS technology fuses powdered metal into parts by melting and fusing the powdered metal selectively in a layer-upon-layer process. Figure 2.1 shows a schematic representation of the DMLS process.

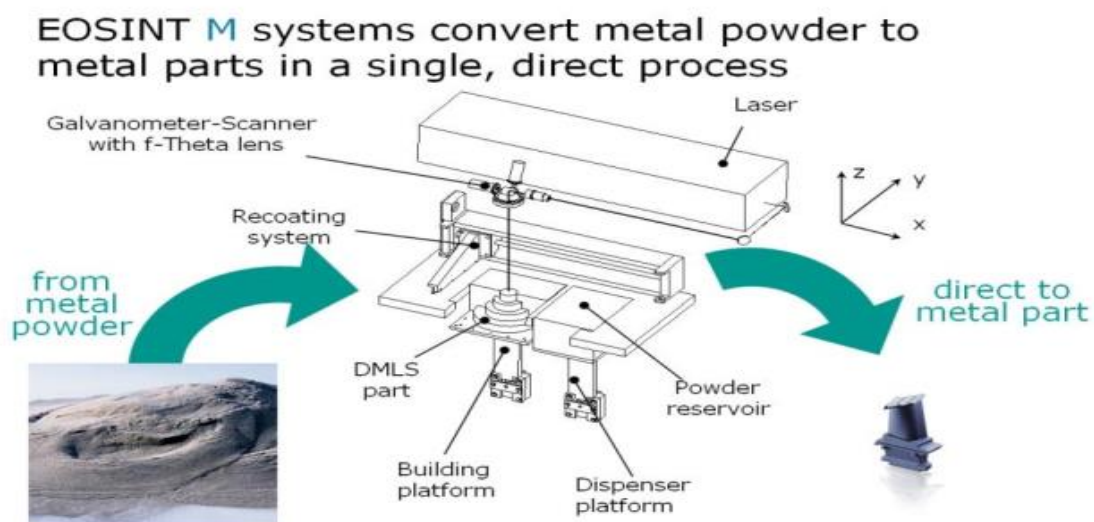


Figure 2.1: Schematic illustration of the DMLS process [20]

The first step in manufacturing based on DMLS is to design the part to be built in a CAD programme. Once complete, the 3D CAD model data is input into the DMLS system which slices the CAD model

into 2D layers and then the computer software-driven build by the DMLS machine begins [21]. The powdered metal is contained in a powder reservoir which can be elevated or lowered by the piston of the powder dispenser. At the beginning of the DMLS build-up when the powder reservoir is full, the piston of the powder dispenser is at the bottom of its trajectory. When operation starts, the recoater arm pushes an amount of powdered metal from the reservoir onto the build platform and creates a uniform layer of the powdered metal on it, in this case Ti6Al4V (ELI). At this time, the build platform is at the top of its trajectory. A high-powered fibre laser with a power of 200 W is used to fuse the metal powder particles into a solid 2D layer based on the geometry of the 2D slice of the 3D CAD file [21]. The laser scans along the X-Y plane, after which the building piston moves down along the Z-axis at a distance equal to the layer thickness and the above-mentioned process begins again. A second layer is built and also fused onto the first layer. This process is repeated until the 3D object is completed.

To understand the nomenclature used in this dissertation for describing the orientation of built specimens and the direction of layer deposition, it must be noted that the recoater arm of the machine moves along the X-axis, while the successive layers are stacked upon each other along the Z-axis.

2.4 Titanium and Titanium alloys

Titanium is a non-ferrous metal, which was first discovered in 1791 by William Gregor and was later given its name in 1793 by Martin Heinrich Klaproth. In its pure form, titanium exists as a hexagonal close-packed (hcp) phase, the alpha (α) phase, within the α phase field, shown in Figure 2.2 [22].

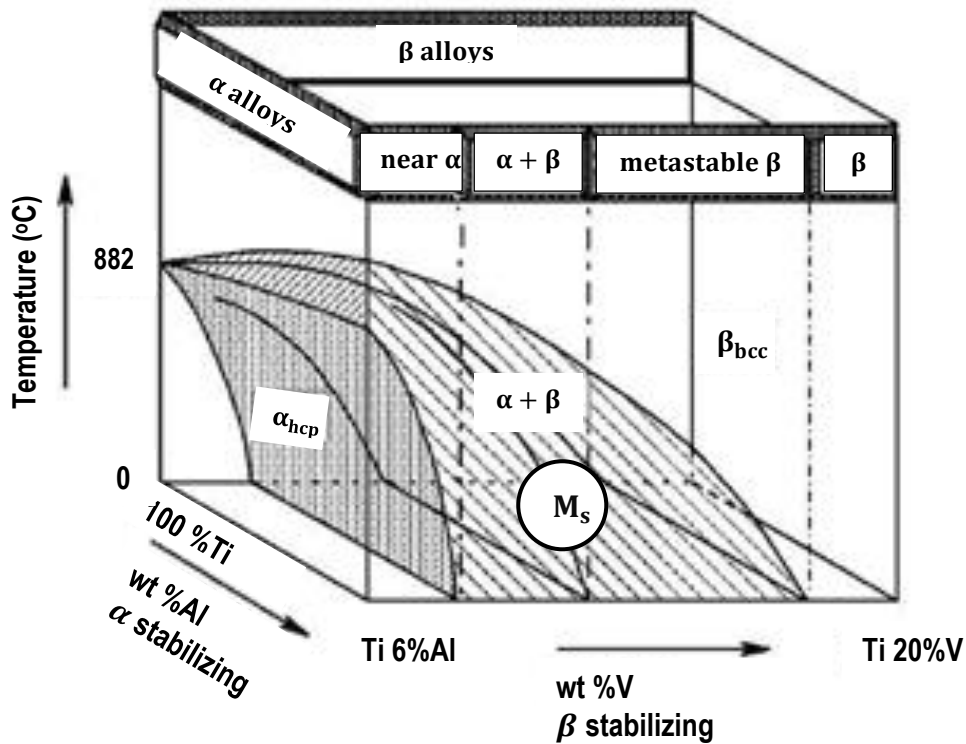


Figure 2.2: 3D phase diagram representing the weight percentage alloying of Ti with Al and V [23]

At temperatures above 882 °C, which marks the beginning of the beta phase field, as shown in Figure 2.2, the α grains transform allotropically to the body centred cubic (bcc) grains, the beta (β) phase, and remain in this form up to the melting temperature at 1670 °C [24][25]. The 882 °C is referred to as the beta transus temperature. The crystal lattices of hcp and bcc structures are shown in Figure 2.3 (a) and (b), respectively.

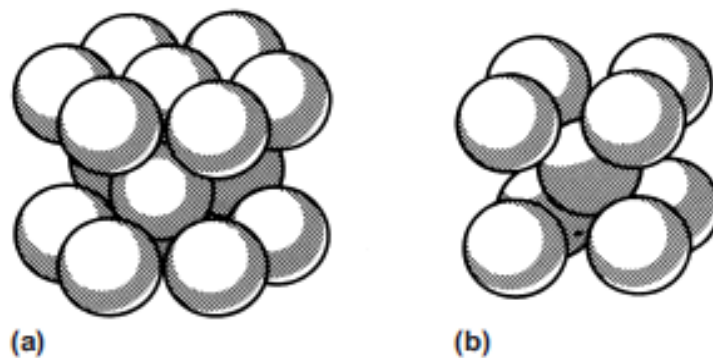


Figure 2.3: Hcp (a) and bcc (b) crystal lattice structures [25]

Titanium that is principally alloyed with aluminium and vanadium can exist as either α alloys, near α alloys, $\alpha + \beta$ alloys or β alloys. Figure 2.2 shows a phase diagram of the titanium α alloys, near α alloys, $\alpha + \beta$ alloys and β alloys with Al and V as the principle alloying elements.

α alloys – These are Ti alloys alloyed with α stabilizing elements. The most widely used α stabilizer is Al. Al is widely used because it has a large solubility in both the α and β phase and it is less dense than Ti; therefore, it lowers the resultant density of the alloy from that of Ti [23]. The addition and increase of an α stabilizer to pure Ti increases the beta transus temperature of the resulting alloy, as seen in Figure 2.2. The beta transus of Ti increases with increase in the weight percentage of Al in Ti until 6 wt% Al has been alloyed [23].

Near α alloys – They are α alloys that contain small amounts of β stabilizers. At room temperature they exist in an hcp phase and upon heating, there exists an α transformation temperature whereby the α phase begins to transform to the β phase until a temperature is reached above which all the α phase has transformed into the β phase (β transus). In the case of vanadium as a β stabilizer, shown in Figure 2.2, the near α alloys contain vanadium from about 1 to 2 wt% [23][22]. Increase of the β stabilizers lowers the transformation temperature of the α to β phase upon heating and the β transus temperature of the resulting alloy, as seen in Figure 2.2.

$\alpha + \beta$ alloys – They have a higher percentage of the β stabilizers than near α alloys. This high percentage of β stabilizers allows for the β phase to be retained at room temperature [23][26]. The retention of the β phase at room temperature allows for the alloy to be amenable to heat treatment, which can tailor the resulting microstructure into different microstructural morphologies [22][25]. This allows for the variance of strength, ductility and fatigue properties in the alloy depending on the heat treatment parameters [25]. Increase of the percentage of beta stabilizer lowers the beta transus temperature, which is an important parameter in heat treatment.

β alloys – They have a sufficiently high percentage of beta stabilizer to lower the beta transus temperature until 100% beta phase remains at room temperature [22].

2.5 Ti6Al4V (ELI)

Ti6Al4V (ELI) (grade 23 Ti alloy) is Ti6Al4V (grade 5 Ti alloy) at higher purity resulting from the reduced chemical compositions of interstitial elements within the alloy. Both the grades are $\alpha + \beta$ Ti alloys with their chemical compositions shown in Table 2.1.

Table 2.1: Stabilizer composition of Ti6Al4V and Ti6Al4V (ELI) [4][27][28]

α stabilizer	Ti6Al4V	Ti6Al4V (ELI)	β stabilizer	Ti6Al4V	Ti6Al4V (ELI)
Aluminium	5.5-6.5%	5.5-6.5%	Vanadium	3.5-4.5%	3.5-4.5%
Oxygen	<0.2%	<0.13%	Iron	<0.3%	<0.25%
Carbon	<0.08%	<0.08%	Hydrogen	<0.015%	<0.012%
Nitrogen	<0.05%	<0.03%			

The two $\alpha + \beta$ Ti alloy grades have Al, O, C and N as α stabilizers and V, Fe and H as β stabilizers. O, C, N, Fe and H are solid solution interstitials [29]. The purity in Ti6Al4V (ELI) is a result of the reduced percentage composition of the solid solution interstitials O, Fe and H as compared to Ti6Al4V shown in Table 2.1 [4][27]. The reduction in these solid solution interstitials particularly O, results in a relatively improved elongation at fracture and fracture toughness at the expense of the tensile strength [4][27][30].

The beta transus temperature of Ti6Al4V (ELI) is around 995 ± 25 °C, which is higher than that of pure Ti as a result of the 6% wt Al alloying element [25][26][31]. The 4% wt V in the alloy allows for a percentage of β phase to be retained at room temperature making the alloy amenable to heat treatment. The heating temperature, the soaking period and the cooling rate of the alloy determine the grain morphology that exists at room temperature. The grain morphology itself can be tailored with respect to the grain size and percentage of the α grains to the β grains [7]. The correct combination of grain morphology, grain size and percentage of the α grains to the β grains lead to an excellent combination of tensile strength, fatigue strength and ductility of the alloy [26][24].

Ti6Al4V (ELI) can exist in four different microstructural morphologies at room temperature as a function of the heat treatment at different parameters in accordance with the phase diagram in Figure 2.2 [25]. The four different microstructural morphologies, as shown in Figure 2.4, are acicular martensite (a), fully lamellar (b), equiaxed (c), and duplex (d). The four microstructures depicted in

Figure 2.4 are arrived at by heat treatment at different parameters of conventionally processed Ti6Al4V, with $\alpha + \beta$ phase being the start microstructure.

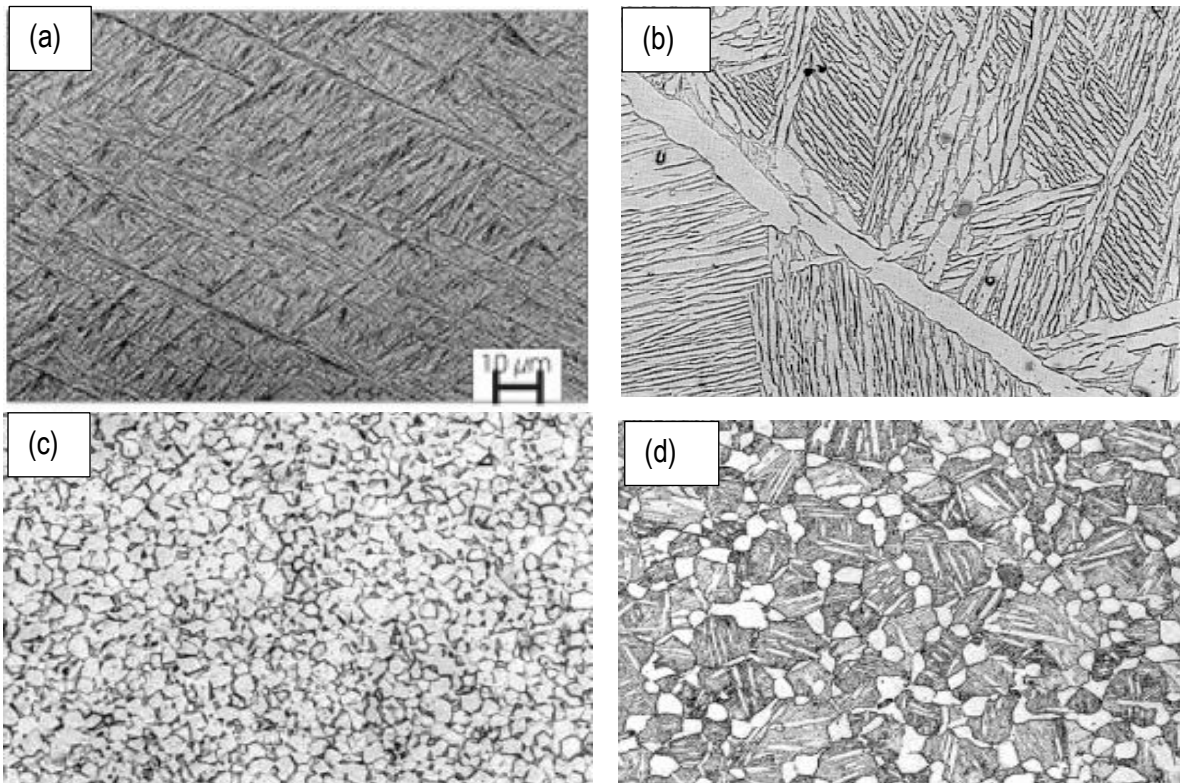


Figure 2.4: Four different Ti6Al4V (ELI) microstructural morphologies: (a) acicular martensitic microstructure, (b) fully lamellar microstructure, (c) equiaxed microstructure and (d) bimodal microstructure [7]

Martensitic (α') microstructure – it is distinguishable by a fine needle-shaped morphology, as seen in a scanning electron microscope (SEM) Figure 2.4 (a). When Ti6Al4V (ELI) is heated to temperatures above the martensite start temperature (M_s), shown in Figure 2.2, and subsequently rapidly cooled (quenched), a non-equilibrium phase transformation of the β grains occurs. The non-equilibrium transformation of the β grains leads to the formation of metastable acicular α' within the prior β grains [32].

Fully lamellar microstructure – as depicted in Figure 2.4 (b), the lamellar microstructure consists of colonies of α grain laths separated by ribs of retained β phase enclosed in an α grain boundary [33]. They are formed when Ti6Al4V (ELI) parts are heated to temperatures in the β phase field and soaked in a furnace for a period of time. At temperatures above the β transus, all the α grains in

Ti6Al4V (ELI) have completely transformed into β grains forming a 100% β phase. Soaking at this temperature allows for the β grains to globulize and grow. Upon slow cooling from these temperatures, α starts to nucleate at the β grain boundaries forming grain boundary α ($\alpha_{g,b}$). The grain boundaries act as effective nucleation sites [34]. Further cooling results in the nucleation of parallel α laths at the α grain boundaries that grow into the β grain. The growth of the α laths results in a lamellar microstructure of Ti6Al4V (ELI) that consists of colonies of α laths separated by retained β grains within $\alpha_{g,b}$. The width of the α lamellae depends on the cooling rate (furnace cooling or air cooling). High cooling (air cooling) rates result in fine α laths and low cooling (furnace cooling) rates result in relatively coarse α laths.

Equiaxed microstructure – comprises equiaxed or primary alpha (α_p) grains with β grain boundaries [35]. The Ti6Al4V (ELI) is heated and furnace soaked within the $\alpha + \beta$ phase field for the α grains to globulize. The heat-treatment temperature at this point is not high enough to allow α grains to diffuse into the β grains but at temperatures high enough to allow for α' to transform to α grains. The equiaxed microstructure is shown in Figure 2.4 (c).

Duplex microstructure – consists of a percentage by volume of α_p grains and colonies of α laths that are separated by ribs of β grain, shown in Figure 2.4 (d). The Ti6Al4V (ELI) is heated within the $\alpha + \beta$ phase field at temperatures that are determined by the desired percentage by volume of α_p to that of colonies of α , as determined from the phase diagram. Upon heating, the α grains transform into β grains at a volume fraction determined by temperature. Increase in temperature increases the volume fraction of β grains in the $\alpha + \beta$ microstructure. During the soaking period, both the α and β grains globulize. The β grains readily transform into α lamellae upon cooling [33]; thus, the presence of lamellae from cooling at temperatures just below the β transus.

Research on the fatigue behaviour of Ti6Al4V indicates that the lamellar microstructure exhibits low crack initiation resistance (low microcrack growth resistance) and good crack propagation resistance [35]. The low microcrack growth resistance is due to the fact that once a crack is initiated in the slip band (fatigue cracks initiate at slip bands within the α lamellae or at α grains along prior β grain boundaries [7]), it finds an easy path at the interfaces of the α/β lamellae. For equiaxed microstructures, fatigue cracks initiate along slip bands within the α grains [7] and the microcracks grow through the α grain which is a more difficult route compared to that of interfaces of α/β lamellae. For this reason, equiaxed microstructure provides better fatigue initiation resistance.

Duplex microstructure is a combination of lamellar and equiaxed microstructures rendering it high resistance to both fatigue crack initiation and fatigue crack propagation [36]. The HCF properties of wrought Ti6Al4V was found to decrease in the order of bi-modal, equiaxed, lamellar and martensite α' [37][38].

2.6 DMLS of Ti6Al4V (ELI)

Manufacturing of Ti6Al4V (ELI) hard tissue prostheses by DMLS is ideal because the ability to customize and the little to no waste characteristics of the process lowers the total cost of an implant and the surgery as compared to conventionally produced Ti6Al4V (ELI). However, DMLS of Ti6Al4V (ELI) results in an irregular surface finish, acicular martensitic α' microstructure, residual stresses and porosity which could give rise to a decrease in the mechanical properties of an implant. The aforementioned characteristics have led to the process requiring post-DMLS process treatments, which vary according to the intended application of the part built. The post-processes include surface polishing, heat treatments and hot isostatic pressing to attain properties similar to or better than those of wrought material.

2.6.1 Ti6Al4V (ELI) acicular α' martensite transformation during DMLS

The equilibrium transformation of Ti6Al4V from the β phase field to room temperature results in lamellar colonies of α separated by ribs of β grains [22]. This is normally through the precipitation of primary α in the β grains with the Burgers relationship of $(0001)_{\alpha} // (110)_{\beta}$, $[11\bar{2}0]_{\alpha} // [111]_{\beta}$ [39]. This occurs at cooling rates lower than 20 °C/s [40]. When the cooling rate is increased to above 410 °C/s, the transformation becomes non-equilibrium, leading to the formation of metastable α' which is characterized by a needle-like morphology. In DMLS, the high temperature and speed of the laser rapidly melts metal powder within a small melt pool (the 80 μm diameter of the laser beam results in a melt pool 100 μm in diameter). Upon the laser beam moving on at a typical speed of 1 m/s, high thermal gradients are being created that lead to cooling rates as high as 10^6 °C/s [41]. The rapid melting of the Ti6Al4V (ELI) powder and the remelting of the previously solidified underlying layers promote epitaxial growth of the β grains in the direction parallel to the direction of the maximum temperature gradient direction (parallel to the laser beam) [42]. Upon cooling and solidifying of the newly fabricated layer and the remelted underlying layers, which was mentioned to be above 10^6 °C/s, the acicular α' nucleate and grow from the boundaries of the columnar β grains,

forming a grain structure of fully acicular α' martensite within the columnar prior β grains at room temperature [42].

2.6.2. Residual stresses induced during DMLS

Residual stresses are stresses that remain within a plastically or elastically deformed material after the load that caused the deformation has been removed. The residual stresses can be desirable or undesirable. For instance, in tension–tension fatigue, compressive residual stresses are desirable, whereas tensile residual stresses are undesirable.

In DMLS, the residual stresses arise from thermal stresses induced during the melting and cooling of the layers. The theoretical explanation of the formation of residual stresses during DMLS is traced back to the high temperature gradient between two consecutive layers where compressive stresses are induced in the melt zone and tensile stresses are induced in the cooler underlying layers during heating, as is represented schematically in the left image in Figure 2.5.

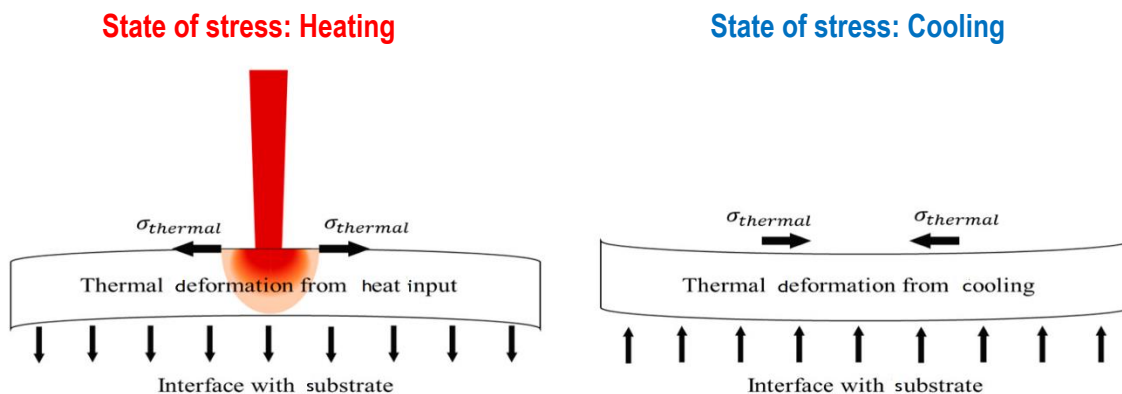


Figure 2.5: Schematic of the state of stress of a layer during heating and during cooling [43]

During the fusion of the top molten layer to the previously solidified layer, the molten layer is restricted from thermally expanding by the solidified layer below it. This induces compressive stresses on the molten layer. During the cooling process, the thermal contraction of the upper layer is restricted by the underlying solidified layer, thus inducing tensile stresses [44]. The above process leaves the top layer under tensile residual stresses and the layer below it under compressive residual stresses. However, when each layer is built, the solidified underlying layers are remelted and subsequently cooled. The contraction of the remelted layers upon cooling is restricted by the underlying solidified layers as they solidify [43]. The remelting of underlying layers is repeated

several times as the layers are built up and a decrease in temperature is found with increasing depth of the layers from the surface [43]. This temperature gradient results in a linear thermal stress gradient that starts from compression at the lowest layers (for cases where parts are attached to a build plate) and then tension at the surface [43][45]. The linear stress profile of the residual stresses only holds for parts that are attached to the build plate [46]. The stress gradient follows the temperature gradient based on the following equation:

$$\sigma_{therm} = \frac{E}{w} (\alpha w - aE) \Delta T \quad (2.1)$$

In the above equation, the symbols, E , α , w , a and ΔT stand for elastic modulus, coefficient of thermal expansion, transverse dimension, allowed contraction, and the change in temperature of the built part, respectively. The allowed contraction (a) takes into account that the lower layers are not absolutely rigid and will therefore contract somewhat even as they resist contraction of the top layers.

Upon removal from the build plate, there is some relaxation of the stresses and the stress profile remains parabolic with tensile stresses at the upper layers and reduced tension at the lower layers of the part, as well as compressive stresses in the intermediate layers, as shown in Figure 2.6 [46][47]. In Figure 2.6, the zero point on the X-axis represents the top surface of the SLM sample.

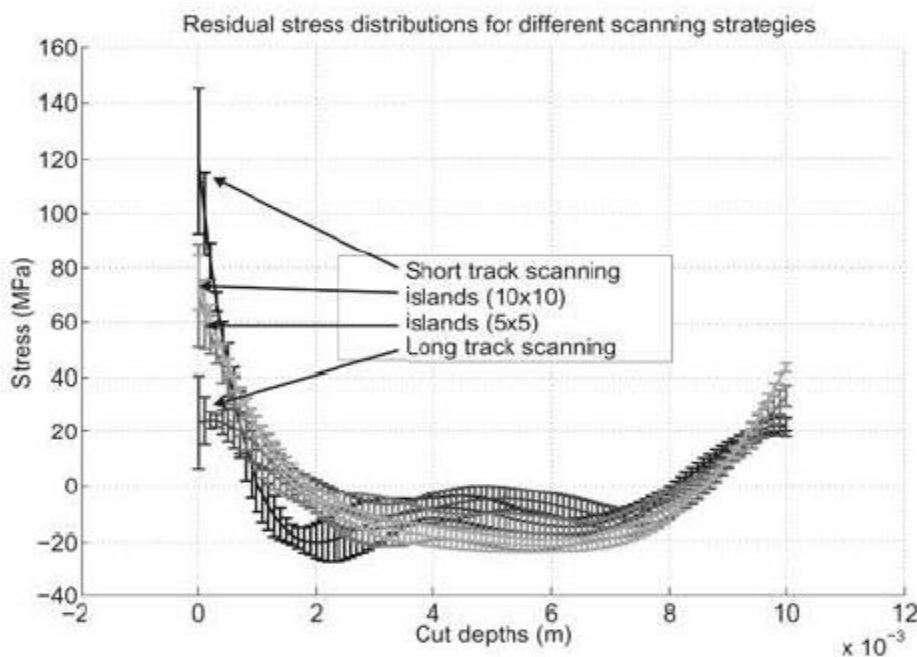


Figure 2.6: Residual stress profile of parts removed from a build plate [46]

The thermal stresses are locked within the SLM parts because of the high cooling rate inherent in the DMLS process [48]. Tensile residual stresses, as mentioned above, are unfavourable in tension–tension fatigue loading because they promote the initiation and propagation of cracks.

2.6.3 Porosity in DMLS

Porosity in DMLS Ti6Al4V (ELI) can arise from the entrapment of gas within a part during melting of the powder. These pores are typically of a spherical geometry [49]. Pores also arise from localized lack of fusion of powder as a result of unmelted or semimelted powder [6][49]. The pores arising from localized lack of fusion of powder are more detrimental than those due to the entrapment of gas because they are much bigger and oval shaped [6][41].

The oval-shaped pores arising from localized lack of fusion of powder are located between two consecutive layers during the DMLS process [6][50]. They are orientated such that their major axes are aligned parallel to the scanning plane of the laser (the X-Y plane of the DMLS machine), as seen in Figure 2.7 [6].

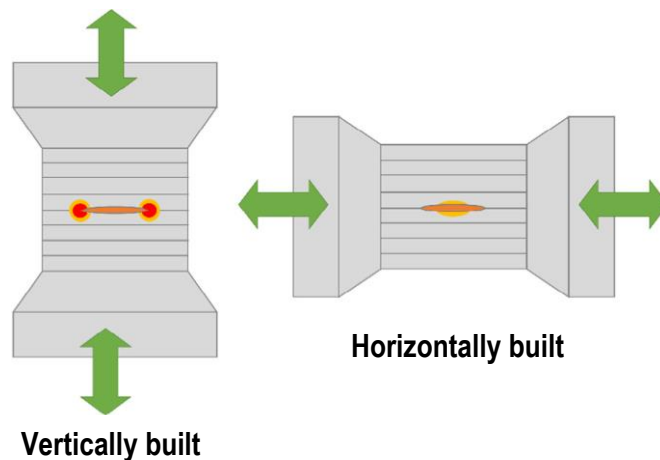


Figure 2.7: The orientation of pores due to localised lack of fusion with reference to the DMLS build direction [50]

The pores bring about anisotropic fatigue properties with respect to the built orientations of samples shown in Figure 2.7, which are the vertical and the horizontal build directions (the Z- and Y-axes of the DMLS machine, see section 2.3). The stress concentration factor of a stress concentration site increases with transverse size of the related flaw with respect to the applied load, as depicted in Figure 2.7. In the building of the fatigue specimens by DMLS, vertically built specimens have pores with their major axes perpendicular to the load axis during tension–tension fatigue testing, while the

horizontally built specimens have pores with their major axes parallel to the load axis [50]. Therefore, the stress concentration factor imposed by a pore in a specimen built and loaded in the vertical DMLS direction is higher than that of a specimen built and loaded in the horizontal DMLS build direction, for pores with the same dimensions.

CRPM has reported close-to-full densification of DMLS Ti6Al4V (ELI) parts, having porosity of about 0.0022% for as-built Ti6Al4V (ELI) [6]. This high densification offers an improvement in fatigue properties of DMLS Ti6Al4V (ELI) as it minimises the possibility of fatigue initiation of cracks and local acceleration of the fatigue crack propagation due to coalescence of pores.

2.7 Heat Treatment of DMLS Ti6Al4V (ELI)

The as-built DMLS Ti6Al4V (ELI) specimens produced at CRPM by an EOSINT M280 machine set to standard process parameters result in a fine acicular α' martensitic microstructure of Ti6Al4V (ELI) within the prior columnar β grain boundaries. This Ti6Al4V (ELI) has high tensile strength, low ductility and internal thermal residual stresses [6][41]. The ductility of the as-built DMLS Ti6Al4V (ELI) specimens does not conform to the ductility specified for medical implants in ASTM F1472–08 [6][41][30]; thus, the need for post-DMLS heat treatment of the Ti6Al4V (ELI). CRPM employs a dual anneal post-DMLS Ti6Al4V (ELI) heat treatment. The first is the stress-relief annealing heat treatment, which alleviates the residual thermal stresses within the parts and is applied to the parts while they are still attached to the build plate. After stress relieving, the parts are cut off from the build plate and the next annealing treatment is applied to facilitate transformation of the α' grain structure and growth of grains in order to improve ductility [6].

The presence of tensile residual stresses in DMLS Ti6Al4V (ELI) test specimens during tension–tension fatigue testing increase the mean stress, which in turn decreases the stress ratio (R) during cyclic loading [50]. Decrease in the R-ratio decreases the fatigue endurance limit [50]. This is because at increased mean stresses, the flaw sizes from which a fatigue crack will initiate decrease and hence the fatigue cracks can initiate and propagate from microflaws (microcrack growth is dependent on the mean stress), in this case the micropores present in SLM Ti6Al4V (ELI) [[50][6]]. Therefore, the fatigue properties of as-built DMLS Ti6Al4V (ELI) can be improved by post-DMLS stress-relief anneal treatment, and further by transformation of the α' grain structure in the as-built DMLS Ti6Al4V (ELI).

The stress-relieving treatment alleviates the internal residual thermal stresses without any significant change in the microstructure. Hence, there is little increase in ductility after this process. Subsequent high-temperature annealing (HTA) for 2 hours at 950 °C of the stress-relieved DMLS Ti6Al4V (ELI) specimens followed by furnace cooling, transforms the acicular α' martensitic grain structure to an $\alpha + \beta$ grain structure, thereby improving the ductility. The resultant ductility of the DMLS Ti6Al4V (ELI) specimens treated to the aforementioned annealing parameters of up to 20% is above the minimum specified in the ASTM F1472-08 of 8% [41]. The aim of this study is to confirm the significance of the CRPM-adopted post-DMLS high-temperature annealing parameters on the HCF properties of Ti6Al4V (ELI).

The response of DMLS Ti6Al4V (ELI) to heat treatment is different from that of conventionally processed Ti6Al4V (wrought and cast) because of its metastable acicular α' as-built microstructure [32]. Conventionally processed Ti6Al4V (ELI) exists in the form of either lamellar, equiaxed or bi-modal microstructures, which were discussed in section 2.5. The microstructural transformations due to high-temperature annealing of both conventional Ti6Al4V and DMLS Ti6Al4V (ELI) to bi-modal microstructures, which are known to have the best fatigue resistance for the Ti6Al4V alloy, are now discussed in some detail.

2.7.1. Single-stage high-temperature annealing of conventionally produced Ti6Al4V (ELI) to a bi-modal microstructure

As noted in section 2.5, the bi-modal microstructure of conventionally processed Ti6Al4V has the best fatigue resistance properties of the various microstructures of the alloy that exist at room temperature [51]. In a bi-modal microstructure, the fatigue properties are affected by the volume percentage and size of the equiaxed α grains and the size of the colonies of α lamellae [7]. HCF resistance of the alloy increases with decrease in the volume fraction of the equiaxed α grains [35] up to a certain percentage. However, this percentage is also affected by the size of the grains, because fine grains have a higher resistance to the propagation of microcracks than coarse grains [22][51][52]. Fine-grained structure results in higher values of yield strength, which in turn requires higher magnitudes of localised stresses to initiate slip in the equiaxed α grains that create slip band fatigue cracks [33]. For the best HCF resistance, the duplex microstructure should have a volume fraction of about 30% of equiaxed α grains and a fine grain size of both the equiaxed α grains and α lamellae colonies [33][35]. The percentage of equiaxed α grains is determined by the prevailing temperature with reference to the Ti6Al4V (ELI) phase diagram, shown in Figure 2.8.

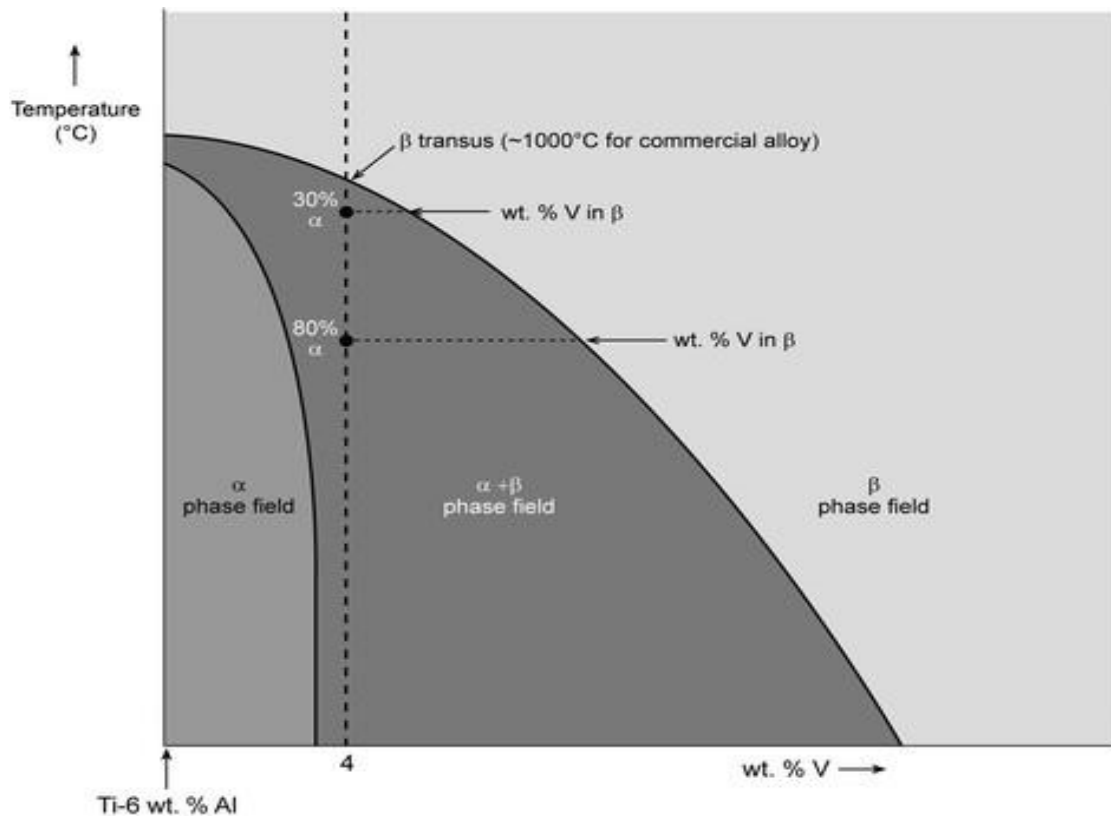


Figure 2.8: Ti6Al4V phase diagram representing 30% and 80% volume fraction of α_p [33]

Upon heating, as the temperature of the alloy approaches the β transus, the α grains transform to β grains. The lever rule with reference to the phase diagram in Figure 2.8 shows that the percentage of equiaxed α grains in the β grains decreases with increase in temperature until above the β transus temperature where all of the α grains have transformed into β grains. Lütjering [35] compared the fatigue properties of Ti6Al4V specimens with 20% and 30% volumes of equiaxed α grains and found that the specimens with 30% equiaxed α grains had the higher fatigue strength [35]. Wu et al. [37] compiled a fatigue database from literature for volume fractions of equiaxed α less than 30%, a range of volume fractions of equiaxed α between 30% and 50% and volume fractions of equiaxed α greater than 50%. They found the volume fraction of specimens with equiaxed α ranging from 30% to 50% to have the highest fatigue strength. It can be concluded from these studies that the ideal volume percentage of equiaxed α grains in a bi-modal microstructure to give best fatigue resistance is 30%. The 30% volume fraction of α grains is obtained at around 950 °C, as seen in the phase diagram in Figure 2.8 [35][33]. Soaking of Ti6Al4V at this temperature allows for the fragmentation and globulization of the remaining α grains to equiaxed α . With the remaining α grains globulized, cooling of Ti6Al4V from this temperature at cooling rates between 1.5

°C/s and 20 °C/s, shown in Figure 2.9, allows the nucleation and growth of lamellar α within the β grains, thereby forming a bi-modal microstructure of Ti6Al4V at room temperature [40].

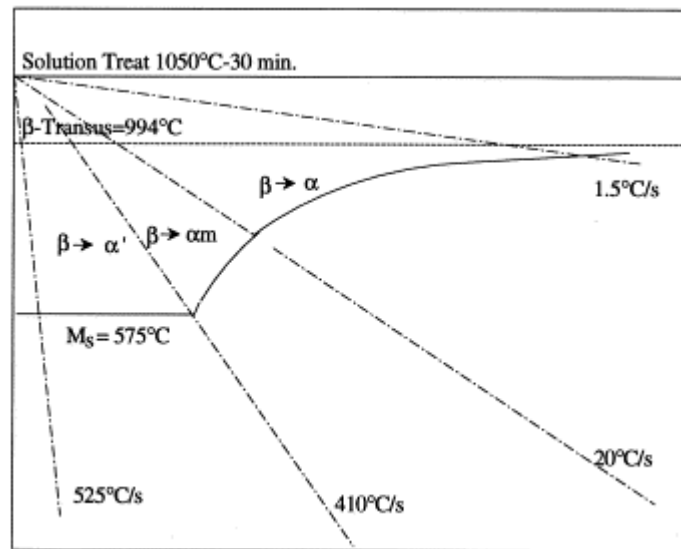


Figure 2.9: Ti6Al4V cooling rates showing the different transformations of β from the β phase field [40]

The size of the grains is determined by the soaking period in the furnace and the cooling rate. Prolonged soaking periods in the furnace of Ti6Al4V (ELI) at 950 °C allows extensive growth of α and β grains that are globular, which upon cooling result in coarse equiaxed α grains and lengthened $\alpha + \beta$ lamellae. The cooling rate from this temperature mostly affects the width of the α lamellae. When the cooling rate increases, the width of the α lamellae that nucleates within the β grains decreases. The width of the α lamellae can be varied for cooling rates ranging from 1.5 °C/s to 20 °C/s as shown schematically in Figure 2.9 [40].

2.7.2. Single-stage high-temperature annealing of DMLS Ti6Al4V (ELI) to a bi-modal microstructure

To tailor the stress-relieved DMLS Ti6Al4V (ELI) into either one of the $\alpha + \beta$ grain morphologies of the alloy, the acicular α' grain structure firstly has to be decomposed. During the heating stage of the high-temperature anneal (HTA) process, the α grains nucleate at the grain boundaries of the α' grains [41]. As the temperature increases towards the β transus temperature and as the α grains continue to nucleate and grow, the surroundings become enriched with the β stabilizer, which leads

to the formation of β grains at the α grain boundaries [41][53][54]. For heat treatments below the β transus, the width of the α laths in DMLS Ti6Al4V (ELI) is more predominantly dependent on the heating temperature than on the soaking period and cooling rate, as opposed to conventionally built Ti6Al4V (ELI) [54][7]. At these high-temperature anneals, the prior columnar β grains are retained at room temperature because the coexistence of the α and β grains prevents further growth of each other [54][55]. At temperatures above the β transus temperature, the prior columnar β grains grow to equiaxed β grains that transform into colonies of $\alpha + \beta$ lamellae upon cooling.

Sallica et al. [56] reported a complete decomposition of the acicular α' martensite to occur in the temperature interval of 730 °C to 850 °C, with stress relieving presumed to occur at 440 °C to 590 °C [56]. Moletsane et al. [6], found small nuclei of globular α grains and α' after stress relieving DMLS Ti6Al4V (ELI) at 650 °C for 3 hours (above the presumed stress-relieving temperatures). The presence of the α grains showed that at these temperatures α' grains have begun to decompose. Yadroitsev et al. [41] reported a complete decomposition of the acicular α' martensite to colonies of $\alpha + \beta$ lamellae with clusters of equiaxed nuclei of globular α after high-temperature annealing of stress-relieved DMLS Ti6Al4V (ELI) at 950 °C for 2 hours followed by furnace cooling. They observed that the $\alpha + \beta$ lamellae were of the same orientation as the acicular α' martensite and were still within the prior β grains. The equiaxed nuclei of globular α were reported to have fragmented from the α grains during the soaking period in the furnace. From the high-temperature anneal at 950 °C for 2 hours (above $\alpha' \rightarrow \alpha + \beta$ temperatures) and furnace cooling of DMLS Ti6Al4V, a duplex microstructure was achieved with lamellar grains within the prior columnar β grains and clusters of equiaxed nuclei of globular α [41][57]. These authors concluded that this microstructure of annealed DMLS Ti6Al4V (ELI) corresponded to the standard for biomedical applications required for annealed Ti6Al4V (ISO 20160, 2006) [41].

From the foregoing analysis, it is apparent that the consequences of HTA of conventionally produced Ti6Al4V and DMLS Ti6Al4V (ELI), both to bi-modal microstructures, include heating of the parts to around 950 °C and soaking them at this temperatures followed by cooling at rates between 1.5 °C/s and 20 °C/s. However, though the bi-modal microstructure of DMLS Ti6Al4V (ELI) obtained from these anneal parameters corresponds to that of standard biomedical Ti6Al4V (ISO 20160, 2006), the equiaxed α grains exist as nuclei of globular α which is not the case in conventionally produced Ti6Al4V (ELI) [41]. Moreover, from the visual inspection of the micrograph presented in the aforementioned references, those of equiaxed nuclei of globular α are less than the 30% volume fraction of equiaxed α suggested to give the best fatigue properties of Ti6Al4V. In this regard, it is

expected that HTA DMLS Ti6Al4V (ELI) specimens will have lower fatigue resistance than conventionally produced Ti6Al4V (ELI) treated with the same post-process anneal treatment.

2.8 Fatigue

Fatigue, as defined by ASTM E1150, is ‘the process of progressive localized permanent structural change occurring in a material subjected to conditions that produce fluctuating stresses (cyclic stresses) and strains at some point or points and that may culminate in cracks or complete fracture after a sufficient number of fluctuations.’ [58]. Fatigue fracture is a three-stage process that consists of crack initiation, crack propagation and sudden fracture of a material. The fatigue life (N_f) of a material is the sum of the number of load cycles it takes for a crack to initiate (N_i) and the number of load cycles it takes for the initiated crack to propagate (N_p) until the material fractures. These load cycles are normally of a sinusoidal form either between maximum and minimum tensile stresses or between maximum tensile stress and maximum compressive stress [59]. N_i depends on the value of the stress concentration factor (K_t) and N_p is dependent on the value of the stress intensity factor (K) [60]. The crack initiates and propagates under the influence of the aforementioned parameters until it reaches a critical length (a_c) which is used to calculate the fracture toughness (K_{IC}) of a material at which it suddenly shears [61]. The sinusoidal action of the cyclic stresses results in a local plastic strain and the generation of 3-dimensional stress fields where a crack initiates, while the tensile component of the cyclic stresses promote the propagation of the crack [58].

2.8.1 Stages of fatigue

Figure 2.10 shows a schematic of the stages of fatigue and the parameters that influence the number of load cycles of each stage.

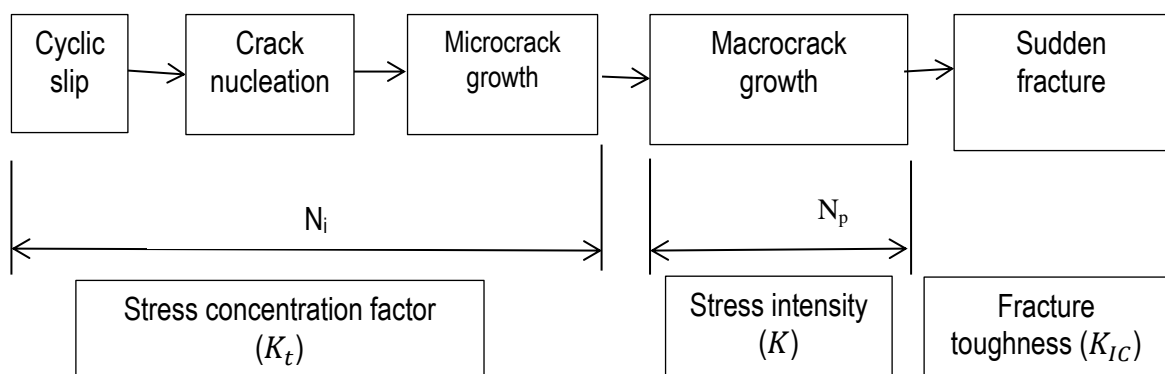


Figure 2.10: Different stages of fatigue life [15]

Stage 1: crack initiation – this is the critical stage in determining fatigue life as it can consume up to and beyond 75% of the fatigue life N_f [62][63] for HCF. The crack initiation life is influenced by the presence of stress concentration sites on the material as they accelerate local plastic deformation that initiates cracks. The stress concentration sites can arise from geometric discontinuities of design and manufacture like notches, holes, keyways and reduction or increase in diameter (component design). For all stress concentration sites, an increase in the stress concentration factor (K_t) leads to a decrease in the number of stress cycles required to cause localized plastic deformation, thereby reducing the number of cycles N_i required to initiate a crack. The stress concentration sites in DMLS Ti6Al4V (ELI) specimens arise from DMLS process-related micropores whose stress intensities during tension–tension loading are increased by the presence of the tensile residual stresses within the specimens [2]. As noted previously in section 2.7, the presence of tensile residual stresses within specimens during tension–tension fatigue testing increases the actual stress loads on the specimen, thereby increasing the mean stress, which in turn increases the stress ratio (R) during cyclic loading [57]. Therefore, the localized plastic deformation is from stress loads that are higher than those that are detected during a particular test.

Fatigue crack initiation for smooth polished flawless fatigue specimens occurs principally by slip plane cracking due to repetitive reversals of the active slip systems at the free surface of the metal, as displayed in Figure 2.11 [64].

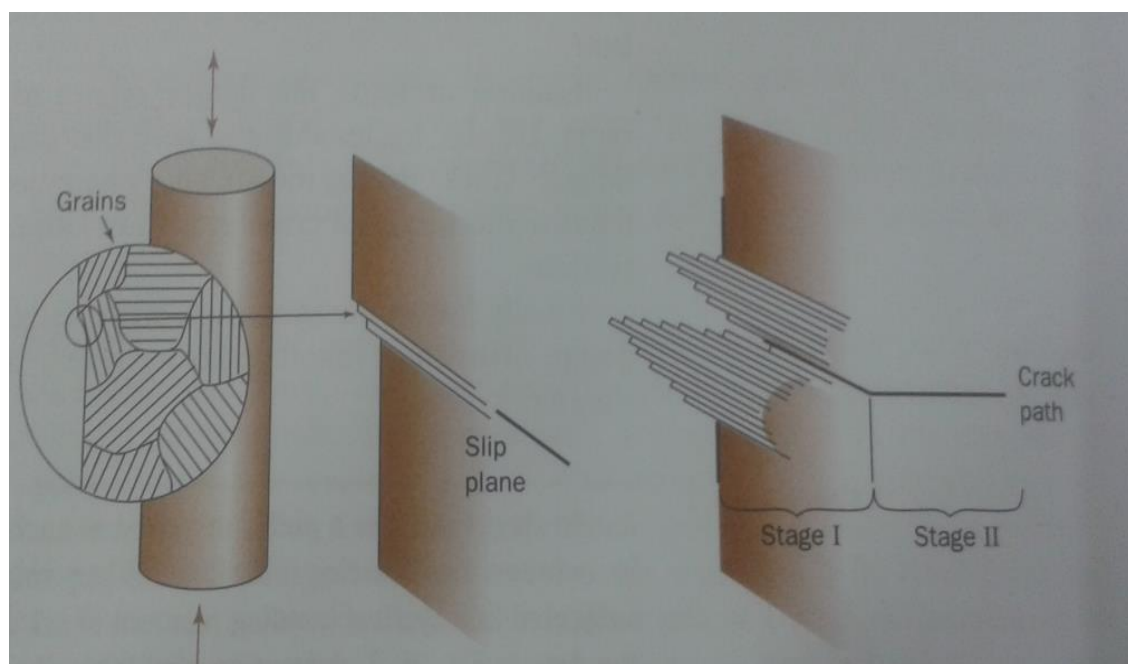


Figure 2.11: Stages in the development of a crack along a slip plane [65]

The cyclic stress drives dislocations on slip planes in crystals at or near the surface of a specimen leading to a pile-up of dislocations and the formation of slip bands as a result of shear strain [66]. After a certain number of these load cycles, the atomic layers at the free surface of a crystal undergo plastic shearing, forming slip bands that are schematically shown in Figure 2.11. The shear bands form extrusions and intrusions which form microstress concentration sites. With continued cyclic loading, the slip bands broaden and intensify to a point where separation occurs within one of the slip bands and a crack nucleates [65][67]. Once nucleated, the microcrack grows at an approximate angle of 45° to the principal stress direction. The microcrack growth is strongly influenced by the microstructure and the mean load stress [58]. It grows along a slip band within a grain until it reaches its boundary. The slip bands are known as persistent slip bands (PSBs) and were discovered by Thompson et al. [68] who revealed that when a rotating bending test was interrupted and a part electro-polished, the bands still appeared at the same point they were during loading.

Stage 2: crack propagation – this covers the largest area of the fatigue fracture surface. In this stage, the crack length becomes sufficient for the stress field at the crack tip to become dominant, and the overall direction of growth changes and becomes perpendicular to the principal stress (tension-driven) [69]. In this stage, the crack propagation is normally of a trans-granular mode forming a ragged zigzagged path (seen in Figure 2.12 (a)) as it navigates along grain boundaries, which is an easy path. Therefore, the phase and size of the grains determined by the process parameters of the heat treatment are important at this stage with regard to the resistance to the growth of cracks. However, this stage is more strongly influenced by the magnitude of the alternating load stresses than the mean stress and the microstructure as for stage 1 [58][70].

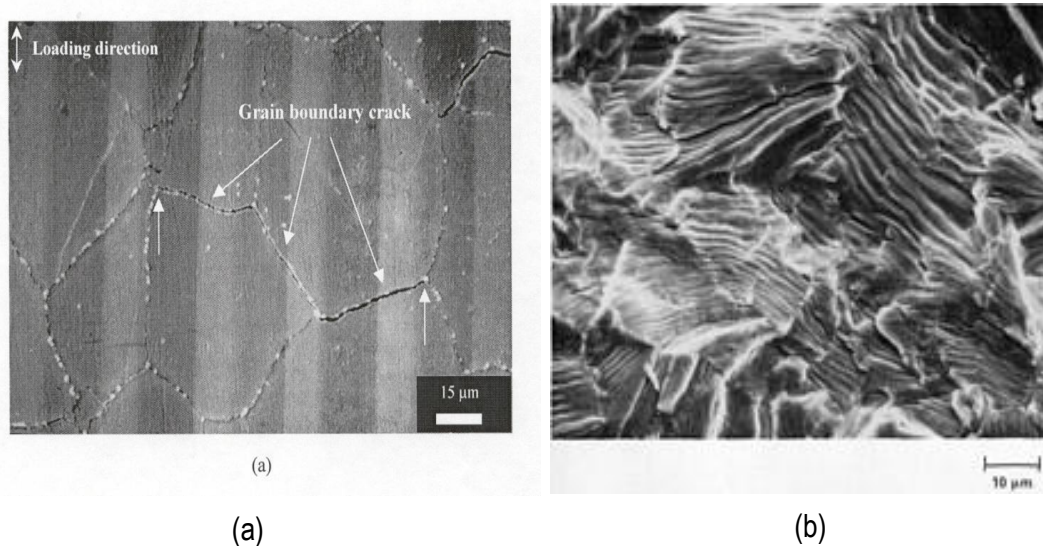


Figure 2.12: (a) Zigzag crack propagation along grain boundaries; (b) fractograph showing fatigue striations [71]

The fracture surfaces at this stage usually show striation marks which are crack arrest marks [62][64][66][70]. Striations similar to the ones shown in Figure 2.12 (b) are perpendicular to the direction of propagation of the crack and bow-out from the area of initiation of the crack, each striation representing one load cycle. The spacing between each successive set of striations is dependent on the magnitude of the alternating stress: increase in the magnitude of the alternating stress increases the spacing [70]. Increase in the magnitude of the alternating stress increases the fatigue crack growth rate ($\frac{da}{dN}$), which is defined by the Paris expression presented as Equation 2.2 [58]:

$$\frac{da}{dN} = C(\Delta K)^m \quad (2.2)$$

Where the symbols C and m are both material constants and ΔK the change in stress intensity factor. This expression was suggested to hold true for cracks advancing within the nominal range of 10^{-5} to 10^{-3} mm/cycle at a constant frequency of loading [70]. Since each striation represents one load cycle $\frac{da}{dN}$, it was concluded to represent the spacing of the striations [70].

Stage 3: final failure – in this stage, the crack has grown until the area of the applied force is so small as to create stresses that are higher than the UTS, thus leading to sudden fracture. The length of the crack at the beginning of this stage is referred to as the critical length (a_c) which, together with the applied stress load, results in the fracture toughness of a material (K_{IC}).

2.8.2 Categories of Fatigue

Fatigue is divided into two categories: low-cycle fatigue (LCF) and high-cycle fatigue (HCF). The two are distinguishable from each other by the magnitudes of the stress loads and the life cycle regimes at which each occurs. The stress levels associated with LCF are high enough to cause plastic deformation of the bulk specimen before fracture, while fatigue fracture in the category of HCF is from bulk stresses within the elastic range, as shown in Figure 2.13 [72].

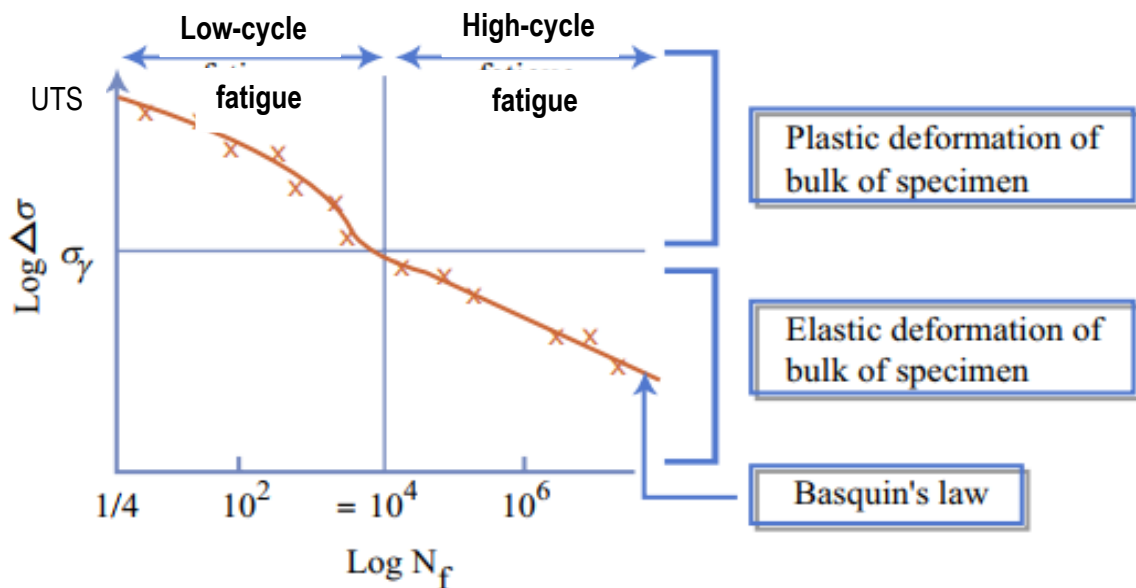


Figure 2.13: S-N curve showing low-cycle fatigue and high-cycle fatigue and corresponding N , σ_y represents the tensile yield strength [72]

The stress in LCF, because it occurs in the plastic region of the test specimens, is not directly related to strain through the elastic modulus but from a hysteresis loop [59][73]. Therefore, the LCF tests are conducted under strain control at constant stress amplitudes and the data points are characterized by a strain against the number of load cycles ($\epsilon - N$) for load cycles not exceeding 10^4 cycles [73][72]. The fatigue data points of LCF are fitted linearly in accordance with Coffin-Manson's law, shown here as Equation 2.3, which gives an inverse relationship of strain (ϵ) and number of load cycles (N);

$$\Delta\epsilon^{pl} = N_f^{-a}C \quad (2.3)$$

Where $\Delta\epsilon^{pl}$ is the change in plastic strain and a and C are constants.

The HCF test is conducted under stress-control mode at constant load amplitudes, because the stress is directly related to the strain through the elastic modulus. The data points are presented on semi-log S-N curves where S is the stress and N is the number of load cycles [74]. In HCF, the stress loads are below the yield stress of the specimens and the load cycles are between 10^4 and 10^7 [59][74]. On the S-N curves, HCF data points of fractured specimens are fitted linearly to Equation 2.4:

$$\Delta S = N_f^{-a} C \quad (2.4)$$

Equation 2.4 gives an inverse relationship of the stress range (ΔS) and number of life cycles (N) of the HCF fractured specimens and is referred to as Basquin's law, where symbols a and C are empirical constants [72]. The linear trend of the HCF fractured test specimens following Basquin's law continues up until about 10^6 load cycles where the curve turns horizontal, corresponding to the highest load of the run-out specimens at 10^7 load cycles [74]. This point is termed as the fatigue endurance limit, giving infinite fatigue life, which is inherent in the S-N curves of iron and its alloys, as well as titanium and its alloys [75][74].

There are two types of fatigue endurances, high-endurance fatigue (HEF) and low-endurance fatigue (LEF). The graph in Figure 2.13 shows LEF at load stresses equivalent to σ_y at load cycles less than 10^4 and HEF for load cycles of 10^6 to infinity (10^7) [73][74]. LEF is used on designs such as for an aircraft fuselage which is pressurized once every flight and may take years before 1000 cycles are accumulated [65]. From prior investigations on the fatigue properties of titanium and its alloys, it was concluded that for high-stress amplitudes (LCF), crack propagation (N_p) dominates the fatigue life (N_f) in a manner such that, $(\frac{N_i}{N_p} = 0.01)$ [7]. Therefore, LCF strength is governed by crack propagation cycles (N_p). The opposite is true for HCF strength, the value of which is predominantly determined by resistance to the initiation of cracks. As mentioned earlier, the focus of this study is on the fatigue properties of Ti6Al4V (ELI) medical implants produced by DMLS, which are expected to operate within the elastic range. The design stress of a DMLS Ti6Al4V (ELI) dynamic medical implant should therefore be based on the HEF of the alloy.

2.8.3 S-N curve

The commonly used method of determining the S-N curve is with an axial fatigue test machine whereby each specimen is loaded at a constant load amplitude at a set frequency. The applied load

is defined by a waveform with specific values of the stress amplitude, mean stress, and stress ratio, as shown in Figure 2.14.

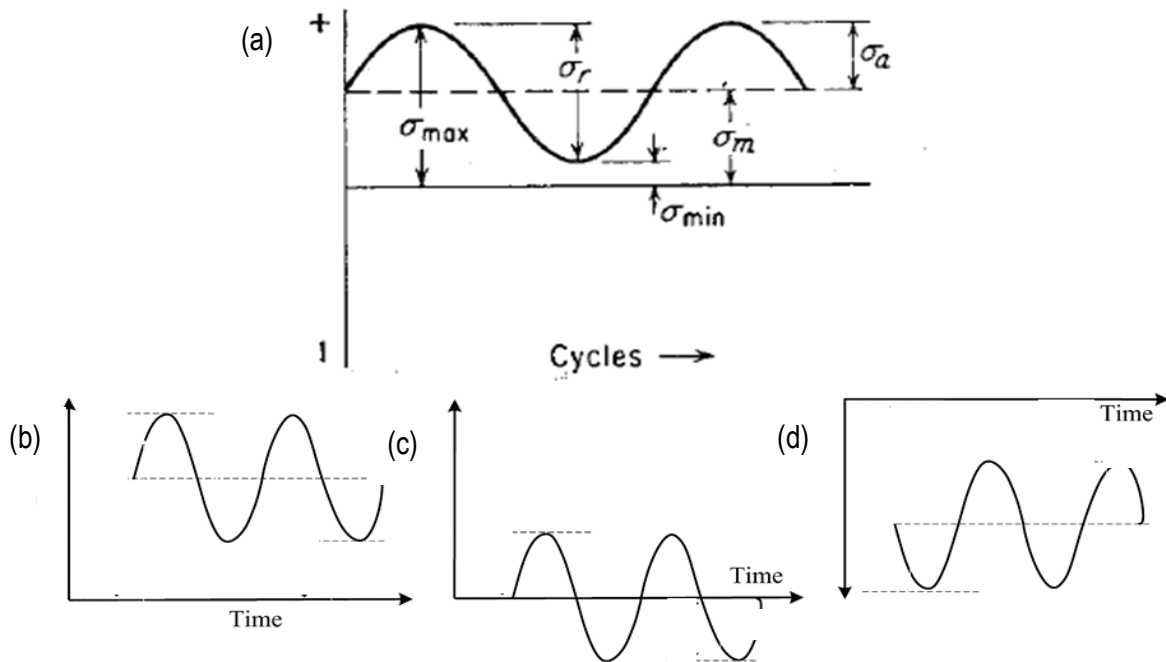


Figure 2.14: Typical fatigue stress cycles

In Figure 2.14 (a), σ_m denotes the mean stress, σ_{max} the maximum stress, σ_{min} the minimum stress, σ_a the stress amplitude and σ_γ the peak-to-peak range. It is evident from Figure 2.14 that:

$$\sigma_m = \frac{\sigma_{max} + \sigma_{min}}{2} \quad (2.5)$$

$$\sigma_a = \frac{\sigma_{max} - \sigma_{min}}{2} \quad (2.6)$$

$$\Delta\sigma = \sigma_\gamma = 2\sigma_a \quad (2.7)$$

$$R = \frac{\sigma_{min}}{\sigma_{max}} \quad (2.8)$$

R is defined as the stress ratio. To construct an S-N curve, the specimens are each subjected to a load at a selected value of σ_{max} with the same prescribed stress ratio, R and frequency. The prescribed R value and frequency have to be the same for all specimens for a set of tests in order to facilitate comparison of the results obtained [76]. The specimens are loaded cyclically until they

fracture or run-out. Run-out is set at 10^5 , 10^6 , 10^7 and 10^8 cycles or other values, as a function of the application. Upon completion of testing of all the specimens, their respective values of σ_{max} or σ_a and corresponding lives (N), represented as a value of $\log_{10}N$, are plotted giving a semi-log S-N curve.

Figure 2.14 (b) (c) and (d) show three different cyclic load regimes for the same σ_a , including tension–tension (Figure 2.14 (b)), tension–compression (Figure 2.14 (c)) or compression–compression (Figure 2.14 (d)). The stress ratios (R) for the compression–compression and tension–tension cyclic load regimes are both positive and lie between 0 and 1 [77]. In the case of tension–compression, the R value is less than zero. As stated here earlier, microcrack growth in the stage of initiation of cracks is influenced by the mean stress. An increase in the mean stress leads to an increase of R, which denotes a transition from tension–compression to either tension–tension or compression–compression fatigue conditions [76][77]. The transition of R from positive to negative increases the fatigue endurance limit of specimens [76].

2.8.4 Fatigue fracture surface

When the fractured fatigue specimens are viewed in a SEM, they portray three distinct areas depicting the three stages of fatigue discussed in section 2.8.1. Figure 2.15 shows a schematic representation of these stages of fatigue.

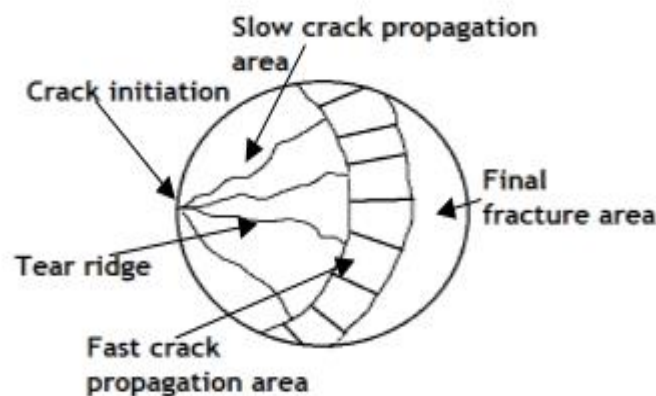


Figure 2.15: Schematic representation of a typical HCF fracture surface.

Crack initiation area – the crack initiation is influenced by the microstructure and the microcrack growth is influenced by the mean stress [58]. For flawless specimens, where the crack initiates from slip cracking, the crack initiation site is characterized by facets similar to cleavages [64].

Crack propagation area – as seen in Figure 2.15, in HCF fractured specimens, crack propagation typically covers the largest portion of the fracture surface, subject to stress levels, and can be subdivided into areas of stable (slow) and unstable (fast) crack propagation. This first stage is influenced by the magnitude of stress of the alternating load and occurs in a trans-granular or inter-granular manner depending on the magnitude of the load stress. The area of stable crack propagation is characterized by crack arrest marks (striations) which represent the position of the crack front during various cycles of crack propagation [62][64][66][70]. The striations are located on the faces of tear ridges and are perpendicular to the direction of propagation of cracks and bow-out from the site of initiation of cracks [67]. The tear ridges that are shown in Figure 2.15 originate from the point of initiation of a faceted crack and spread out to the area of stable propagation cracks. Their elevation increases with depth into the area of stable propagation of cracks and die out in the zone of overload; an area of unstable propagation cracks (fast propagation of cracks). In this area, the propagation of cracks is consistent with that of a monotonic loading and is characterized by shallow dimples.

Final fracture area – after the area of unstable propagation of cracks, the stresses ahead of the crack exceed the yield stress and the specimen finally fails and separates by shear. The final fracture shear surface is characterized by cleavage at about 45° .

2.8.5. Linear elastic fracture mechanics

The discontinuities present in the DMLS parts in the form of surface irregularities and porosity are sites of stress concentration, which could act as sites of crack initiation during HCF testing [78][79][80][81]. In this project, and in order to comply with test standards (ASTM E466-15 and ISO 12106), the test specimens for HCF testing were machined and polished. This specimen preparation process removed any existing DMLS-related surface irregularities, thus limiting the measured HCF properties to those of the bulk metal.

The DMLS process-related pores are small (maximum pore sizes of $132\ \mu\text{m}$ and $205\ \mu\text{m}$ were reported by Moletsane et al. [6] and Yadroitsev et al. [41], respectively) compared to the dimensions

of the HCF test specimens (gauge diameter of 5 mm and a gauge length of 25 mm) and can be treated as cracks within an infinitely large body. The schematic in Figure 2.16 shows a crack in an x-y plane of an infinitely large body exposed to a change in stress ($\Delta\sigma$) acting in the direction of the z-plane [82].

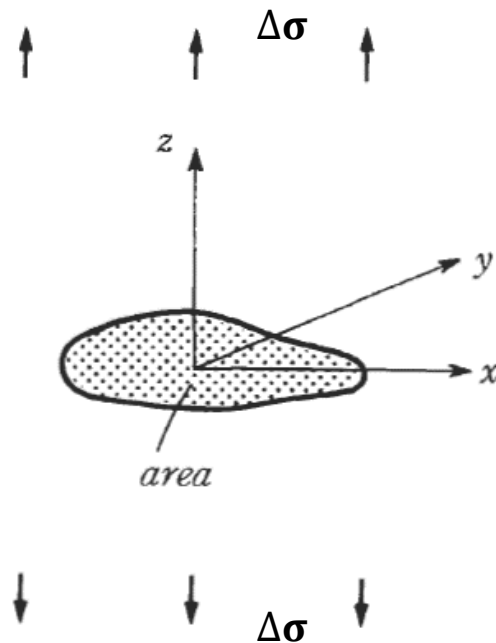


Figure 2.16: An internal crack of a denoted area within an infinitely large body [82].

The DMLS process-related pores result in a change in stress intensity factor (ΔK) during dynamic loading, the magnitude of which depends on the applied change in stress ($\Delta\sigma$), the projected pore area normal to the direction of action of the change in stress ($\Delta\sigma$), similar to the one shown in Figure 2.16, and its location, whether internal or at the surface. The initiation of cracks from these pores can be explained using the theory of linear elastic fracture mechanics (LEFM) applied to fatigue loading, where initiation and propagation of cracks from small defects and non-metallic inclusions are described by expression 9 [82][83][84]:

$$\Delta K = C\Delta\sigma\sqrt{\pi\sqrt{Area}} \quad (2.9)$$

In the above equation, the constant C is taken to be 0.65 for surface defects or non-metallic inclusions and 0.5 for internal defects or non-metallic inclusions [82][83][84]. A pore or inclusion that

results in a value of ΔK , which is larger than the change in stress intensity threshold (ΔK_{th}), will lead to propagation of the crack and eventual failure of the loaded object.

2.9 Summary

This chapter presented literature on additive manufacturing in general and with reference to direct metal laser sintering in particular. The manufacture of Ti6Al4V (ELI) parts by DMLS was discussed. It was noted that the acicular α' martensitic microstructure of DMLS Ti6Al4V (ELI) has the poorest fatigue properties of the four morphologies of the alloy that exist at room temperature. Porosity and surface irregularities in DMLS specimens are identified as sources of stress concentration whose intensities in tension–tension fatigue are increased by the presence of tensile residual stresses. Literature on phase transformation of the DMLS Ti6Al4V (ELI) alloy during high-temperature annealing (HTA) was presented to show this as a feasible way of improving the fatigue properties of the alloy. HTA was shown to lead to relaxation of residual stress and recrystallization of the acicular α' martensite microstructure, thereby negating the influence of both on fatigue resistance. The theory behind fatigue failure was then discussed with emphasis on HCF, the plot of the S-N curve and the HCF fracture surface. It was shown that the DMLS process related pores can be assumed to be pre-existing cracks thus Murakami's equation for the stress intensity can be used to estimate the stress intensities they impose.

CHAPTER 3 METHODOLOGY

3.1 Introduction

This research project aims at determining the HCF properties of post-DMLS Ti6Al4V (ELI) stress-relieved and HTA parts and their level of conformity to the internationally accepted specifications for such parts produced through conventional manufacturing routes. This was done by the HCF tension–tension testing of two sets of DMLS Ti6Al4V (ELI) specimens; as-built and post-DMLS stress relieved followed by HTA. Prior to HCF testing, a set of as-built specimens were investigated using ultrasonic through testing in order to determine the level of homogeneity and orthotropy in them. The specimens were then machined and polished down to the dimensions of fatigue test specimens specified in relevant standards. The stress-relieved plus HTA specimens were machined and polished down to the dimensions of tensile and fatigue test specimens specified in relevant standards. The test polished specimens were then scanned with a micro-CT scanner in order to locate and measure any inherent DMLS process-related pores. Upon completion of tensile and fatigue testing, the fracture surfaces of the tested specimens were studied under an optical microscope and in a scanning electron microscope to identify the origin of cracks and trace the propagation of cracks through the specimens.

3.2 DMLS Building of the Specimens

Two sets of 30 Ti6Al4V (ELI) rectangular bar specimens with width (W) of 12 mm, depth (D) of 12 mm and length (L) of 60 mm were built. The specimens were built by an EOSINT M 280 DMLS machine set to the standard process parameters, tabulated in Table 3.1, in an argon processing environment.

Table 3.1: Standard process parameters of the EOSINT M 280 DMLS machine

Parameter	Laser power (W)	Beam diameter (μm)	Scan speed (mm/s)	Hatch spacing (μm)	Layer thickness (μm)	Powder bed temperature ($^{\circ}\text{C}$)
Value	170	80	1200	100	30	45

One set of specimens was to be tested in the as-built condition (no post heat treatment) and the other set was to be heat treated prior to testing. As discussed in section 2.3, the DMLS machine

always fuses successive layers onto each other along the Z-axis of the machine. For both sets of specimens, ten bar specimens were built with their longitudinal axes orientated parallel to the X-axis, ten with their longitudinal axes parallel to the Y-axis and ten with their longitudinal axes parallel to the Z-axis of the machine, as shown in Figure 3.1 and shall hereafter be referred to as X-, Y- and Z-built specimens (see Nomenclature list).

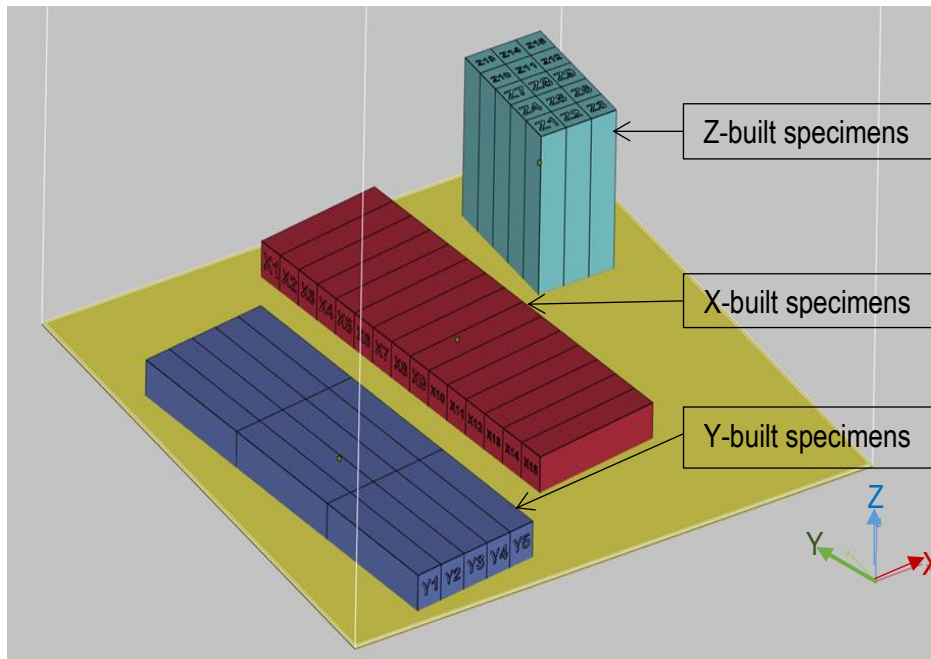


Figure 3.1: CAD model of 45 bar specimens on the DMLS build platform

Figure 3.1 shows a CAD model of the DMLS build platform with square bar specimens orientated along the three build axes of the machine.

Figure 3.2 shows the laser scanning strategy used to build the specimens in the EOSINT M 280 machine.

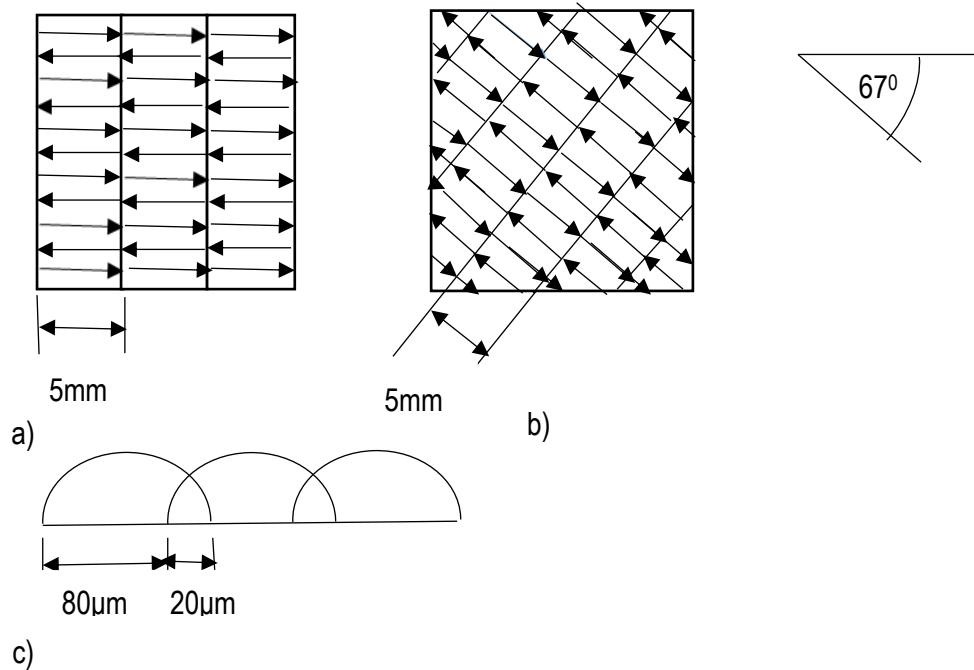


Figure 3.2: Layer-upon-layer laser scan strategy, (a) layer one showing strips with the back and forth laser scan strategy, (b) layer two showing an angle shift of the direction of the strips, (c) the layer hatch spacing and overlap of the melt pool.

A layer is formed by 5 mm wide strips in which the laser melts the powder in the back and forth patterns shown in Figure 3.2 (a) and (b) with the arrows representing the back and forth laser pattern. As the laser melts the powder, it forms a melt pool (hatch spacing) that is 100 μm wide, which overlaps with a previously melted track by 20 μm (hatch overlap), as shown on Figure 3.2 (c). The scanning is done at a speed of 1200 mm/s. When a layer is complete, the orientation of the back and forth laser strip scan pattern is rotated through an angle of 67° to build a subsequent layer, as seen in Figure 3.2 (b). The angle of the scan pattern rotates by 67° for each successive layer built until the part is complete. The Ti6Al4V (ELI) powder used for building the specimens in the present work was obtained from TLS Technik GmbH with a particle size range of <40 μm .

3.3 Calculation of Density

The density of the as-built samples was determined from measured values of weight and dimensions for the specimens in accordance with the equation:

$$\rho = \frac{m}{W \times B \times L} \quad (\text{g}/\text{cm}^3) \quad (3.1)$$

The width (W) and depth (D) of the bars were measured using a micrometre screw gauge (accuracy ± 0.005 mm) and the lengths (L) were measured using a Vernier calliper (accuracy ± 0.05 mm). It was appreciated that this approach would lead to an underestimation of the value of density. However, this would apply equally to all specimens. The bars were weighed on a WTC 200 Precision Balance (accuracy ± 0.0005 g).

3.4 Ultrasonic Testing for Homogeneity and Orthotropy

The Panametric NDT machine of the Department of Physics at Vaal University of Technology, with a 40 MHz 0° wave probe with a crystal size of $\varnothing 10$ mm, was used to determine the through-thickness wave velocity in the DMLS Ti6Al4V (ELI) specimens. The testing was performed according to the ASTM E 494-95 standard [85]. A coupling gel was used between the wave probe and the specimen to ensure there was no gap of air between the two. A total of eight ultrasonic through-thickness transmissions were done at equally spaced distances along the length of each specimen; four through the width, four through the depth and one through the length. The test data obtained was in terms of a round-trip transit time recorded for travel of a longitudinal wave from the ultrasonic probe to the extreme edge of the specimen and back to the point of start.

Due to constraints of time and malfunction of the ultrasonic shear probe signal injection, only the longitudinal back echo ultrasonic test was carried out. This meant that values of Poisson's ratio (ν), shear modulus (G) and Young's modulus (E) could not be calculated. However, calculated values of the longitudinal velocity (C_L) were considered adequate for use in investigating the existence or lack of heterogeneity and anisotropy of the material.

3.5 Post Heat Treatment

The second set of 30 DMLS Ti6Al4V (ELI) bar specimens were stress relieved and thereafter HTA-treated to recrystallize their acicular α' martensite grains to form a lamellar microstructure. Figure 3.3 shows the profiles of the post-DMLS stress relieving and subsequent HTA heat treatments.

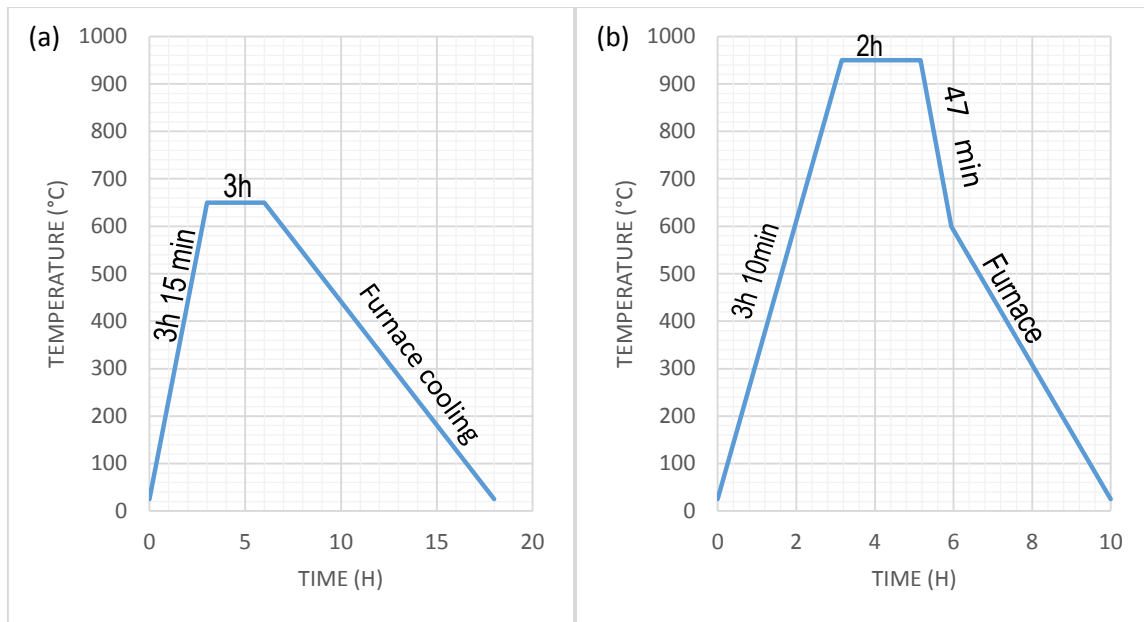


Figure 3.3: (a) Stress-relieving heat treatment parameters and (b) high-temperature annealing heat treatment parameters

Prior to the HTA treatment, while the specimens were still attached to the build platform, they were stress relieved by heating to 650 °C at a rate of 3.3 °C/min, held isothermally at this temperature for 3 hours and then furnace cooled to room temperature, as shown in Figure 3.3 (a). This was to relieve the specimens of the internal thermal residual stresses resulting from the DMLS process. The stress-relieving treatment was done in a horizontal carbolite furnace filled with argon to create an inert atmosphere that would limit the chances of the Ti6Al4V (ELI) reacting with oxygen. After stress relieving, the specimens were cut from the build platform using a wire electrical discharge machine and were thereafter placed in a horizontal vacuum tube furnace for recrystallization. The recrystallization tube furnace was heated at a rate of 5 °C/min to 950 °C which is above the $\alpha' \rightarrow \alpha + \beta$ temperature [57] and below the $\alpha + \beta \rightarrow \beta$ precipitation temperature [86]. At this temperature, the α' grain structure had completely transformed into the $\alpha + \beta$ phase. The parts were then held at 950 °C for 2 hours followed by controlled furnace cooling at a rate of 7.5 °C/min to 600 °C, after which the furnace was switched off with the specimens kept in it overnight to cool to room temperature. The HTA was done under high vacuum of 10^{-5} Torr. The parameters for the HTA are shown in Figure 3.3 (b).

3.6 Machining of Tensile and Fatigue Test Specimens

Six square bars from the HTA DMLS Ti6Al4V (ELI) specimens (two orientated along each of the three machine axes) were machined and polished down to round uniaxial tensile test specimens with threaded grip ends, according to ASTM E8/E8M (with a gauge length four times the gauge diameter). For the fatigue specimens, the as-built Ti6Al4V (ELI) bars were machined after the density calculations and the ultrasonic testing had been done, while the HTA specimens were machined after application of the stress relieving and HTA heat treatments. All these fatigue specimens were machined and polished down to round HCF tension–tension specimens with tangentially blending fillets between the test section and the ends, according to ASTM E466 (with a gauge length four times the gauge diameter). The dimensions of the tensile and fatigue test specimens are shown in Appendix 1.

The machining was done by turning the square bars on a centre lathe. The first step was to turn the specimens down to the nominal diameter of the standard specimen plus 0.25 mm at a feed rate of 0.5 mm per pass. This was followed by turning of the centre profile down to its true diameter plus 0.25 mm at a feed rate of 0.2 mm per pass. The specimens were then ground to give a fine finish. They were finally polished in the longitudinal direction on a Morrison Specimen Polishing Machine using an 800 grit paper for 15 minutes, followed by a 1200 grit paper for 20 minutes. Polishing was carried out in the longitudinal direction of the specimens to avoid introducing scratches in the critical transverse direction. For both the turning and grinding processes, a Castrol Biocut CE Plus cutting fluid was used. The resulting surface finish from the foregoing machining and polishing procedure was 0.10 μm .

3.7 Micro-CT Scanning of High-Temperature Annealed Specimens

The gauge lengths of the specimens were micro-CT scanned using the General Electric V/TomeX L240 scanner system at the Stellenbosch University Central Analytical Facilities, set to optimum parameters. The X-ray source was set to 160 KV and 100 μA and a copper beam filtration of 0.5 mm, with a voxel size set to 15 μm . The acquisition time for the images was set to 333 ms per image and was recorded in 800 rotation steps during a full 360 degree rotation of the sample. At each step position, the first image was discarded and the subsequent two images averaged to provide high quality. The detector shift was activated to minimize ring artefacts and an automatic

scan optimizer was activated to eliminate artefacts due to possible movement of the specimens or drift of the X-ray spot. Reconstruction was performed in system-supplied Datos reconstruction software. Visualization and analysis were performed in Volume Graphics VGStudioMax 3.1 software. Further details of the hardware can be found in reference [87], and the optimization procedure to obtain the high-quality data that was used in this work is detailed in reference [88]. For all specimens, the projected area of each pore identified in micro-CT data in the location of the eventual fracture plane (suspected to be crack initiation pores), was used to calculate a stress-intensity factor (ΔK). In this work, three selected data sets (X12, Y12 and Z12) were further analysed by first selecting 2 mm sections in the vicinity of the fracture plane, followed by further image smoothing and defect analysis. This allowed the proper identification of all pores in the location of final failure and therefore, identification of the “killer pores”. It also availed more detailed information on the pores. Visualization of this region alone was simplified by using colour coding to show the distance of the pores relative to the surfaces of the respective specimens.

3.8 Tensile Testing

The machined and polished stress-relieved plus HTA DMLS Ti6Al4V (ELI) tensile test specimens were tension-tested at the ISO 17025-accredited CSIR Mechanical Testing Laboratory in Pretoria, South Africa on an Instron 1342 servo-hydraulic testing machine with a clip-on extensometer of 12.5 mm. The tests were conducted at a strain rate of 0.5 mm/min and 1.5 mm/min after removal of the extensometer.

3.9 Fatigue Testing

HCF tension–tension fatigue tests of the machined DMLS Ti6Al4V (ELI) specimens were carried out at the ISO 17025-accredited CSIR Mechanical Testing Laboratory in Pretoria, South Africa following the test criteria tabulated in Table 3.2.

Table 3.2: Tension–tension fatigue test criteria

Test standards	ASTM E466 – 15 and ISO 1099
Equipment	50 kN Instron 1342, Axial, Servo Hydraulic
R-ratio	0.1
Control mode	Stress control mode
Frequency	10 Hz
Temperature	20 \pm 2 °C
Run-out	5 \times 10 ⁶

The testing of the specimens was conducted at constant amplitudes of stress loads under a controlled force mode according to ASTM E466 – 15 and ISO 1099. Ten specimens were cycled under tension–tension fatigue in order to provide data for the plots of each of the semi-log₁₀ S-N curves presented in this project. The run-out number of load cycles from which the fatigue endurance limits of each set of the tested specimens were estimated, was set at 5,000,000 load cycles.

The 0.2% offset proof strength of the as-built DMLS Ti6Al4V (ELI) was reported to be 1098±2 MPa from publications on the tensile properties of CRPM-produced specimens [6][41]. Therefore, the first specimen in each set of the as-built DMLS Ti6Al4V (ELI) specimens was tested at 675 MPa (61% of the 0.2% offset proof strength) in order to obtain fracture at a fairly short number of load cycles. This was based on Dieter's recommendation that the highest value for σ_{max} is to be set at around two-thirds of the 0.2% proof strength [76]. The expected fatigue endurance limit for Ti and its alloys is in the range 45–60% of their 0.2% offset proof strengths, which translates to 490–660 MPa for as-built DMLS Ti6Al4V (ELI) [6][41][89]. This sets the limiting maximum value of σ_{max} . However, due to the presence of the residual stresses in as-built DMLS Ti6Al4V (ELI) specimens discussed in section 2.6.2 and suggested to reduce the fatigue strength of specimens, the next specimen in each set of the as-built DMLS Ti6Al4V (ELI) was cycled at the σ_{max} of 360 MPa, which is 31% of the 0.2% proof strength. At this maximum stress level, a run-out of the specimen was expected. The remaining specimens were cycled at σ_{max} levels set at intervals between 675 MPa and 360 MPa.

The maximum stress levels for each set of HTA DMLS Ti6Al4V (ELI) specimens were set between 675 and 450 MPa. These maximum stress levels are 82% and 55% of the 0.2% offset proof strength of HTA DMLS Ti6Al4V (ELI) specimens, as determined in this project. At the maximum stress level of 675 MPa, fracture of the specimens was expected at a fairly low number of load cycles and at 450 MPa, the specimens were expected to run-out as it is within the range of the fatigue endurance limit of Ti and its alloys. The stress load levels for each of the tested DMLS Ti6Al4V (ELI) specimens are presented in tables preceding their respective semi-log₁₀ S-N curves in chapter 4.

3.10 Metallographic Analysis

Metallographic analyses of both the as-built- and stress-relieved plus HTA-treated DMLS Ti6Al4V (ELI) specimens in the three mutually orthogonal DMLS build orientations were performed. This was achieved by cutting small cross-sections from bars in each of the three DMLS build orientations for

both the as-built- and stress-relieved plus HTA-treated DMLS Ti6Al4V (ELI) specimens using a wire electron discharge machine. The cross-sections were mounted in a Multi-fast non-conductive resin in a Citopress-1 machine shown in Figure 3.4 (a). This mounting process takes 5.5 minutes, of which 3.5 minutes are for heating and compacting of the Multi-fast granules to a temperature of 180 °C at a pressure of 250 bar followed by subsequent water cooling for 2 minutes. The mounted specimens were ground and polished using the Struers Tegramin-25 machine shown in Figure 3.4 (b) according to the guidelines suggested by Struers for Ti6Al4V.

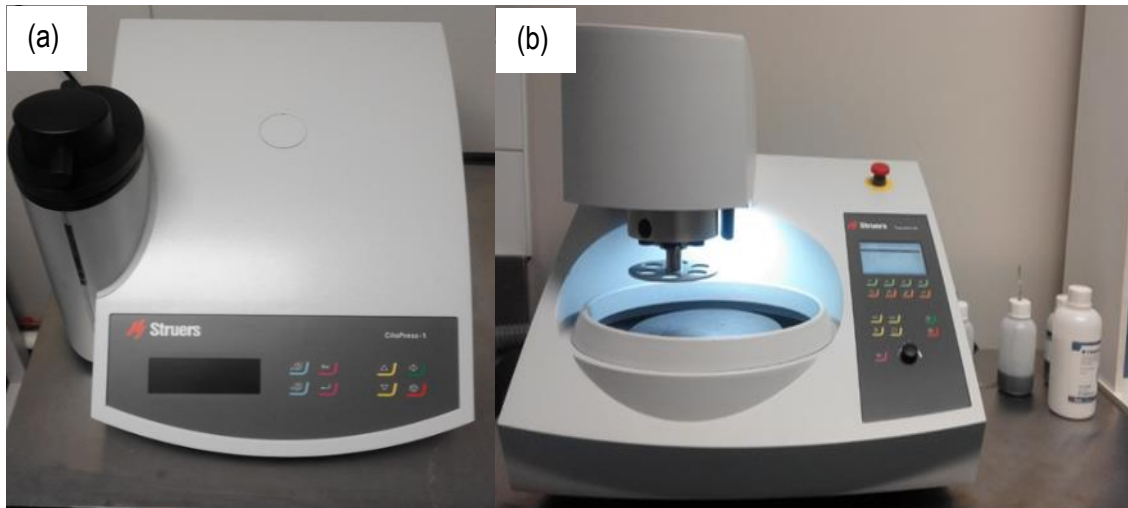


Figure 3.4: (a) Citopress-1 and (b) Struers Tegramin-25 machines

Table 3.3 shows the sequence for the grinding and polishing of mounted specimens and materials used, as recommended for the Struers Tegramin-25.

Table 3.3: The recommended grinding and polishing procedure for the Struers Tegramin-25

Process	Disc	Lubricant	Force (N)	Speed (rpm)	Time (min)
Coarse Grinding	320 SiC	Water	25	300	1.50
Fine Grinding	MD-Largo	DiaPro All/Lar.9	30	150	5.00
First Polishing	MD-Mol	DiaPro Mol.3	25	150	2.20
Final Polishing	MD-CHEM	OP-S Suspension	20	150	1.50

The first step in the grinding and polishing process was grinding the surfaces of the specimens with a silicon carbide (SiC) grinding paper of 320 grit with water as a cooling and lubricating medium. The specimens were further ground to a fine surface finish on an MD-largo disk using a Diapro diamond suspension with a particle size of 9 μm . After fine grinding, the specimens were polished using a 3 μm particle size Diapro diamond suspension on an MD-Mol cloth disc. Finally, the specimens were given a mirror finish by polishing with an Op-S suspension on an MD-Chem disc. After each of the

aforementioned grinding and polishing stages, the specimens were cleaned with tap water and then in the UC-02 ultrasonic cleaner, shown in Figure 3.5 (a), for 3 minutes.

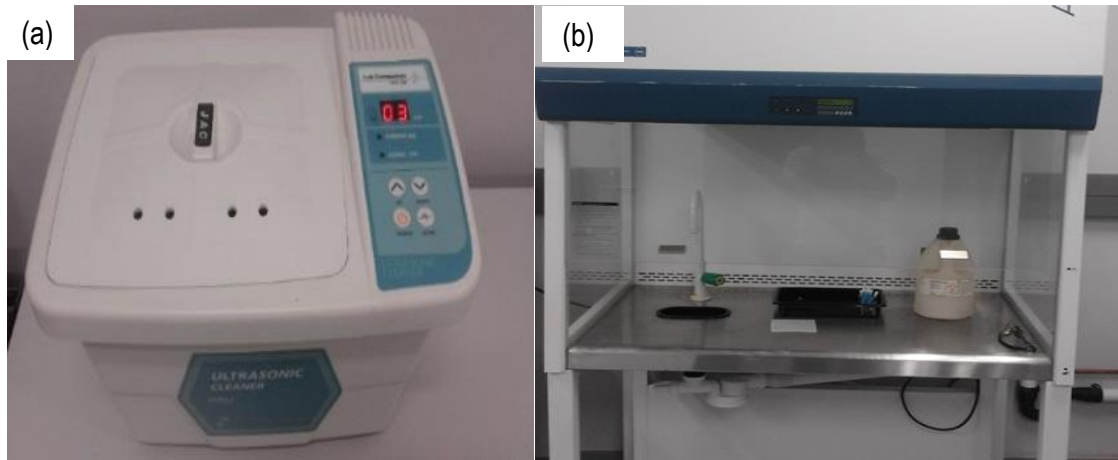


Figure 3.5: (a) Ultrasonic cleaner and (b) ESCO fume hood

When the grinding and polishing process was complete, the specimens were etched in the ESCO fume hood, shown in Figure 3.5 (b), with a Kroll's reagent to reveal the grain structure of the specimens. The Kroll etchant is a solution of 5 ml of nitric acid (HNO_3), 10 ml of 48% concentrated hydrofluoric acid (HF) and 85 ml of water (H_2O).

The microstructures of the etched specimens were viewed and captured by the ZEISS Axio Scope A1 optical microscope shown in Figure 3.6.

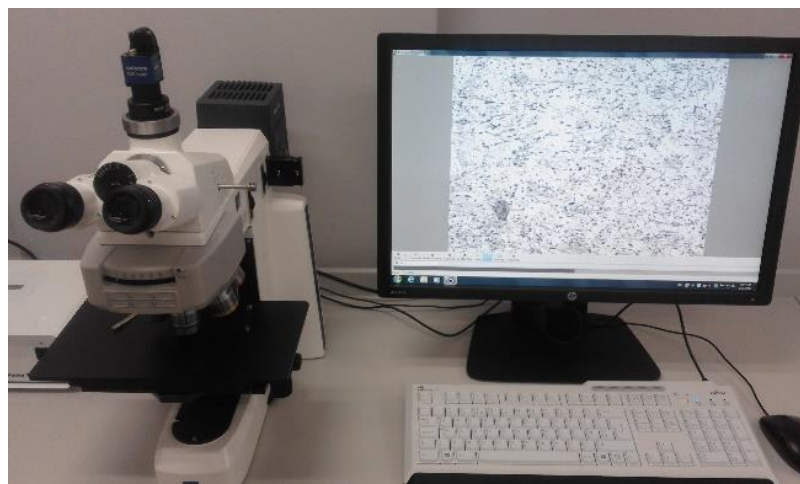


Figure 3.6: ZEISS Axio Scope A1 optical microscope

3.11 Fractography

The fracture mechanisms of tensile- and HCF-fractured DMLS Ti6Al4V (ELI) specimens were analysed in a JOEL JSM-7800F scanning electron microscope (SEM) shown in Figure 3.7. The analysis was done using the secondary electron imaging (SEI) mode of the SEM under 10–20 KV at working distances up to 10 mm.



Figure 3.7: JOEL JSM-7800 SEM

CHAPTER 4 RESULTS AND DISCUSSIONS

4.1 Introduction

This chapter presents the results from the tests conducted following the test procedures described in chapter 3 and the discussion thereof. It includes results and discussion of the ultrasonic through-thickness tests for orthotropy and homogeneity of as-built specimens. This is followed by metallographic analysis of the as-built, uniaxial tensile tests and tension–tension fatigue tests of both as-built- and stress-relieved plus HTA specimens. The fatigue properties found for the as-built- and stress-relieved plus HTA specimens, as well as the characteristics of their fracture surfaces are presented and discussed. Micro-CT scan results of pore size and location in these specimens are also discussed. The results for the as-built- and stress-relieved plus HTA-treated specimens are also compared here.

4.2 Density

It was found that all of the bar specimens had a constant geometry throughout except for specimens 11 to 15 which had a step along the width. Therefore, specimens 11 to 15 were left out in the calculations of density.

The average densities, density expressed as percentage of the theoretical density, and the respective standard deviations for the as-built DMLS Ti6Al4V (ELI) X-, Y- and Z-built bar specimens are given in Table 4.1.

Table 4.1: Calculated values of densities of the specimens tested for various build orientations

Number of specimen	10	5	10
Build orientation	X	Y	Z
Average density (g/cm ³)	4.26±0.05	4.38±0.05	4.28±0.05
% of the theoretical density	96	99	97
Standard deviation	0.05	0.22	0.01
Percentage variation of the mean density from the theoretical density	-3.84%	-1.13%	3.39%

The theoretical density of wrought Ti6Al4V (ELI) for surgical implants is 4.43 g/cm³ [90]. The overall average density as percentage of the theoretical density in Table 4.1 is 97%. The calculated values of density compared well with the theoretical value, with percentage variations of the mean values from the theoretical density of -3.84%, -1.13% and 3.39% in the X-, Y- and Z-built specimens, respectively. These percentage variations are all below the highest measurement percentage error of 5% arising from use of the Vernier calliper and are therefore considered acceptable. The small percentage variations indicate that the density of DMLS Ti6Al4V (ELI) has no discernible dependency on the build orientation.

4.3 Ultrasonic Longitudinal Test Results

The calculated values of ultrasonic longitudinal velocity for as-built DMLS Ti6Al4V (ELI) X-, Y- and Z-built specimens are presented in Tables 4.2, 4.3 and 4.4 respectively, and are discussed after each table of results. The following ASTM E494-48 equation was used to calculate the ultrasonic longitudinal velocities of the specimens [85].

$$\text{Ultrasonic longitudinal velocity } (C_L) = \frac{\text{thickness}}{\frac{1}{2} \text{round-trip transit time}} \quad (4.1)$$

4.3.1 Orthotropy in the X-, Y- and Z-built as-built DMLS Ti6Al4V (ELI) specimens

4.3.1.1 X-built specimens

Table 4.2 shows the average ultrasonic longitudinal velocities (C_L) recorded and standard deviations for the X-built specimens along the x-, y- and z-axes.

Table 4.2: x-, y- and z- axis average values of C_L for X-built specimens

Echo transmission direction	x-axis	y-axis	z-axis
Signal average round-trip time (4t) (s)	39.51×10^{-6}	7.2×10^{-6}	8.22×10^{-6}
Thickness of transmission (mm)	60	11	12
Average longitudinal velocity (m/s)	6084	6154	6230
Standard deviation	71.25	59.2	197.56

In the X-built specimens, the average ultrasonic velocities are seen in Table 4.2 to increase in the order, x-, y- and z-axis. This would imply orthotropy. The determined values of velocity as percentage of the theoretical velocity are 98.6%, 99.7% and 100.9% in these three directions, respectively. The standard deviations of the mean velocities in the three mutually orthogonal directions are small, namely 1.17%, 0.96% and 3.17% in the x-, y- and z-axis directions, respectively. This implies a small scatter of data from the mean, from one specimen to the other in the same direction. Therefore, it is reasonable to conclude that the X-built DMLS Ti6Al4V (ELI) specimens are homogeneous.

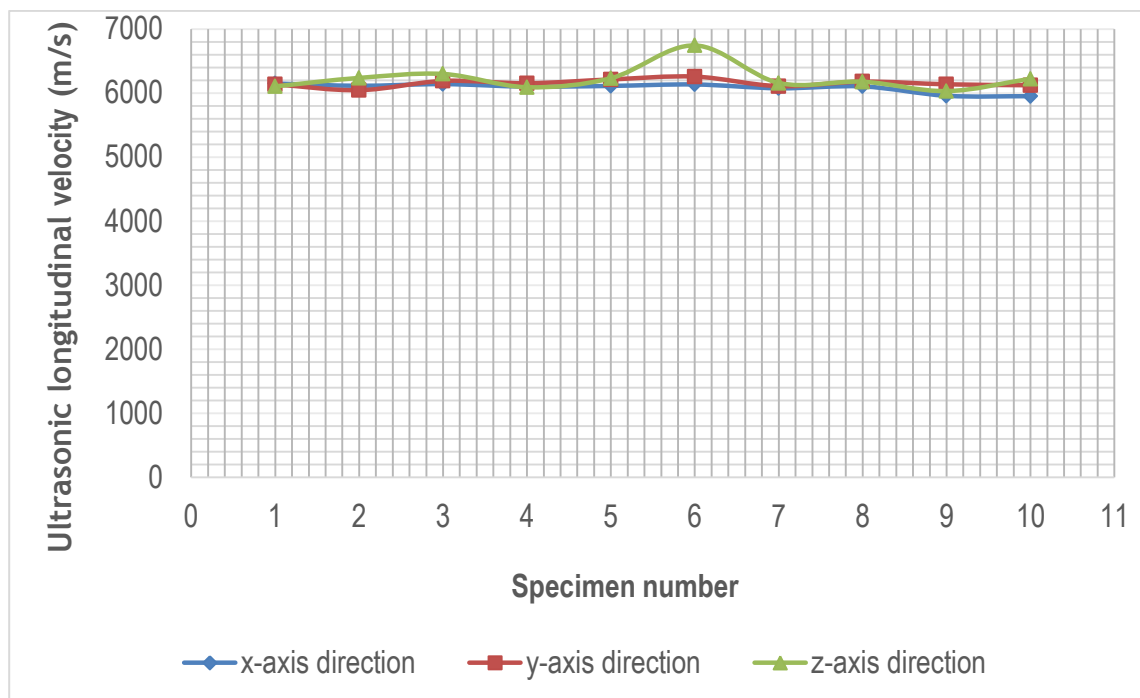


Figure 4.1: Average values of C_L in the x-, y- and z-axis directions for the X-built specimens

The curves in Figure 4.1 are clustered together with an outlier for specimen X-6 in the z-axis direction. It is evident from the clustering of the data that the directional variation of the ultrasonic velocity is small. The X-built as-built DMLS Ti6Al4V (ELI) specimens may therefore be taken to be isotropic, within the limits of experimental error.

4.3.1.2 Y-built specimens

Table 4.3 shows the measured average ultrasonic longitudinal velocities and standard deviations of the Y-built specimens in the x-, y- and z-axis directions. The average velocities are seen in the table

to increase in the order of y-, x- and z-axis and are percentages of the theoretical velocity of 98.6%, 98.9% and 99.4%, respectively.

Table 4.3: x-, y- and z-direction average values of C_L for Y-built specimens

Echo transmission direction	x-axis	y-axis	z-axis
Signal average round-trip time (4t) (s)	7.32×10^{-6}	39.38×10^{-6}	8.03×10^{-6}
Thickness of transmission (mm)	11	60	12
Average (m/s)	6105	6087	6135
Standard deviation	164.36	58.44	117.64

The standard deviations of the mean velocities in the three mutually orthogonal directions are small compared to the mean values, being 2.69%, 0.96% and 1.92% in the x-, y- and z-axis directions, respectively. This implies a small scatter of data from the mean, from one specimen to the other in the same direction. As was observed for the X-built specimens, it is therefore reasonable to conclude that the Y-built as-built DMLS Ti6Al4V (ELI) specimens are homogeneous.

Figure 4.2 shows the ultrasonic longitudinal velocities of the 10 Y-built specimens in the x-, y-, and z-axis directions.

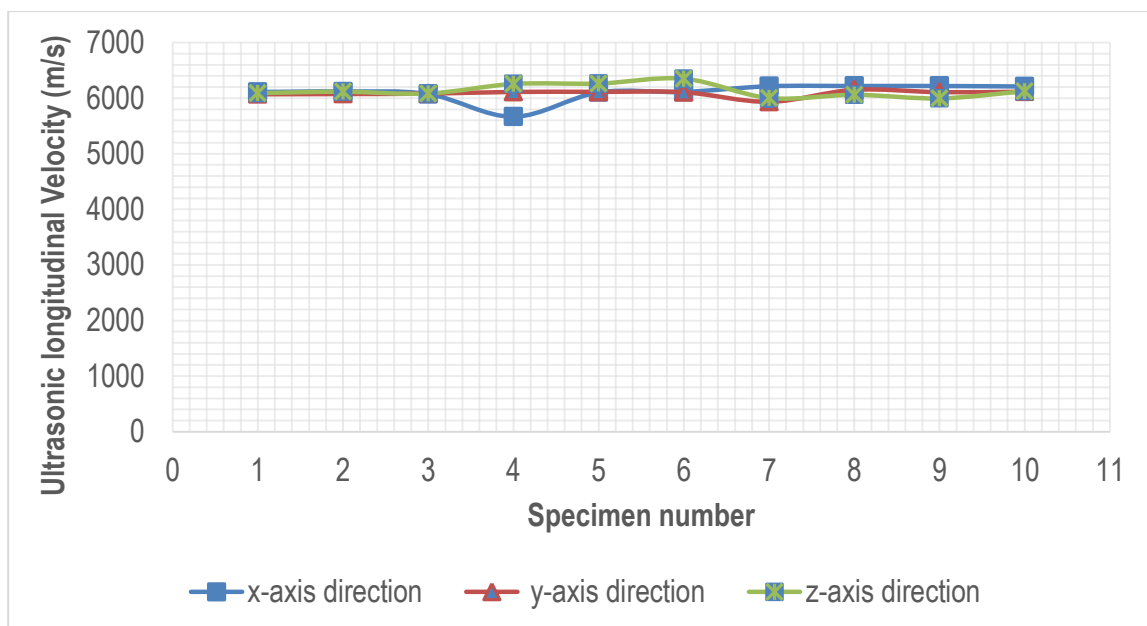


Figure 4.2: Average values of C_L in the x-, y- and z-axis directions for the Y-built specimens

The curves in Figure 4.2 are clustered together with an outlier for specimen 4 in the x-axis direction. Therefore, the Y-built DMLS Ti6Al4V (ELI) specimens may be taken to be isotropic, within the limits of experimental error.

4.3.1.3 Z-built specimens

Table 4.4 shows the measured average ultrasonic longitudinal velocities and standard deviations of the Z-built as-built DMLS Ti6Al4V (ELI) specimens in the x-, y- and z-axis directions, respectively.

Table 4.4: x-, y- and z-direction average values of C_L for Z-built specimens

Echo transmission direction	x-axis	y-axis	z-axis
Signal average round-trip time ($4t$) (s)	7.20×10^{-6}	7.17×10^{-6}	40.51×10^{-6}
Thickness of transmission (mm)	11 mm	11 mm	60 mm
Average (m/s)	6166	6199	6058
Standard deviation	100.33	154.13	192.23

In the Z-built specimens, the average ultrasonic velocities also portray an orthotropic characteristic, as was seen in the previous two tables, with an increase in this case in the order, z-, x- and y-axis. These velocities as percentages of the theoretical velocity are 98.2%, 99.9% and 100.4% in these three directions, respectively. The standard deviations of the mean velocities in the three mutually orthogonal directions are small compared to the mean values, being 1.63%, 2.49% and 3.17% in the x-, y- and z-axis directions, respectively. This implies a small scatter of data from the mean, from one specimen to the other in the same direction. As was observed for the other two mutually orthogonal-direction-built specimens, it is therefore reasonable to conclude that the Z-built DMLS Ti6Al4V specimens are homogeneous, as evident from the curves of velocity shown in Figure 4.3.

Figure 4.3 shows the ultrasonic longitudinal velocities of the 10 Z-built specimens in the x-, y-, and z-axis directions.

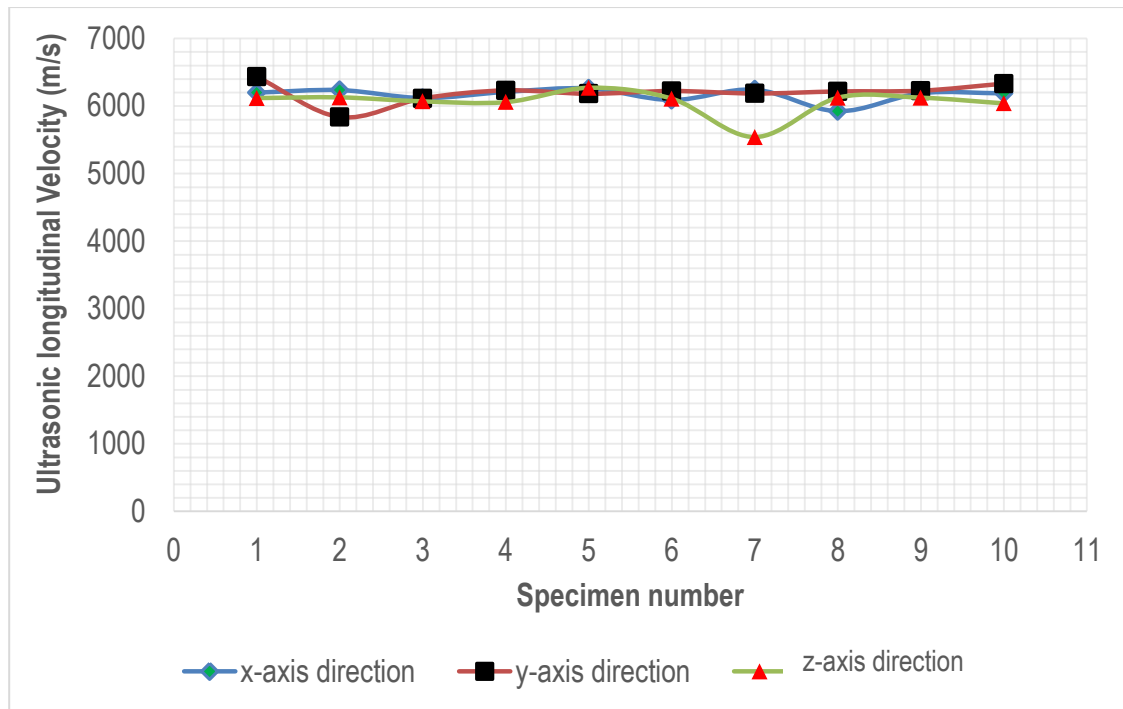


Figure 4.3: Average values of C_L in the x-, y- and z-axis directions for the Z-built specimens

As was the case for the X- and Y-built specimens, the results of longitudinal velocity in the x-, y- and z-directions are seen in Figure 4.3 to be clustered, with exceptions of the values for specimens 2 and 7 for the y-axis and z-axis directions, respectively. This denotes isotropy of the DMLS Ti6Al4V (ELI) material, within the limits of experimental error.

Comparing the mean values for the three cases discussed so far, the X-, Y- and Z-built specimens show that the ultrasonic longitudinal velocities increase from the x-axis direction through to the z-axis direction for the X-built specimens, from the y-axis direction through to the z-axis direction for the Y-built specimens, and from the z-axis direction through to the y-axis direction for the Z-built specimens. The fact that the lowest velocity in each case is in the longitudinal axis direction of each respective set of specimens implies higher densities of the DMLS Ti6Al4V (ELI) material in this direction. There is, however, no apparent order in the relative magnitudes of the ultrasonic longitudinal velocities with reference to the remaining two mutually orthogonal directions in each set of specimens, despite the build strategy being the same in all specimen-orientation directions.

4.3.2 Homogeneity in the X-, Y- and Z-built as-built DMLS Ti6Al4V (ELI) specimens

The ultrasonic through-thickness test was used to test the presence or lack of homogeneity only along the lengths of the test bars as this provided opportunity to obtain a number of readings along one surface. For the X-built specimens, the ultrasonic signal was injected in both the x- and y-axis directions separately, at different positions along the length of the bars. Similarly, for the Y- and Z-built specimens, the ultrasonic signal was injected in both the z- and x-axis directions and the x- and y-axis directions, respectively.

4.3.2.1 X-built specimens

Table 4.5 shows the average ultrasonic longitudinal velocities for ten specimens, measured at intervals of 15 mm along the length of each specimen. The average velocities given in the table are for transmission of an ultrasonic wave in the y- and z-axis directions.

Table 4.5: Average values of longitudinal velocity (C_L) in the y- and z-axis directions of the X-built specimens

Position	1	2	3	4	Average	Standard deviation
Number of specimens	10	10	10	10		
y-axis direction average ultrasonic longitudinal velocity C_L (m/s)	6196.2	6162.52	6112.97	6145.6	6153.93	34.042
Standard deviation	156.37	79.08	112.04	90.74		
z-axis direction average ultrasonic longitudinal velocity C_L (m/s)	6375.14	6196.15	6143.95	6182.95	6224.55	102.81
Standard deviation	596.81	225.5	161.95	96.42		

The standard deviations of the y-axis direction and z-axis direction transmission of an ultrasonic signal taken along the length of the X-built specimens equal to 0.55% and 1.65% of the calculated mean values, respectively. These are very small deviations, as is evident from inspection of the curves shown in Figure 4.3.

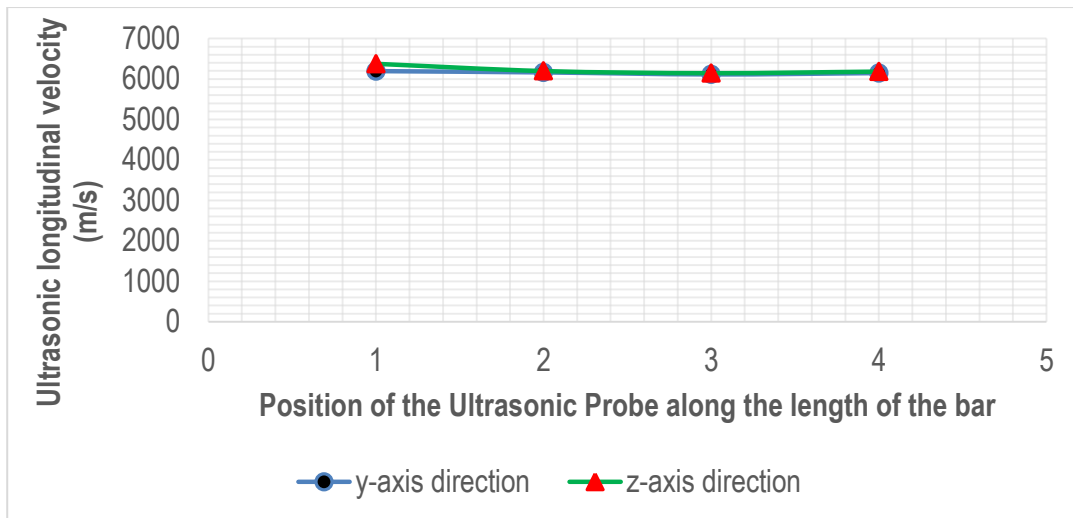


Figure 4.4: Ultrasonic longitudinal average velocities in the y- and z-axis directions of the X-built bars

It can be concluded from the data in Table 4.5 and from the two curves in Figure 4.4 that the DMLS Ti6Al4V (ELI) material is homogeneous in the X-built specimens.

4.3.2.2 Y-built specimens

Table 4.6 shows the average ultrasonic longitudinal velocities for ten specimens, measured at intervals of 15 mm along the length of each specimen. The average velocities given in the table are for transmission of an ultrasonic wave in the z- and x-axis directions.

Table 4.6: Average values of longitudinal velocity (C_L) in the x- and z-axis directions of the Y-built specimens

Position	1	2	3	4	Mean	Standard deviation
Number of specimens	10	10	10	10		
x-axis direction average ultrasonic longitudinal velocity C_L (m/s)	6085.65	6069.75	6147.21	6118.21	6105.21	34.51
Standard deviation	206.40	239.97	135.85	137.33		
z-axis direction average ultrasonic longitudinal velocity C_L (m/s)	6140.67	6069.23	6124.14	6205.07	6134.78	55.93
Standard deviation	269.60	115.15	199.13	115.47		

The standard deviations of the x-axis direction and z-axis direction transmission of an ultrasonic signal taken along the length of the Y-built specimens are equal to 0.57% and 0.91% of the calculated mean values, respectively. These are very small deviations, as is evident by inspection of the curves shown in Figure 4.4.



Figure 4.5: Ultrasonic longitudinal average velocities in the x- and z-axis directions of the Y-built bars

As was the case for the X-built specimens, the data in Table 4.6 and the two curves in Figure 4.5 lead to the conclusion that the DMLS Ti6Al4V (ELI) material is homogeneous in the Y-built specimens.

4.3.2.3 Z-built specimens

Table 4.7 shows the ultrasonic longitudinal average velocities for ten specimens measured at intervals of 15 mm along the length of each specimen. The average velocities given in the table are for transmission of an ultrasonic wave in the x- and y-axis directions.

Table 4.7: Average values of longitudinal velocity (C_L) in the x- and y-axis directions of the Z-built specimens

Position	1	2	3	4	Mean	Standard deviation
Number of specimens	10	10	10	10		
x-axis direction average ultrasonic longitudinal velocity C_L (m/s)	6221.11	6154.48	6213.89	6076.17	6166.41	67.16
Standard deviation	43.74	144.08	23.63	342.48		
y-axis direction average ultrasonic longitudinal velocity C_L (m/s)	6103.23	6389.11	6191.75	6111.23	6198.83	133.00
Standard deviation	415.82	673.99	107.71	290.35		

The standard deviations of the x-axis direction and y-axis direction transmission of an ultrasonic signal taken along the length of the Z-built specimens are equal to 1.09% and 2.15% of the calculated mean values, respectively. These are very small deviations, as is evident by inspection of the curves shown in Figure 4.6.

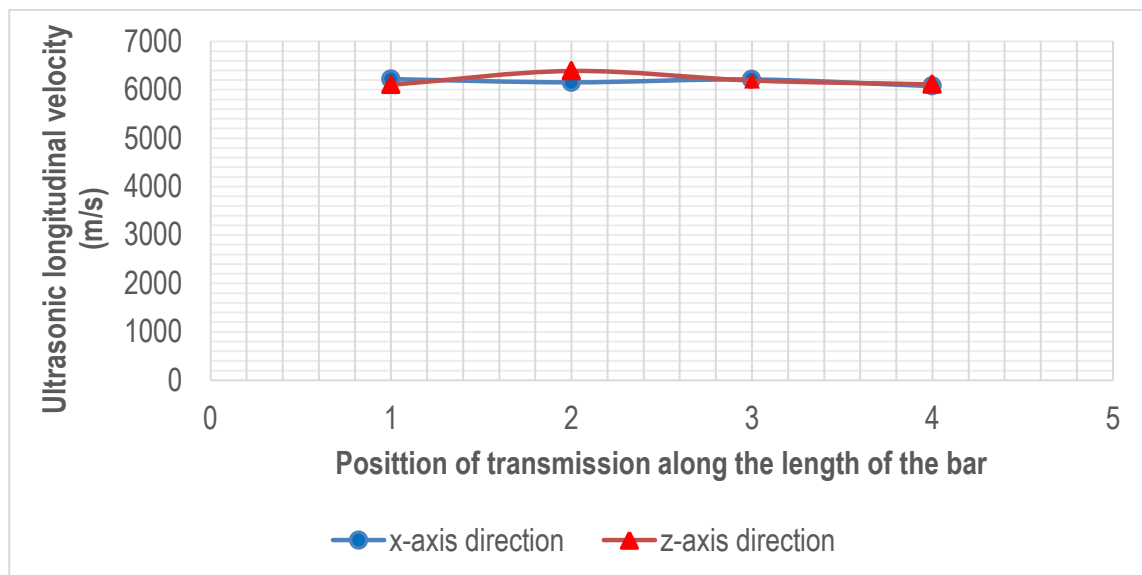


Figure 4.6: Ultrasonic longitudinal average velocities in the x- and y-axis directions of the Z-built bars

As in the previous two cases, the data in Table 4.7 and the two curves in Figure 4.6 lead to the conclusion that the DMLS Ti6Al4V (ELI) material is homogeneous in the Z-built specimens.

4.4 Microstructural Analysis of DMLS Ti6Al4V (ELI) Specimens

The mechanical properties of Ti6Al4V (ELI) specimens depend on their grain morphology. For heat treatment of the alloy at temperatures above the β phase field, increase in the cooling rate moderately increases the alloy's yield stress and elongation [91]. The moderate increase in the yield stress and the elongation holds true for cooling rate increases up to water quenching, above which the yield stress increases drastically and the elongation drops [91]. This is because of a transformation of the beta alloy into a metastable acicular α' martensite microstructure at cooling rates above water quenching. The above discussion explains the high yield stress and low elongation of as-built DMLS Ti6Al4V (ELI). The metastable α' microstructure also has a poor crack initiation resistance because the elongated grains of the acicular α' martensite provide effective slip planes. Therefore, the decomposition of the acicular α' martensitic microstructure into the $\alpha + \beta$ microstructure upon heating above the beta transus temperature and subsequent cooling, increases the ductility and lowers the yield strength, which leads to an increase in fatigue strength.

This section shows the micrographs and discusses the microstructure of as-built DMLS Ti6Al4V (ELI) specimens produced in this work. It also shows micrographs and discusses the microstructures of DMLS Ti6Al4V (ELI) specimens after stress relieving and high-temperature annealing heat treatment as produced in this study.

4.4.1 As-built DMLS Ti6Al4V (ELI)

Figure 4.7 shows micrographs of as-built DMLS Ti6Al4V (ELI) specimens that were produced and sectioned across and along the direction of build-up of the layers, respectively. The micrographs show a basket-weave microstructure of needles within prior β columnar grains.

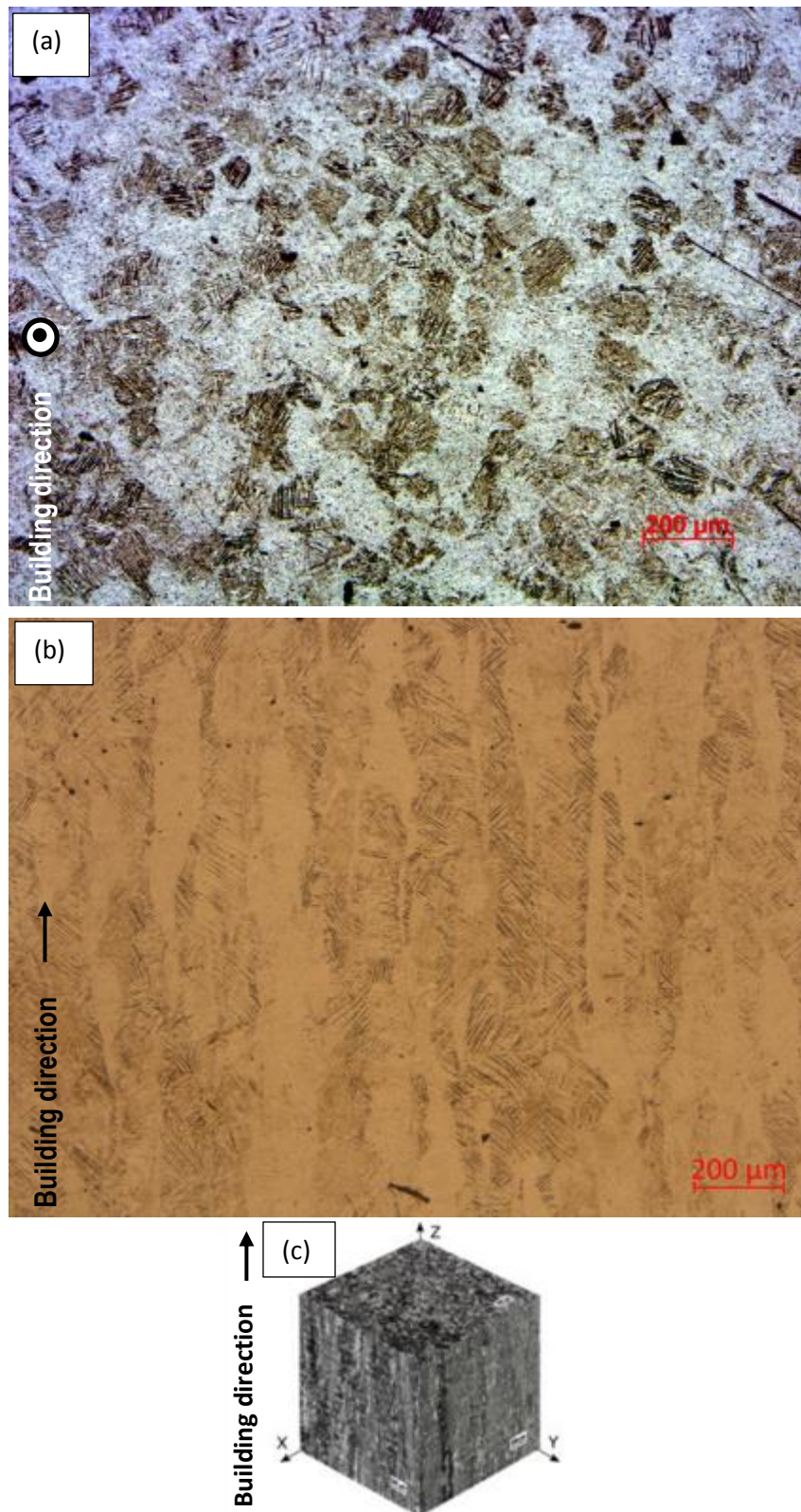


Figure 4.7: Micrograph of as-built DMLS Ti6Al4V (ELI) sectioned in the x, y plane (a) and micrograph of as-built DMLS Ti6Al4V (ELI) sectioned in the x, z plane (b).

Figure 4.7 (a) presents a micrograph of an as-built Ti6Al4V (ELI) specimen sectioned in the x-y plane (see also Figure 4.7 (c)), which shows equiaxed primary β grains that have transformed into fine basket weaves of α' grains that appear bright and coarse colonies of acicular α' that appear dark. The average diameter of these equiaxed transformed β grains was determined based on ASTM E112 and was found to be 80 μm .

Figure 4.7 (b) presents a micrograph of the same specimen sectioned in the x-z plane, showing fine (bright areas) and coarse (dark areas) basket weaves of acicular α' grains within the prior β columnar grains. The maximum width of the acicular α' grains presented in Figure 4.7 was approximated to be 2.6 μm , which conforms to an article by Ter Haar et al. [92] that the width of the acicular α' grains ranges from 1 μm to 3 μm .

4.4.2 Stress-relieved and high-temperature annealed DMLS Ti6Al4V (ELI)

Figure 4.8 shows a micrograph of stress-relieved DMLS Ti6Al4V (ELI) sectioned in the y-z plane of an X-built specimen.

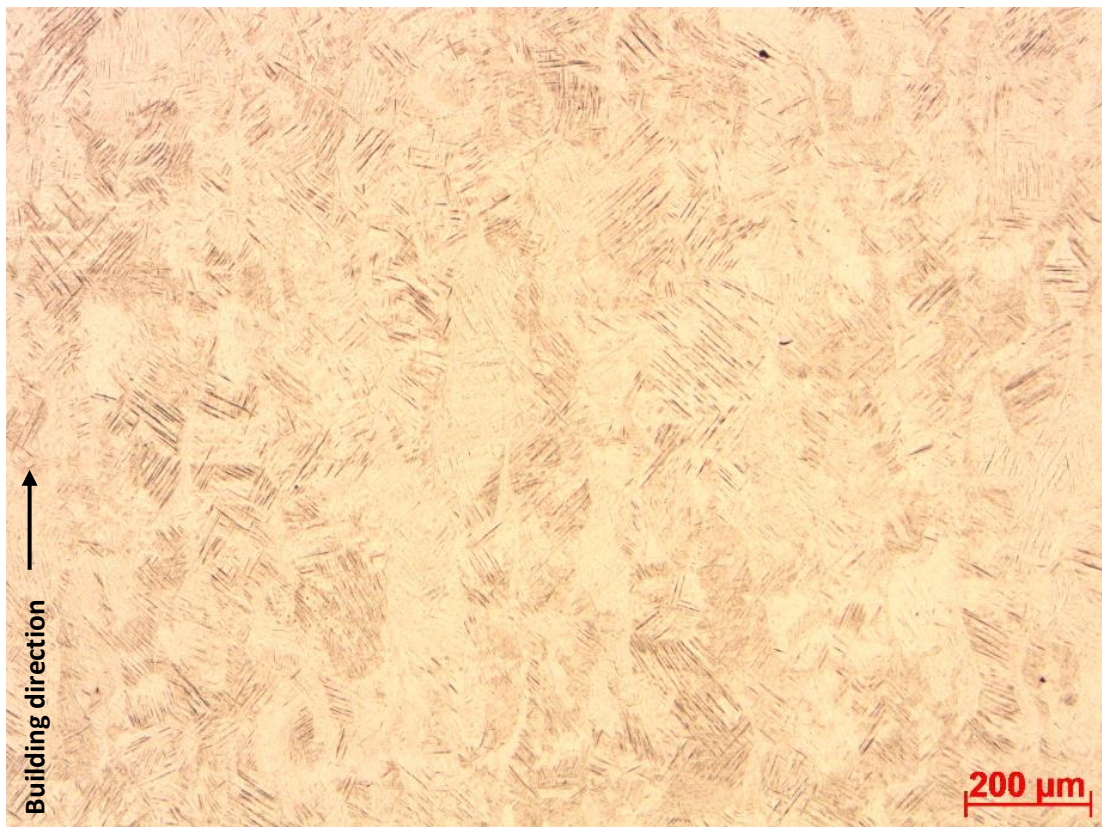


Figure 4.8: Micrograph of an X-built specimen after stress relieving

It is evident from Figure 4.8 that there was no decomposition of the α' basket-weave structure within the prior β grains which were found in the as-built DMLS Ti6Al4V (ELI) after the stress-relieving process. Therefore, the stress relieving of as-built DMLS Ti6Al4V (ELI) does not change the grain structure and grain morphology of the specimens (compare Figure 4.7 (b) with Figure 4.8). However, the stress relieving improved the ductility and therefore fatigue resistance of the DMLS Ti6Al4V (ELI) [41][6][93].

Figure 4.9 shows micrographs of the X- and Y-built DMSL Ti6Al4V (ELI) specimens (horizontally built specimens) after stress relieving followed by HTA. The micrograph of the X-built specimen is for a section in the y-z plane and that of the Y-built specimen is in the x-z plane (see Figure 4.7 (c) for a detail of the z, y and z axes).

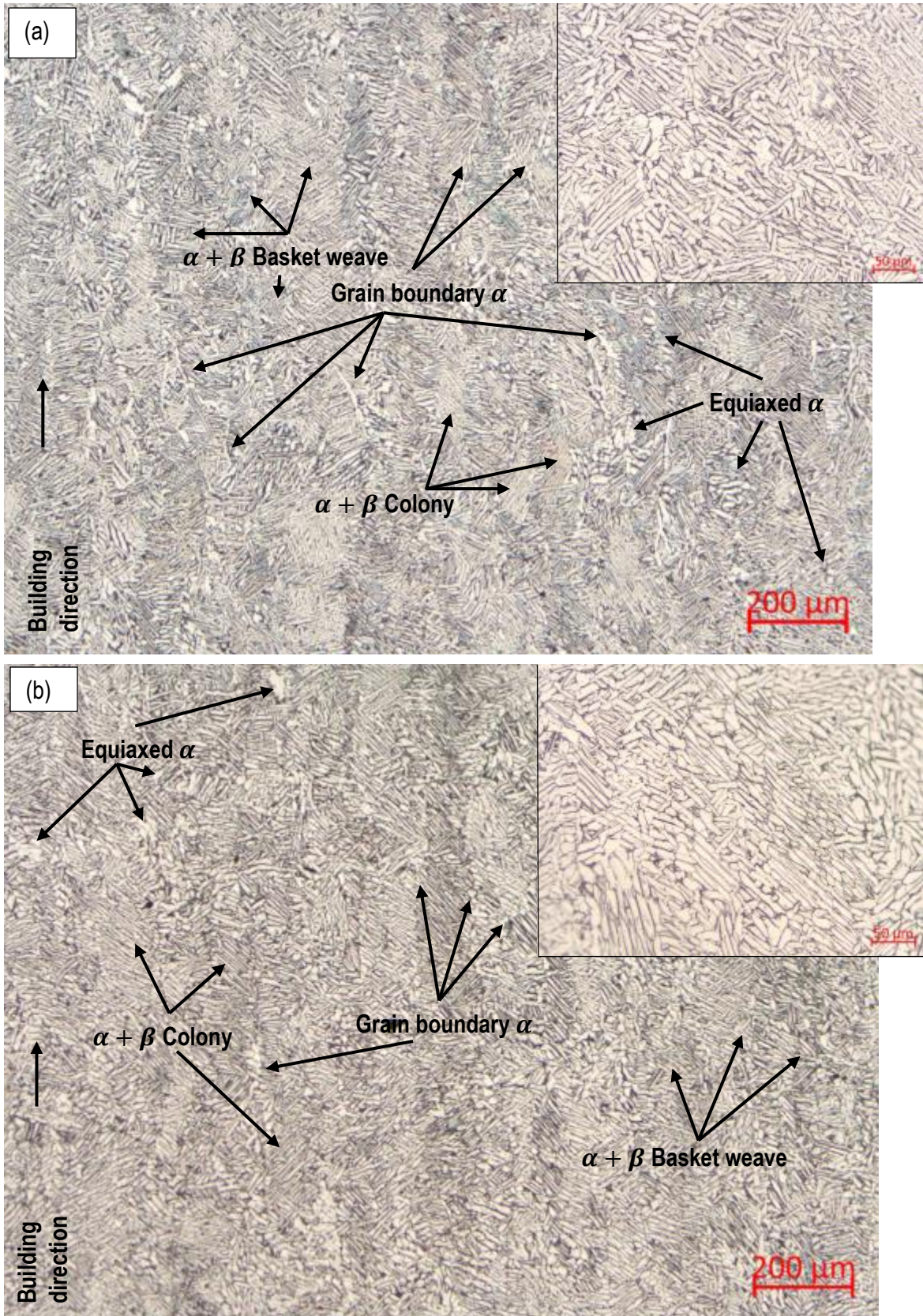


Figure 4.9: Micrographs of DMLS Ti6Al4V (ELI) stress relieved, followed by HTA at 950 °C for 2 h and furnace cooled (a) X-built specimen and (b) Y-built specimen

The HTA of the DMLS Ti6Al4V (ELI) specimens at 950 °C resulted in a complete decomposition of the non-equilibrium α' grain structure to an equilibrium $\alpha + \beta$ grain structure. The grains consist of basket weaves and colonies of $\alpha + \beta$ lamellae with uneven distributions of nuclei of equiaxed α grains indicated by the red, yellow and blue arrows, respectively, in Figures 4.9 (a) and (b). However, the morphology of the prior β columnar grains formed by epitaxial growth of the β grains during the DMLS process, whose grain boundaries are indicated by green arrows in Figures 4.9 (a) and (b), did not change. These arrows also indicate α phase that had nucleated along these grain boundaries. Figure 4.9 (a) and (b) represent the grain structure that is parallel to the DMLS layer build-up direction and perpendicular to the fatigue loading axes for the X- and Y-built specimens. The average width of the α laths in the X-built HTA DMLS Ti6Al4V (ELI) specimens (Figure 4.9 (a)) was found to be 6.1 μm and that in the Y-built HTA DMLS Ti6Al4V (ELI) specimens (Figure 4.9 (b)) was 6.7 μm .

Figure 4.10 shows micrographs of Z-built DMSL Ti6Al4V (ELI) specimens (vertically built specimen) after stress relieving followed by HTA. The micrograph is for a section in the x-y plane (see Figure 4.7 (c) for a detail of the z-, y- and z-axes).

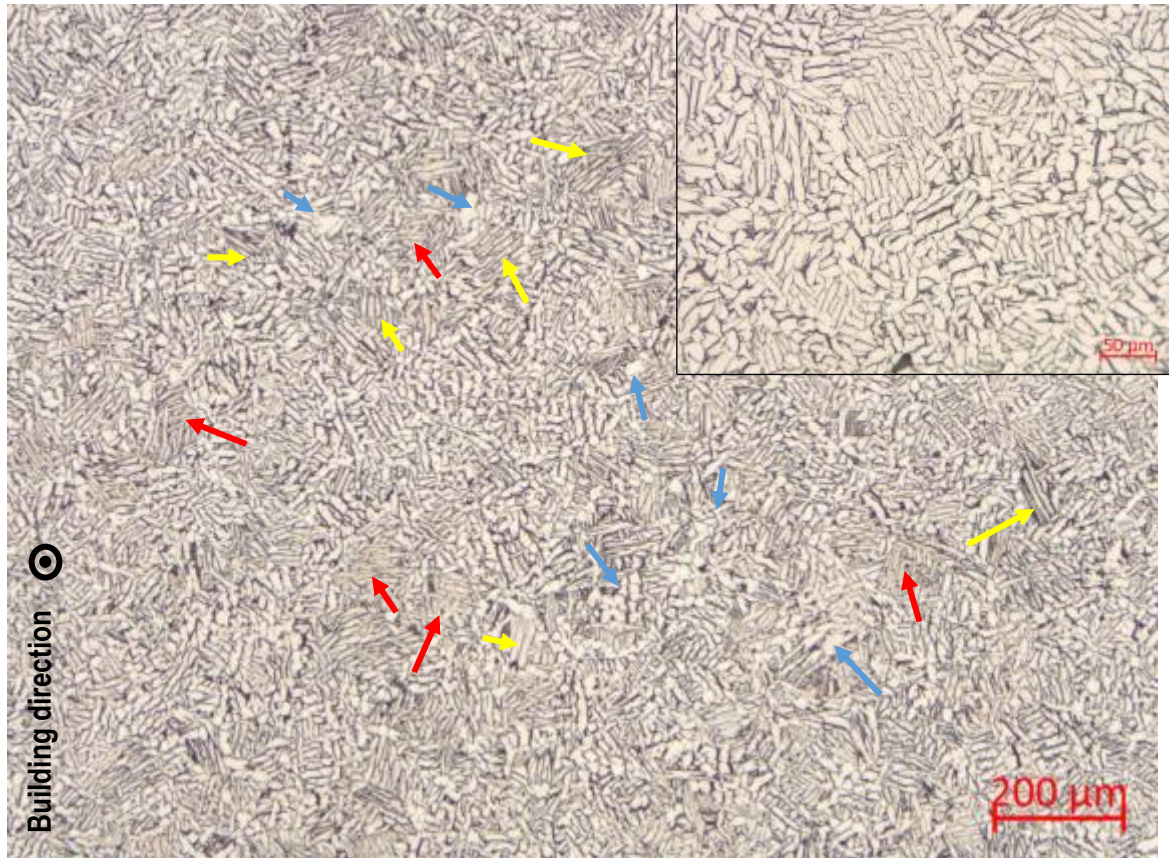


Figure 4.10: Micrograph of DMLS Ti6Al4V (ELI) stress relieved followed by HTA at 950 °C for 2 h and furnace cooled, for Z-built specimens

This micrograph shows complete decomposition of the α' grain structure to the $\alpha + \beta$ grain structure. From this micrograph, colonies of $\alpha + \beta$ grains (indicated by yellow arrows in Figure 4.10) are seen. The $\alpha + \beta$ colonies are separated by fragmented plate-like α grains with β grain boundaries [92]. An uneven distribution of nuclei of equiaxed α grains (indicated by blue arrows in Figure 4.10) resulting from the fragmented α laths is observed. There is a higher distribution of these equiaxed α nuclei than in the X- and Y-built specimens shown in Figure 4.10. The average width of the colonies of α laths was found to be $5.5 \mu\text{m}$ and the average width of the fragmented plate-like α grains was found to be $7.5 \mu\text{m}$.

It is evident from the foregoing that HTA following on stress relieving leads to complete decomposition of the acicular martensitic microstructure into colonies of $\alpha + \beta$ grains that are separated by fragmented plate-like α grains with β grain boundaries or equiaxed α grains. This has an effect of increasing the ductility and decreasing the strength of DMLS Ti6Al4V (ELI) and therefore enhances the alloy's fatigue resistance.

4.5 Tensile Properties

Tensile tests were performed to identify whether the static tensile properties of stress-relieved and HTA DMLS Ti6Al4V (ELI) specimens produced in this study conform to the standard specifications of the conventionally produced Ti6Al4V (ELI) parts intended for hard tissue prostheses. The graphs of tensile stress against strain of the high-temperature annealed DMLS Ti6Al4V (ELI) specimens built in the X-, Y- and Z-built orientations are shown in Figure 4.11. The curve for specimens 2, 3, 4, 5 and 6 were presented translated on the x-axis scale to the right hand from zero by 0.009, 0.015, 0.023, 0.031 and 0.038 for a clear display of any similarities or contrasts of the tensile properties of the tested specimens. In Figure 4.11, the numbers 1 and 2 indicate specimens X-1 and X-2, 3 and 4 specimens Y-1 and Y-2 and 5 and 6 specimens Z-1 and Z-2.

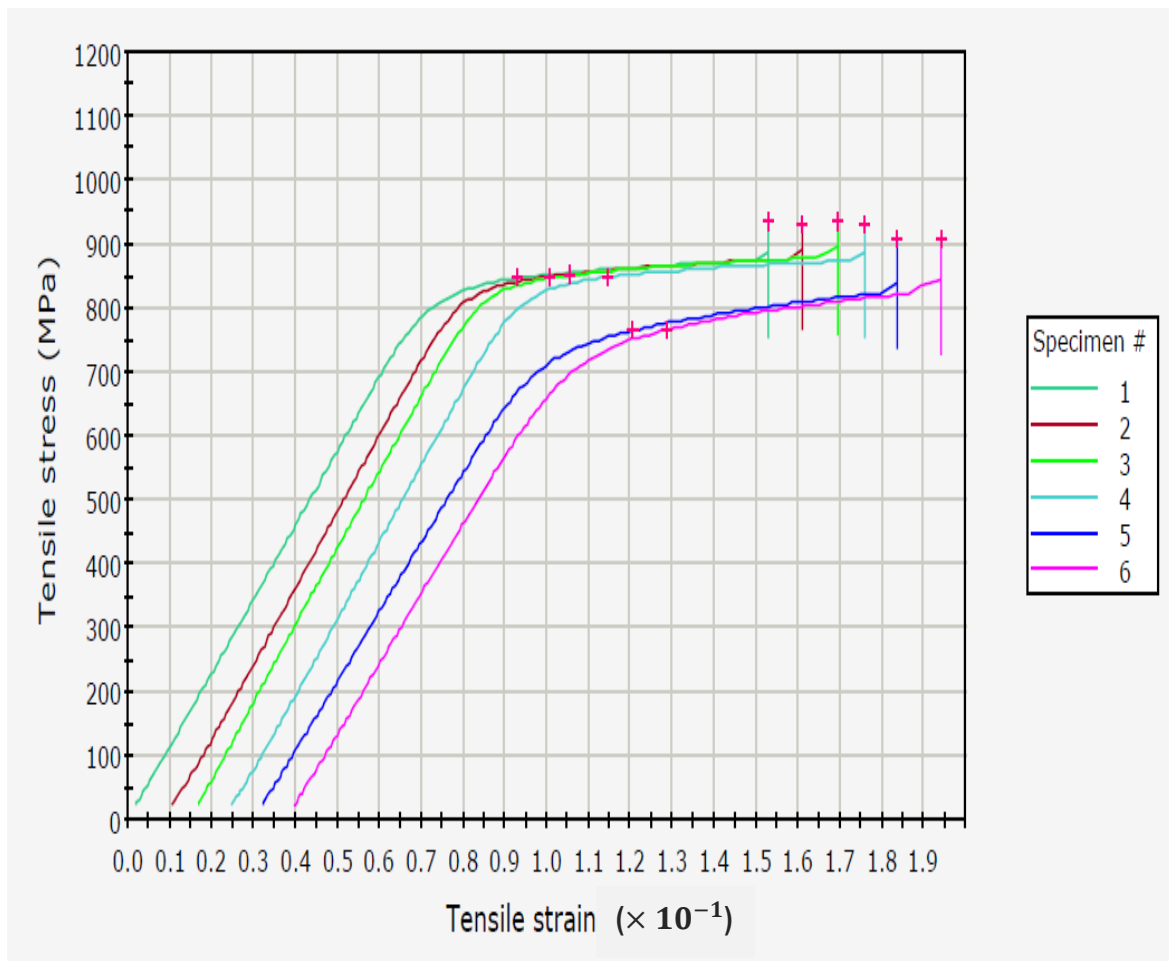


Figure 4.11: Stress–strain graph of the stress-relieved and HTA DMLS Ti6Al4V (ELI)

A summary of the results from these tensile tests with reference to Figure 4.11 is presented in Table 4.8.

Table 4.8: Tensile properties of stress-relieved and HTA-treated X-, Y- and Z-built Ti6Al4V (ELI) specimens

Specimen designation	Tensile stress at yield (offset 0.2%) (MPa)	Modulus of elasticity (GPa)	Strain at yield	UTS (MPa)	Strain at fracture (%)
X-1	846.	116	0.73	933	15.68
X-2	849	120	0.71	928	13.92
Y-1	851	120	0.71	936	18.84
Y-2	848	120	0.71	931	17.56
Z-1	765	108	0.71	908	14.88
Z-2	765	108	0.71	911	14.96
Mean	821	115	0.71	925	16
Standard deviation	39.32	5.37	0.008	10.85	1.70
Coefficient of variation (%)	4.79	4.66	1.13	1.17	10.62

The values of the 0.2% offset yield stress, ultimate tensile stress (UTS) and the modulus of elasticity of the stress-relieved and HTA DMLS Ti6Al4V (ELI) specimens increase in the order of Z-, X- and Y-built specimens. The values of UTS for the tested specimens show a low coefficient of variation (CV) of 1.17%. This low CV indicates a small degree of scatter of the values of UTS from their mean, with a highest percentage variance of 1.78% being for Z-built specimens. From this low CV, the UTS of stress-relieved and HTA DMLS Ti6Al4V (ELI) specimens can be concluded to be isotropic with reference to their mutually orthogonal orientations of build, because the percentage variances fall within the experimental error. The values of the 0.2% offset yield stress and the modulus of elasticity show similarly small values of CV, being 4.79% and 4.66%, respectively. These higher values of CV compared to those of the UTS indicate a higher degree of scatter of the values of 0.2% proof stress and the modulus of elasticity from their mean values. The higher values of CV result from the higher percentage variances of the specimens built in the Z-direction, with the highest being 7.2% and 6.79%, respectively. It is, therefore, reasonable to conclude that some anisotropy of the 0.2% yield strength and modulus of elasticity of high-temperature annealed DMLS Ti6Al4V (ELI) specimens exist with reference to their orientations of build. Despite the anisotropy in the 0.2% yield strength and the modulus of elasticity resulting from the Z-built specimens, the elastic strain is isotropic, averaging 0.71% with a CV of 1.13%. The values of strain at fracture of the tested specimens show the highest degree of scatter of the tabulated tensile properties with a CV of 10.62% resulting from a highest percentage variance of 15.22% from a Y-built specimen (Y-1).

Table 4.9: The sums of DMLS process-related pore areas projected in the x-y planes (perpendicular to the load axis) on the fracture planes and cross-sections above and below the fracture planes of the tensile specimens

Location of pores	X-1 (mm ²)	X-2 (mm ²)	Y-1 (mm ²)	Y-2 (mm ²)	Z-1 (mm ²)	Z-2 (mm ²)
Fracture plane \pm 0.5 mm	0.02323	0.0161	0.0246	0.03194	0.02323	0.0176
3 \pm 0.5 mm above fracture plane	0.02065	0.0117	0.0140	0.00833	0.03014	0.0176
3 \pm 0.5 mm below fracture plane	0.01362	0.0094	0.0127	0.02999	0.02098	0.0178
6 \pm 0.5 mm above fracture plane	0.05069	0.0026	0.0079	0.04061	0.00985	0.0191
6 \pm 0.5 mm below fracture plane	0.02126	0.0124	0.0129	0.03313	0.01203	0.0059
9 \pm 0.5 mm above fracture plane	0	0	0	0	0	0
9 \pm 0.5 mm below fracture plane	0.01654	0.016	0.0184	0.03612	0.02452	0

The UTS of a specimen is determined by dividing the maximum applied force with the measured original cross-sectional area of the specimen [76]. The projected areas of the pores in a cross-sectional plane perpendicular to the loading axis reduces the actual cross-sectional area of the specimen, thereby leading to higher stresses in the built metal. The pores inherent in the DMLS specimens reduce the actual cross-sectional areas of the specimens and are expected to lower the tensile properties of the specimens and determine the locations of the planes of fracture in the specimens. From Table 4.9 it can be seen that there is no direct correlation of the sum of projected pore areas in the x-y planes, which are perpendicular to the loading axis, with the location of the fracture planes of the specimens. For the plane located 6 mm above the fracture planes of specimens X-1, Y-2 and Z-2, the sum of projected pore areas is higher than that of the pores located on the respective specimen fracture planes. Larger sums of projected pore areas were also located on the plane 9 mm below the fracture planes of specimens Y-2 and Z-1. For the fracture planes, the highest sum of the projected pore areas was located in specimens Y-2 and Y-1, which is contrary to the results recorded in Table 4.8 that show the two specimens to have the highest values of UTS. The planes of fracture are seen in Table 4.9 to coincide with the planes of largest projected sums of pore areas only in two (X-2 and Y-1) of the six specimens analysed. It can therefore be inferred that DMLS process-related pores do not have an effect on the location of the fracture plane and the anisotropy in the tensile properties of DMLS specimens. This can be attributed to the DMLS process-related pores being at a microscale resulting in an insignificant percentage difference of 99.84% from measured cross-sectional area of the specimens for the highest sum of projected pore areas on a fracture plane (specimen Y-2).

Figures 4.12, 4.13 and 4.14 show the SEM SEI fractographs of the fractured stress-relieved and HTA DMLS Ti6Al4V (ELI) tensile test specimens X-2, Y-2 and Z-2, respectively.

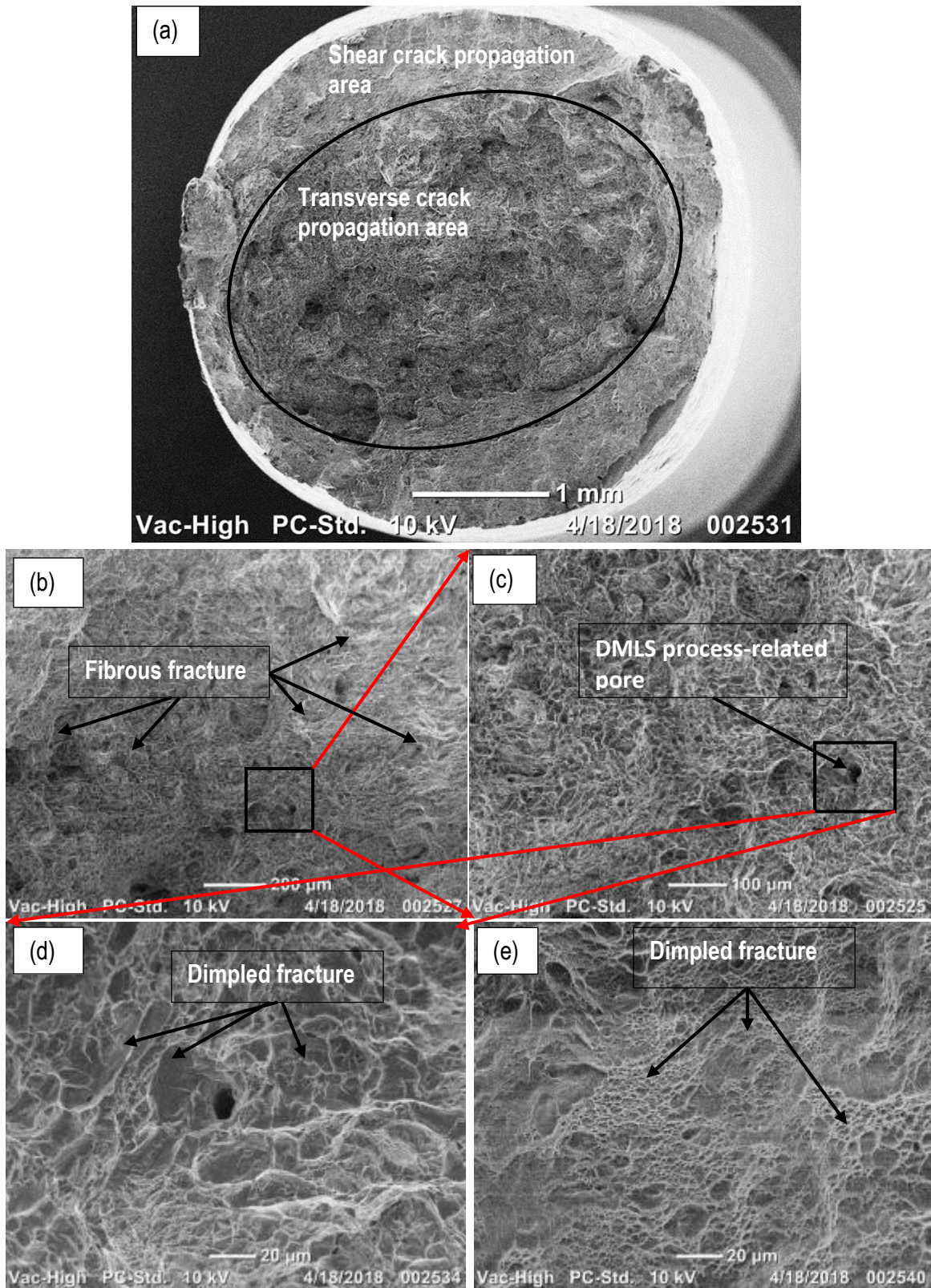


Figure 4.12: (a) Overall fractograph of specimen X-2 (b) a magnified micrograph of the transverse crack propagation area (c) further magnification of the transverse crack propagation area around a pore (d) high magnification of the transverse crack propagation area around a pore (e) high magnification of the shear lip area

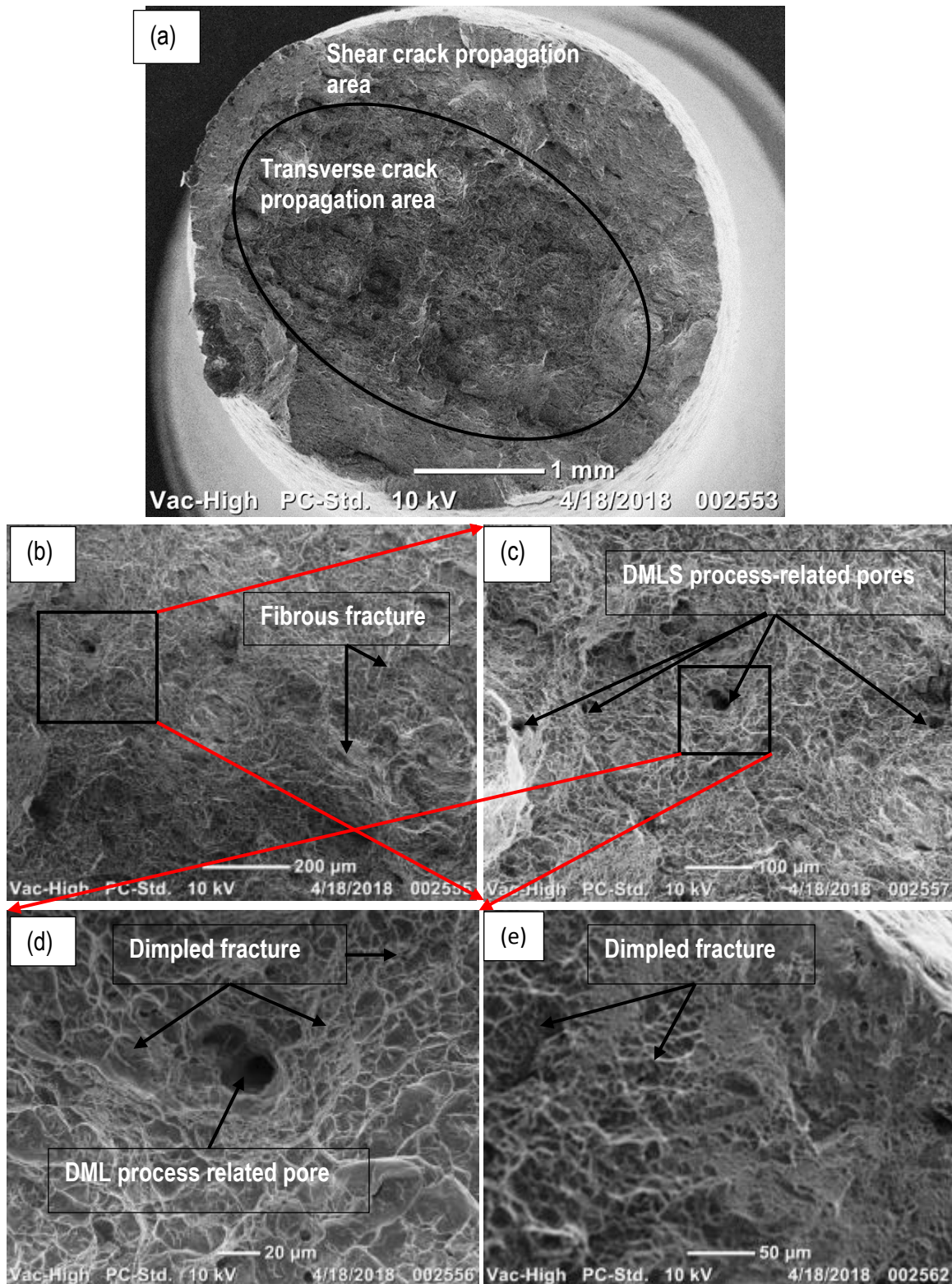


Figure 4.13: (a) Overall fractograph of specimen Y-2 (b) a magnified micrograph of the transverse crack propagation area (c) further magnification of the transverse crack propagation area around a pore (d) high magnification of the transverse crack propagation area around a pore (e) a micrograph of the shear lip area

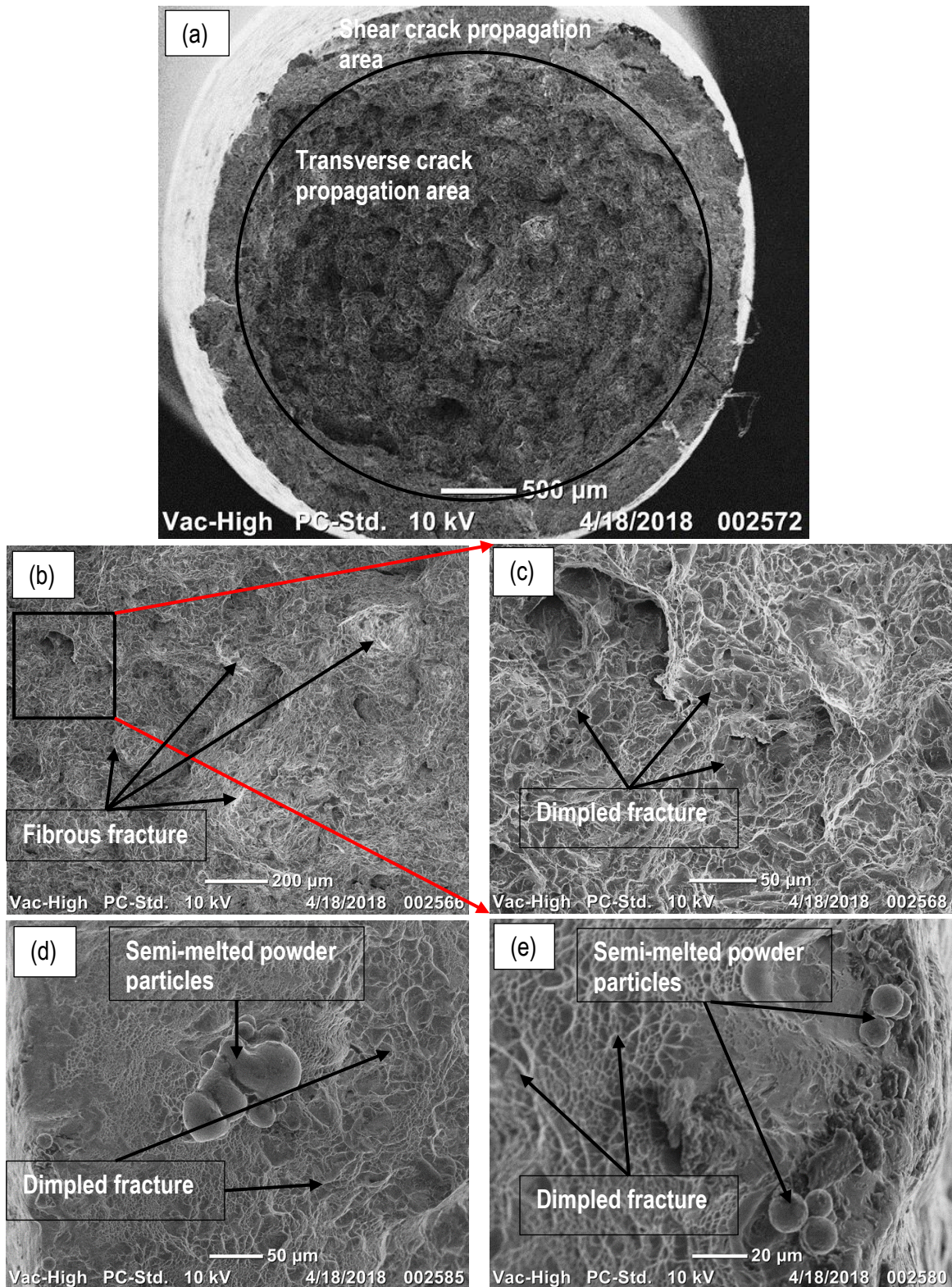


Figure 4.14: (a) Overall fractograph of specimen Z-2 (b) a magnified micrograph of the transverse crack propagation area (c) further magnification of the transverse crack propagation area (d) and (e) high magnifications of the shear lip areas around semi-melted areas

The fractographs shown in Figures 4.12 (a), 4.13 (a) and 4.14 (a) of the X-2, Y-2 and Z-2 specimens, representing the specimens built with their longitudinal axes orientated parallel to the three mutually orthogonal DMLS axes, show a fibrous and dull zone and a smooth and shiny zone that are typical of the cup and cone fracture mode with pronounced necking around the zone of fracture. These features are indicative of transverse propagation of cracks in the central flat areas of the fracture surface (encircled in Figures 4.12 (a), 4.13 (a) and 4.14 (a)) and shear propagation of cracks inclined at about 45° to the longitudinal direction of the specimens in the cup or cone lip areas on the peripheries of the specimens. On a macroscale, these features represent a brittle fibrous and ductile shear fracture on the central and shear lip areas, respectively [94][95]. Upon increase in the magnification of the areas of transverse propagation of cracks seen in Figures 4.12 (b), 4.13 (b) and 4.14 (b), the fibrous nature of the fracture surfaces becomes more pronounced which indicates a ductile fracture at a microscale [41]. Further increase in magnification in these areas of transverse propagation of cracks reveals dimples as seen in Figures 4.12 (c), 4.13 (c) and 4.14 (c) (magnifications from the encircled areas in Figures 4.12 (b), 4.13 (b) and 4.14 (b)). The dimples are characteristic of nucleation and coalescence of voids that are typical of ductile fracture [94][95]. Similar dimples are also seen on the shear lip areas shown in Figures 4.12 (d), 4.13 (e) and 4.14 (e) and (d). Therefore, the tensile specimens of stress-relieved and HTA-treated DMLS Ti6Al4V (ELI) exhibit ductile fracture [94][95].

It is evident from the foregoing results and analysis that the effect of HTA following on a stress relieving improves ductility at the expense of the UTS and the 0.2% offset proof stress of DMLS Ti6Al4V (ELI) specimens. They showed a minimum increase of 40% in ductility and maximum decreases of 22% and 27% in the 0.2% offset proof stress and UTS, respectively. These percentage of increase in ductility and decrease in 0.2% offset proof stress and UTS are with reference to the report on the horizontally built DMLS Ti6Al4V (ELI) tensile properties by Moletsane et al. [6]. The improvement in the ductility of the stress-relieved and HTA specimens is made evident by the mainly dimpled fracture mode in both the transverse crack propagation areas shown in Figures 4.12, 4.13 and 4.14 as opposed to the mixed fracture modes of dimpled and cleavage fracture reported by Moletsane et al. [6] and Yadroistev et al. [41] for as-built specimens. A dimpled fracture mode on a micro-scale is associated with ductility and a cleavage fracture mode with brittleness [94][95]. The cleavage fracture indicates a trans-granular fracture mode, which implies high resistance to crack propagation as opposed to the inter-granular fracture mode indicative of dimpled fracture; thus, the drop in the 0.2% offset proof stress and UTS after stress relieving and HTA of DMLS Ti6Al4V specimens.

4.6 Fatigue Properties

4.6.1 Introduction

The fatigue loads of machined and polished ($R_a \approx 0.1 \mu m$) DMLS Ti6Al4V (ELI) specimens orientated along the X-, Y- and Z-axes and their respective life cycles are tabulated and presented on semi-log S-N curves in this section. The data from the fractured specimens in each of the three orientations of build is fitted to linear semi-log S-N curves according to Basquin's law. The linearized curves of the fractured specimens from each set of specimens portray an inverse relationship between the maximum stress (S) and the $\log_{10}N$ until a point where each reaches its respective fatigue endurance limit. The fatigue endurance limits for each set of specimens are estimated from the data points with the highest value of S at which failure of the respective specimens does not occur after 5,000,000 load cycles. At the respective endurance limits, all the curves are plotted as horizontal lines intersecting with the linearized inclined curves to form knee points typical of S-N curves of iron, titanium and their respective alloys.

The fatigue cracks of the fractured DMLS Ti6Al4V (ELI) specimens in this project that were analyzed in a SEM were found to have initiated from surface and sub-surface DMLS process-related pores resulting from the localized lack of complete fusion of the Ti6Al4V (ELI) powder particles, and from surface facets. The DMLS process-related crack initiation pores were taken as pre-existing cracks and their change in stress intensity factors (ΔK) were calculated using the principle of LEFM, discussed in section 2.7.5 and compared with the threshold change in stress intensity factor (ΔK_{th}) of DMLS Ti6Al4V found in literature.

In their publication on the crack-growth behaviour of SLM Ti6Al4V, Leuders et al. [96] reported the average threshold stress intensity factor for cyclically loaded, as-built SLM Ti6Al4V specimens at a stress ratio $R = 0.1$ to be $1.4 MPa m^{0.5}$ for the propagation of a crack in a direction parallel to the build layer (Z-built specimens) and $1.7 MPa m^{0.5}$ for the propagation of a crack across the build layers (X- and Y-built specimens). In the same publication, Leuders et al. [96] reported a threshold stress intensity factor $\Delta K_{th} = 3.9 MPa m^{0.5}$ after heat treating SLM Ti6Al4V specimens at $800 \text{ }^\circ\text{C}$ and $1050 \text{ }^\circ\text{C}$ followed by furnace cooling for both heat treatments. Konecna et al. [97] reported a threshold stress intensity factor of $\Delta K_{th} = 3.5 MPa m^{0.5}$ for SLM Ti6Al4V specimens that were stress relieved at $380 \text{ }^\circ\text{C}$ for 8 hours. In another publication on the crack growth of SLM Ti6Al4V with the same stress-relieving treatment parameters, Konecna et al. [98] reported a fatigue

threshold of $\Delta K_{th} = 3.7 \text{ MPa m}^{0.5}$. Comparison of stress intensity factors obtained in their publication to those that were published by Becker et al. [99] in which the values of ΔK_{th} were not given, Konecna et al. [98] concluded that for low values of ΔK the crack growth rates of as-built DMLS Ti6Al4V are higher than those of stress-relieved SLM Ti6Al4V, with two orders of magnitude. This conclusion is consistent with lower values of threshold stress intensity factors that were obtained by Leuders et al. [96] of $\Delta K_{th} = 1.4 \text{ MPa m}^{0.5}$ and $1.7 \text{ MPa m}^{0.5}$ for vertically and horizontally built as-built SLM Ti6Al4V. From the above references, it can be concluded that as-built DMLS Ti6Al4V specimens have lower threshold stress intensity factors and therefore experience higher rates of propagation of cracks (da/dN) at lower loads than post-DMLS heat-treated Ti6Al4V samples for the same applied loads. While the change in threshold stress intensity factors from the case of as-built to stress-relieved Ti6Al4V is significant (150% and 164%, and 100%, and 118%) for the propagation of a crack across and along the build layers, respectively, it is relatively small for the change from stress-relieved to heat-treated Ti6Al4V at (11.429% and 5.405%) for the two cases quoted here, respectively. The foregoing values of ΔK_{th} for horizontally and vertically orientated as-built DMLS Ti6Al4V (ELI) specimens of $1.7 \text{ MPa m}^{0.5}$ and $1.4 \text{ MPa m}^{0.5}$ are adopted here for use in analysis and so is the ΔK_{th} of stress-relieved and HTA DMLS Ti6Al4V (ELI) of $3.9 \text{ MPa m}^{0.5}$, for all three the build directions.

4.6.2 Fatigue test results for the as-built fatigue specimens

The fatigue fracture cracks of all the fractured DMLS as-built Ti6Al4V (ELI) specimens tested in this work were observed to initiate from surface DMLS process-related pores with the exception of specimen Y-20, whose fracture crack initiated from a sub-surface DMLS process-related pore. These surface and sub-surface crack initiation DMLS process-related pores were taken to be pre-existing cracks. The values of ΔK for these pores were calculated using Murakami's expression [82] given here as Equation (2.9). The projected areas of these crack initiation pores normal to the stress load direction were measured from the respective fractographs using the SketchAndCalc Area Calculator. The values of ΔK for the DMLS process-related crack initiation pores that were calculated in this way were compared with the values of threshold stress intensity (ΔK_{th}) of as-built DMLS Ti6Al4V adopted here from literature. The theory of ΔK_{th} states that at values of ΔK below the ΔK_{th} , the crack growth rate ($\frac{da}{dN}$) is so small that crack propagation is considered not to occur [58]. However, it is evident from Equation (2.9) in section 2.8.5 that an increase in the magnitude of the applied stress load increases the resultant value of ΔK , which if then greater than the ΔK_{th} ,

results in an increase in the crack growth rate thereby reducing the number of life cycles to failure [100]. An increase in the magnitude of the applied stress load also implies a decrease of the critical fatigue crack length [100]. Therefore, specimens with pores whose values of ΔK are below ΔK_{th} and that are exposed to relatively low stress loads will theoretically withstand an infinite number of load cycles to failure.

4.6.2.1 X-built specimens

Table 4.10 shows values of maximum tension–tension fatigue stresses and the corresponding number of load cycles to failure of X-built Ti6Al4V (ELI) specimens that were tested here. It also shows the stress range, the square root of the areas of crack initiation pores measured from the fractographs by a sketch-and-calculate software and the related calculated values of change of stress intensity (ΔK). The loading direction for these specimens is seen from Figure 3.1 in section 3.2 to be parallel to the plane of the build layers.

Table 4.10: Dimensions of DMLS process-related initiation pores for fatigue failure cracks and their stress intensity ranges for selected load stress data of X-built as-built DMLS Ti6Al4V (ELI) specimens

Specimen designation	Maximum stress (σ_{max}) (MPa)	Stress range ($\Delta\sigma$) (MPa)	Fatigue life N_f (cycles)	\sqrt{area} (μm)	Change of stress intensity ΔK ($MPa m^{0.5}$)
X-2	675	607.5	896,033	24.70	3.478
X-6	671	603.9	43,107	50.03	4.921
X-1	612	551.0	179,794	31.78	3.574
X-3	549	494.1	478,851	33.90	3.314
X-4	486	437.4	181,753	41.74	3.256
X-9	486	437.4	281,508	51.53	3.617
X-8	450	405.0	5,000,000	-	-
X-5	432	388.8	5,000,000	-	-
X-10	360	324.0	5,000,000	-	-

* $\Delta K_{th} = 1.7 MPa m^{0.5}$ for crack propagation across the as-built DMLS Ti6Al4V layers at $R = 0.1$ [96].

Figure 4.15 presents a semi-log S-N curve of the maximum stress against the number of load cycles (S-N) for the X- built DMLS Ti6Al4V (ELI) specimens based on the data shown in Table 4.10.

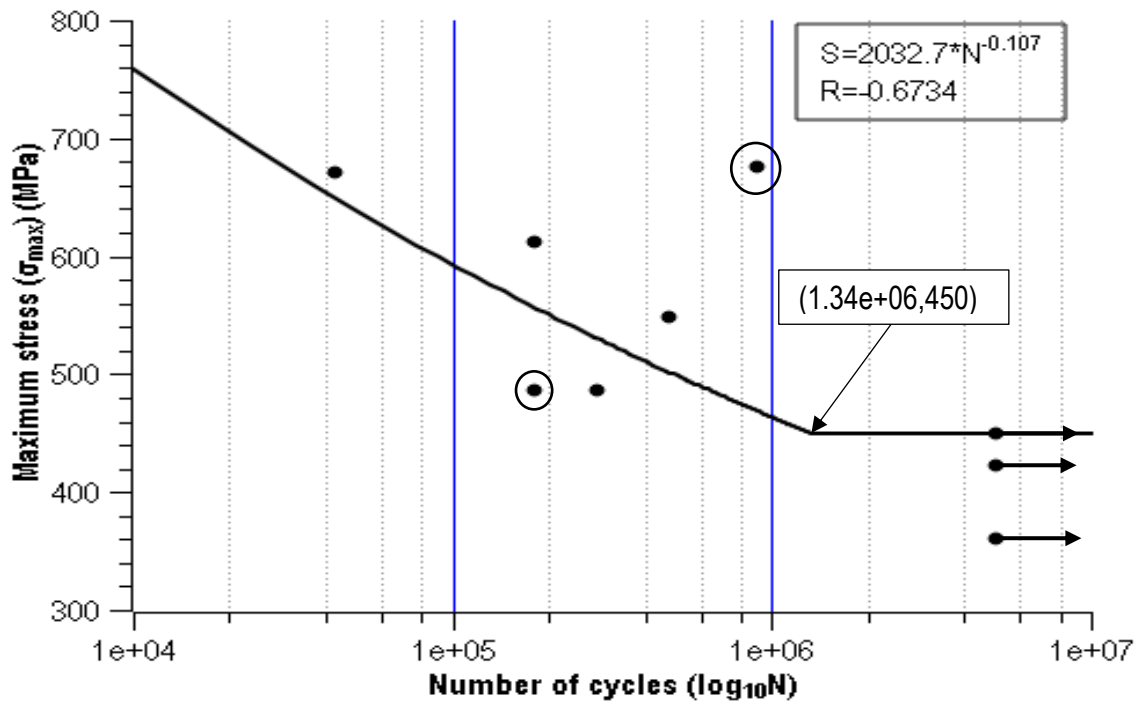


Figure 4.15: Semi- \log_{10} S-N curve for as-built X-built specimens

Linearization of the curve shown in Figure 4.15, for the as-built DMLS Ti6Al4V (ELI) X-built specimens, was carried out without taking into account the outliers; specimens X-2 and X-4 shown as encircled dots in Figure 4.15. The correlation coefficient (R) of -0.6734 obtained indicates a moderate inverse linear relationship between σ_{max} and $\log_{10} N$. Back extrapolation of this curve gives a fatigue strength of 760 MPa at 10^4 load cycles (69% of the 0.2% offset proof strength of horizontally orientated as-built DMLS Ti6Al4V (ELI) reported by Moletsane et al. [6] and Yadroistev et al. [41]) and a knee point at 1,340,000 load cycles, where the curve turns horizontal. This fatigue strength at 10^4 load cycles is contrary to a theory by Ashby et al. [72] who suggested that the fatigue strength of metallic materials at 10^4 load cycles is equal to the 0.2% offset proof strength of the material, as shown in Figure 2.3 in section 2.8.2. The horizontal level of the curve represents the fatigue endurance limit which is estimated from the highest value of σ_{max} of the run-out specimens indicated by the arrows shown in Figure 4.15 [101]. The fatigue endurance limit in this case is 450 MPa and it is 43% of the 0.2% proof strength of horizontally orientated as-built DMLS Ti6Al4V (ELI) reported by Moletsane et al. [6] and Yadroistev et al. [41].

Specimen X-2 showed a high number of cycles to failure at high loads, whereas specimen X-4 showed a low number of cycles to failure at low loads. These results are contrary to expectations. The fractographs of these outlier specimens were compared to those of specimens that did not

exhibit this unexpected behaviour on the semi-log S-N plot but which were exposed to almost equal magnitudes of stress loads. To this end, therefore, specimen X-2 (high maximum stress and high number of cycles to failure) was compared to specimen X-6 (high maximum stress and low number of cycles to failure). Similarly, specimen X-4 (low maximum stress and low number of cycles to failure) was compared to specimen X-9 (low maximum stress and a comparatively high number of cycles to failure) with the results shown in Figures 4.16, 4.17, 4.18 and 4.19.

Figure 4.16 shows SEI SEM fractographs of specimen X-2 that was cycled at a maximum stress of 675 MPa and which fractured at 896,033 cycles: high maximum stress and high number of life cycles.

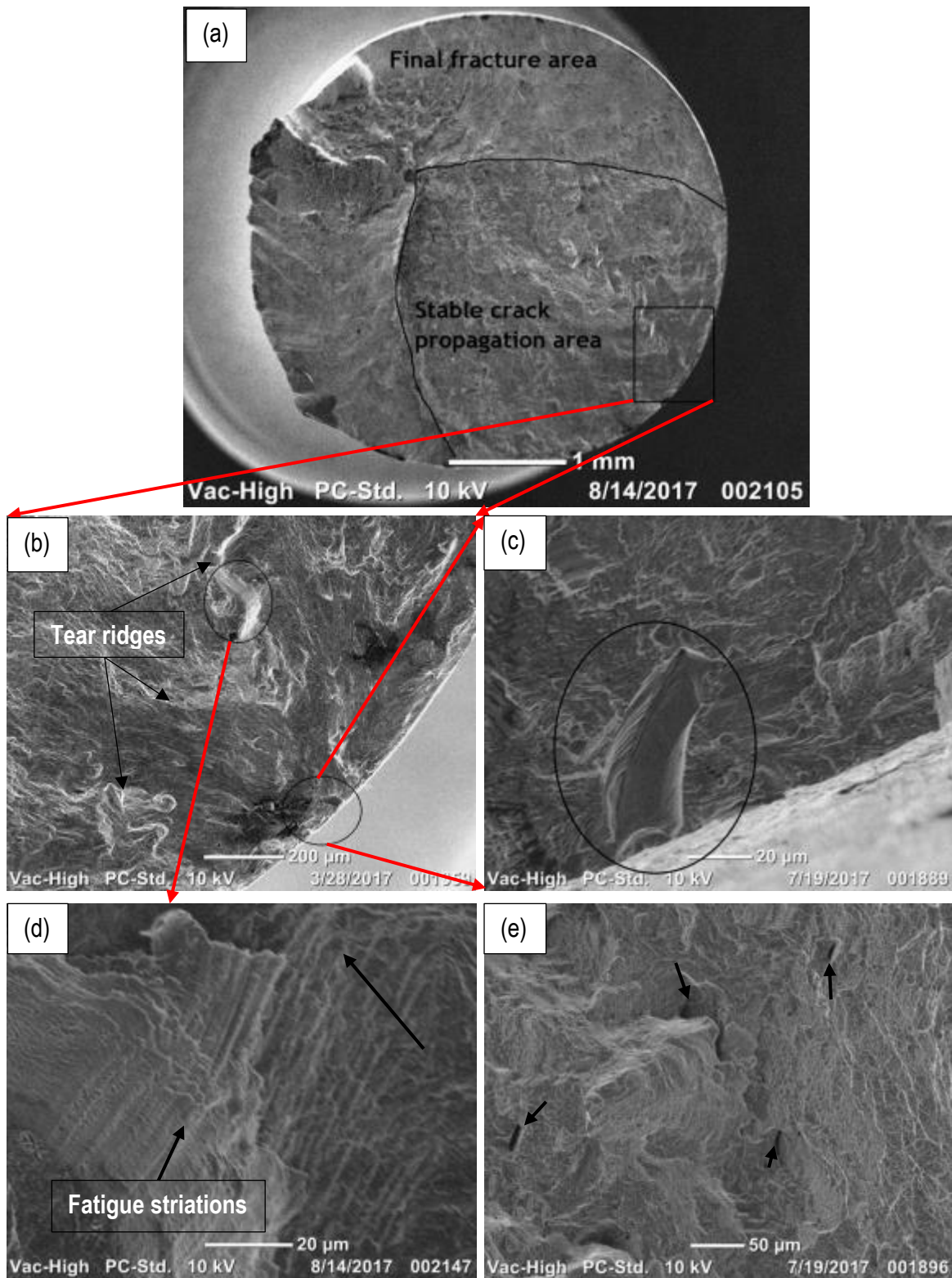


Figure 4.16: (a) Overall fractograph of specimen X-2 (b) a magnified area around the crack initiation site (c) further magnification of the area around the crack initiation site (d) high magnification of the path of crack propagation showing fatigue striations (e) a magnified area of crack propagation with DMLS process-related pores

Fatigue fracture of the specimen initiated from a surface DMLS process-related pore of $\sqrt{area} = 24.70 \mu m$ encircled in Figure 4.16 (c) which was concluded to be the flaw area that had the highest stress concentration factor within the gauge volume of the specimen. The pore had the lowest \sqrt{area} of the DMLS process-related crack initiation pores in the X-built as-built DMLS specimens. The low \sqrt{area} of this crack initiation pore resulted in a relatively low change of stress intensity factor of $\Delta K = 3.478 MPa m^{0.5}$ at its tip. This ΔK is 51% higher than the adopted value of ΔK_{th} of $1.7 MPa m^{0.5}$, at a value of σ_{max} that is 33% higher than the estimated endurance limit, which led to fracture of the specimen at 18% of the set number of run-out cycles.

The specimen fractured because the value of ΔK from its crack initiation pore tip was significantly higher than the value of ΔK_{th} which implies that propagation of the crack would occur. However, the value of ΔK from the crack initiation pore in this specimen is seen in Table 4.10 to be lower than that of other specimens with values of σ_{max} within the same range, a possible reason for the relatively high number of life cycles at this high value of σ_{max} .

The relatively fine fatigue striations, indicative of the high number of cycles to failure shown in Figure 4.16 (d), bow-out from the crack initiation pore in the direction indicated by the arrow in the micrograph. The fatigue striations were magnified from the face of one of the tear ridges that diverge from the crack initiation site encircled in Figure 4.16 (b). From the overall fractograph in Figure 4.16 (a), it can be seen that the tear ridges, which are characteristic of stable crack propagation, run through the entire crack propagation area up until the area of final fracture. Internal micropores were identified in this region and were all found to be elongated in the direction of the tear ridges, as indicated by arrows in Figure 4.16 (e). This elongation is indicative of successive layers of the DMLS build process. This is consistent with the observation by Yadollahi et al. [50] that such pores are normally oval in shape and are located between two successive layers, with the major axis parallel to the layers.

Figure 4.17 shows SEI SEM fractographs of specimen X-6 that was cycled at maximum stress of 671 MPa and which fractured at 43,107 cycles: high maximum stress and low number of life cycles.

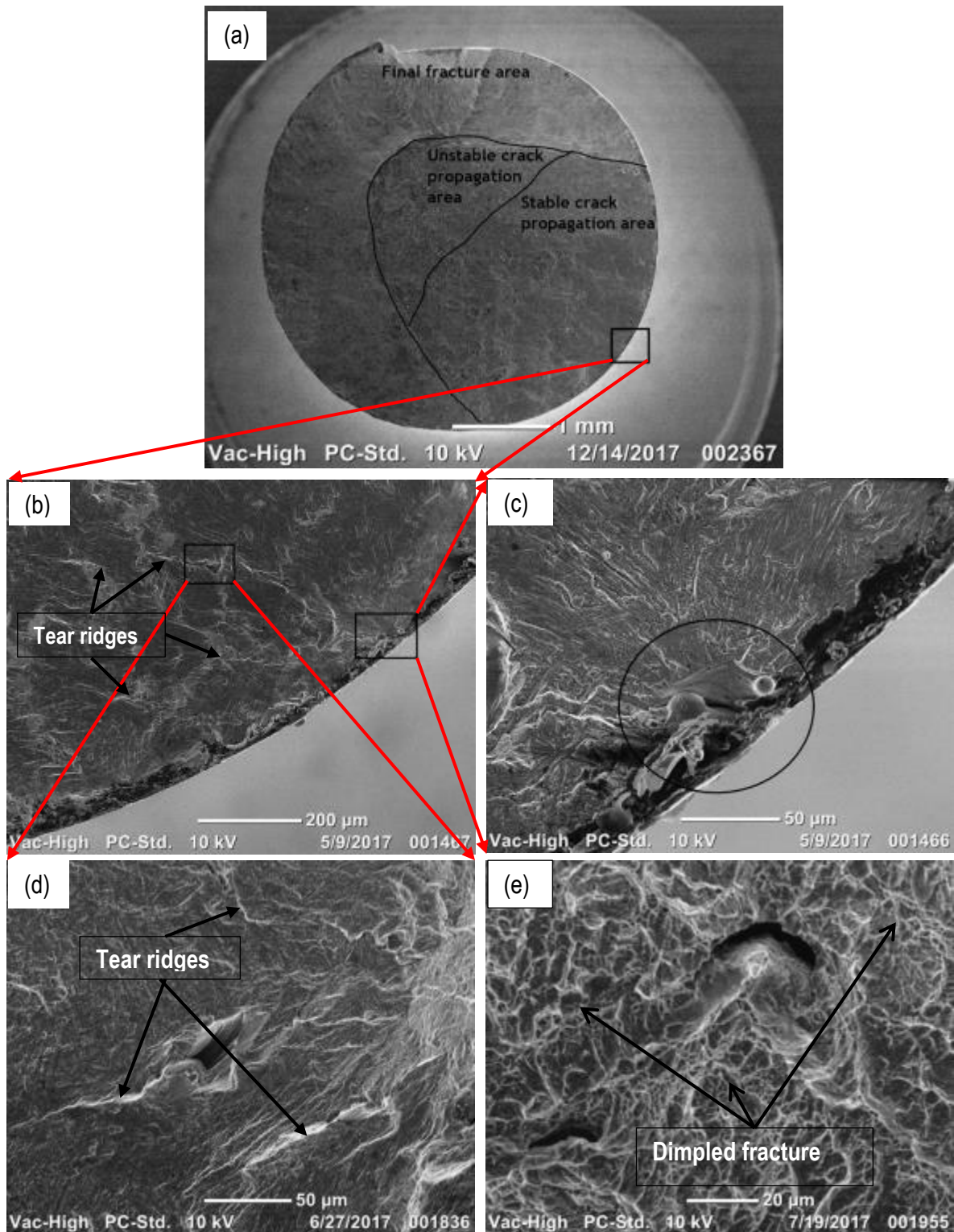


Figure 4.17: (a) Overall fractograph of specimen X-6 (b) a magnified area around the crack initiation site (c) further magnification of the area around the crack initiation site (d) high magnification of the area of stable crack propagation around a DMLS process-related pore (e) a magnified unstable crack propagation area

The fatigue fracture features of specimen X-6 include an area with tear ridges, an area with shallow dimples and a shear area shown in Figure 4.17 (a). The tear ridges diverge from a crack initiation point and spread across the fracture plane, as shown in Figure 4.17 (b) and at high magnification in Figure 4.17 (d), which indicates a constant rate of increase of the crack length (stable propagation cracks). The spread of the tear ridges on the fracture plane continues until the critical crack length is attained at which propagation becomes unstable. Areas of monotonic propagation of cracks are characterized by shallow dimples, such as the ones shown in Figure 4.17 (e). Fatigue failure in this specimen initiated from a DMLS process-related surface pore with $\sqrt{area} = 50.03 \mu m$ identified from the origin of the tear ridges and encircled in Figure 4.17 (c). The \sqrt{area} of this crack initiation pore at $\sigma_{max} = 671 MPa$ (33% higher than the estimated endurance limit) resulted in a change of stress intensity factor $\Delta K = 4.921 MPa m^{0.5}$ at its tip. Internal micropores of similar orientation and geometry as the crack initiation pore were located in the stable crack propagation areas and their major axes were aligned with the tear ridges, as seen in the Figure 4.17 (d), as is the case in specimen X-2.

The ΔK at the crack initiation pore tip in this specimen was 29% higher than that of specimen X-2 and 65% higher than the ΔK_{th} . Therefore, the rate of propagation of the pore tip is expected to be higher than that for the pore in specimen X-2 at similar values of maximum stress load. Similar to the case for specimen X-2, the micropores located in the stable crack propagation area provided an easy path for the propagating crack by locally accelerating the rate of propagation of the crack upon its contact with these pores. The aforementioned effect of microporosity on the propagation of fatigue cracks and the high stress load (66% of the 0.2% proof stress [6][41]) on the specimen are thought to have led to fracture of the specimen at a fairly low number of cycles. This is also in line with the proposal by Dieter et al. [101] that at stress loads that are about two-thirds of the specimen's tensile strength, fracture is expected to occur at a fairly low number of load cycles.

Figures 4.18 and 43 show SEI SEM fractographs of specimens X-4 and X-9, respectively, that were cycled at a maximum stress of 486 MPa and which fractured at 181,753 cycles: low maximum stress and low number of life cycles and 281,508 cycles: low maximum stress and a slightly higher number of life cycles.

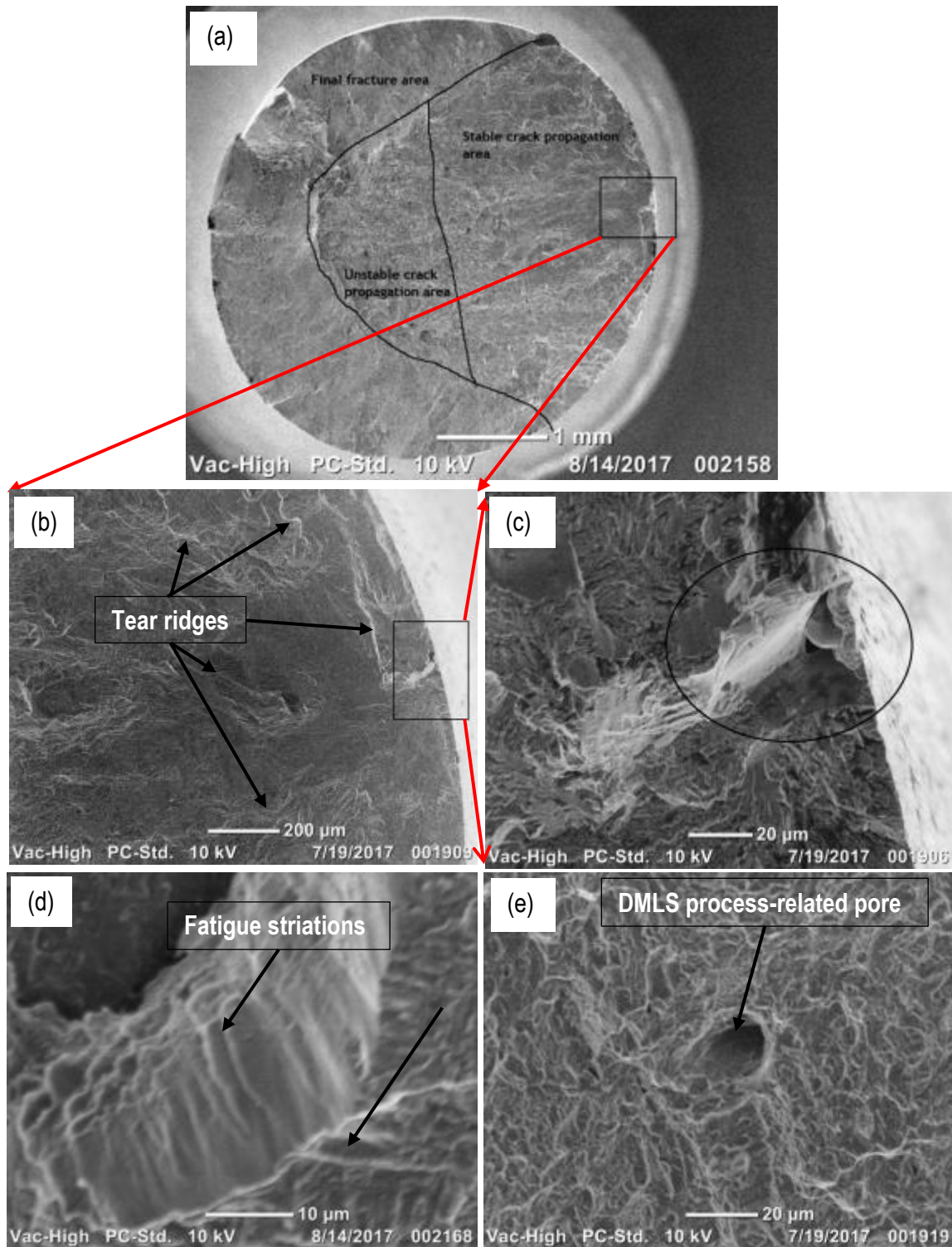


Figure 4.18: (a) Overall fractograph of specimen X-4 (b) a magnified area around the crack initiation site (c) further magnification around the crack initiation site (d) high magnification of fatigue striations in an area of stable crack propagation (e) micrograph showing shallow dimples in an area of unstable crack propagation

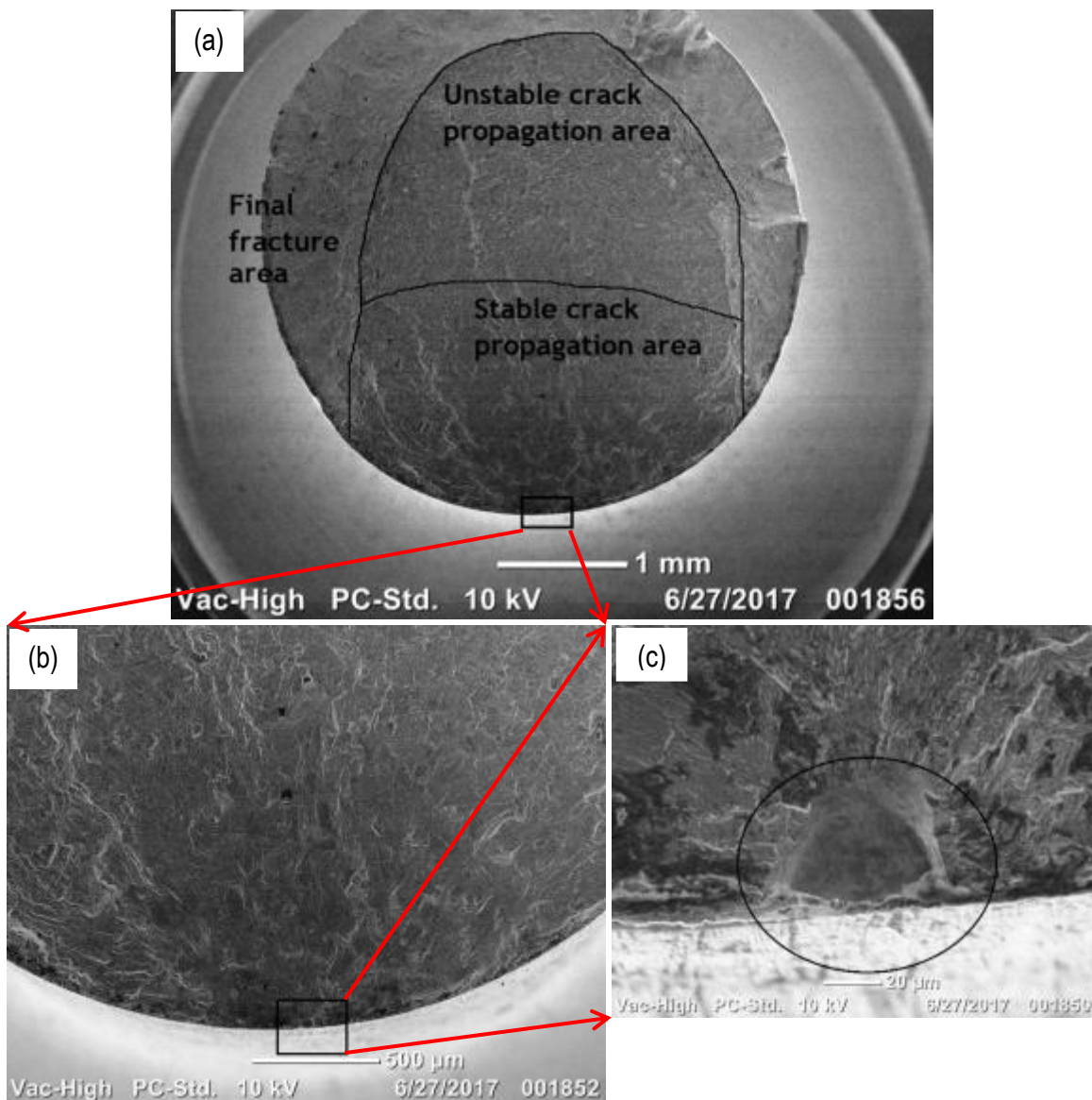


Figure 4.19: (a) Overall fractograph of specimen X-9 (b) a magnified area around the crack initiation site (c) further magnification around the crack initiation site

Fatigue failure in specimen X-4 initiated from a DMLS process-related surface pore of $\sqrt{area} = 41.74 \mu m$ encircled in Figure 4.18 (c) which resulted in a value of $\Delta K = 3.256 MPa m^{0.5}$ at a value of $\sigma_{max} = 486 MPa$. This value of ΔK is 10% lower than the ΔK of the crack initiation pore in specimen X-9, which was loaded at the same value of σ_{max} . The crack initiation DMLS process-related pore in specimen X-9 has a $\sqrt{area} = 51.53 \mu m$ and is encircled in Figure 4.19 (c) which resulted in a value of $\Delta K = 3.617 MPa m^{0.5}$ at a value of $\sigma_{max} = 486 MPa$. The areas of crack propagation for both specimens are divided into zones of stable and unstable crack

propagation, as indicated in Figures 4.18 (a) and 43 (a). On the fracture surface of specimen X-4, fatigue striations (Figure 4.18 (d)) occur on the face of a tear ridge in the area of stable crack propagation and bow-out is evident from the crack initiation pore and in the direction indicated by an arrow in the figure. Internal micropores occur in both crack propagation areas of specimen X-4 which is not the case on the fracture surface of specimen X-9.

The values of ΔK for the two specimens, specimens X-4 and X-9, were 47% and 53% higher than the adopted value of ΔK_{th} , respectively. This implies that there was crack propagation at the tips of the identified failure pores in both specimens. The number of load cycles to failure for the two specimens are shown in Table 4.10 to be 3.6% and 5.6% of the set run-out number of life cycles. The higher value of ΔK in specimen X-9 would indicate a higher rate of crack propagation. However, the existence of internal pores on the fracture surface of specimen X-4 is expected to accelerate propagation of the identified fracture crack and is thought to be the reason for fatigue failure of the specimen at a lower number of life cycles than specimen X-9. The coarse striations shown on the fracture surface in Figure 4.18 (d) for specimen X-4 are a sign of a low number of cycles to fracture.

4.6.2.2 Y-built specimens

Table 4.11 shows values of the maximum tension–tension fatigue stresses and the corresponding numbers of load cycles to failure of the Y-built Ti6Al4V (ELI) specimens that were tested here. It also shows the stress range, the square root of the areas of the crack initiation pores measured from the fractographs by a sketch-and-calculate software and their related calculated values of change of stress intensity ΔK . The loading direction for these specimens is seen from Figure 3.1 in section 3.2 to be parallel to the plane of the build layers.

Table 4.11: Dimensions of DMLS process-related initiation pores for fatigue failure cracks and their stress intensity ranges for selected load stress data of Y-built as-built DMLS Ti6Al4V (ELI) specimens

Specimen designation	Maximum stress (σ_{max}) (Mpa)	Stress range ($\Delta\sigma$) (MPa)	Fatigue life N_f (cycles)	\sqrt{area} (μm)	Change in stress intensity ΔK ($MPa m^{0.5}$)
Y-11	675	607.5	72,925	56.60	5.265
Y-12	612	550.8	297,396	32.44	3.614
Y-18	549	494.1	83,464	54.08	4.186
Y-16	549	494.1	287,984	59.92	4.406
Y-13	549	494.1	1,110,187	24.00	2.789
Y-19	500	450.0	130,072	44.90	3.474
Y-20	495	445.5	1,678,140	60.63	3.074
Y-14	486	437.4	3,295,499	31.07	2.809
Y-17	486	437.4	5,000,000	-	-
Y-15	423	380.7	5,000,000	-	-

* $\Delta K_{th} = 1.7 MPa m^{0.5}$ for crack propagation across the as-built DMLS Ti6Al4V layers at $R = 0.1$ [96].

Figure 4.20 presents a semi-log curve of the maximum stress against the number of load cycles of the Y- built DMLS Ti6Al4V (ELI) specimens based on the data shown in Table 4.11.

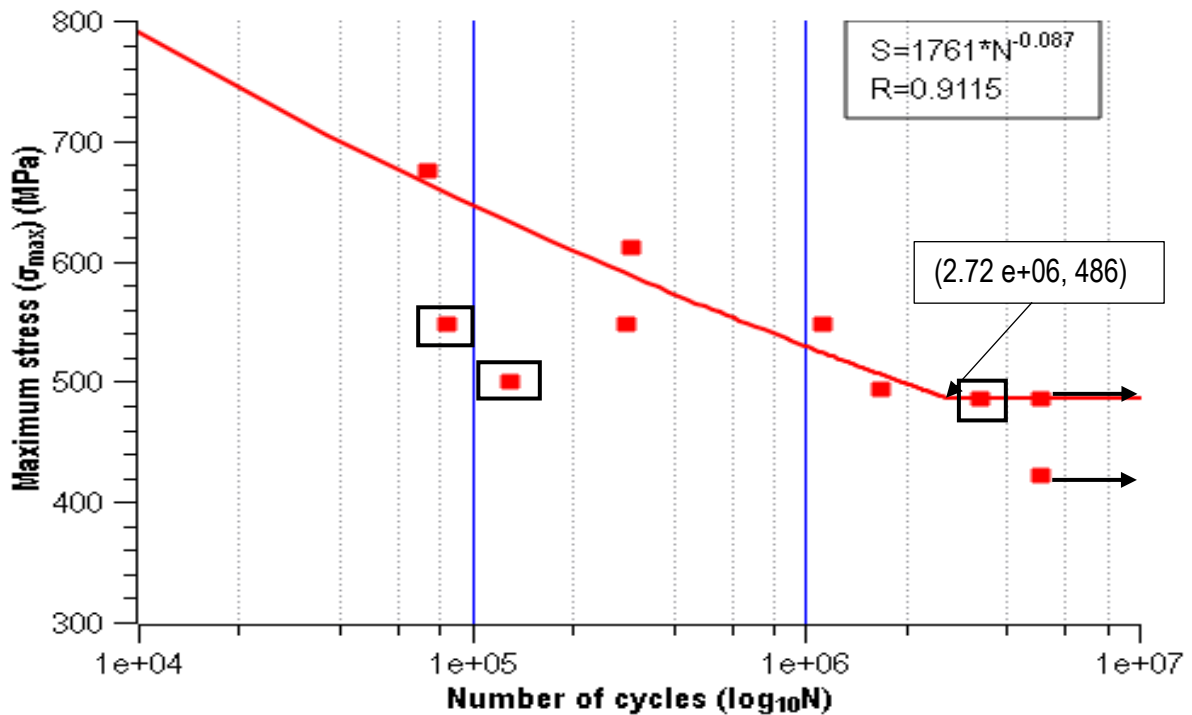


Figure 4.20: Semi- \log_{10} S-N curve for as-built Y-built specimens

A linear curve was fitted to the data in Table 4.11 ignoring the outliers Y-14, Y-18 and Y-19, which are indicated by data points enclosed in squares in Figure 4.20. The data points show a strong inverse linear relationship with a correlation coefficient (R) of -0.9115. The linear curve turns horizontal at a fatigue strength of $\sigma_{max} = 486 \text{ MPa}$ at 2,720,000 load cycles. The horizontal level of the curve is the estimated fatigue endurance limit given by the highest value of σ_{max} for the run-out specimens, indicated by arrows in Figure 4.20. This endurance limit is 48% of the 0.2% offset proof stress for horizontally built as-built DMLS Ti6Al4V (ELI) reported by Moletsane et al. [6] and Yadroistev et al. [41]. Back extrapolation of the linearized curve gives a value of the fatigue strength of 790 MPa at 10^4 load cycles which is 72% of the 0.2% offset proof stress for horizontally orientated as-built DMLS Ti6Al4V (ELI) reported in references [6][41]. This fatigue strength at 10^4 load cycles is less than the 0.2% offset proof stress which was suggested to be the fatigue strength of metallic components at this number of load cycles.

Specimen Y-14 was excluded because it failed at 3,295,499 cycles, whilst loaded at the estimated fatigue endurance limit. Specimens Y-18 and Y-19 showed exceptionally low numbers of cycles to failure at stress loads that are above the estimated endurance limit. The fractographs of the outlier specimens, specimens Y-18 and Y-19, were compared to that of the specimens with similar stress loads in the semi-log S-N curve, whose fatigue lives were accepted, in an attempt to identify the causes of their unexpected behaviour. To this end, specimen Y-19 was compared to specimen Y-14 and specimen Y-18 to specimen Y-13. Their SEI SEM fractographs are displayed in Figures 4.21, 4.22, 4.23 and 4.24.

Figure 4.21 shows SEI SEM fractographs of specimen Y-19 that was cycled at a maximum stress of 500 MPa and which fractured at 130,072 cycles: low maximum stress and low number of life cycles.

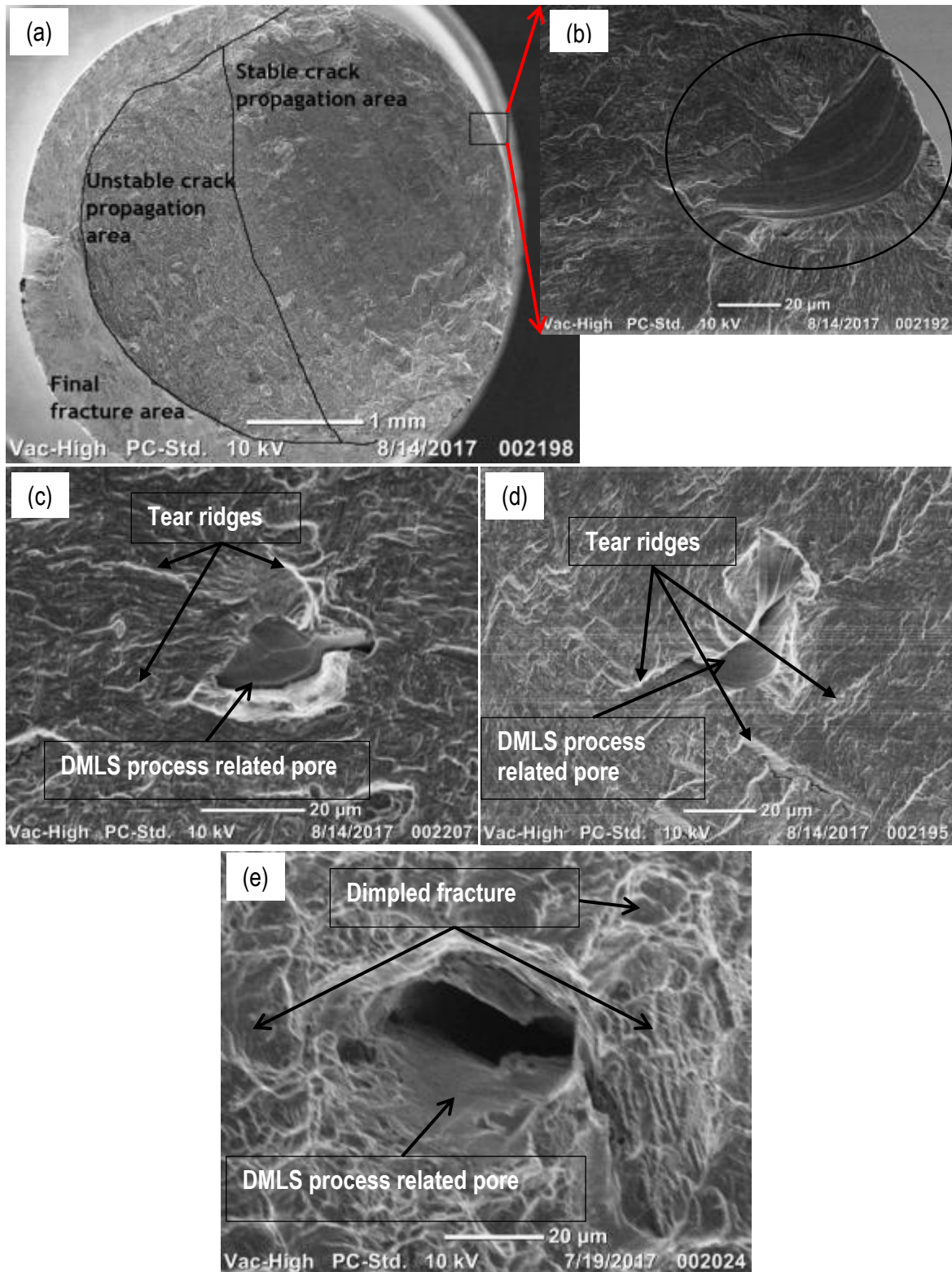


Figure 4.21: (a) Overall fractograph of specimen Y-19 (b) high magnification of an area around the crack initiation site (c) and (d) high magnification of DMLS process-related pores on a stable crack propagation area and (e) high magnification of a DMLS process-related pore on an unstable crack propagation area

The surface of the fatigue fracture for specimen Y-19 is characterized by an area with tear ridges which is characteristic of stable crack propagation, shown at high magnification in Figures 4.21 (c) and (d), and an area with shallow dimples which is characteristic of unstable crack propagation shown in Figure 4.21 (e). The fatigue fracture crack initiated from a surface DMLS process-related pore of $\sqrt{area} = 44.90 \mu m$ that is encircled in Figure 4.21 (b,) which was identified from the tear ridges diverging from it, shown in Figure 4.21 (a). The \sqrt{area} from this pore that was measured from the fractographs resulted in a value of $\Delta K = 3.474 MPa m^{0.5}$ at its tip. Multiple comparatively smaller pores, with reference to the crack initiation pore of similar geometry and orientation to those depicted in Figure 4.21 (c), (d) and (e), were located in the stable and unstable crack propagation areas.

The value of ΔK for this crack initiation pore was 51% higher than the adopted value of ΔK_{th} . Therefore, there was propagation of the crack tip for the identified fatigue fracture crack. The internal pores located on the stable and unstable crack propagation areas provided an easy path for stable crack propagation upon contact with the crack tip of the identified fatigue fracture crack. The aforementioned effects are thought to have led to failure of the specimen at a low number of cycles; 2.6% of the set number of run-out life at the σ_{max} of 2.8% above the endurance limit.

Figure 4.22 shows SEI SEM fractographs of specimen Y-14 that was cycled at a maximum stress of 489 MPa and which fractured at 3,295,499 cycles: low maximum stress and high number of life cycles.

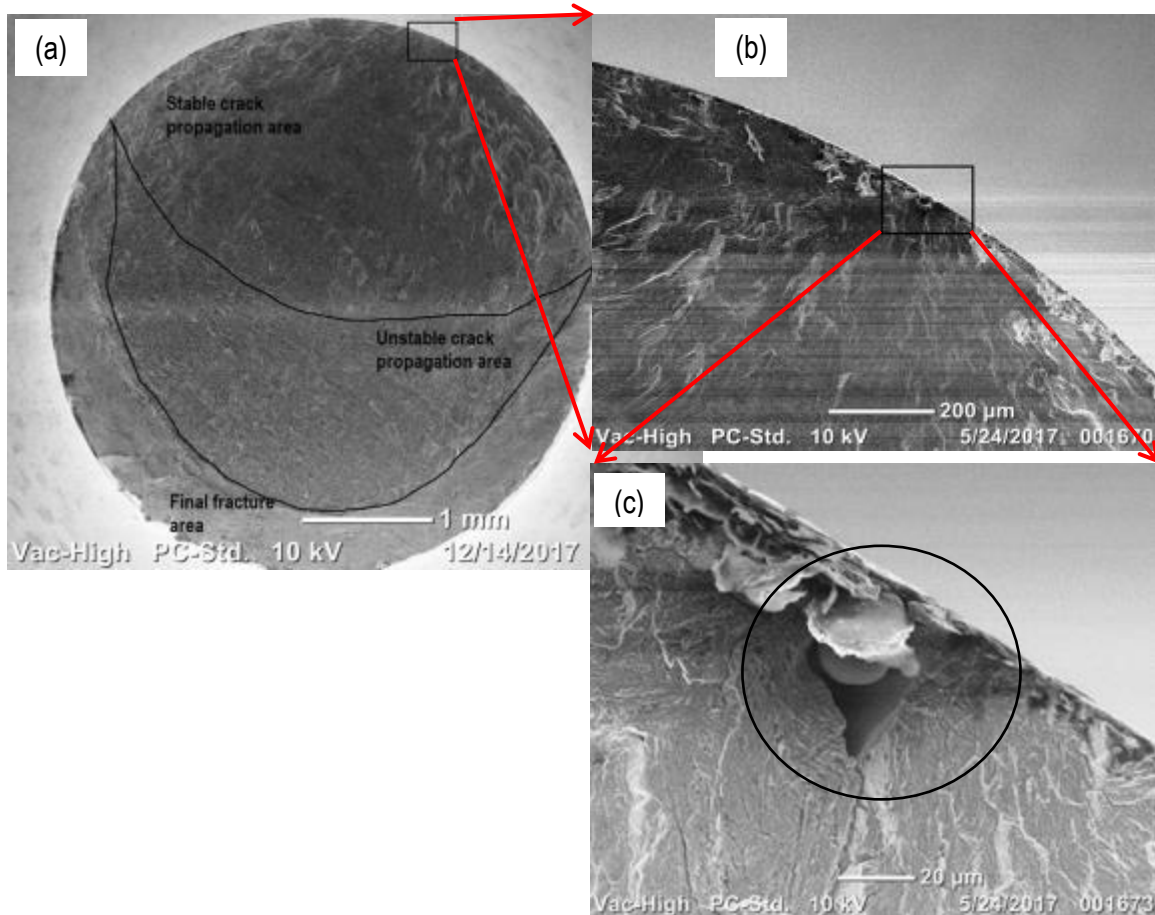


Figure 4.22: (a) Overall fractograph of specimen Y-14 (b) increased magnification of an area around the crack initiation area and (c) high magnification of the crack initiation area

Fatigue fracture in this specimen initiated from a DMLS process-related surface pore of $\sqrt{area} = 31.07 \mu m$ encircled in Figure 4.22 (c). This \sqrt{area} resulted in a value of $\Delta K = 2.809 MPa m^{0.5}$ at $\sigma_{max} = 486 MPa$ (the estimated endurance limit). The crack propagation area is divided into stable and unstable crack propagation zones in which no DMLS process-related pores were located.

The relatively low ΔK at the tip of this crack initiation pore, which is 39% higher than ΔK_{th} at a σ_{max} equal to the estimated fatigue endurance limit, is thought to have resulted in a lower rate of propagation of the pore tip. This resulted in fracture of the specimen at 65% of the set number of the run-out life. This number of load cycles lies in the range of the HCF endurance limit life of iron and titanium metals and their respective alloys (10^6 to 10^7), [74].

Figures 4.23 and 4.24 show SEI SEM fractographs of specimen Y-18 and Y-13 that were cycled at a maximum stress of 549 MPa and which fractured at 83,464 cycles and 1,110,187 cycles

respectively: intermediate maximum stress and low number of life cycles to failure and intermediate stress and high number of cycles to failure, respectively.

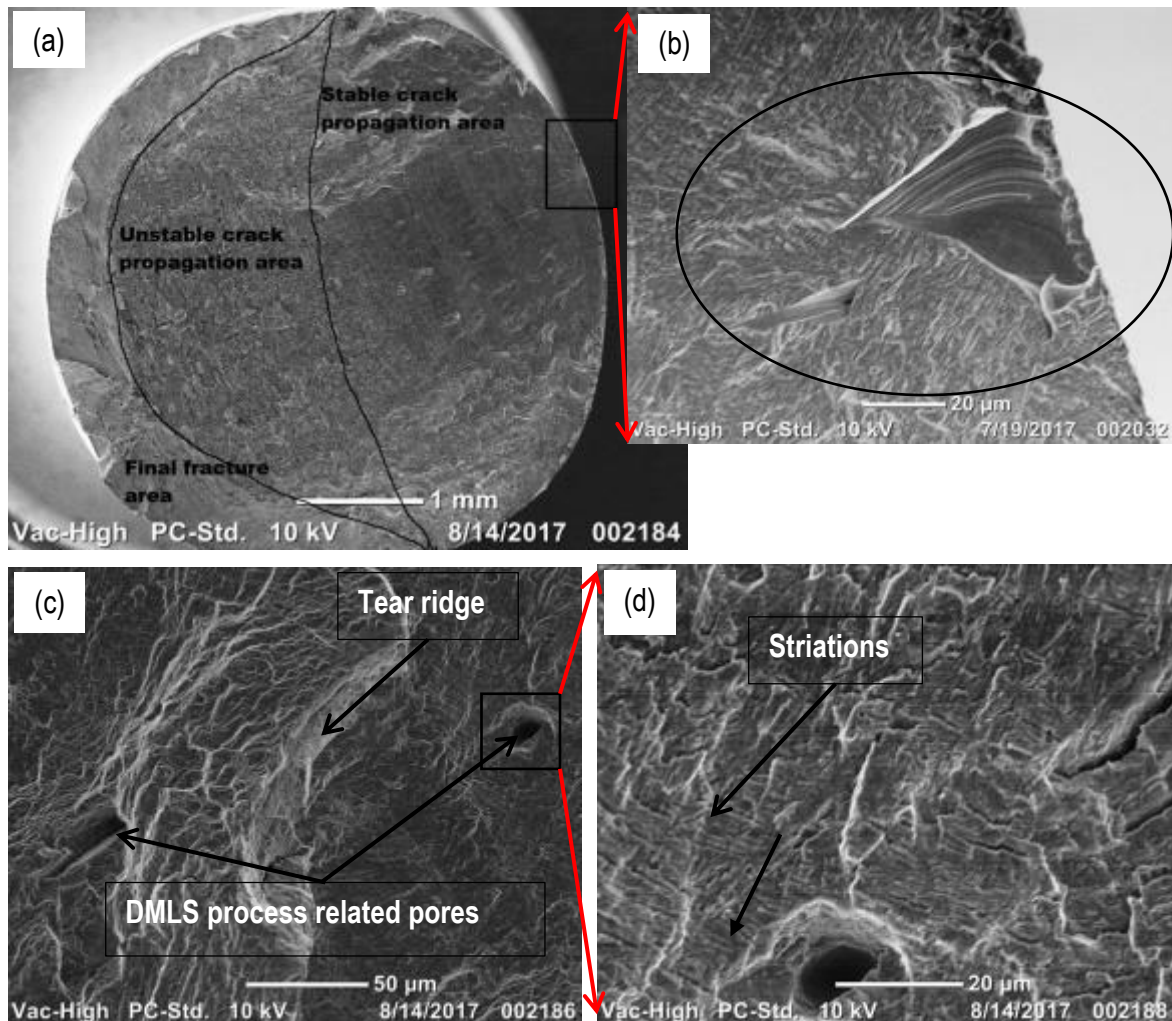


Figure 4.23: (a) Overall fractograph of specimen Y-18 and (b) high magnification of crack initiation site (c) high magnification of the area of stable crack propagation and (c) higher magnification of the area of stable crack propagation, indicating fatigue striations

The fatigue fracture crack of specimen Y-18 initiated from a surface DMLS process-related pore of $\sqrt{area} = 54.08 \mu m$ that is encircled in Figure 4.23 (b). This \sqrt{area} of the pore measured from the fractograph resulted in $\Delta K = 4.186 MPa m^{0.5}$ at $\sigma_{max} = 549 MPa$. The fracture surface had fatigue features of the site of crack initiation, as well as areas of stable crack propagation and unstable crack propagation. Multiple micropores were located on the fracture surface of this specimen.

Specimens Y-18 and Y-13 fractured from cracks that initiated from surface DMLS process-related pores with values of ΔK that were 59% and 39% higher than the value of ΔK_{th} , respectively. These values of ΔK that are above the value of ΔK_{th} at a value of σ_{max} that is 11% above the estimated fatigue endurance limit, led to fractures of the specimens at 1.7% and 22% of the set number of run-out load cycles, respectively. Specimen Y-13, shown in Figure 4.24, fractured from a crack that initiated from a surface DMLS process-related pore of $\sqrt{area} = 24.00 \mu m$ with a change in stress intensity of $2.789 \text{ MPa } m^{0.5}$ encircled in Figure 4.24 (c).

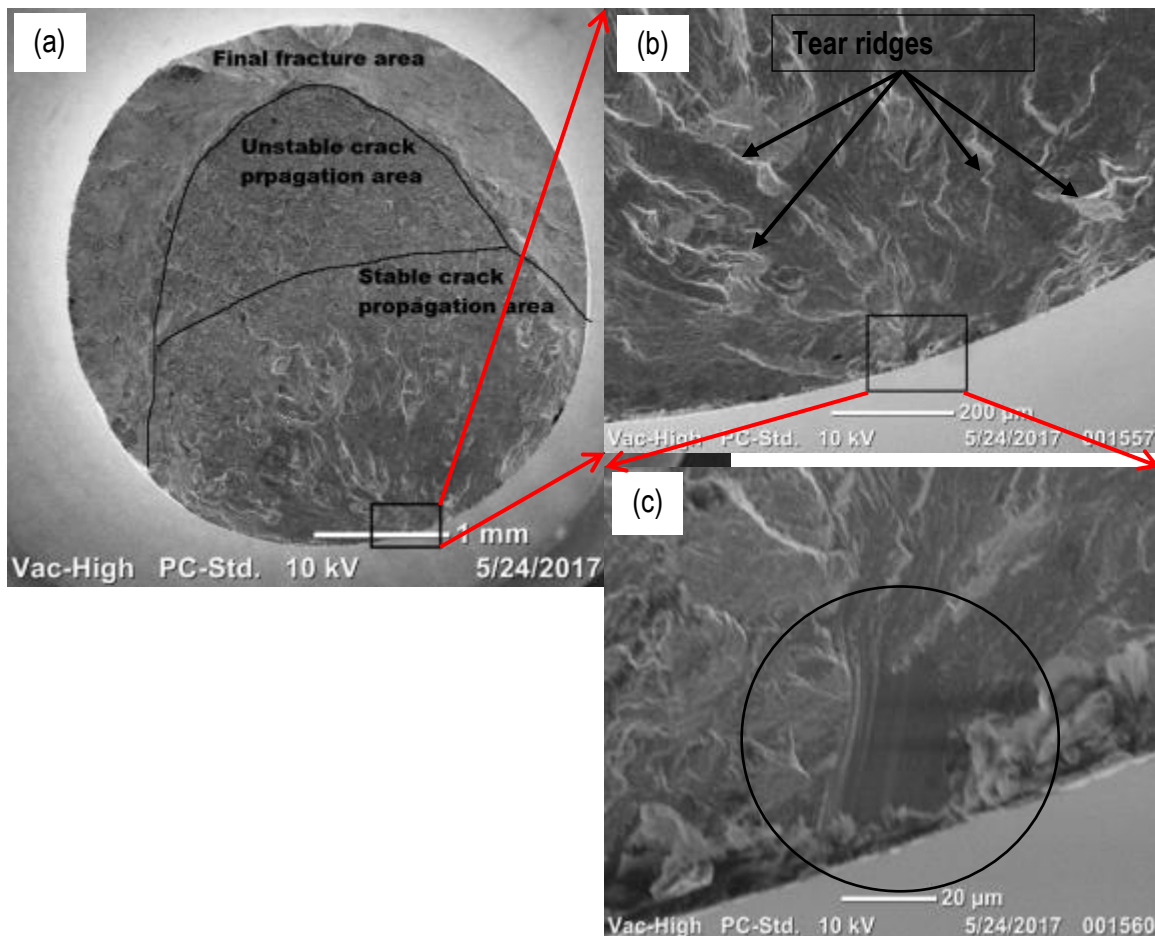


Figure 2.24: (a) Overall fractograph of specimen Y-13 (b) a magnified area around the crack initiation site (c) further magnification around the crack initiation site

The value of ΔK from a crack initiation pore in specimen Y-13 that is lower than that for specimen Y-18 implies a lower rate of propagation of the crack than that in specimen Y-18. Propagation of the crack in specimen 18 accelerated locally upon contact of its tip with each of the pores located on its fracture surface. These DMLS process-related pores and the higher value of ΔK are thought to have

resulted in specimen Y-18 failing at 7.5% of the number of load cycles to failure of specimen Y-13 for the same maximum stress load.

4.6.2.3 Z-built specimens

Table 4.12 shows values of the maximum tension–tension fatigue stresses and the corresponding number of load cycles to failure of the Z-built Ti6Al4V (ELI) specimens that were tested in this study. It also shows the stress range, the square root of the areas of crack initiation pores measured from the fractographs by a sketch-and-calculate software and their related calculated values of stress intensity change ΔK . The loading direction for these specimens is seen from Figure 3.1 in section 3.2 to be perpendicular to the plane of the build layers.

Table 4.12: Dimensions of DMLS process-related initiation pores for fatigue failure cracks and their stress intensity ranges and selected load stress data of Z-built as-built DMLS Ti6Al4V (ELI) specimens

Specimen designation	Maximum stress (σ_{max}) (Mpa)	Stress range ($\Delta\sigma$) (MPa)	Fatigue life N_f (cycles)	\sqrt{area} (μm)	Change in stress intensity ΔK (MPa $m^{0.5}$)
Z-21	675	607.5	28,348	41.10	4.487
Z-22	612	550.8	57,891	39.40	3.983
Z-30	612	550.8	76,252	42.05	4.115
Z-23	549	494.1	399,838	35.57	3.395
Z-29	549	494.1	822,565	25.00	2.846
Z-24	486	437.4	92,862	54.37	3.715
Z-28	486	437.4	5,000,000	-	-
Z-25	423	380.7	97,743	72.46	3.733
Z-27	423	380.7	5,000,000	-	-
Z-26	360	324	5,000,000	-	-

* $\Delta K_{th} = 1.4 \text{ MPa } m^{0.5}$ for crack propagation parallel to the as-built DMLS Ti6Al4V layers at $R = 0.1$ [96].

Figure 4.25 presents a semi-log S-N curve of the maximum stress against the number of load cycles of the Z-built DMLS Ti6Al4V (ELI) specimens based on the data shown in Table 4.12.

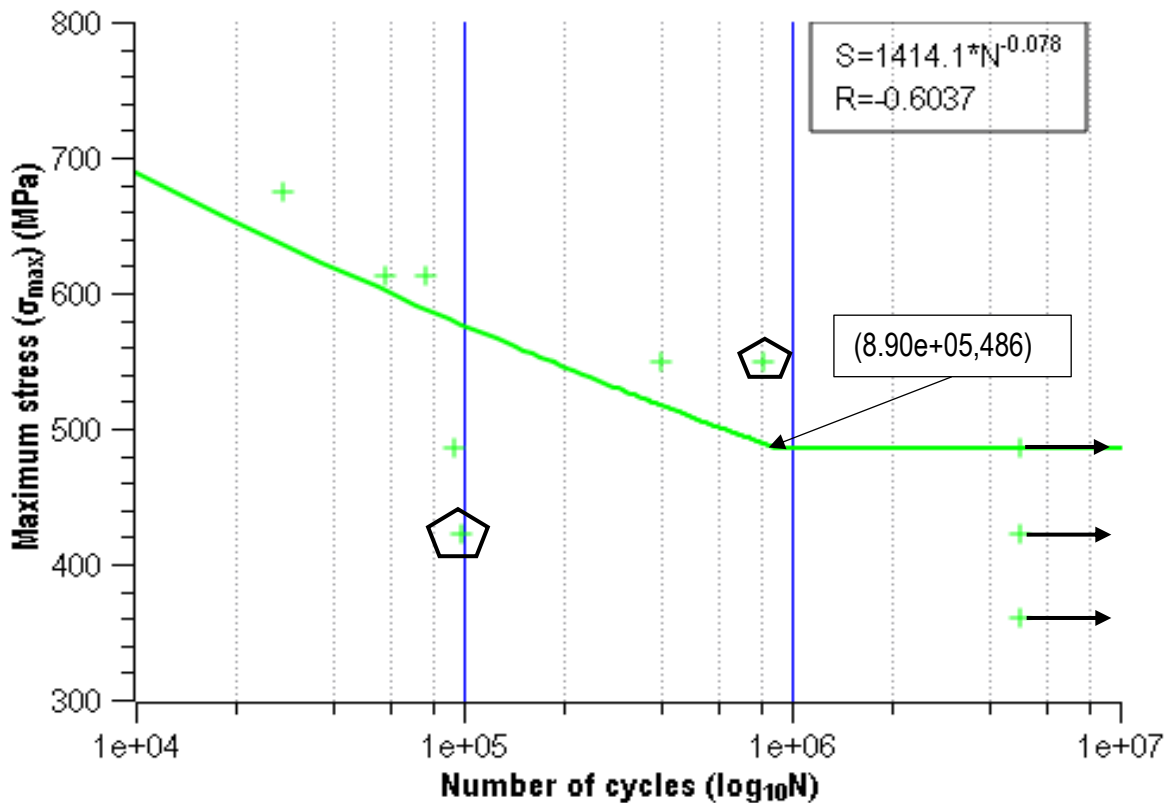


Figure 4.25: Semi- \log_{10} S-N curve for as-built Z-built specimens

Linear curve fitting through the fatigue data for the fractured specimens was done without including the fatigue data from specimens Z-29 and Z-25, indicated by data points enclosed in pentagons in Figure 4.25, because they were considered to be outliers. The correlation coefficient (R) of -0.6037 given by these scattered data points is moderate. The curve gives a fatigue strength of 688 MPa at 10^4 load cycles which is 76% of the 0.2% offset proof strength of vertically orientated as-built DMLS Ti6Al4V (ELI) reported by Yadroistev et al. [41]. The curve forms a knee at a fatigue strength of 486 MPa and at 890,000 load cycles where it turns horizontal. The highest value of σ_{max} of the run-out specimens, indicated by arrows in Figure 4.25, gives an estimate of the fatigue endurance limit. This fatigue endurance limit is 54% of the 0.2% offset proof strength of as-built DMLS Ti6Al4V (ELI) reported by Yadroistev et al. [41].

Specimen Z-29 showed a high number of cycles to failure at an intermediate load whereas specimen Z-25 showed a low number of cycles to failure at a low load (below the endurance limit). The fracture surfaces of these outliers were studied in a SEM to identify the reason for their unexpected behaviour. Their SEI fractographs are shown in Figures 4.26 and 4.27. The fractographs of the

fracture surface of specimen Z-29 are also compared to those of specimen Z-23, which was loaded at the same maximum stress level but failed at a low number of cycles.

Figures 4.26 and 4.27 show the fractographs of specimen Z-29 and Z-23 which were cycled at a maximum stress of 549 MPa and which fractured at 822,565 and 399,838 cycles, respectively: intermediate maximum stress and high number of life cycles to failure and intermediate maximum stress and low but acceptable number of cycles to failure.

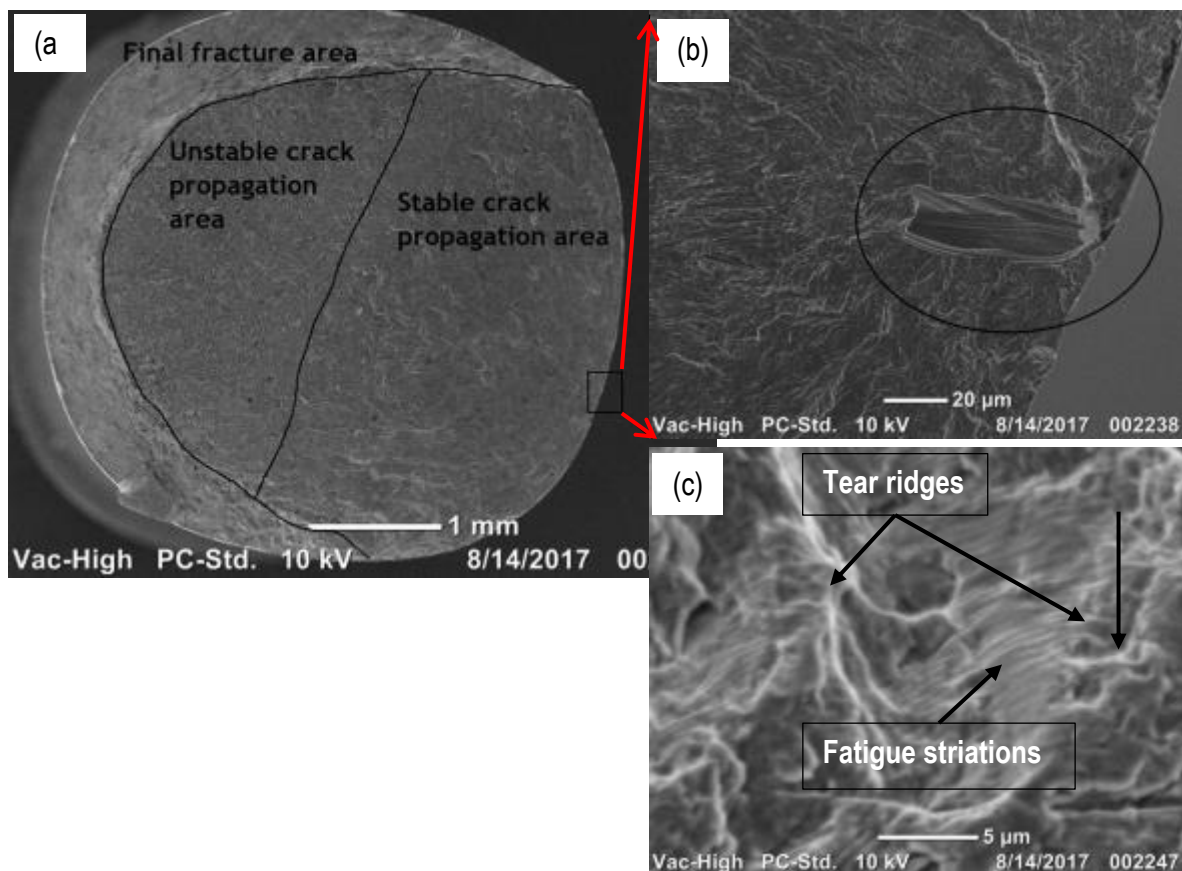


Figure 4.26: (a) Overall fractograph of the specimen Z-29 (b) high magnification of an area around the crack initiation site and (c) high magnification on a tear ridge showing fatigue striations

The fatigue fracture surfaces of specimens Z-29 and Z-23 were both characterized by site of crack initiation (from a DMLS process-related surface pore), an area of stable and unstable crack propagation and an area of final fracture, all shown in Figure 4.26 (a). Specimen Z-29 fractured from a crack that initiated from a DMLS process-related surface pore that is encircled in Figure 4.26 (b).

The crack initiation pore had a value of $\Delta K = 2.846 \text{ MPa m}^{0.5}$ at its tip and had an $\sqrt{\text{area}} = 25.00 \text{ }\mu\text{m}$ at $\sigma_{\text{max}} = 549 \text{ MPa}$. This was lower than the value of $\Delta K = 3.394 \text{ MPa m}^{0.5}$ at the crack initiation pore tip of specimen Z-23, encircled in Figure 4.27 (b), whose is $\sqrt{\text{area}} = 35.57 \text{ }\mu\text{m}$.

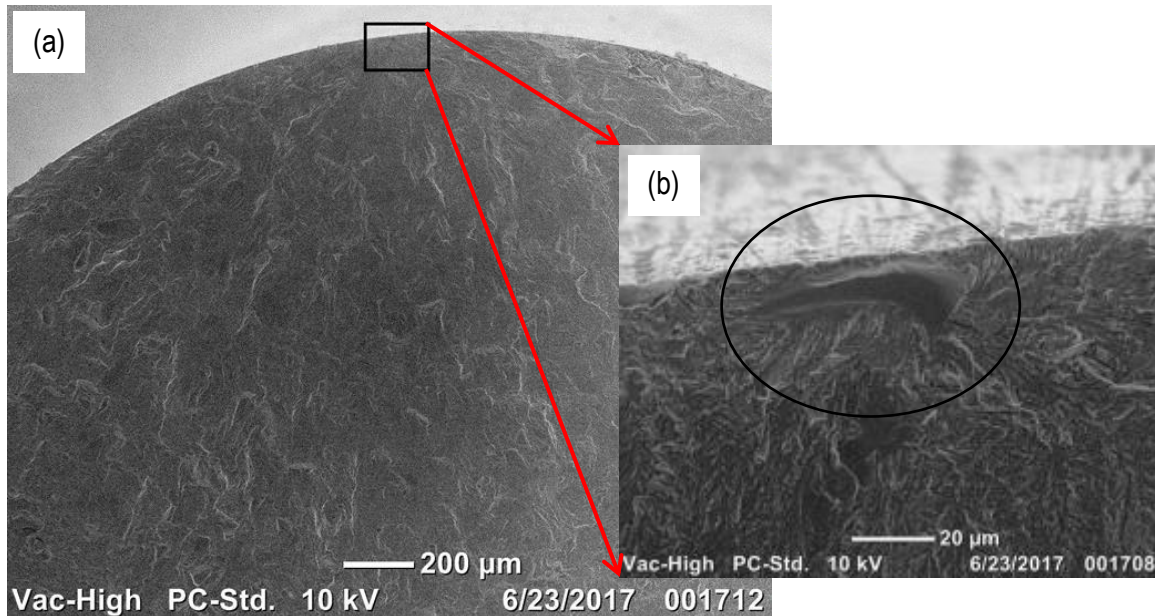


Figure 4.27: Fractograph of specimen Z-23 in the area of stable propagation of a crack and (b) high magnification of an area around the site for initiation of a crack

Specimens Z-29 and Z-23 failed from crack initiation pores with values of ΔK that were 51% and 59% higher than the value of ΔK_{th} , respectively. These values of ΔK that were both above the value of ΔK_{th} at a value of σ_{max} that was 11% above the estimated fatigue endurance limit, led to failure of the specimens at 16% and 8% of the set run-out number of load cycles, respectively. Specimen Z-29 is thought to have failed at a higher number of life cycles than specimen Z-23 because it had the lower value of ΔK of the two imposed on it by its crack initiation pore. No internal pores were located on the fracture surfaces of both the specimens, which implies the absence of accelerated propagation of cracks in the vicinity of the crack initiation pores, as was the case in most of the specimens that failed after low numbers of life cycles discussed here previously. The fine fatigue striations in the zone of stable crack propagation for specimen Z-29, shown in Figure 4.26 (c), attest to the high number of life cycles endured by the specimen before failure.

Figure 4.28 shows the SEI SEM micrographs of specimen Z-25 which was cycled at a maximum stress of 423 MPa and which fractured after 97,743 cycles: low maximum stress and low number of life cycles.

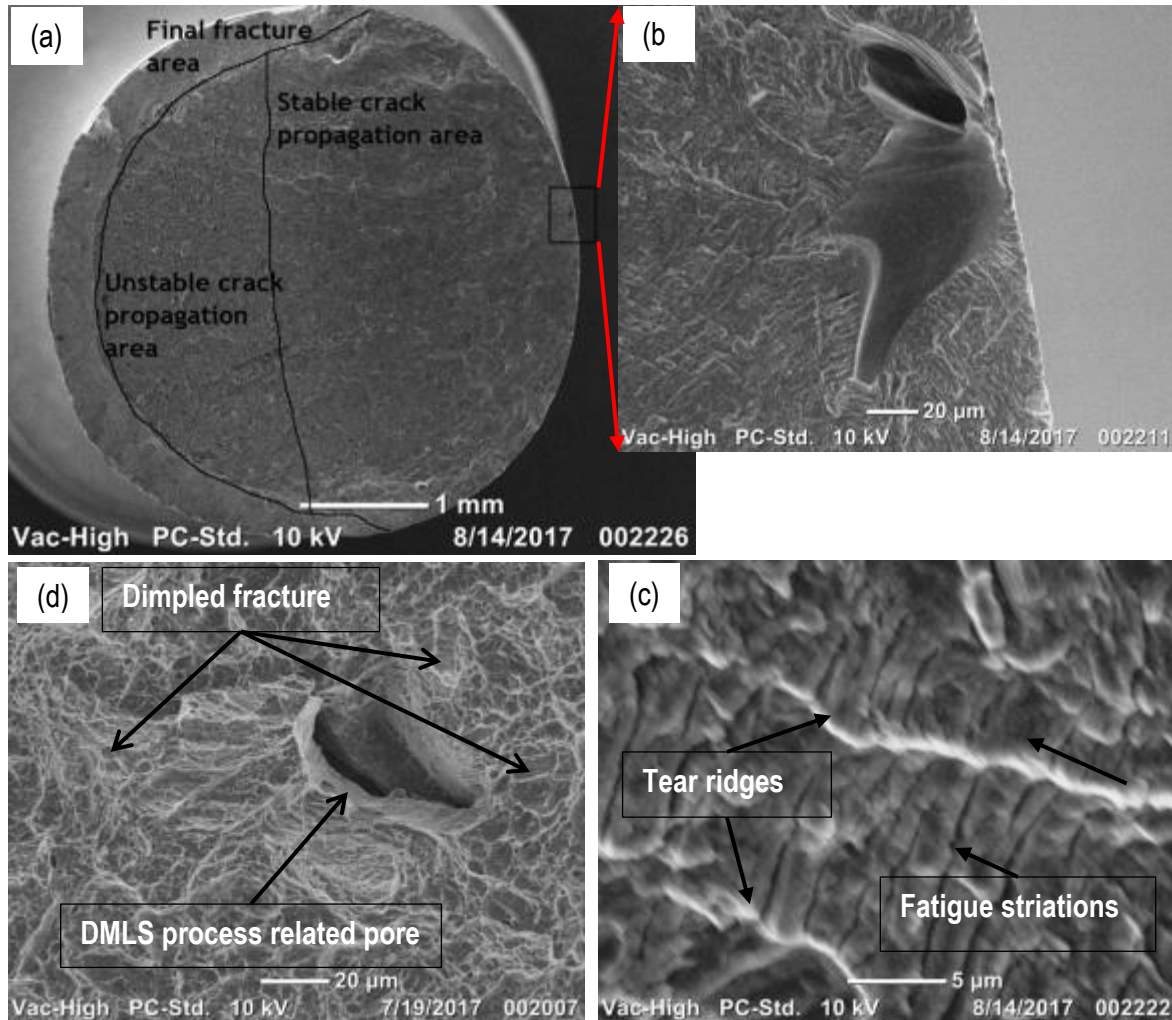


Figure 4.28: Overall fractograph of specimen Z-25 and (b) high magnification of an area around the site of crack initiation (c) high magnification of the area of stable propagation of a crack around a pore and (d) high magnification of the area of stable propagation of a crack, showing fatigue striations

Fatigue crack fracture of specimen Z-25 initiated from a DMLS process-related surface pore with a measured \sqrt{area} of $72.46 \mu m$, which was the biggest \sqrt{area} of the DMLS process-related crack initiation pores in the DMLS Ti6Al4V (ELI) as-built specimens tested in this series of experiments. This crack initiation pore resulted in a value of $\Delta K = 3.733 MPa m^{0.5}$ at $\sigma_{max} = 450 MPa$. This value of ΔK is 62% higher than the value of ΔK_{th} resulting from the highest value of \sqrt{area} of

all crack initiation pores of the fractured specimens discussed in this project, while the value of σ_{max} for the specimen is 7% below the estimated endurance limit. This resulted in the specimen fracturing after a low number of load cycles at a low maximum stress level.

4.6.2.4 Influence of microstructure on the mode of fracture

In order to investigate the influence of the DMLS orientations of build on the fatigue properties of as-built Ti6Al4V (ELI) with respect to orientation of the grain structures, sections were cut from the X-, Y- and Z-built as-built DMLS Ti6Al4V (ELI) specimens that fractured upon application of a fatigue load of the same magnitude. The cuts were made on planes that were orthogonal to the respective orientations for each specimen, as shown in the schematic in Figure 4.29, and the surfaces were then prepared for metallographic analysis. Specimens X-1, Y-12 and Z-22 that were selected for use in this exercise, failed from the application of a maximum cyclic load of $\sigma_{max} = 671 \text{ MPa}$, at 179,794.00, 297,396.00 and 57,891.00 load cycles, respectively.

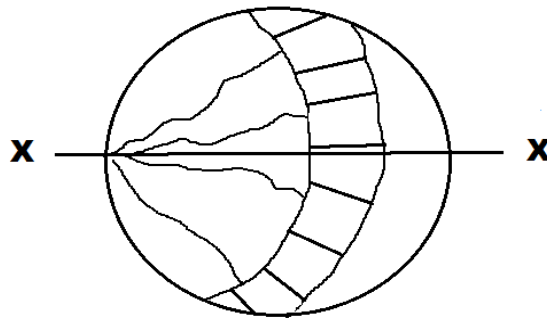


Figure 4.29: Schematic of a fracture surface with the line X-X indicating the section line of cut for metallographic preparation

The sections through the fracture surfaces were cut from the point of crack initiation along a plane running through the centre of the fracture surface, as indicated by the section line X-X in Figure 4.29. The differing influences of the microstructures of the three specimens that represent three mutually orthogonal DMLS orientations were observed to be attributed to the orientation of the prior β columnar grains with regard to the fatigue loading axis. Specimens X-1 and Y-12 were found to have the same orientation of the prior β columnar grains, with their longitudinal axes being perpendicular to the longitudinal axes of the specimens, which was also the axial direction of the fatigue load. On the other hand, the longitudinal axes of the prior β columnar grains in specimen Z-22 were parallel

to the axial direction of the fatigue load. The paths of propagation of fatigue failure cracks in specimens X-1 and Y-12 were observed to cut across the longitudinal axis of the prior β columnar grains. The path of propagation of the fatigue failure crack in specimen Z-22 was observed to primarily run along the grain boundaries that were aligned with the longitudinal axis of the prior β columnar grains. In this regard, specimens X-1 and Y-12 are hereinafter referred to as horizontally oriented specimens and specimen Z-22 as a vertically oriented specimen. The overall micrographs showing the paths of propagation of cracks for horizontally and vertically oriented specimens are presented in Figures 4.30 and 4.31.

4.6.2.4.1 Horizontally oriented as-built specimens

Figure 4.30, shows the stitched optical micrograph (a series of micrographs combined into a panoramic view) of the path of propagation of the fatigue failure crack for the horizontally oriented as-built DMLS Ti6Al4V (ELI) specimen X-1, which was cycled under tension–tension at a maximum stress load of 671 MPa, and which fractured after 179,794 cycles. The black area of the micrographs that follow is the mounting resin of the specimens and the bright areas are the specimens.

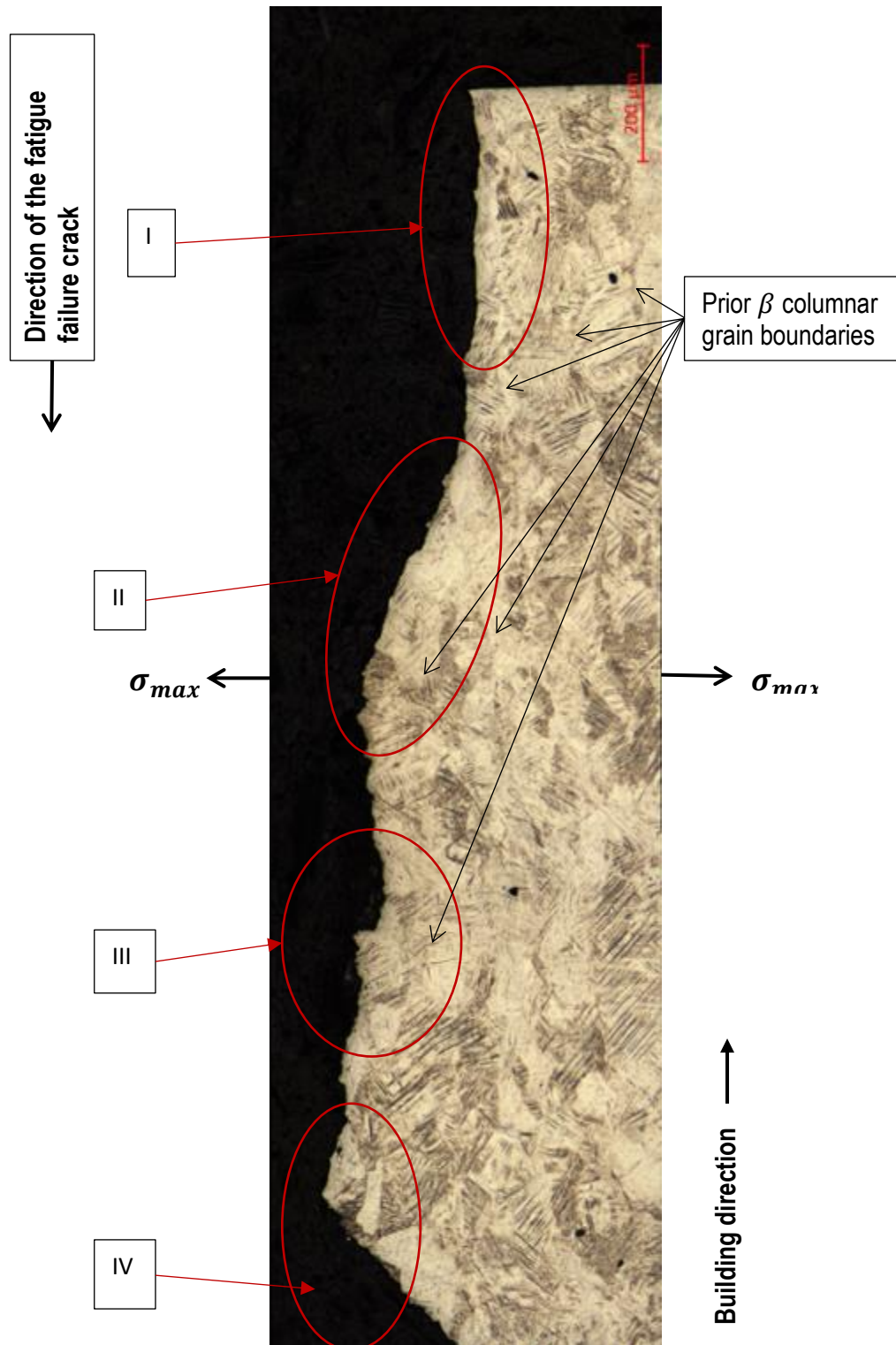


Figure 4.30: A stitched micrograph of specimen X-1 showing propagation of the fatigue failure crack

Figures 4.31 (a) and (b) show the magnified micrographs of the path of the fatigue failure crack for specimen X-1 around the parts labelled I and II in Figure 4.30, respectively.

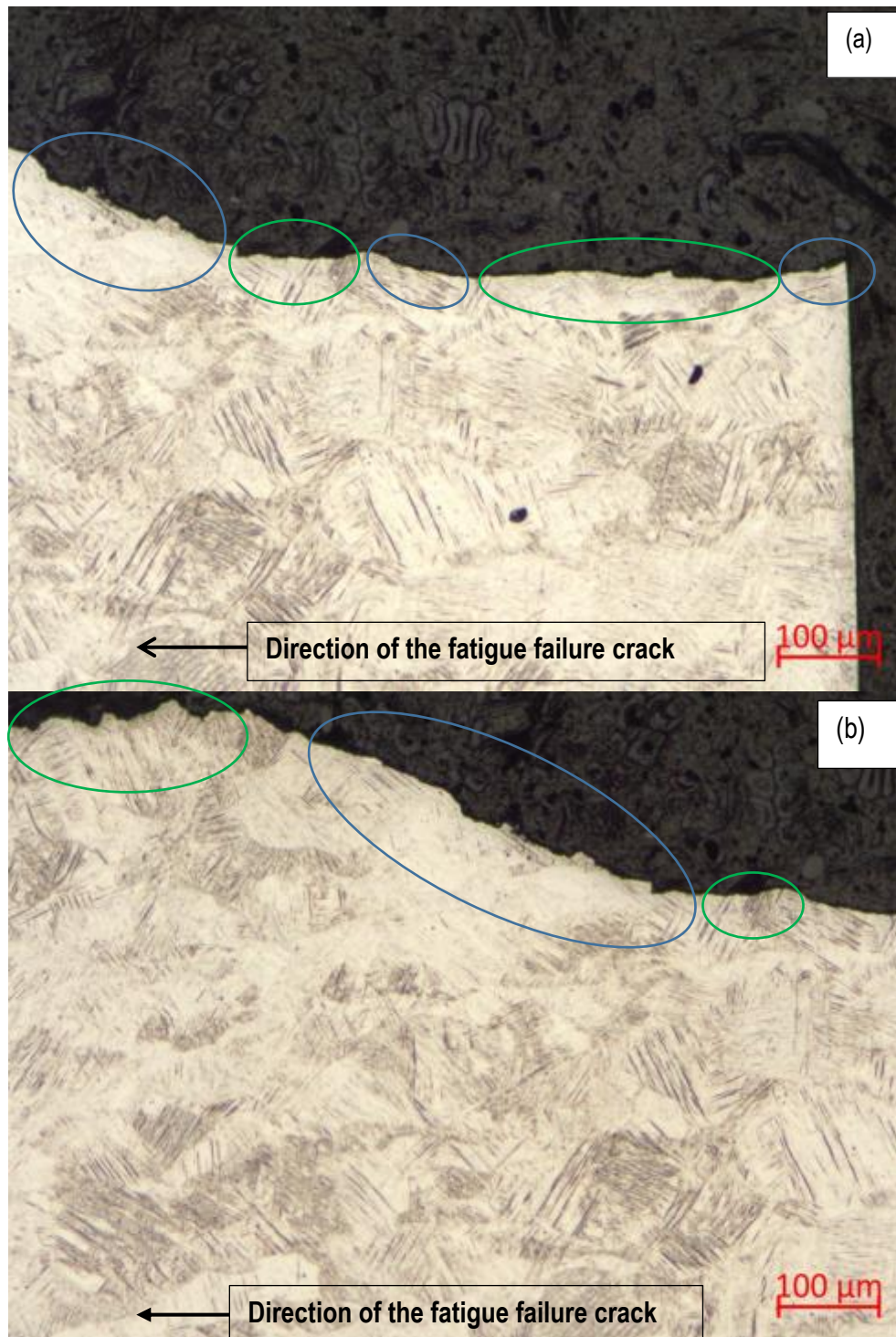


Figure 4.31: (a) A micrograph of specimen X-1 around the enclosed area labelled I in Figure 4.30 and (b) a micrograph of specimen X-1 around the enclosed area labelled II in Figure 4.30

Figures 4.32 (a) and (b) show the magnified micrographs of the path of the fatigue failure crack for specimen X-1 around the sections labelled III and IV in Figure 4.30.

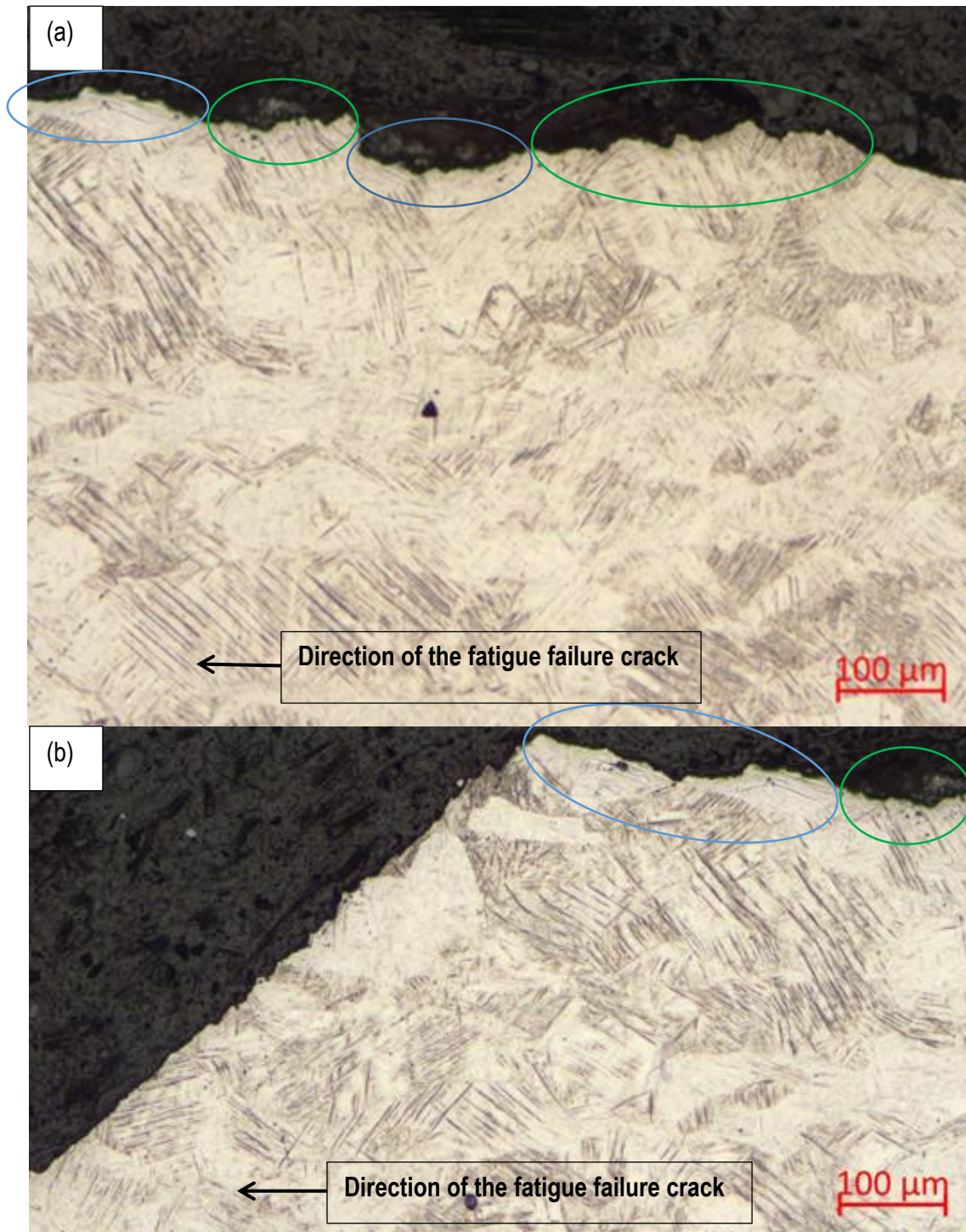


Figure 4.32: (a) A micrograph of specimen X-1 around the enclosed area labelled III in Figure 4.30 and (b) a micrograph of specimen X-1 around the enclosed area labelled IV in Figure 4.30

Propagation of the fatigue failure crack in this specimen in relation to the prior β columnar grains was both inter-granular and trans-granular. This was determined by following the crack path in

Figure 4.30 along and through the fine (bright areas) and coarse (dark areas) within the prior β columnar grains. The path of propagation of the fatigue failure crack in the trans-granular mode of propagation was at angles less than 90° across the longitudinal axis of the fine and coarse prior β columnar grains; their grain boundaries acting as crack deflectors along the angles of their orientation. Moreover, the direction of the fatigue failure crack is parallel to the longitudinal axes of the columnar grain boundaries. Therefore, there was limited interaction of the fatigue failure crack with the boundaries of the prior β grains.

Regarding the acicular α' basket weave, the fatigue failure crack also propagated in both inter-granular and trans-granular modes. These features were identified from the higher magnification micrographs in Figures 4.31 (a) and (b) and 4.32 (a) and (b), where the features for the inter-granular mode of fracture are enclosed in blue ovals and those for trans-granular fracture modes are enclosed in green ovals. The trans-granular mode of propagation of the fatigue failure crack, which is characterized by a fairly flat surface of propagation, was found to be dominant at an area close to the site of crack initiation (area of stable propagation of the fatigue failure crack) magnified in Figure 4.31 (a). The fatigue failure crack cuts across the acicular α' martensite grains. The fracture mode changed to inter-granular fracture as the crack progressed through to the area of unstable propagation of the fatigue failure crack, where the crack is seen to propagate parallel to the acicular α' grains and therefore forms a zig-zag path that is typical of inter-granular fracture (see Figures 4.32 (a) and (b)).

4.6.2.4.2 Vertically built specimens

Figures 4.33 shows the stitched optical micrographs of the fatigue failure crack path of the vertically built as-built DMLS Ti6Al4V (ELI) specimen Z-22 that was cycled under tension–tension at a maximum stress load of 671 MPa and which fractured after 57,891 cycles.

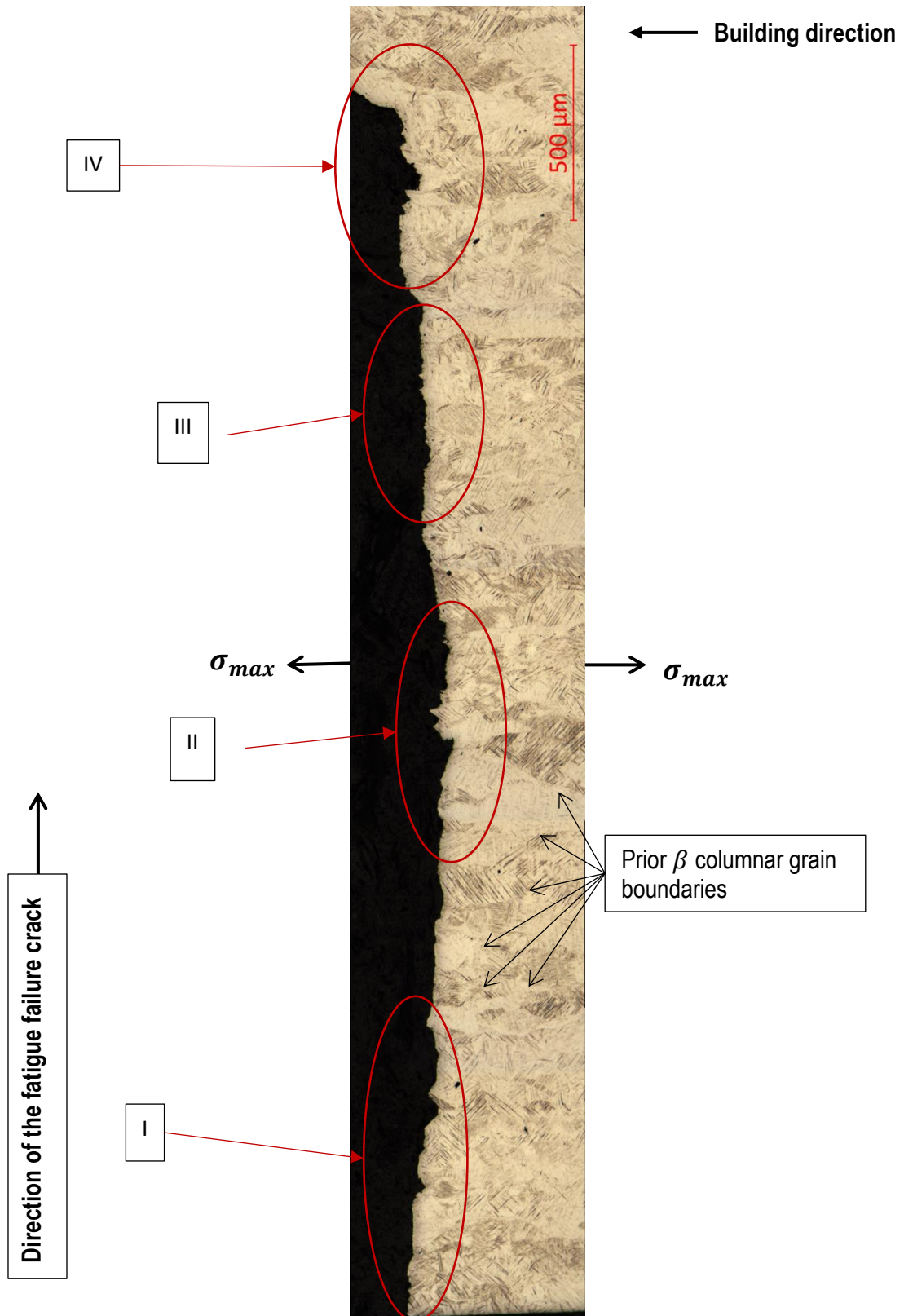


Figure 4.33: A stitched micrograph of specimen Z-22 showing crack propagation

Figures 4.34 (a) and (b) show the magnified micrographs of the path of the fatigue failure crack for specimen Z-22 around the parts labelled I and II in Figure 4.33, respectively.

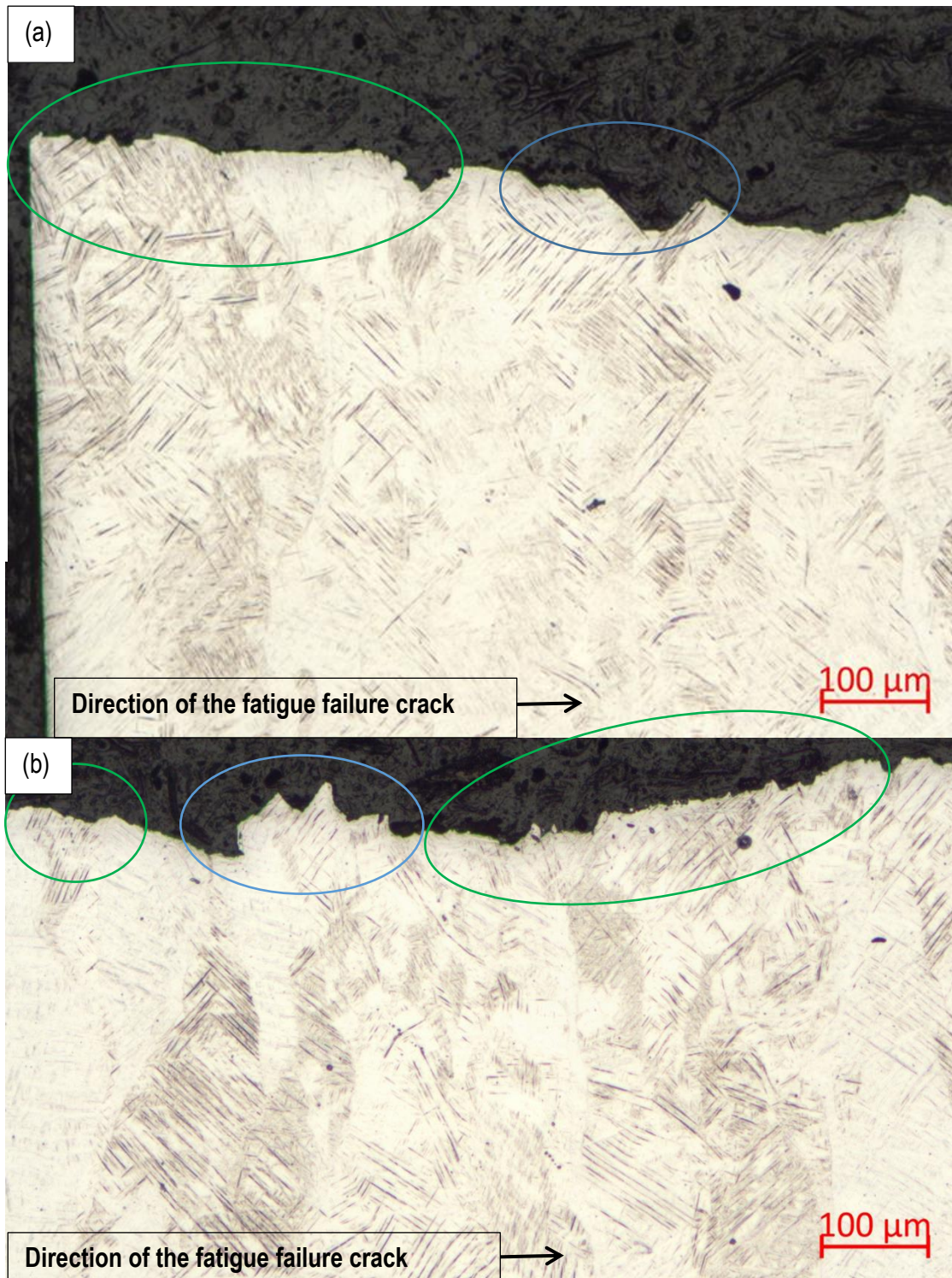


Figure 4.34: (a) A micrograph of specimen Z-22 around the enclosed area labelled I in Figure 4.33 and (b) a micrograph of specimen Z-22 around the enclosed area labelled II

Figures 4.35 (a) and (b) show the magnified micrographs of the path of the fatigue failure crack for specimen Z-22 around the sections labelled III and IV in Figure 4.33.

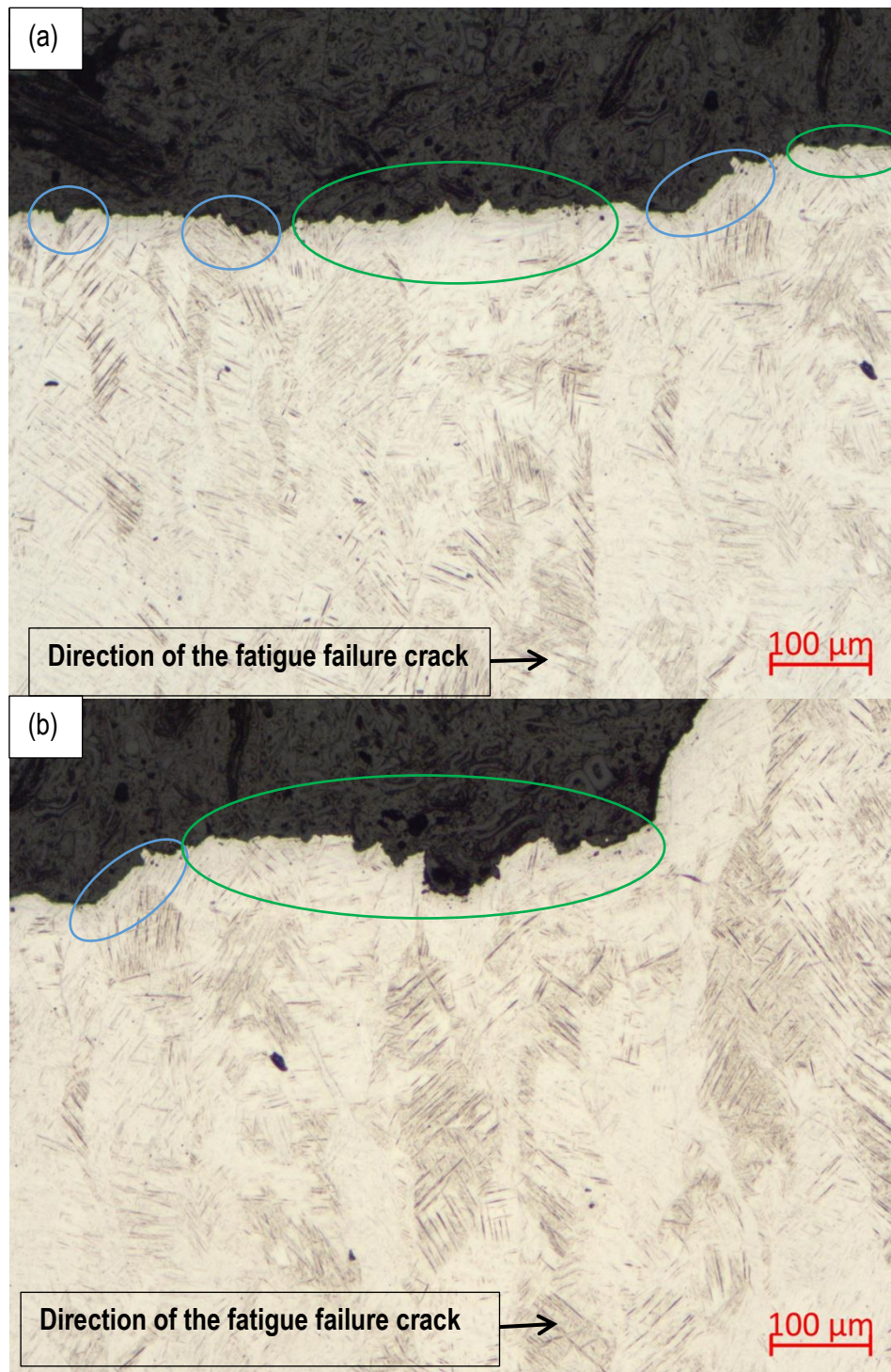


Figure 4.35: (a) A micrograph of specimen Z-22 around the enclosed area labelled III in Figure 4.33 and (b) a micrograph of specimen Z-22 around the enclosed area labelled IV

The mode of propagation of the fatigue failure crack in this specimen with regard to the prior β columnar grains was predominantly trans-granular as the crack was perpendicular to the longitudinal axes of the prior β columnar grains (see Figure 4.33). This maximized the number of prior β columnar grain boundaries that resisted propagation of the crack.

Figures 4.34 (a) and (d) and 4.34 (a) and (d) showed similar features of fracture modes in specimen Z-22 as in specimen X-1 in Figures 4.31 and 4.32, which consist of both inter-granular and trans-granular cracks across the α' basket weaves. The distinctive features of these inter-granular and trans-granular fracture modes are enclosed in blue and green ovals, respectively, in Figures 4.34 (a) and (d) and 4.34 (a) and (d).

From the micrographs in Figures 4.30 and 4.33, it can be concluded that the fatigue fracture modes of horizontally and vertically oriented as-built DMLS Ti6Al4V (ELI) specimens regarding the acicular α' basket weaves are similar and consist of inter-granular and trans-granular fracture modes. For both specimens it is seen that the areas around the sites of crack initiation (stable propagation of cracks) are dominated by trans-granular modes of fracture through the acicular α' basket weaves, which is characterized by fairly flat paths of fracture (Figure 4.31 (a) and Figure 4.34 (a)). As the fatigue failure crack propagates towards the section of unstable propagation before final fracture, the mode of fatigue fracture changes to inter-granular fracture along the acicular α' martensite grains. The fatigue failure crack tends to grow along the acicular α' grains thus forming a ragged zig-zagged crack path. The only difference between the horizontally and vertically oriented specimens lies in the propagation of fatigue failure cracks across and along the prior β columnar grains in the former and latter directions respectively, with prior β grain boundaries offering limited fatigue resistance in the horizontally oriented and maximum resistance in the vertically oriented specimens. The contrast can be seen by a fairly flat crack path in a vertically oriented specimen (as is evident in Figure 4.33) as opposed to zig-zag crack paths in a horizontally oriented specimen (as is evident in Figure 4.30).

The grains resist propagation of cracks thus causing the cracks to navigate along the grain boundaries and around the grains. This results in a lower fatigue life as opposed to those cases where cracks pass right through the grains. With this in mind, the fatigue lives of the horizontally oriented specimens were expected to be higher than those of the vertically oriented specimens, as is evident from an inspection of Tables 4.10, 4.11 and 4.12.

4.6.1 Fatigue test results of stress-relieved and HTA-treated fatigue specimens

The fatigue cracks of the fractured stress-relieved and HTA DMLS Ti6Al4V (ELI) specimens were seen to have initiated from surface and sub-surface DMLS process-related pores and from surface facets. There was, however, an exception of one Y-built specimen which failed from an internal crack initiation from facets in the metal. The specimens were micro-CT scanned for porosity prior to HCF testing. After HCF testing, with the aid of the SEI SEM fractographs and the position of the fracture plane along the loading axis, the DMLS process-related initiation pores for the fatigue failure cracks were identified from the micro-CT data. The projected areas of these identified initiation pores for the fatigue failure cracks, normal to the loading axis as measured from the micro-CT scans, were used to calculate the values of ΔK imposed by them on their respective specimens. The micro-CT data from the run-out specimens was used to estimate the value of ΔK_{th} of the specimens. This was done by identifying the largest projected pore area normal to the loading axis and suggesting that its resultant value of ΔK was less than the ΔK_{th} value. The micro-CT data was also used to determine the distribution of the DMLS process-related pores on the fracture planes of respective specimens.

4.6.1.1 X-built specimens

Table 4.13 shows values of the maximum tension–tension fatigue stresses and the corresponding number of load cycles to failure or run-out of the tested specimens. It also shows the stress range, the square root of the micro-CT scan measured crack initiation areas and the related calculated values of ΔK .

Table 4.13: Dimensions of DMLS process-related initiation pores for fatigue failure cracks and their stress intensity ranges for selected load stress data of X-built stress relieved plus HTA DMLS Ti6Al4V (ELI) specimens

Specimen designation	Maximum stress (σ_{max}) (MPa)	Stress range ($\Delta\sigma$) (MPa)	Fatigue life (N_f)	\sqrt{area} (μm)	Change in stress intensity factor (ΔK) ($\text{MPa m}^{0.5}$)
X-10	675	607.5	74,209	56.12	5.24
X-9	650	585.0	88,015	75.76	5.86-
X-8	630	567.0	108,969	75.76	5.68
X-4	612	550.8	786,191	77.97	5.60
X-6	580	522.0	659,769	92.79	5.79
X-5	549	494.1	2,416,680	Facets	-
X-3	530	477.0	110,284	89.39	5.21
X-12	520	468.0	2,580,515	65.80	4.37
X-11	486	437.4	2,949,384	-	-
X-7	450	405.0	5,000,000	86.49	4.34

The cracks of the fractured specimens initiated from surface and sub-surface DMLS process-related pores. The values of ΔK presented in Table 4.13 were calculated from the principles of LEFM using Murakami's expression [6] given in this dissertation as Equation (2.9) with the projected areas of the pores normal to the loading axis measured from micro-CT scans of the respective specimens. From Table 4.13 it can be seen that an increase in the value of ΔK leads to a decrease in the number of load cycles to failure. This is because the increase in the value of ΔK at the pore tip increases the rate of propagation of fatigue failure [102]. This conclusion does not apply to specimen X-11, which fractured at the grip ends and was considered as an outlier. The largest DMLS-related identified micro-CT scan pore in specimen X-7, which was considered to have experienced a run-out, had a calculated value of $\Delta K = 4.34 \text{ MPa m}^{0.5}$. This has been taken here as a value below the threshold change in stress intensity factor (ΔK_{th}). This is, however, higher than $\Delta K_{th} = 3.9 \text{ MPa m}^{0.5}$ reported by Leuders et al. [96] for SLM Ti6Al4V specimens that were heat treated at 800 °C and 1050 °C followed by furnace cooling.

Figure 4.36 presents a semi-log S-N curve of the maximum stress against the number of load cycles for the X-built stress-relieved plus HTA DMLS Ti6Al4V (ELI) specimens.

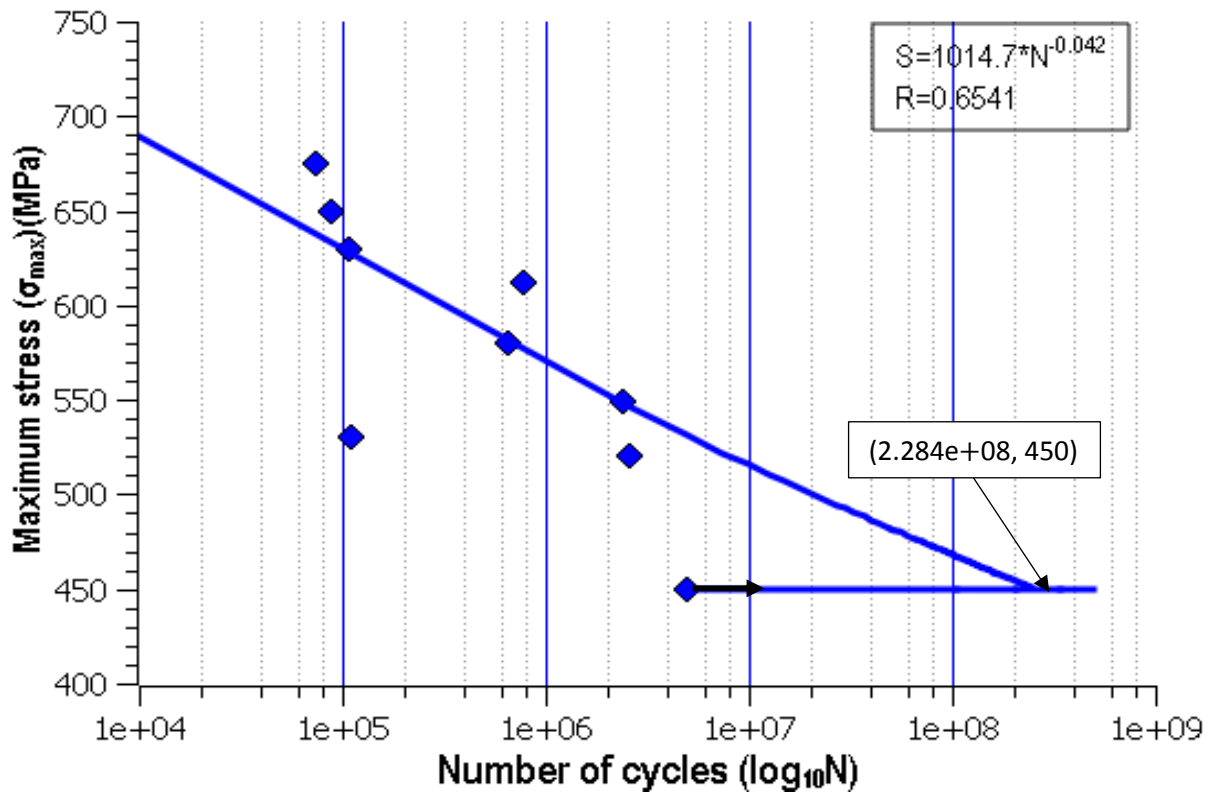


Figure 4.36: Semi-log S-N curves for stress-relieved plus HTA DMLS Ti6Al4V (ELI) X-built specimens

The semi-log S-N plot in Figure 4.36 shows the typical curve profile of steels and titanium alloys of linearly decreasing magnitude of S with $\log_{10} N$, up to a point defining the endurance limit. It is noted that the endurance limit in this case is higher than the set run-out of 5,000,000 cycles at which testing was stopped and used to estimate the endurance limit, as run-out is typically selected according to the expected application [15]. The fatigue endurance limit of the X-built DMLS stress-relieved plus HTA Ti6Al4V (ELI) specimens is seen in Figure 4.36 to be $\sigma_{max} = 450$ MPa, which is the value for specimen X-7 that is indicated by an arrow in Figure 4.36 [101]. This endurance limit is at a level of 53% with reference to the average 0.2% offset proof strength of the X-built stress-relieved plus HTA specimens.

Specimen X-11, encircled in Figure 4.36, was not included in the linearization of the fractured specimens as it fractured from the grip ends and was regarded as an outlier. The correlation coefficient (R) of -0.737 indicates a strong inverse linear relationship between σ_{max} and $\log_{10} N$ for the X-built DMLS stress-relieved plus HTA Ti6Al4V (ELI) specimens. Extrapolation of the linearized curve for the fractured specimens gives a fatigue strength of 690.4 MPa (81% of the averaged 0.2% offset proof stress of the X-built stress-relieved plus HTA specimens) at 10^4 load cycles and

intersects with the horizontal curve for the estimated fatigue endurance limit at 55,690,000 load cycles, as indicated in Figure 4.36. This estimate of the knee point is higher than the value estimated earlier on in this dissertation for the as-built X-built DMLS Ti6Al4V (ELI). This implies an increase in the number of load cycles to failure of DMLS Ti6Al4V (ELI) specimens after the application of the stress-relieving plus HTA process.

Figure 4.37 shows SEI SEM fractographs of specimen X-3 that was cycled at a maximum stress of 530 MPa and which fractured at 110,284 cycles: low maximum stress and low number of life cycles.

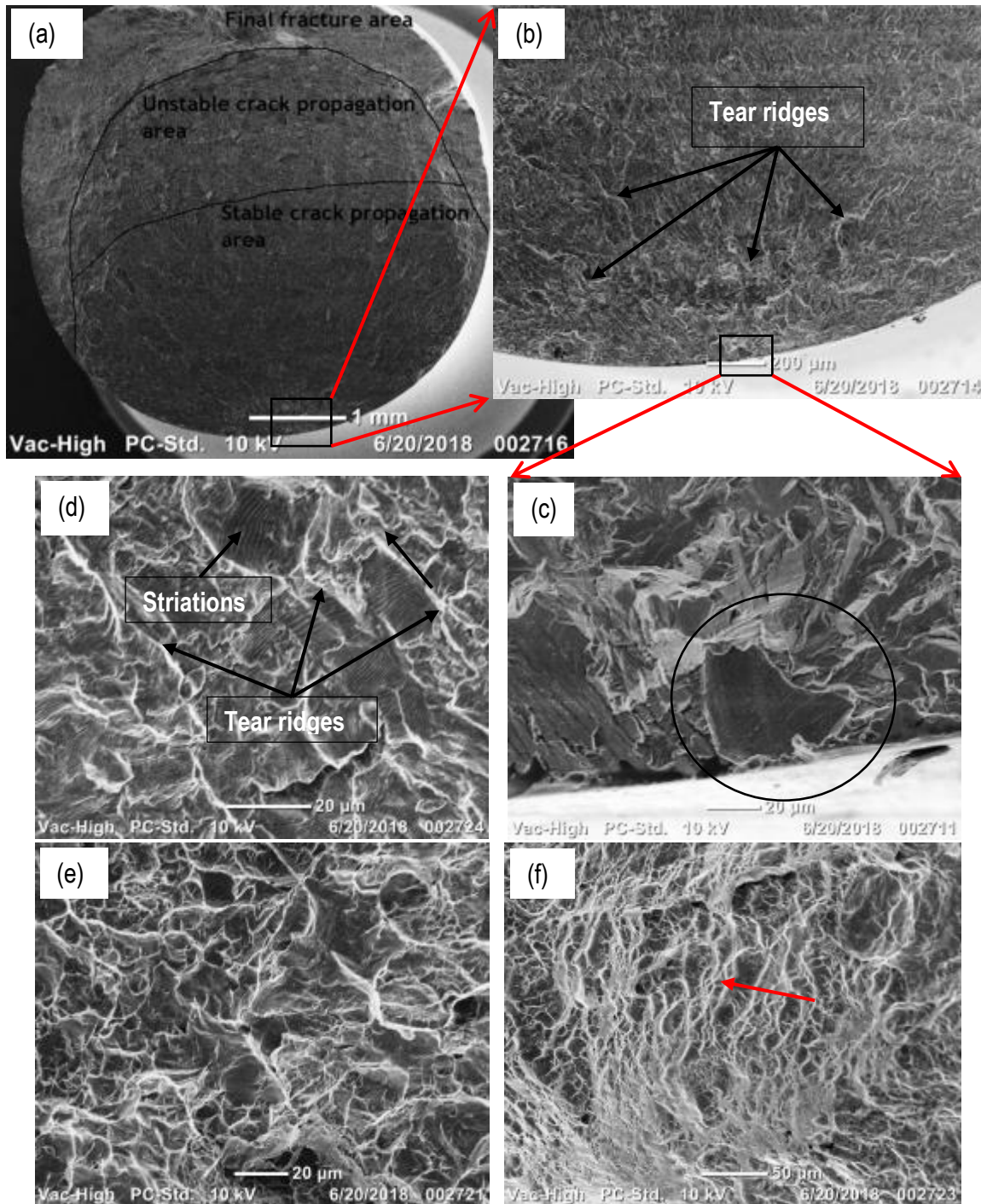


Figure 4.37 (a) Overall fractograph of specimen X-3; (b) a magnified area around the area of initiation of the fatigue failure crack; (c) high magnification of the site of initiation of the fatigue failure crack, with the crack initiation pore encircled; (d) high magnification of the area of stable propagation of the fatigue failure crack, showing fatigue striations; (e) high magnification of the area of unstable propagation of the fatigue failure crack, showing shallow dimples and (f) high magnification of the final area of fracture, showing shallow dimples

Figure 4.38 shows micro-CT scan images of specimen X-3 around ± 2 mm off the plane of fracture.

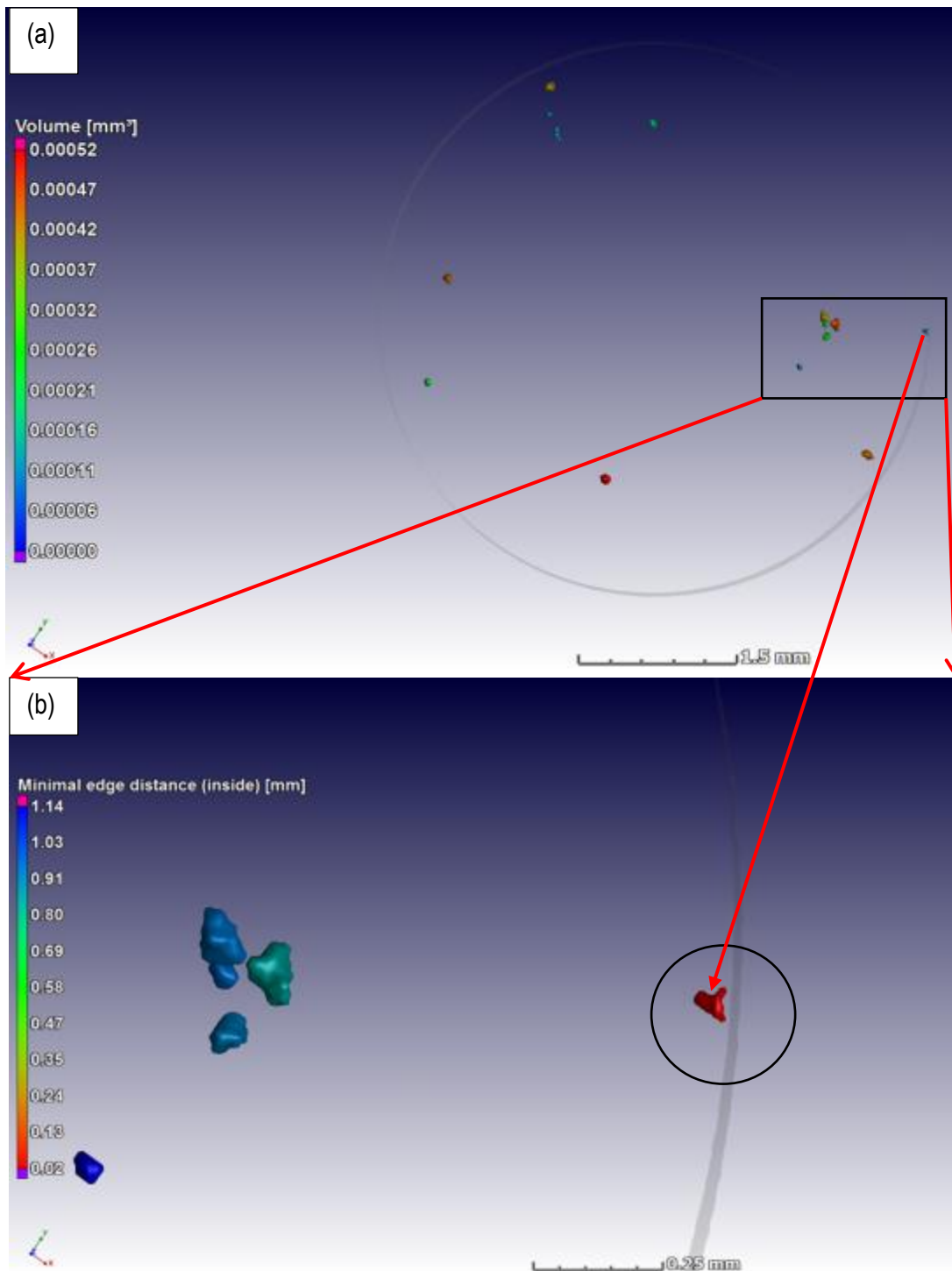


Figure 4.38: (a) Overall micro-CT scan image of specimen X-3 showing porosity at ± 2 mm off the plane of fracture and (b) high magnification of the micro-CT scan image around the crack initiation pore

Figure 4.37 (a) shows an overall fractograph of specimen X-3 in which the four stages of fatigue; crack initiation, stable crack propagation, unstable crack propagation and the final fracture and are shown at high magnification in Figures 4.37 (c), (d) (e) and (f). The site of initiation of the fatigue failure crack in this specimen was located by following the tear ridges that diverge from it, which are identified by the bright river-like lines seen in Figure 4.37 (a) and at high magnification in Figure 4.37 (b). At high magnification of the site of the initiation of the fatigue failure crack shown in Figure 4.37 (c), a surface DMLS process-related pore resulting from localized lack of fusion of Ti6Al4V (ELI) particles was located and taken to be the crack initiator. This pore was also located on the micro-CT data and is encircled in Figure 4.38 (b). It was not the biggest pore, as seen in Figure 4.38, but it had the lowest edge distance to the surface of all the specimens. The immediate area around the DMLS process-related crack initiation pore shown in the fractograph in Figure 4.37 (c) was faceted (early stage of crack propagation). High magnification of the stable crack propagation area away from the crack initiation site revealed fatigue striation marks that bow-out from the crack initiation site in the directions indicated by the arrows in Figure 4.37 (d). At high magnification of the area of unstable propagation of the fatigue failure crack shown in Figure 4.37 (e), shallow dimples were located which are indicative of monotonic loading. Similar shallow pores were also located on the area of final fracture with the direction of shear, indicated by an arrow shown in Figure 4.37 (f). The faceted area around the site of initiation of the fatigue failure crack, pronounced fatigue striations in the area of stable propagation of the fatigue failure crack and the shallow dimples resulting from the coalescence of pores in both the area of unstable propagation of the fatigue failure crack and the area of final fracture are all indicative of improved ductility of the stress-relieved plus HTA DMLS Ti6Al4V (ELI) specimens from their as-built state.

It is thought that specimen X-3 failed after a small number of load cycles at a relatively intermediate load because its fatigue failure crack initiated from a DMLS process-related pore which resulted in a value of ΔK which was 16.7% higher than the estimated ΔK_{th} for the stress-relieved plus HTA DMLS specimen built in the X-orientation. This implies a high rate of propagation of the fatigue failure crack, thus leading to failure of the specimen at a low number of load cycles (2.2% of the set number of run-out cycles) at the intermediate maximum stress level $\sigma_{max} = 530 \text{ MPa}$, which is 15% above the estimated fatigue endurance limit.

Figure 4.39 shows SEI SEM fractographs of specimen X-5 that was cycled at a maximum stress of 549 MPa and which fractured at 2,416,680 cycles: intermediate maximum stress and high number of cycles to failure.

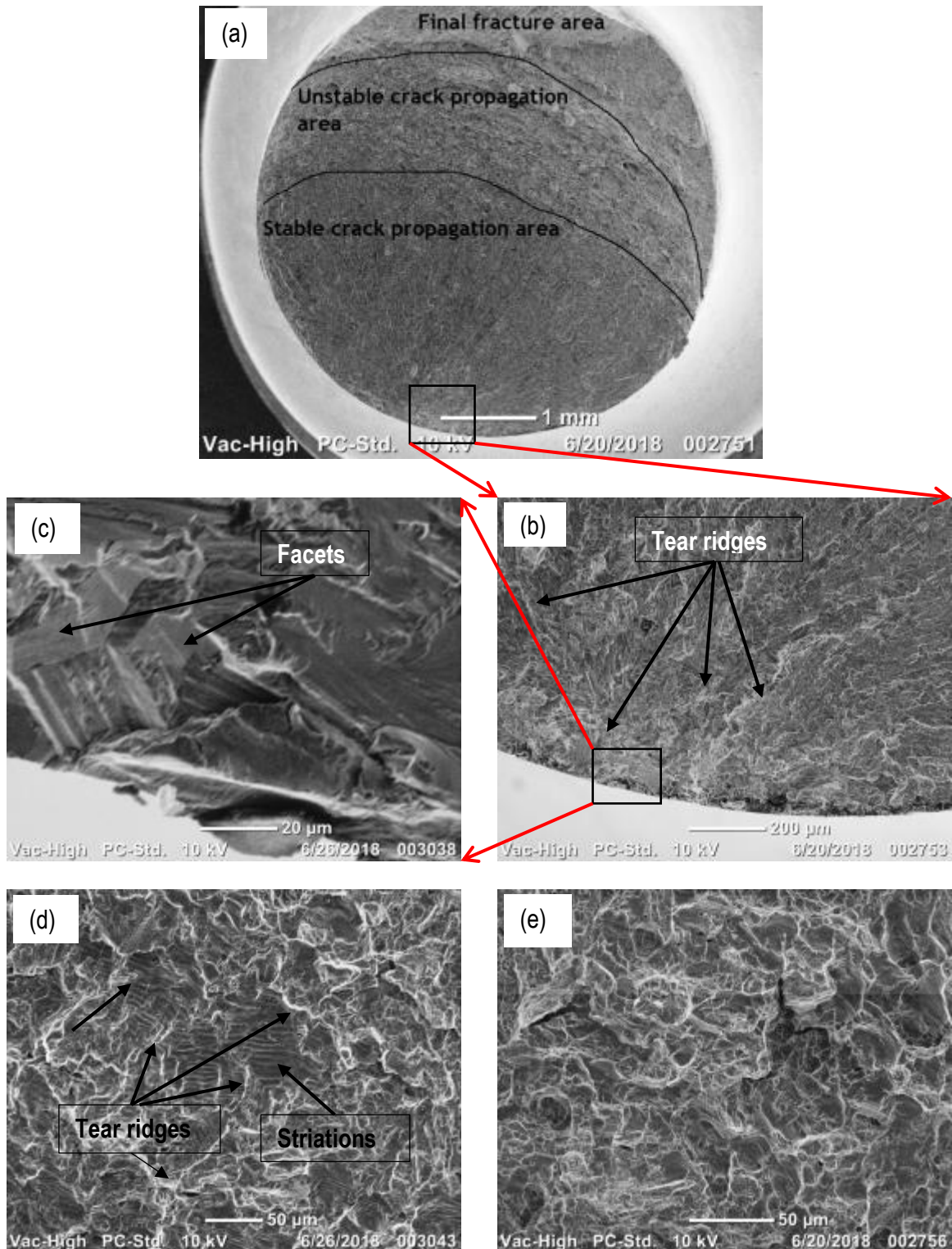


Figure 4.39: (a) Overall fractograph of specimen X-5; (d) magnified area around the crack initiation site; (c) high magnification of the crack initiation site showing an area with facets; (d) high magnification of the area of stable crack propagation showing fatigue striations and (e) high magnification of the area of unstable crack propagation showing fine shallow dimples

Figure 4.40 shows a micro-CT scan image of the distribution of pores at ± 2 mm off the plane of fracture of specimen X-5

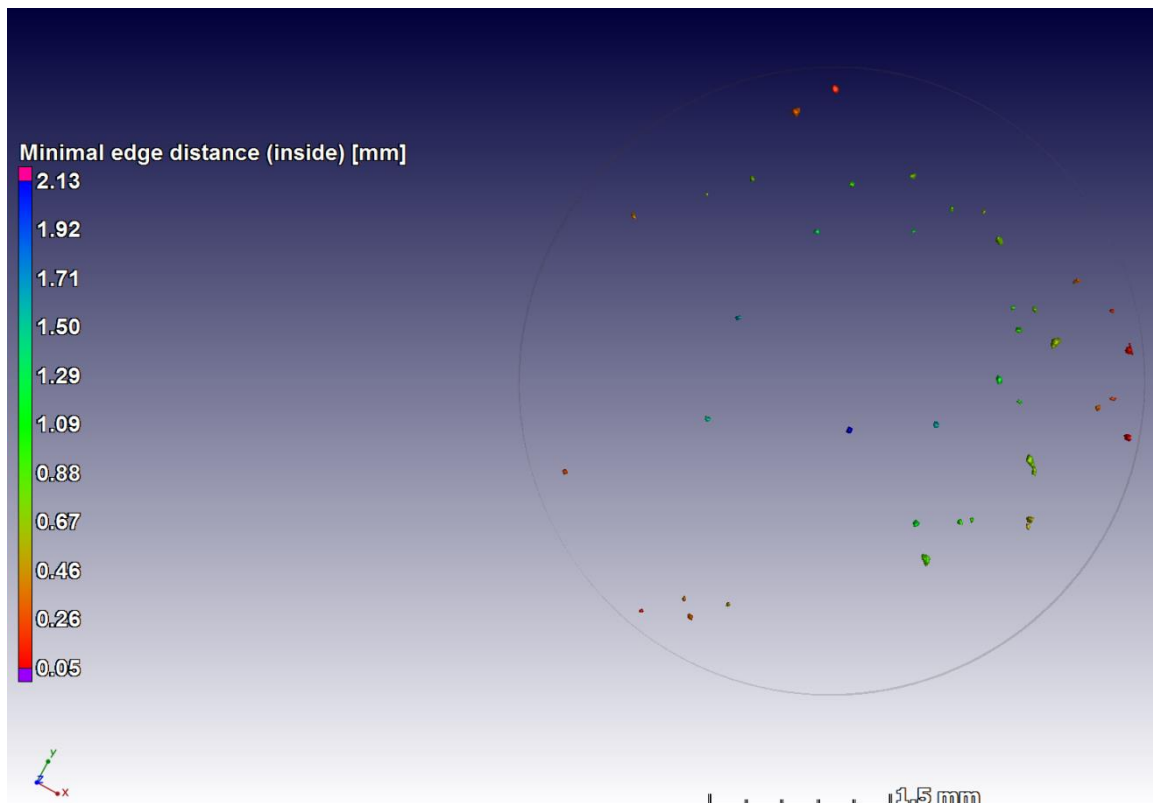


Figure 4.40: Overall micro-CT scan image of specimen X-5 showing porosity at ± 2 mm off the plane of fracture

Figure 4.39 (a) shows an overall fractograph of specimen X-5 with the corresponding distribution of pores at the fracture plane ± 2 mm, shown in Figure 4.40. The overall fractograph consists of the four typical fatigue stages of DMLS Ti6Al4V (ELI) identified in this project. These stages are crack initiation, stable crack propagation, unstable crack propagation and the final fracture. The crack initiation site, stable crack propagation area and unstable propagation area are shown at high magnifications in Figures 4.39 (c), (d) and (e). These fracture features are similar to the ones located in specimen X-3 and discussed under Figure 4.37 above. The only difference between the two specimens is that the crack initiation site of specimen X-5 was from facets as opposed to a DMLS process-related pore in specimen X-3. The initiation from the faceted areas can be linked with Figure 4.33 from which was seen that the initiation was from surface pores on the fracture plane, which from this investigation was seen to be detrimental to the fatigue properties. The faceted area from the crack initiation site is shown in Figure 4.39 (c), which is an indication of crack initiation from dislocation movement along the slip planes, which for Ti6Al4V is associated with the α grains

[103][104][105]; hence, the high number of load cycles to failure (48% of the set number of run-out cycles) at intermediate stress loads (18% above the estimated fatigue endurance limit). However, it can be seen from Figure 4.40 that the distribution of pores on ± 2 mm of the fracture plane of this specimen is higher than that of specimen X-3 (see Figure 4.38), which was loaded at a similar stress load but failed after a lower number of cycles. Therefore, it can be inferred that increased localised plastic deformation at the tip of a sub-surface DMLS process-related pore is more detrimental to the fatigue properties than the increased localised propagation rate of the crack upon contact with internal DMLS process-related pores.

Figure 4.41 shows SEI SEM fractographs of specimen X-9 that was cycled at a maximum stress of 650 MPa and which fractured at 88,015 cycles: high maximum stress and low number of cycles to failure.

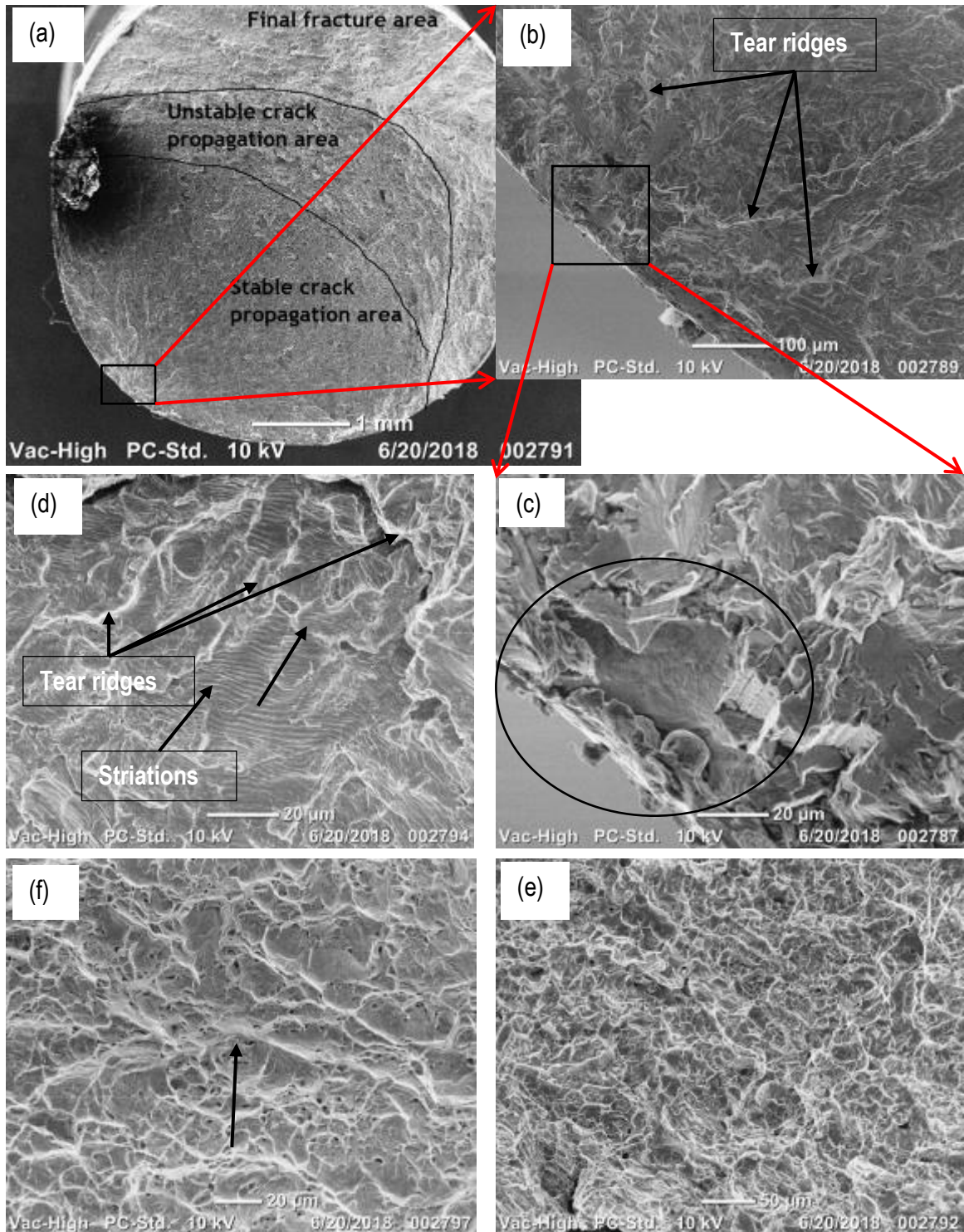


Figure 4.41: Overall fractograph of specimen X-9; (b) a magnified area around the area of initiation of the fatigue failure crack ; (c) high magnification of the site of initiation of the fatigue failure crack with the crack initiation pore encircled; (d) high magnification of the area of stable propagation of the fatigue failure crack, showing fatigue striations; (e) high magnification of the area of unstable propagation of the fatigue failure crack, showing

shallow fine dimples and (f) high magnification of the area of final fracture, showing shallow dimples

Figure 4.42 shows micro-CT scan images of specimen X-9 around ± 2 mm off the plane of fracture.

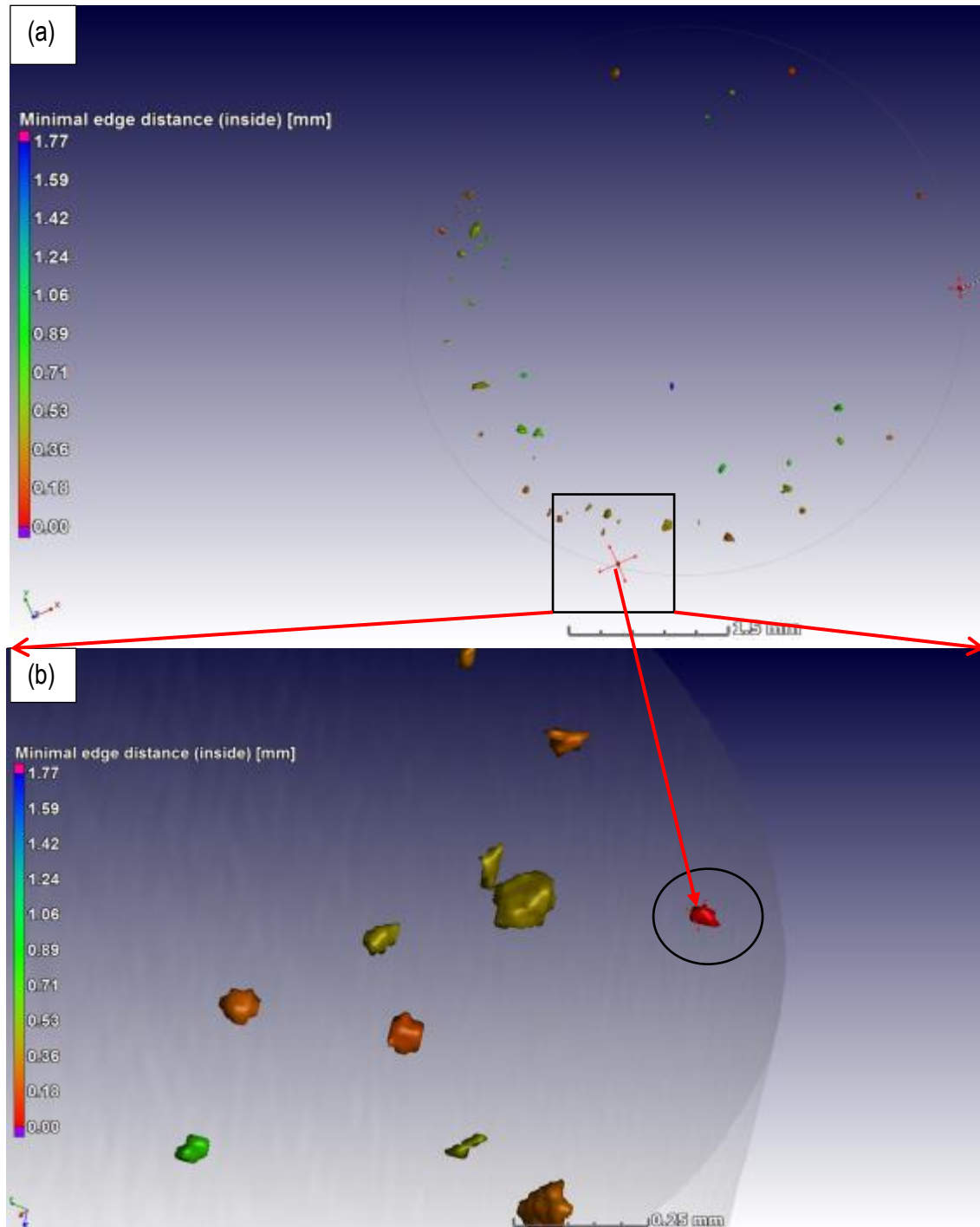


Figure 4.42(a) Overall micro-CT scan image of specimen X-9 showing porosity at ± 2 mm off the plane of fracture and (b) high magnification of the micro-CT scan image around the crack initiation pore

The features of the surfaces of fatigue fracture for specimen X-9 are similar to those of specimen X-3, explained under Figure 4.37. They consist of a crack that initiated from a DMLS process-related pore, an area of stable propagation of the fatigue failure crack, an area of unstable propagation, the fatigue failure crack and an area of final fracture. These features are shown at high magnifications in Figures 4.41 (c), 4.41 (d), 4.41 (e) and 4.41 (f), respectively. The number of load cycles to failure for this specimen are in line with the theory by Dieter et al. [101], which suggests that specimens loaded at maximum stress loads that are around two-thirds of the UTS of the material fail after a short number of cycles. The specimen was loaded at 70% of the UTS reported in section 5.6 and fractured after 1.76% of the set number of run-out cycles. The micro-CT image of the distribution of pores presented in Figure 4.42 (a) shows surface pores and the fatigue failure crack was seen to have initiated from a pore which had a high distribution of pores around it. From this fact it can be suggested that crack initiation from ΔK of the surface pores is also influenced by the ΔK of pores in an immediate area around it (accelerated early crack propagation).

4.6.1.2 Y-built specimens

Table 4.14 shows values of the maximum tension–tension fatigue stresses and the corresponding number of load cycles to failure or run-out of the Y-built test specimens. It also gives calculated values of ΔK from the DMLS process-related crack initiation pores of the respective specimens.

Table 4.14: Dimensions of DMLS process-related initiation pores for fatigue failure cracks and their stress intensity ranges for selected load stress data of Y-built stress relieved plus HTA DMLS Ti6Al4V (ELI) specimens.

Specimen designation	Maximum stress (σ_{max}) (MPa)	Stress range ($\Delta\sigma$) (MPa)	Fatigue life (N_f)	\sqrt{area} (μm)	Change in stress intensity factor (ΔK) (MPa m ^{0.5})
Y-10	675	607.5	66,318	69.14	5.82
Y-9	650	585.0	119,685	70.36	5.65
Y-8	630	567.0	119,271	internal	-
Y-4	612	550.8	125,337	83.85	5.81
Y-6	580	522.0	167,471	-	-
Y-5	549	494.1	2,660,077	85.84	4.06
Y-3	530	477.0	2,357,928	-	-
Y-12	520	468.0	125,582	86.49	5.01
Y-11	486	437.4	2,092,051	98.94	5.01
Y-7	450	405.0	5,000,000	87.81	4.37

The fractures from this set of specimens were from cracks initiating from DMLS process-related pores located either at the surface, sub-surface (the minimum edge distance of the pore smaller than the projected diameter of the pore) or within the cross-section of the specimens. Table 4.14 shows a similar trend of the decrease in the magnitude of the stress intensity factors with the increase in the number of load cycles. This conclusion applies to all specimens shown in the table with the exception of specimens Y-3, Y-6 and Y-8. Specimens Y-3 and Y-6 fractured at the grip ends and were considered as outliers. The internal crack initiation pore within specimen Y-8 could not be located on the micro-CT scan data and therefore the value of ΔK from this pore could not be calculated. The largest DMLS-related identified micro-CT scan pore occurred in specimen Y-7, which was considered to have experienced a run-out and had a calculated value of $\Delta K = 4.37 \text{ MPa } m^{0.5}$. This is taken here as a value below the ΔK_{th} for Y-built specimens. However, specimen Y-5 fractured and had a value of ΔK below the value of $\Delta K = 4.37 \text{ MPa } m^{0.5}$. This is thought to have resulted from the relatively high magnitude of the stress load in specimen Y-5, as increase in the magnitude of the stress load without a decrease in the value of ΔK results in a decrease in the number of load cycles to failure. This is also applicable to flawless specimens where cracks initiate from dislocation movements.

Figure 4.43 presents a semi-log S-N curve of the maximum stress against the number of load cycles for the stress-relieved plus HTA Y-built DMLS Ti6Al4V (ELI) specimens.

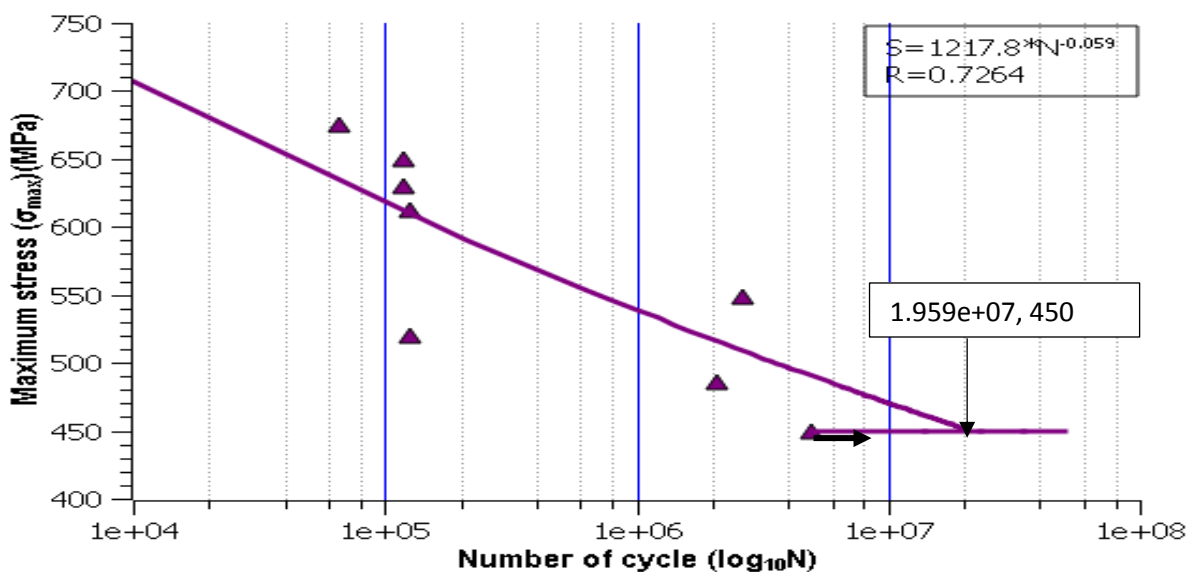


Figure 4.43: Semi-log S-N curve for stress-relieved plus HTA DMLS Ti6Al4V (ELI) Y-built specimens

The fatigue endurance limit for the Y-built stress-relieved plus HTA DMLS Ti6Al4V (ELI) is seen in the semi- \log_{10} S-N plot in Figure 4.43 to be $\sigma_{max} = 450$ MPa. This was estimated from the run-out specimen Y-7, indicated by an arrow on the figure. This is 53% of the average 0.2% offset proof strength of the Y-built stress-relieved plus HTA DMLS Ti6Al4V (ELI) specimens presented in Table 4.8. The fractured specimens showed a strong inverse linear relationship between σ_{max} and $\log_{10} N$ with a correlation coefficient (R) of -0.737. Linearization of the fractured specimens was carried out excluding outlier specimens Y-3 and Y-8, encircled in Figure 4.43. Extrapolation of this linearized curve gave a fatigue strength of 706 MPa at 10^4 load cycles, which is 82% of the 0.2% offset proof strength for the Y-built stress-relieved plus HTA DMLS Ti6Al4V (ELI) specimens shown in Table 4.14. The inclined linear curve in Figure 4.43 intersected the endurance limit of 450 MPa resulting in a knee point at 34,4860,000 load cycles, which is higher than the set run-out of 5,000,000 cycles. This number of cycles is higher than that of the as-built Y-built DMLS Ti6Al4V (ELI) fractured specimens, which implies that the post-DMLS stress-relieving plus HTA of Ti6Al4V (ELI) specimens resulted in an increase in the number of load cycles to failure.

Figure 4.44 shows SEI SEM fractographs of specimen Y-11 that was cycled at a maximum stress of 486 MPa and which fractured at 2,092,051 cycles: high maximum stress and high number of cycles to failure.

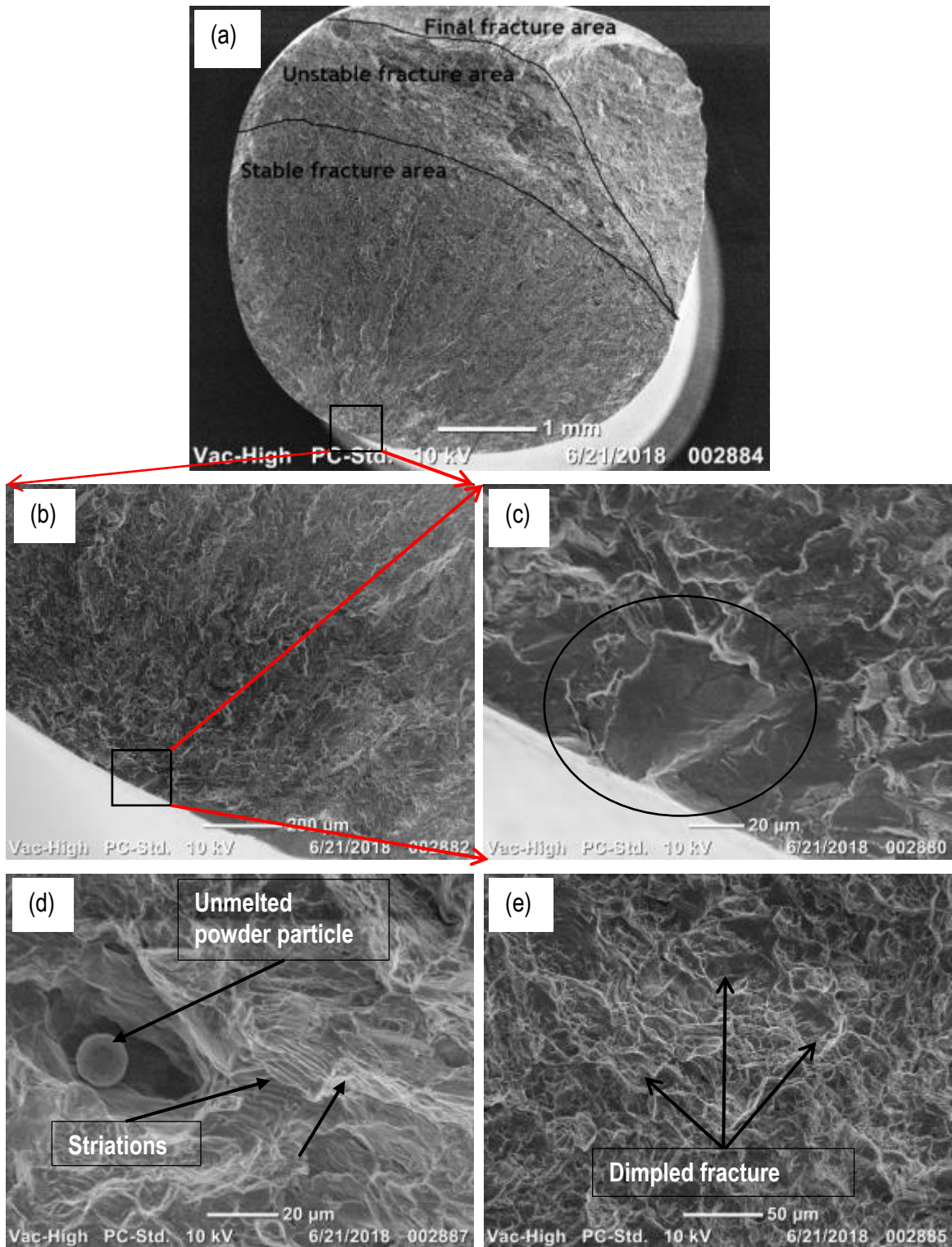


Figure 4.44: (a) Overall fractograph of specimen Y-11; (b) magnified area of around the site of initiation of the fatigue failure crack showing; (c) high magnification of the site of initiation of the fatigue failure crack, showing an area with facets; (d) high magnification of the area of stable propagation of the fatigue failure crack, showing fatigue striations and (e) high

magnification of the area of unstable propagation of the fatigue failure crack, fine shallow dimples

Figure 4.45 shows micro-CT scan images of specimen Y-11 around ± 2 mm off the plane of fracture.

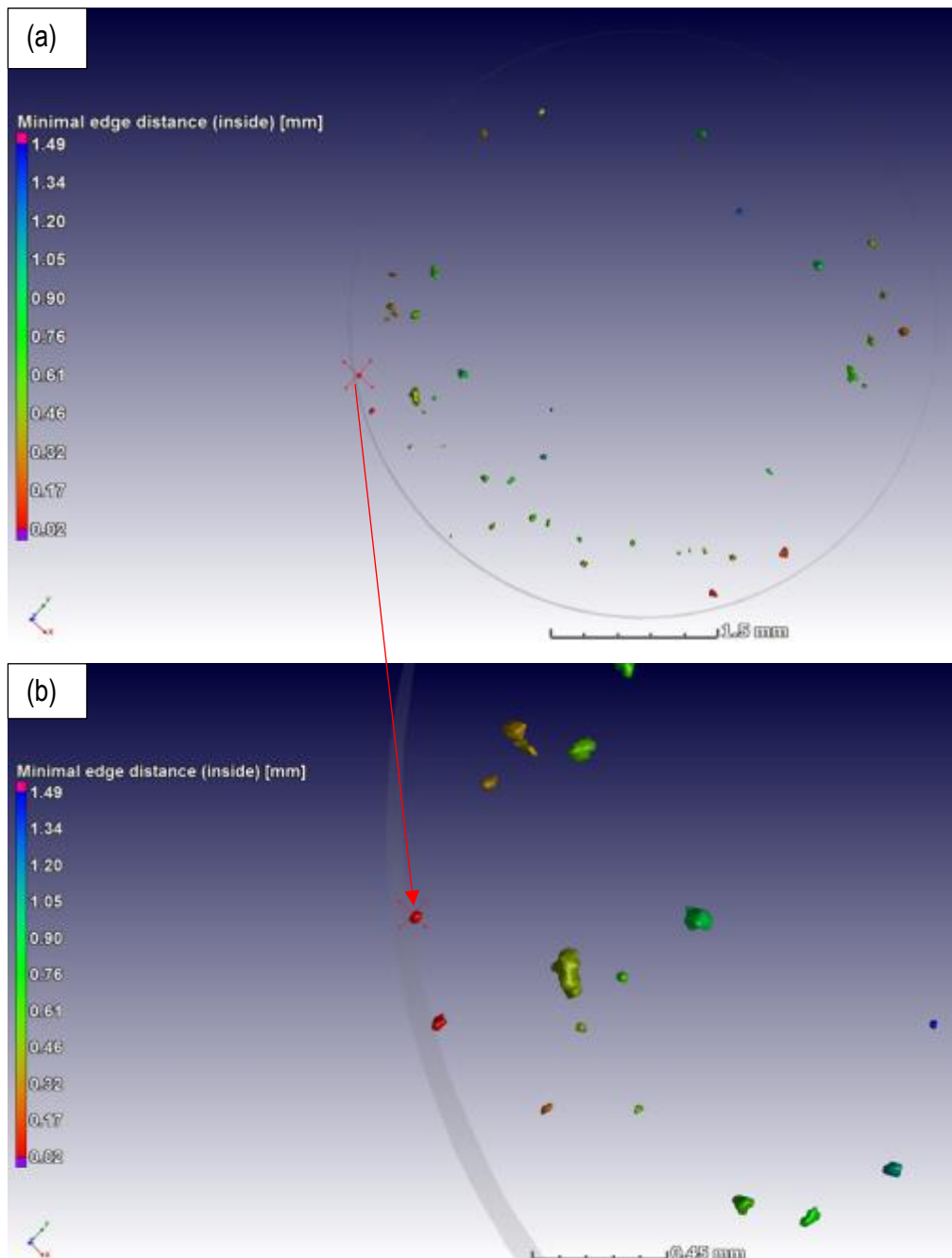


Figure 4.45: Overall micro-CT scan image of specimen Y-11 showing porosity at ± 2 mm off the plane of fracture and (b) high magnification of the micro-CT scan image around the crack initiation pore

Specimen Y-11 fractured from a crack that initiated from a surface DMLS process-related pore with a $\sqrt{area} = 98.94 \mu m$, which resulted in a value of $\Delta K = 5.01 MPa m^{0.5}$ at its tip. This pore is marked by a cross on the micro-CT image at ± 2 mm off the plane of fracture in Figure 4.45 (a) and at a higher magnification in Figure 4.45 (b). This value of ΔK was higher than the estimated value of ΔK_{th} for stress-relieved plus HTA DMLS Ti6Al4V (ELI) specimens built in the Y-orientation by 13%, which led to a high rate of propagation of the fatigue failure crack that gave rise to fatigue failure at 42% of the set number of run-out cycles. However, this number of cycles to failure falls within the range of HCF endurance limit life for iron and titanium metals and their respective alloys of (10^6 to 10^7) [74]. The features of fatigue fracture in this specimen consisted of the DMLS process-related crack initiation pore shown in Figure 4.44 (c). This crack initiation pore had tear ridges diverging from it and covering an area denoted as an area of stable propagation of the fatigue failure crack on the overall fractograph shown in Figure 4.44 (a). Fatigue striations similar to the ones shown in Figure 4.44 (d) were located on the concave areas between tear ridges. The fatigue striations were more pronounced in areas of stable propagation of the fatigue failure crack, approaching the areas of unstable propagation of the fatigue failure crack. The tear ridges died out in the area of unstable propagation of the fatigue failure crack in which the mode of fracture changed from cyclic fracture to monotonic fracture, indicated by the shallow coalescence of pores shown in Figure 4.44 (e).

Figure 4.46 shows SEI SEM fractographs of specimen Y-8 that was cycled at a maximum stress of 630 MPa and which fractured at 119,271 cycles: high maximum stress and low number of cycles to failure.

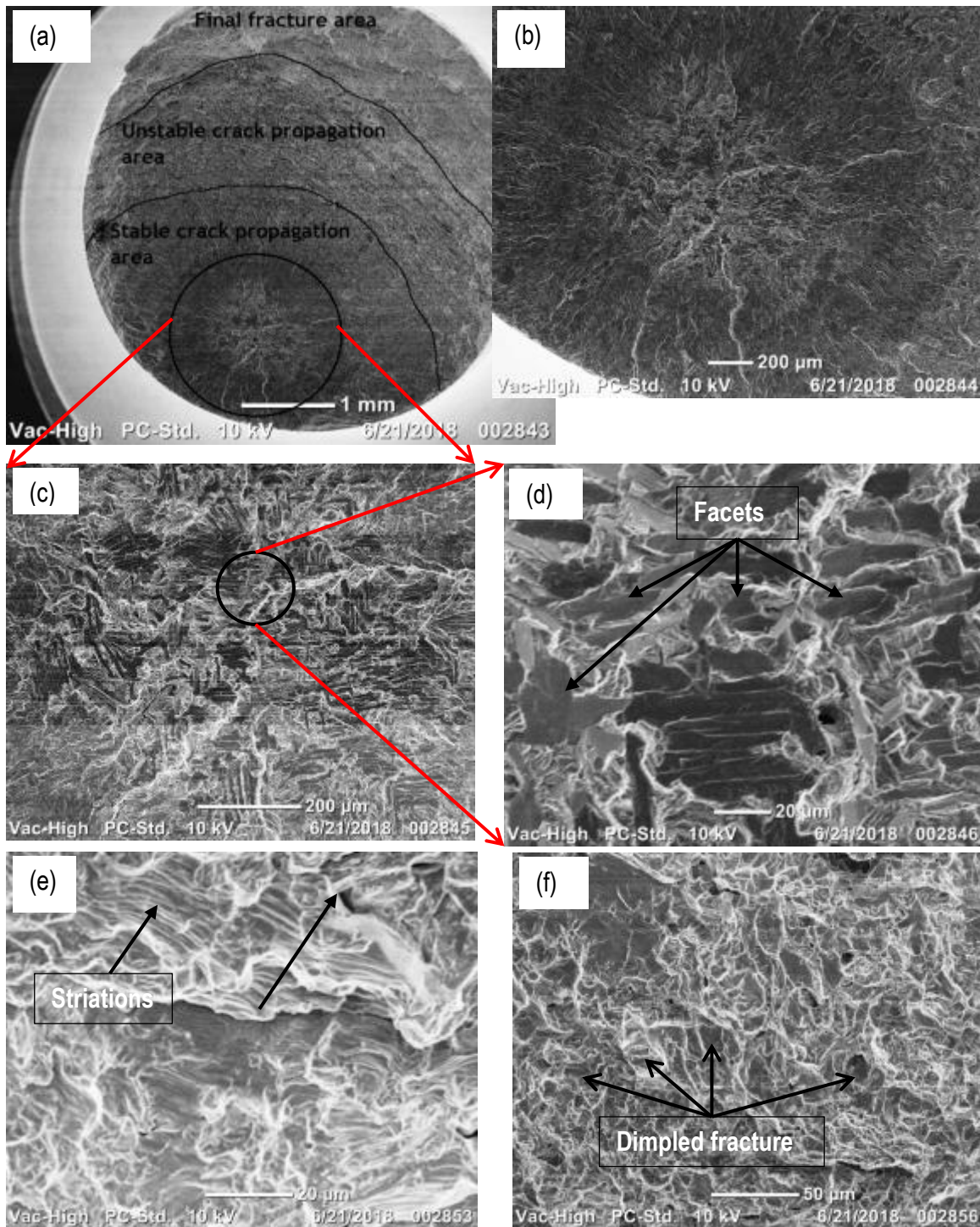


Figure 4.46: (a) Overall fractograph of specimen Y-8; (b) magnification around an internal site of the initiation of a fatigue failure crack, showing a fish-eye morphology; (c) higher magnification around the site of initiation of a fatigue failure crack, showing facets on α lath grains; (d) high magnification showing the site of initiation of faceted cracks ; (e) high magnification of the area of stable propagation of the fatigue failure crack and (f) high magnification of the area of unstable propagation of the fatigue failure crack .

Figure 4.47 shows micro-CT scan images of specimen Y-9 around ± 2 mm off the plane of fracture with the pores highlighted in green being closest to the site of initiation of the fatigue failure crack.

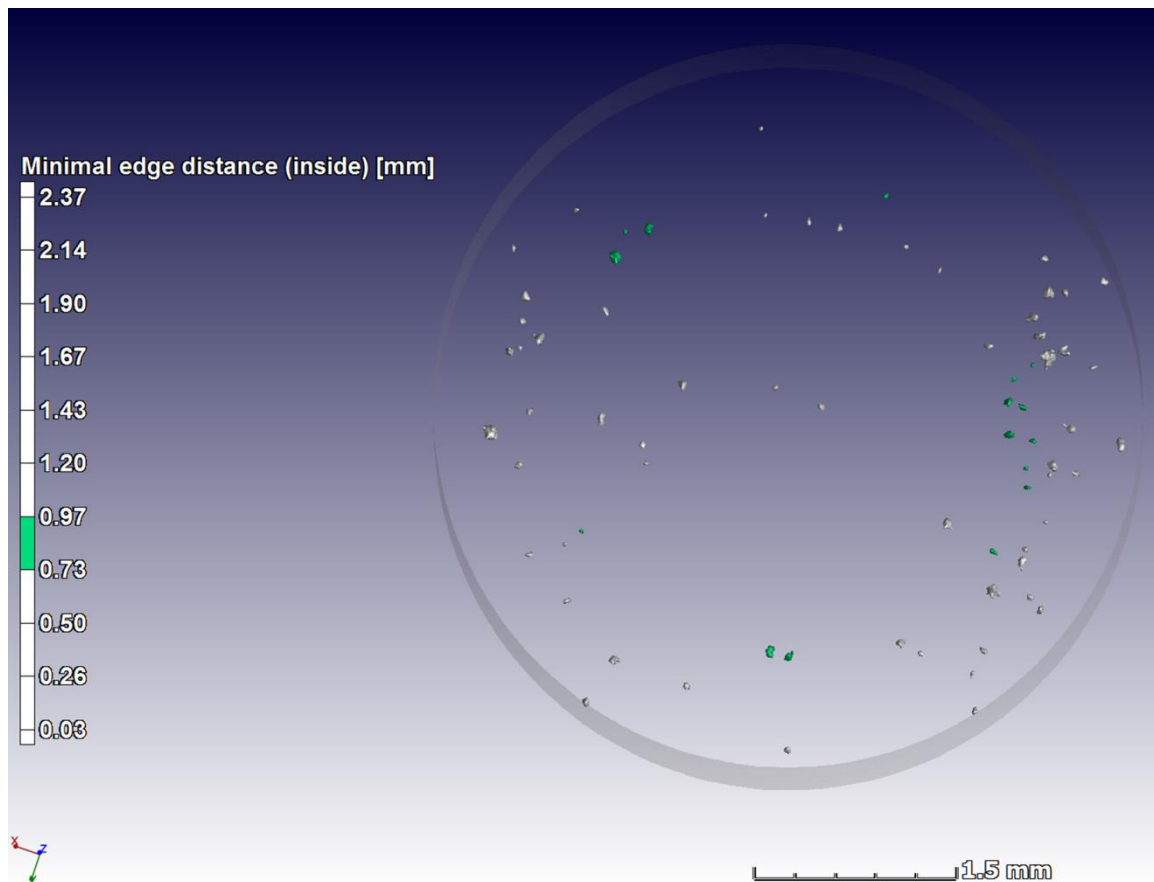


Figure 4.47: Overall micro-CT scan image of specimen Y-8 showing porosity at ± 2 mm off the plane of fracture

Specimen Y-8 was cycled at 68% of the average UTS of the stress-relieved plus HTA DMLS Ti6Al4V (ELI) Y-built specimen and failed at 2.4% of the set number of run-out cycles. This number of cycles to failure relative to the applied stress load was high. It is noted that fracture in this specimen initiated from internal facets, such as the ones shown in Figure 4.46 (d), as opposed to the rest of the specimens that failed from cracks initiating from sites of stress concentrations induced by surface DMLS process-related pores. However, Figure 4.47 shows a number of DMLS micro-CT scan detected pores (highlighted in green) at the approximate edge distance of the site of initiation for the aforementioned fatigue failure crack, which could not be identified with the SEM as crack initiators on the fractograph around the site of initiation of the fatigue failure crack. The faceted crack initiations in Ti6Al4V are proposed to be induced by the restrictions in operative slip systems and dislocation pile-ups at grain boundaries, which result in stress concentrations high enough to induce cleavages on these slip planes [103][104][105][106]. Once initiated, such cracks propagate parallel

to the α lamellae grain boundaries, forming facets at the α laths, as seen in Figures 4.46 (c) and (d) [104][106]. From this faceted area, the cracks grow into a fisheye morphology at a stable propagation with the formation of striations toward the area of unstable propagation of the fatigue failure crack, as is seen at high magnification in Figure 4.46 (e). The formation of these striations continued up to an area of unstable propagation of the fatigue failure crack, from where the crack started propagating by the coalescence of pores, as seen in Figure 4.46 (f). This continued until the specimen finally sheared.

4.6.1.3 Z- Built specimens

Table 4.15 shows values of the maximum tension–tension fatigue stresses and the corresponding number of load cycles to failure or run-out of the Z-built stress-relieved plus HTA test specimens. It also gives calculated values of the value of ΔK from the DMLS process-related crack initiation pores of the respective specimens.

Table 4.15: Dimensions of DMLS process-related initiation pores for fatigue failure cracks and their stress intensity ranges for selected load stress data of Z-built stress-relieved plus HTA DMLS Ti6Al4V (ELI) specimens

Specimen designation	Maximum stress (σ_{max}) (MPa)	Stress range ($\Delta\sigma$) (MPa)	Fatigue life (N_f)	\sqrt{area} (μm)	Change in stress intensity factor (ΔK) (MPa m ^{0.5})
Z-10	675	607.5	49,922	74.63	5.75
Z-9	650	585.0	57,240	87.12	6.30
Z-8	630	567.0	82,205	facets	-
Z-4	612	550.8	71,609	75.76	5.52
Z-6	580	522.0	142,196	76.88	5.27
Z-5	549	494.1	165,857	77.59	5.01
Z-3	530	477.0	1,575,455	facets	-
Z-12	520	468.0	156,868	124.62	6.02
Z-11	486	437.4	5,000,000	80.44	4.52
Z-10	450	405.0	1,575,455	105.0	4.78

All the fatigue failure cracks in the fractured specimens in this set initiated from surface DMLS process-related pores, except for specimens Z-3 and Z-8, which failed in a faceted crack initiation mode. From Table 4.15, a similar trend to those of the results shown in Table 4.13 and 4.14 is seen, with an increase in the σ_{max} leading to an increase in the value of ΔK , which in turn leads to a decrease in the number of load cycles to failure. An increased projected area of the crack initiation pore from which the value of ΔK is calculated also increases the value of ΔK at lower loads, as

seen from specimen Z-12. The largest DMLS-related identified micro-CT scan pore in specimen Z-11, which was considered to have experienced a run-out, had a calculated value of $\Delta K = 4.52 \text{ MPa } m^{0.5}$. This has been taken here as a value below the threshold change in the stress intensity factor for the Z-built specimens.

Figure 4.48 presents a semi-log S-N curve of the maximum stress against the number of load cycles for the Z-built stress-relieved plus HTA DMLS Ti6Al4V (ELI) specimens.

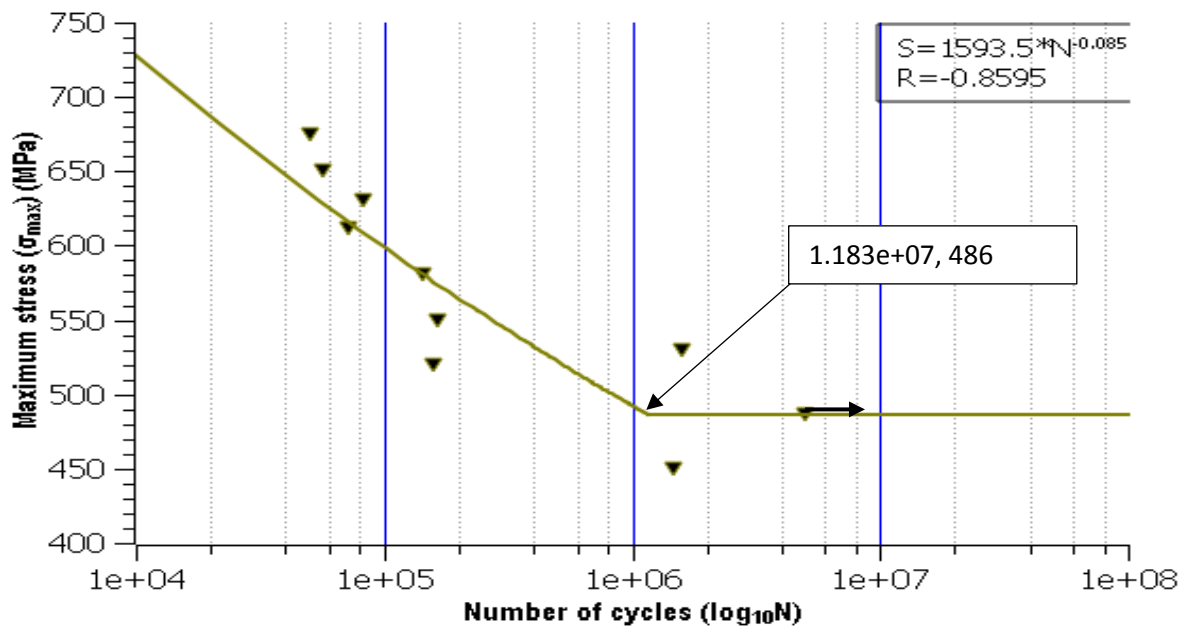


Figure 4.48: Semi-log S-N diagram for stress-relieved plus HTA DMLS Ti6Al4V (ELI) Z-built specimens

Linear curve fitting for the fractured specimens in Figure 4.48 gives rise to a correlation coefficient $R = -0.859$. The linearized curve intercepts the horizontal curve for the endurance limit at 1,183,000 cycles forming a knee point there. It also gives a fatigue strength of 730 MPa at 10^4 number of load cycles. The fatigue endurance limit was estimated to be at $\sigma_{max} = 486 \text{ MPa}$ for the run-out specimen Z-11, indicated by an arrow in Figure 4.48. This endurance limit and the fatigue strength at 10,000 load cycles are 64% and 95% of the average 0.2% proof strength for Z-built stress-relieved plus HTA DMLS Ti6Al4V (ELI) specimens presented in Table 4.8.

Figure 4.49 shows SEI SEM fractographs of specimen Z-7 that was cycled at a maximum stress of 450 MPa and which fractured at 1,456,818 cycles: low maximum stress and high number of cycles to failure.

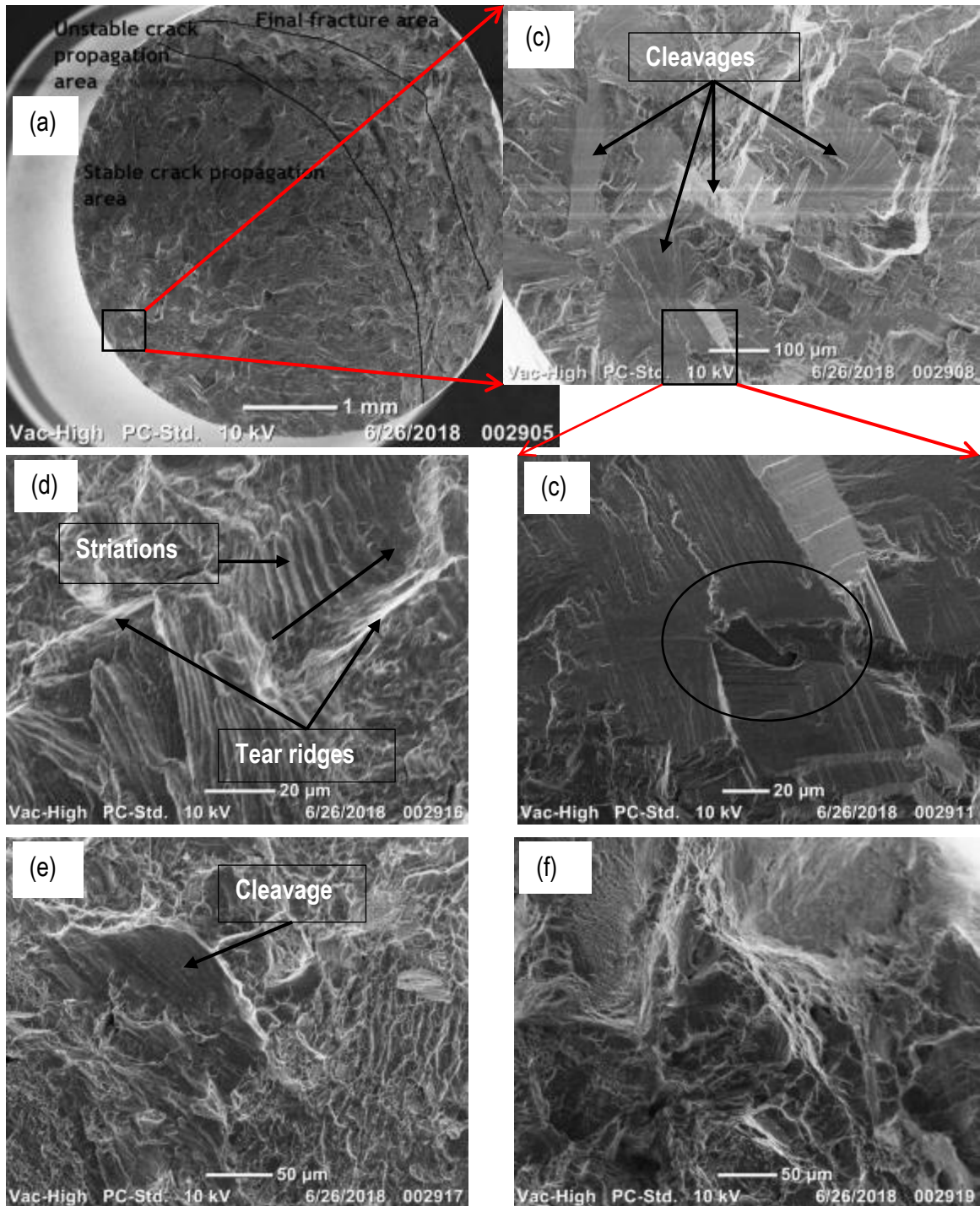


Figure 4.49: (a) Overall fractograph of specimen Z-7; (b) a magnified area around the site of initiation of the fatigue failure crack; (c) high magnification of the site of initiation of the fatigue failure crack, with the crack initiation pore encircled; (d) high magnification of the area of stable propagation of the fatigue failure crack, showing fatigue striations; (e) high magnification of the area of unstable propagation of the fatigue failure crack, showing shallow dimples and (f) high magnification of the area of final fracture, showing shallow dimples

Figure 4.50 shows micro-CT scan images of the distribution of pores from specimen Z-7 around ± 2 mm off the plane of fracture.

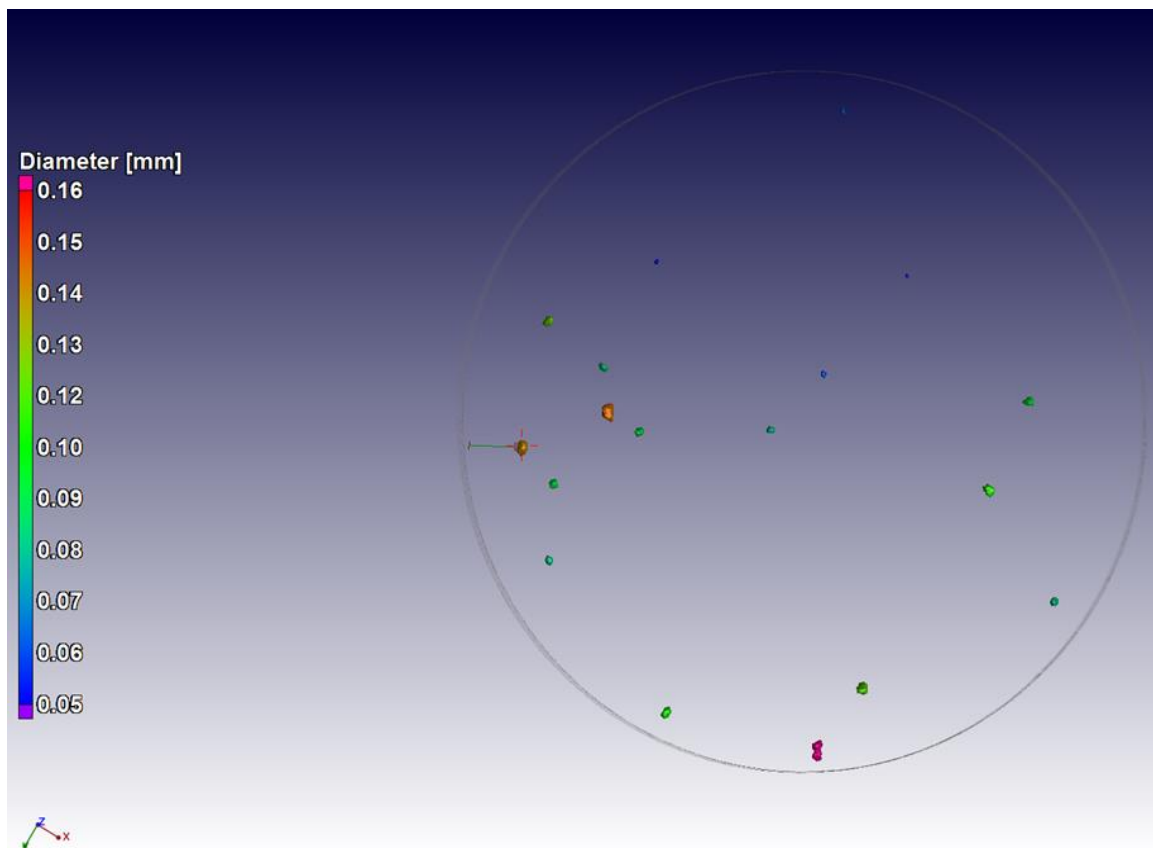


Figure 4.50: Overall micro-CT scan image of specimen Z-7 showing porosity at ± 2 mm off the plane of fracture

The fatigue fracture from specimen Z-7 initiated from a sub-surface DMLS process-related pore that had the highest $\sqrt{\text{area}}$ of the crack initiation pores in this set of specimens. The pore is encircled in Figure 4.49 and marked with a cross in Figure 4.50. The projected area of this pore, at a stress load 7% lower than the estimated endurance limit, resulted in a ΔK 5% higher than the estimated ΔK_{th} , which resulted in failure at 29% of the set number of run-out cycles. The number of cycles to failure of this specimen lies between the typical range for the HCF endurance limit life of iron and titanium metals and their respective alloys (10^6 to 10^7) [74]. The features of the stable crack propagation fracture surfaces are similar to those discussed in a publication by Janecek et al. [104], which suggested that “Fatigue crack initiation and propagation at low stress loads is associated with low energy cleavage fracture that propagates at well-defined low-index crystallographic planes.” Such cleavage fractures are shown in Figures 4.49 (b) and (c). However, the same cleavages were

located in areas of unstable crack propagation as well as in the area of final fracture. A cleavage fracture resulting from monotonic failure implies brittle fracture.

Figure 4.51 shows SEI SEM fractographs of specimen Z-3 that was cycled at a maximum stress of 530 MPa and which fractured after 1,575,455 cycles: high maximum stress and high number of cycles to failure.

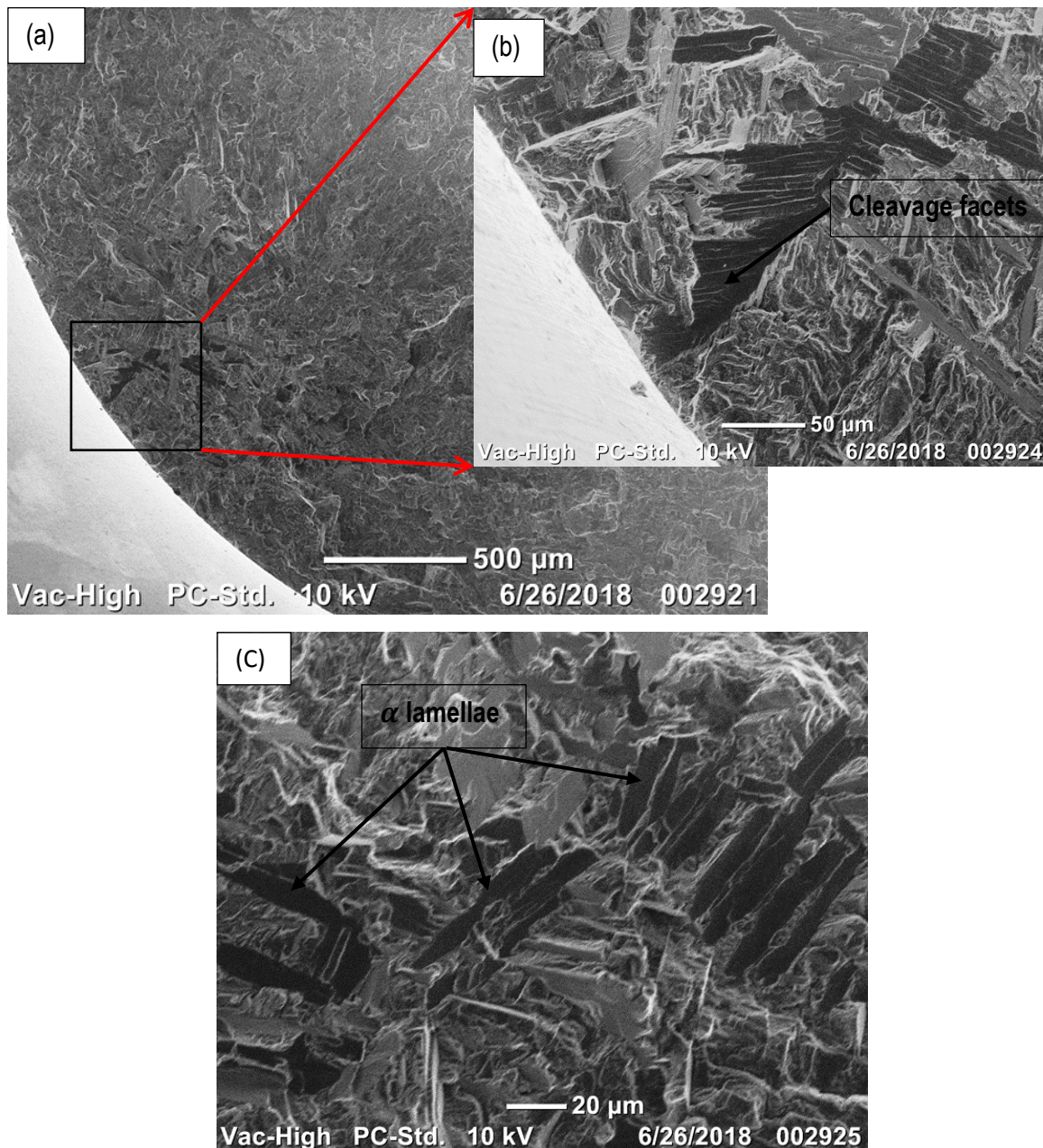


Figure 4.51 Overall fractograph of specimen Z-3; (b) magnified and (c) high magnification areas of around the site of initiation of fatigue failure crack, showing facets at α laths

Figure 4.51 (a) is a fractograph of specimen Z-3 which shows tear ridges converging towards the site of initiation of the fatigue failure crack. Fatigue fracture of this specimen occurred from a crack that initiated from facets at the α laths shown in Figure 4.51 (b). The faceted areas from the site of initiation of the fatigue failure crack shown in Figure 4.51 (b) are an indication of the initiation of cracks from the movement of dislocations along slip planes, which for Ti6Al4V, is associated with the α grains [103][104][105]; hence, the high number of load cycles to failure (32% of the set number of run-out cycles) at intermediate stress loads (8.3% above the estimated fatigue endurance limit). No DMLS process-related pores on this fracture plane were located on the fractograph and the micro-CT scan data.

4.6.1.4 Comparison of the stress-relieved plus HTA X-, Y- and Z-built fracture planes

Figure 4.52 shows SEI SEM fractographs of specimen X-12, which was cycled at a maximum stress of 520 MPa and fractured at 2,580,515 cycles.

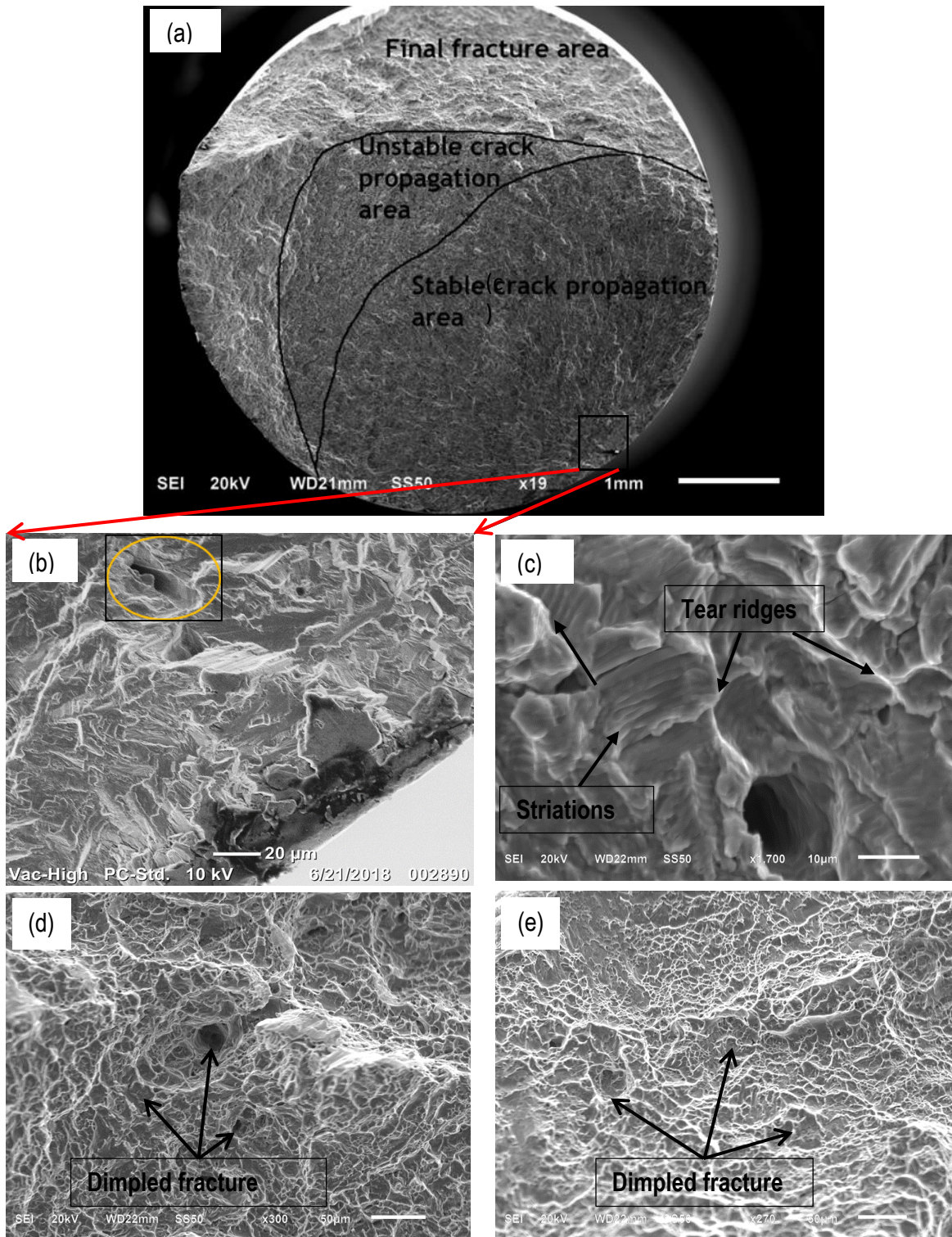


Figure 4.52: (a) Overall fractograph of specimen X-12; (b) a magnified area around the site of the fatigue failure crack initiation with the crack initiation pore encircled; (c) high magnification of the area stable crack propagation showing fatigue striations with the arrow indicating the direction of the fatigue crack propagation; (d) high magnification of the area of unstable crack propagation showing a shallow dimpled fracture mode (e) high magnification of the area of the shear lip showing a dimpled fracture mode

Figure 4.53 shows the micro-CT scan image on the plane of fracture for specimen X-12, with the crack initiation pore indicated by a cross. This crack initiation pore had an area of 0.00433 mm² resulting in a value of $\Delta K = 4.37 \text{ MPa m}^{0.5}$.

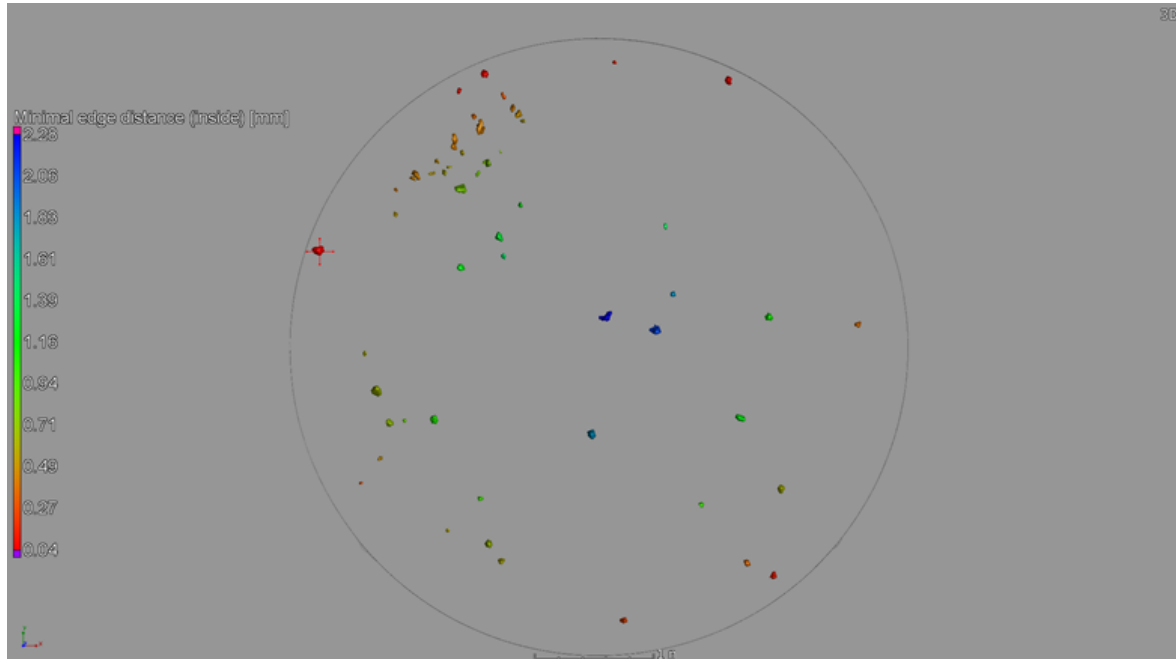


Figure 4.53: Micro-CT scan image on the plane of fracture for specimen X-12, with the crack initiation pore marked with a cross

Figure 4.54 shows SEI SEM fractographs of specimen Y-12, which was cycled at a maximum stress of 520 MPa and fractured at 125,582 cycles.

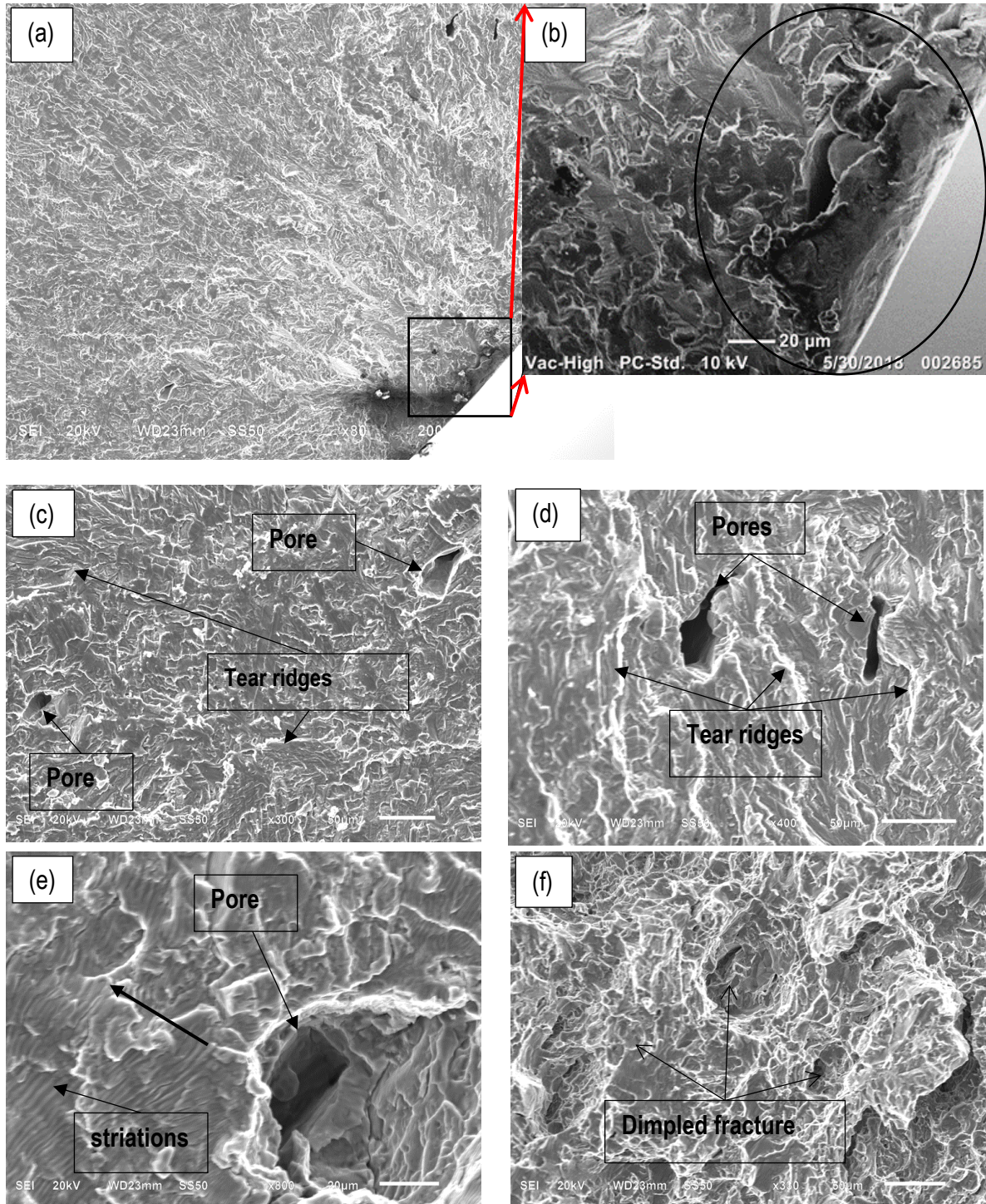


Figure 4.54: (a) High magnification fractograph of specimen Y-12 around the area of stable crack propagation; (b) a high magnification of the site of the fatigue crack initiation with the crack initiation pore encircled; (c), (d) and (e) high magnification of the area of stable crack propagation around DMLS process-related pores and (f) high magnification of the area of unstable crack propagation showing shallow dimples

Figure 4.55 shows the micro-CT scan image on the plane of fracture of specimen Y-12, with the crack initiation pore indicated by a cross. This crack initiation pore had an area of 0.00748 mm² resulting in a value of $\Delta K = 5.01 \text{ MPa m}^{0.5}$.

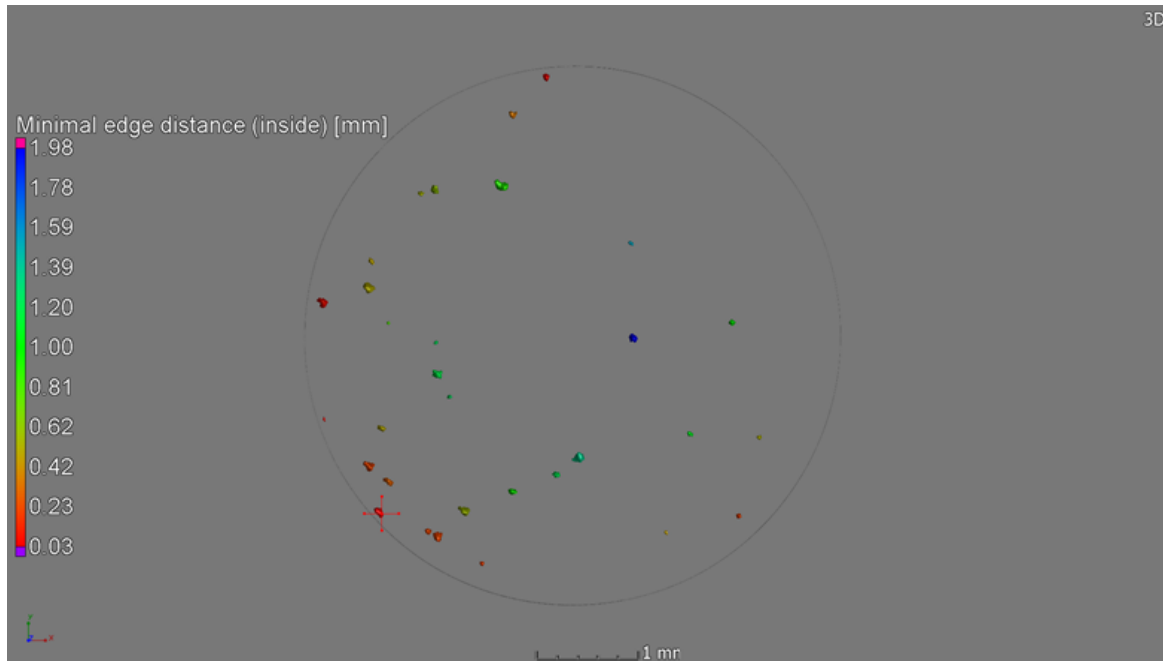


Figure 4.55: Micro-CT scan image on the plane of fracture for specimen Y-12, with the crack initiation pore marked with a cross

Figure 4.56 shows SEI SEM fractographs of specimen Z-12, which was cycled at a maximum stress of 520 MPa and fractured at 156,868 cycles.

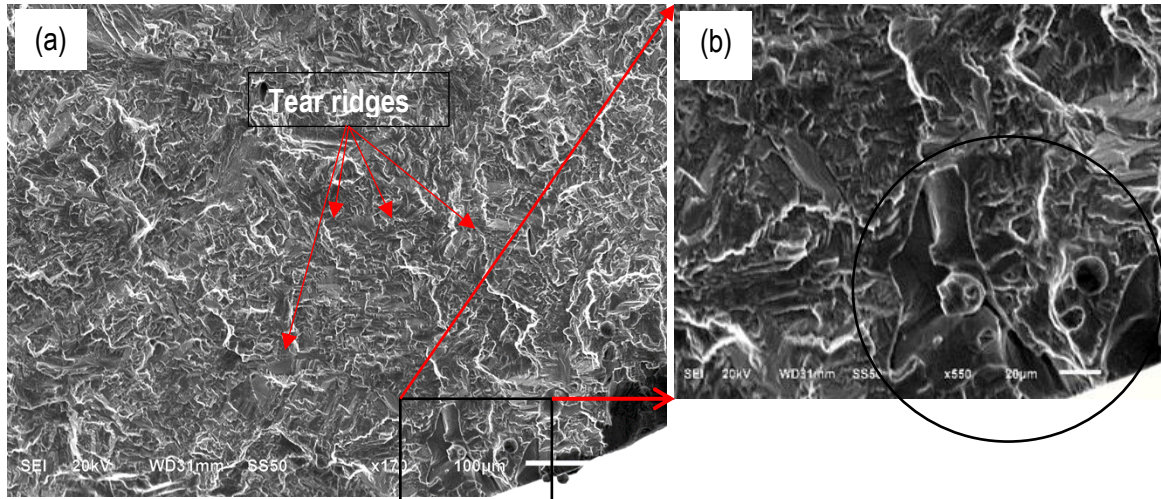


Figure 4.56: A magnified fractograph of specimen Z-12 around the crack initiation pore; (b) high magnification around the site with the crack initiation pore encircled

Figure 4.57 shows the micro-CT scan image on the plane of fracture for specimen Z-12, with the crack initiation pore indicated by a cross. This crack initiation pore had an area of 0.01553 mm² resulting in a value of $\Delta K = 6.02 \text{ MPa m}^{0.5}$.

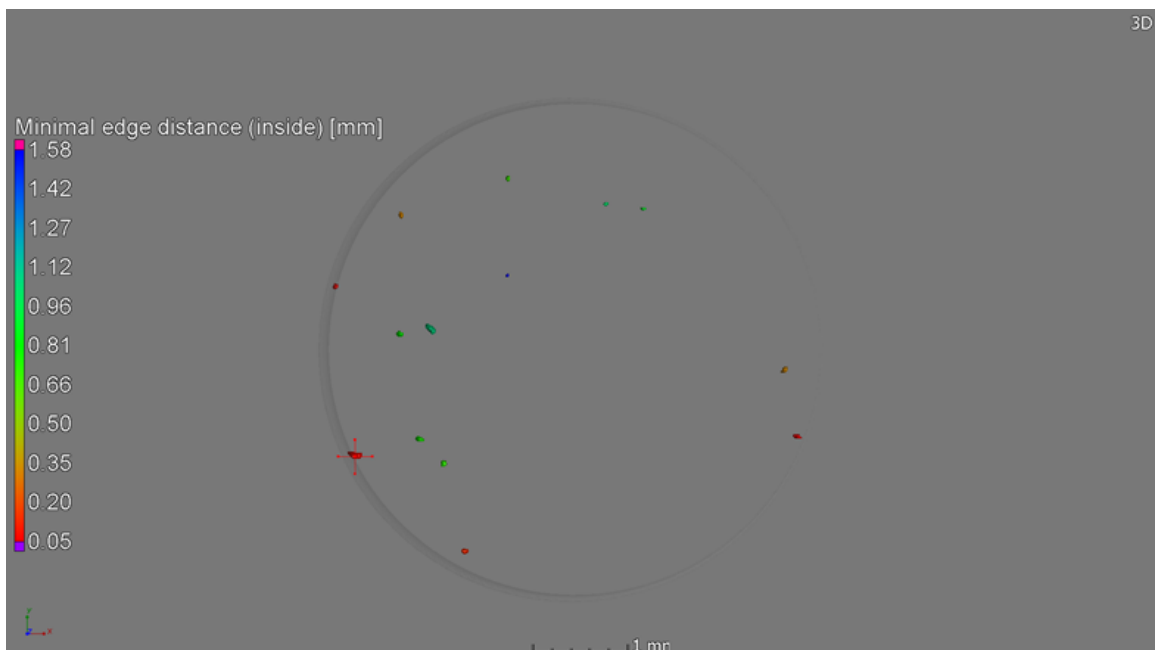


Figure 4.57: Micro-CT scan image on the plane of fracture for specimen Z-12, with the crack initiation pore marked with a cross

The fractographs and the micro-CT scan images for the planes of fracture of specimens X-12, Y-12 and Z-12 are shown in Figures 4.52, 4.54 and 4.56 and Figures 4.53, 4.55 and 4.57, respectively. The ΔK values calculated for the crack initiation pores of these specimens increase in the order of specimen X-12, Y-12 and Z-12 following their projected areas that increase in the same order. It is thought that specimen X-12 showed the highest number of load cycles to failure of these three specimens because its crack initiated from a pore with the lowest value of ΔK , which implies the lowest rate of propagation of the fatigue failure crack of the three specimens. The value of ΔK for the crack initiation pore in specimen Z-12 was lower than that from specimen Y-12 but the specimen failed at a higher number of load cycles than specimen Y-12. The shorter specimen life of specimen Y-12 is attributed to a high distribution of internal pores around the crack initiation pore, as can be seen in Figure 4.55, which implies an accelerated propagation of the fatigue failure crack through merging of the crack tip with these pores in the early stage of propagation of the crack.

4.6.1.5 Influence of microstructure on the mode of fracture

In order to investigate the microstructural influence of stress-relieved plus HTA DMLS Ti6Al4V (ELI) specimens in the three mutually orthogonal DMLS orientations, specimens loaded at the same stress load were sectioned and prepared for metallographic analysis in the same way discussed in section 5.7.2.4. Specimens X-12, Y-12 and Z-12, that were selected for use in this exercise failed from the application of a maximum cyclic load $\sigma_{max} = 520 \text{ MPa}$, at 2,580,515; 125,582 and 156,868 load cycles, respectively.

4.6.1.5.1 X-built specimen

Figure 4.58 shows a stitched micrograph of the propagated fatigue failure crack of stress-relieved plus HTA DMLS Ti6Al4V (ELI) specimen X-12, which was cycled under tension–tension at a maximum stress load of 520 MPa and which fractured at 2,580,515 cycles.

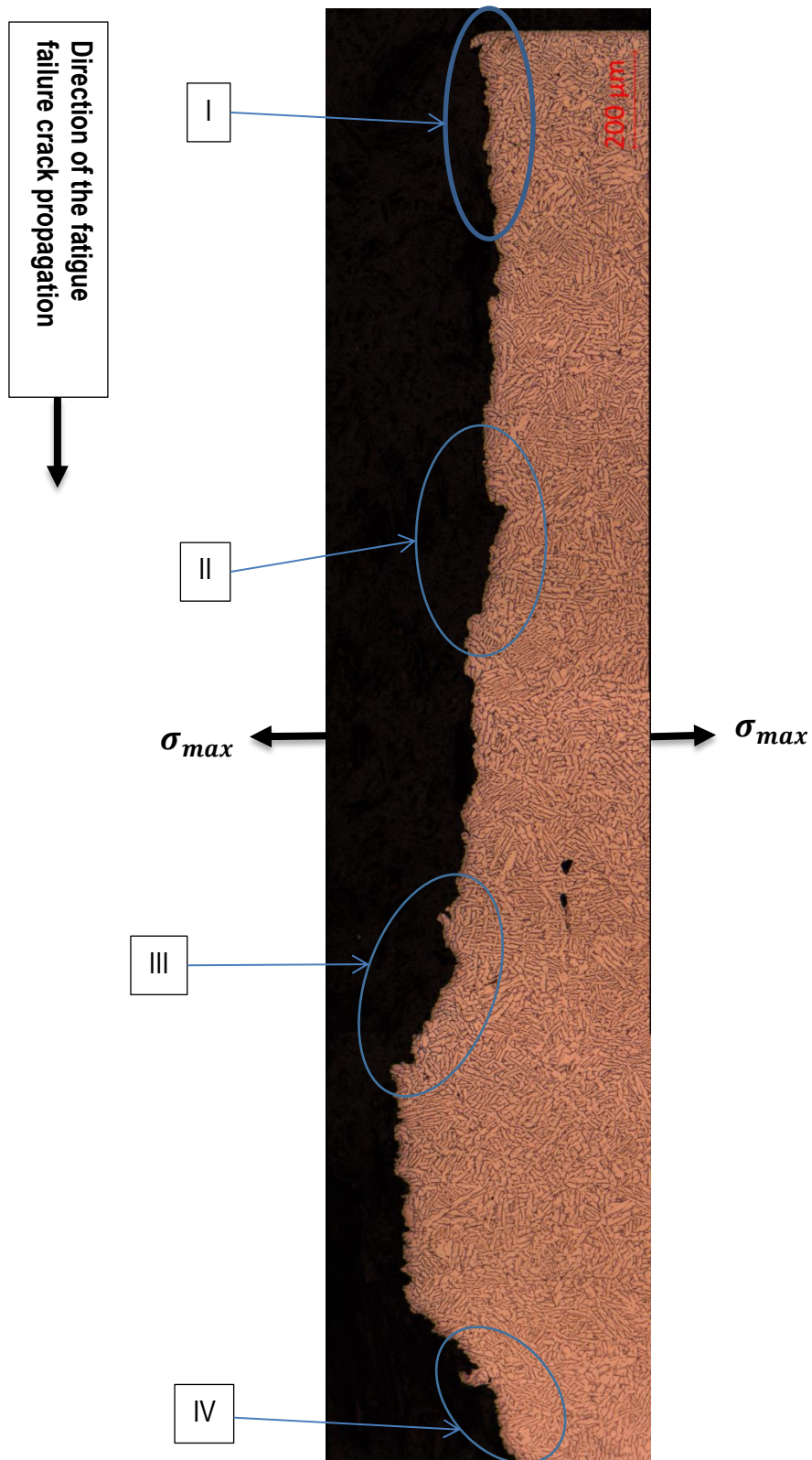


Figure 4.58: (a) A stitched micrograph of HTA specimen X-12 showing the fatigue failure propagated crack

Figures 4.59 (a), (b), (c) and (d) show the magnified micrographs of the crack path of specimen X-12 around the enclosed sections in Figure 4.58 labelled I, II, III and IV, respectively.

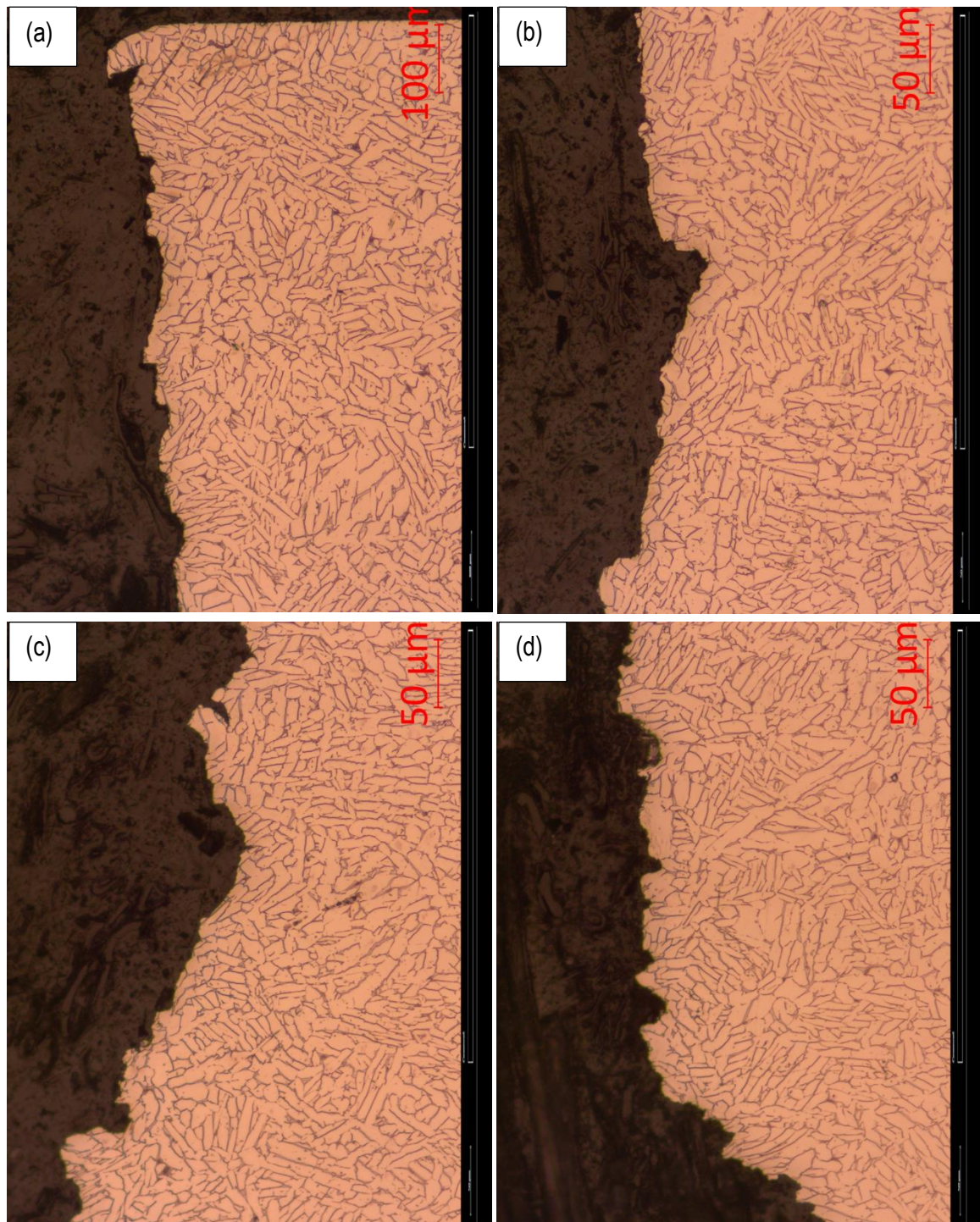


Figure 4.59: (a) A micrograph of specimen X-12 around the enclosed area labelled I in Figure 4.58 and (b) a micrograph of specimen X-12 around the enclosed area labelled II, (c) a micrograph of specimen X-12 around the enclosed area labelled III in Figure 4.58 and (d) a micrograph of specimen X-12 around the enclosed area labelled IV in Figure 4.58

4.6.1.5.2 Y-built specimen

Figure 4.60 shows a stitched micrograph of the fatigue failure propagated crack of stress-relieved plus HTA DMLS Ti6Al4V (ELI) specimen Y-12, which was cycled under tension–tension at a maximum stress load of 520 MPa and which fractured at 125,582 cycles.

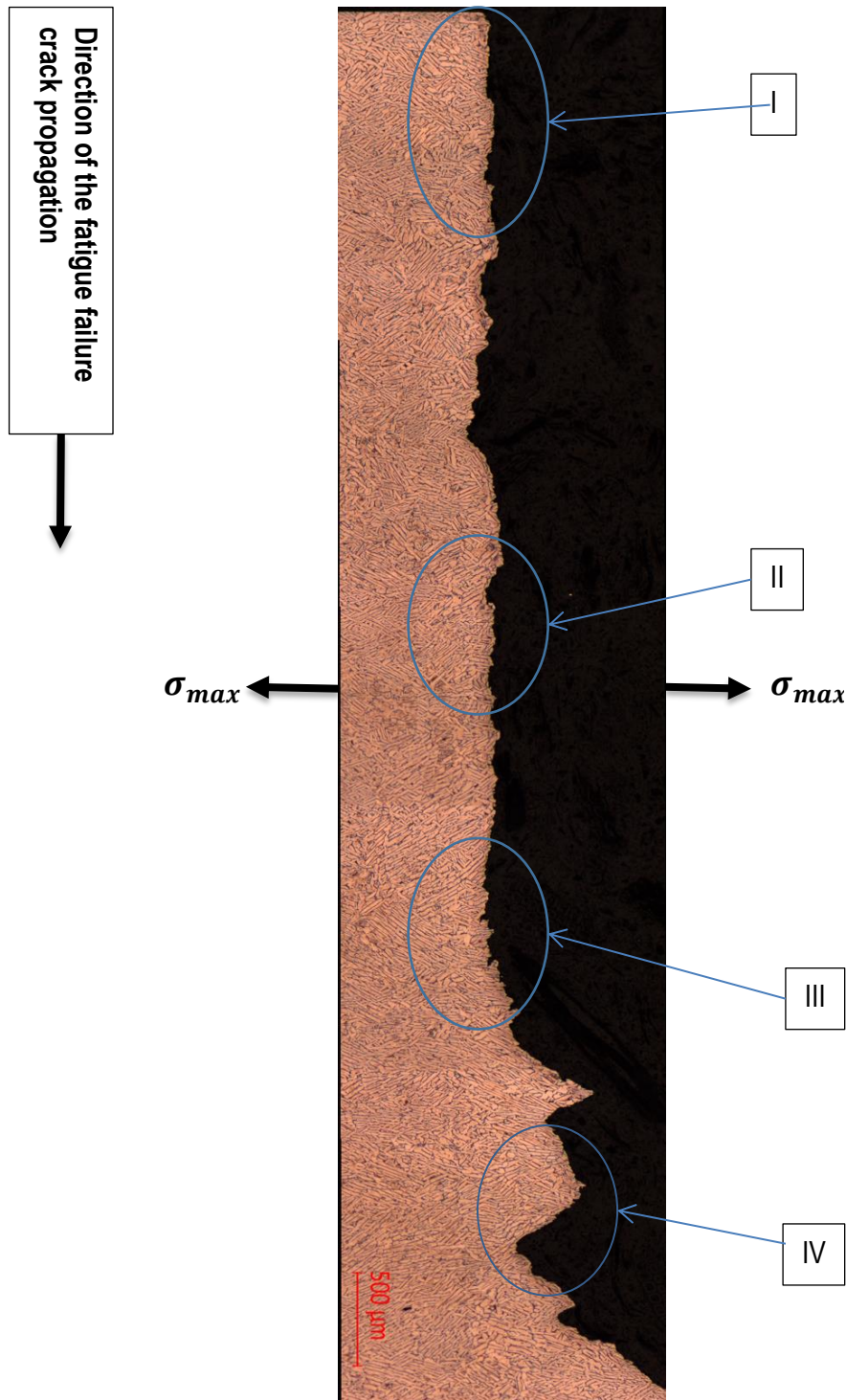


Figure 4.60: A stitched micrograph of specimen Y-12 showing the fatigue failure propagated crack

Figures 4.61 (a), (b), (c) and (d) show the magnified micrographs of the crack path of specimen Y-12 around the enclosed sections in Figure 4.60 labelled I, II, III and IV, respectively.

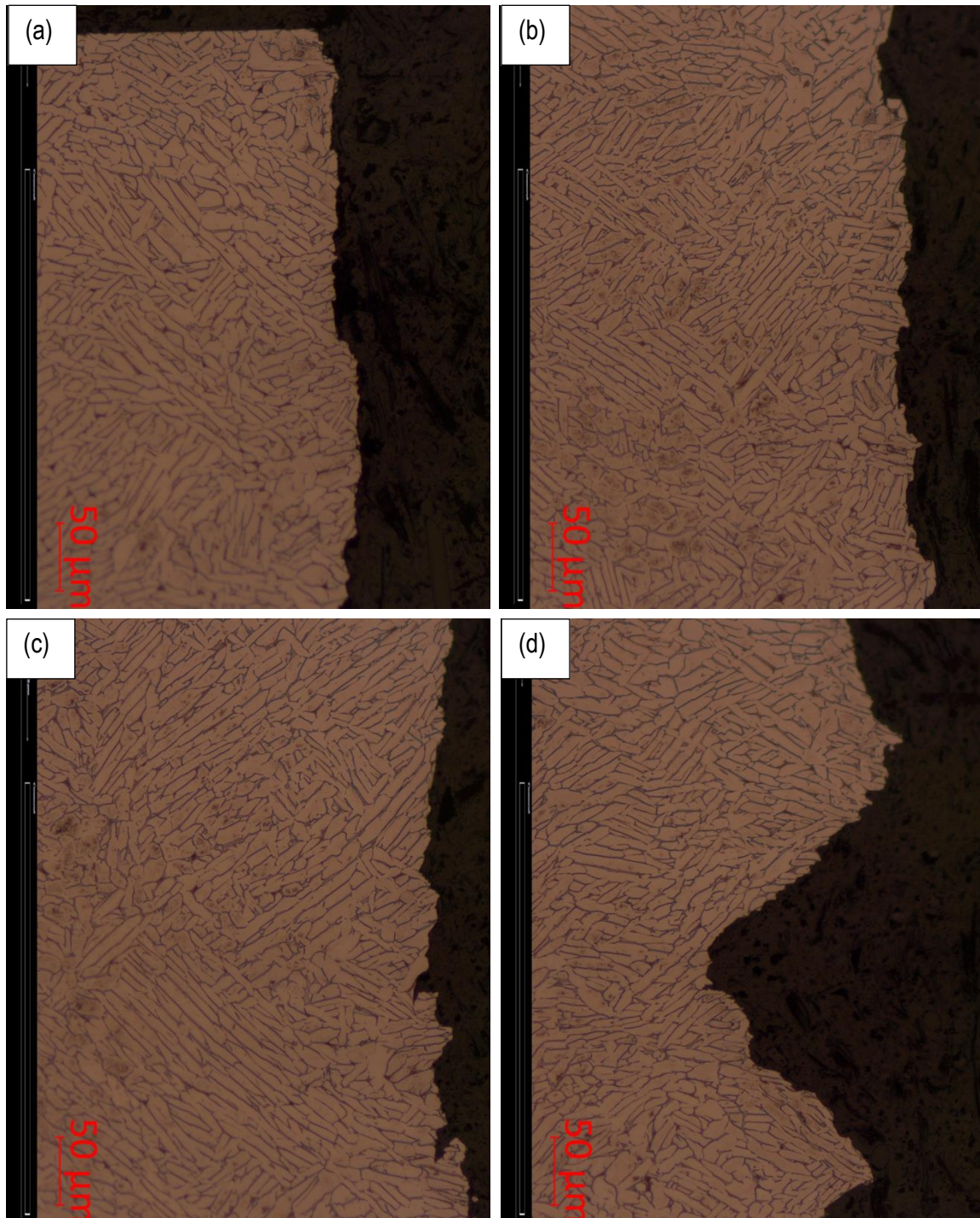


Figure 4.61: (a) A micrograph of specimen Y-12 around the enclosed area labelled I in Figure 4.60 and (b) a micrograph of specimen Y-12 around the enclosed area labelled II in Figure 4.60, (c) a micrograph of specimen Y-12 around the enclosed area labelled III in Figure 4.60 and (d) a micrograph of specimen Y-12 around the enclosed area labelled IV in Figure 4.60

4.6.1.5.3 Z-built Specimen

Figure 4.62 shows a stitched micrograph of the fatigue failure propagated crack of stress-relieved plus HTA DMLS Ti6Al4V (ELI) specimen Z-12, which was cycled under tension–tension at a maximum stress load of 520 MPa and which fractured at 156,868 cycles.

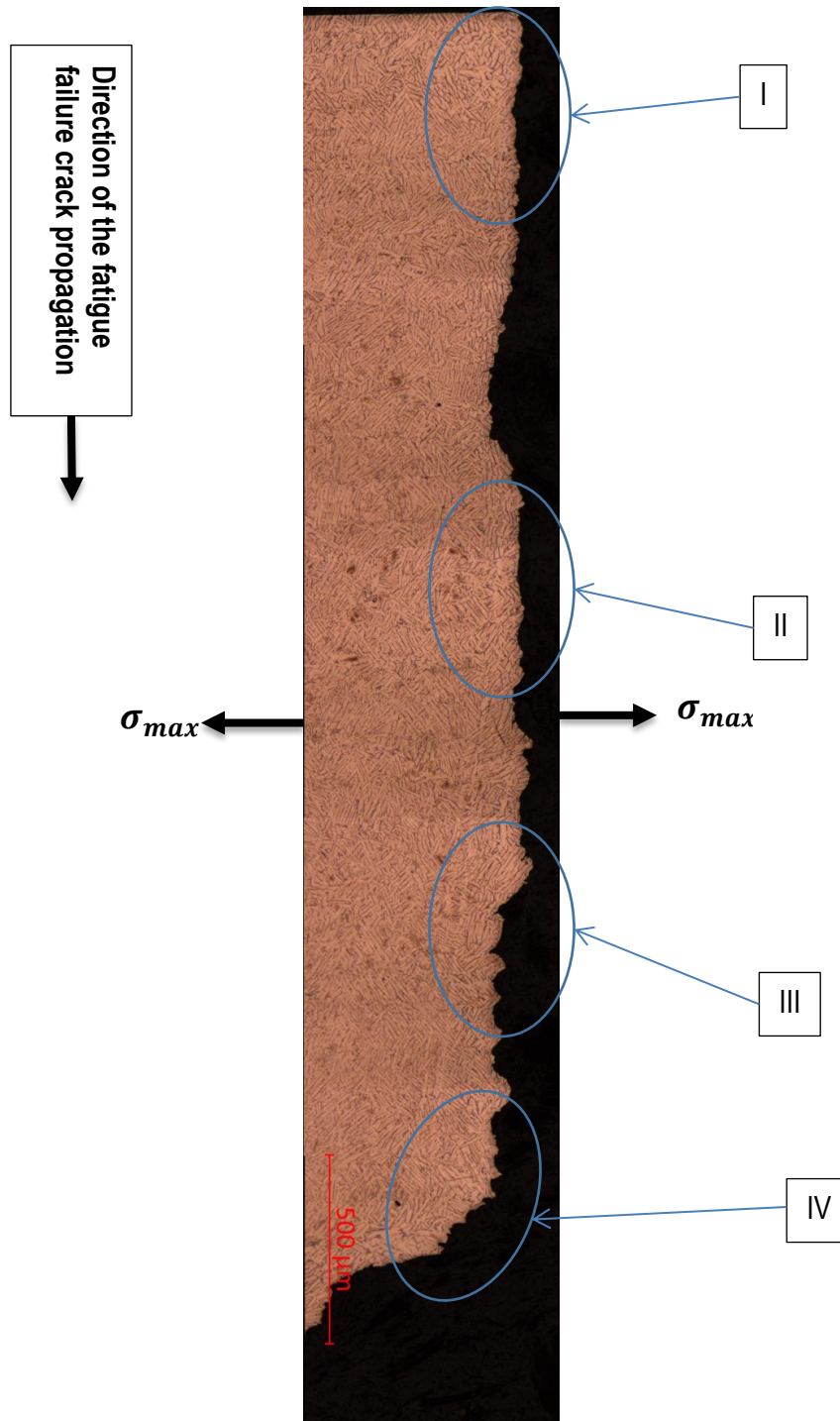


Figure 4.62: A stitched micrograph of specimen Z-12 showing the fatigue failure propagated crack

Figures 4.63 (a), (b), (c) and (d) show the magnified micrographs of the crack path of specimen Z-12 around the enclosed sections in Figure 4.62 labelled I, II, III and IV, respectively.

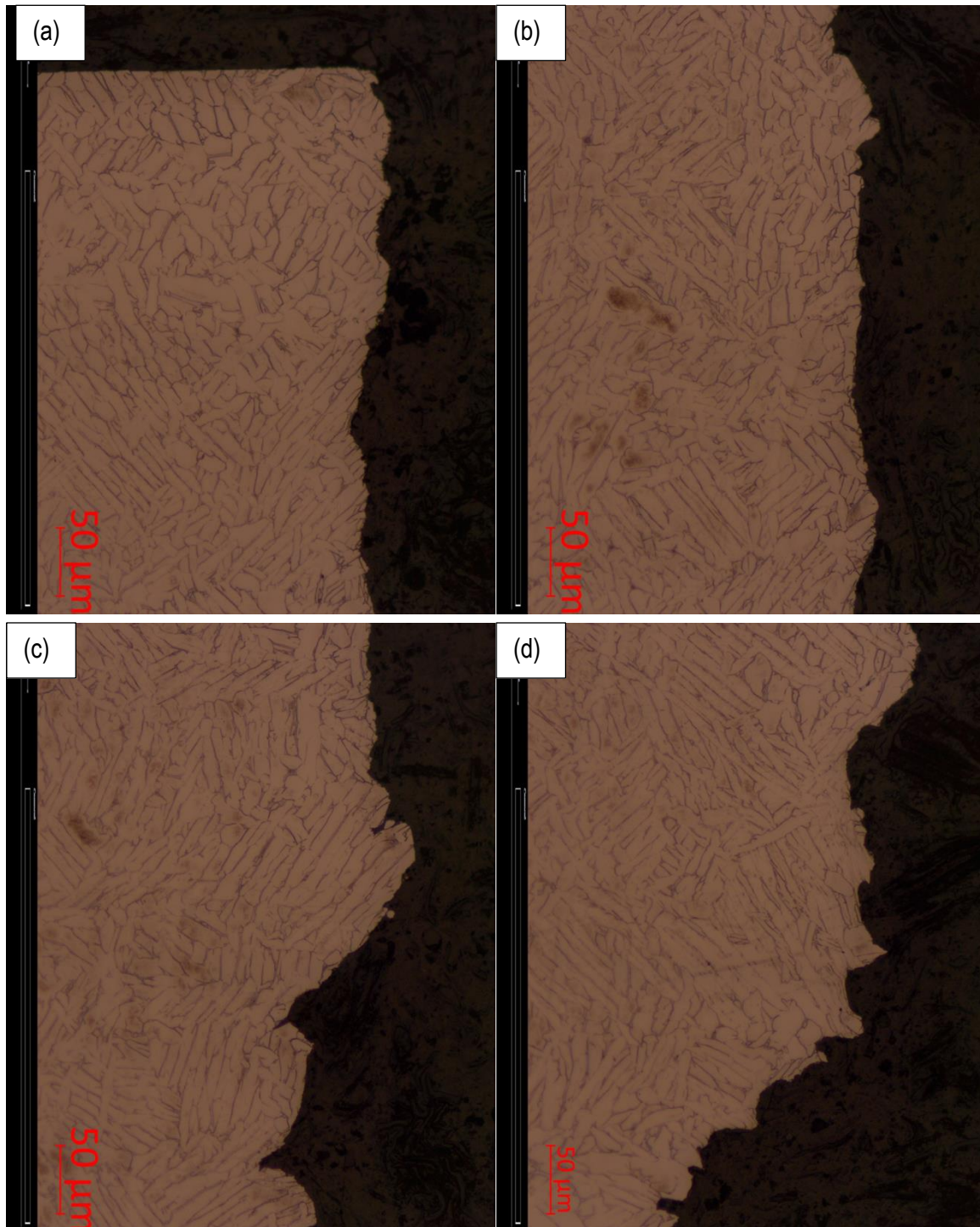


Figure 4.63: (a) A micrograph of specimen Z-12 around the enclosed area labelled I in Figure 4.62 and (b) a micrograph of specimen Z-12 around the enclosed area labelled II in Figure 4.62, (c) a micrograph of specimen Z-12 around the enclosed area labelled III in Figure 4.62 and (d) a micrograph of specimen Z-12 around the enclosed area labelled IV in Figure 4.62

In section 4.4, the complete decomposition of acicular α' martensite and subsequent growth of $\alpha + \beta$ grains within the columnar prior β grain was reported. This same grain morphology is evident in Figures 4.58, 4.60 and 4.62. However, the only difference between the grain morphology of these figures and the one discussed in section 4.4 is that no grain boundary α grains are visible in these figures, thus their influence on the fatigue crack path will not be discussed here. The micrographs shown in Figures 4.58, 4.60 and 4.62 exhibit fairly flat fracture paths of specimens X-12, Y-12 and Z-12, except for areas approaching the area of final fracture. The flat fracture path evident in Figures 4.59 (a) and (b), 4.61 (a) and (b) and 4.63 (a) and (b) for specimens X-12, Y-12 and Z-12, shown at high magnifications, is typical of a trans-granular mode of fatigue fracture. The zig-zagged growth path of the fatigue failure crack seen in the areas approaching the area of final fracture are characteristic of the inter-granular mode of fatigue fracture. However, high magnifications of these areas shown in Figures 4.59 (d), 4.61 (d) and 4.63 (d) show the mode of propagation of the fatigue failure cracks to be trans-granular as well. Therefore, the fatigue fracture mode of stress-relieved plus HTA DMLS Ti6Al4V (ELI) specimens oriented in all three mutually orthogonal directions are trans-granular as opposed to the mixed trans-granular and inter-granular fracture modes of the as-built Ti6Al4V (ELI) specimens. The inter-granular fatigue fracture mode of the as-built specimens is a result of deflection of the crack by the grains of acicular α' martensite, which gives rise to a higher fatigue crack growth resistance as opposed to the case for HTA specimens.

4.6.2 Summary

The major part of the fatigue life of a specimen lies in the crack initiation stage [62][66]. Fatigue cracks initiate from localised cyclic plastic deformation in the microstructure, for which the rate of deformation is intensified by the presence and size of stress concentration sites [107][102]. All the fractured as-built DMLS Ti6Al4V (ELI) specimens failed from cracks which initiated from DMLS process-related surface pores with values of ΔK that were higher than the reported values of ΔK_{th} in literature, which were adopted for use here. A low value of ΔK at the tip of the crack initiation pore of a specimen, resulting from either a low stress load or a low projected area of the pore or even both, results in an increase in the number of load cycles to failure of the specimen. This is evident from specimen X-2, which fractured after a high number of load cycles despite it being loaded at a high value of σ_{max} , because its fatigue failure crack initiated from a pore that had the lowest \sqrt{area} amongst the set tested here, thereby resulting in a low ΔK . The presence of internal DMLS process-related pores on the fracture plane of specimens also lowers the number of load cycles to failure due to coalescence of the pores with the advancing crack, which was the case in specimen X-4.

Figure 4.64 shows superimposed semi- \log_{10} S-N curves for as-built DMLS Ti6Al4V (ELI) specimens oriented in the X-, Y- and Z-directions

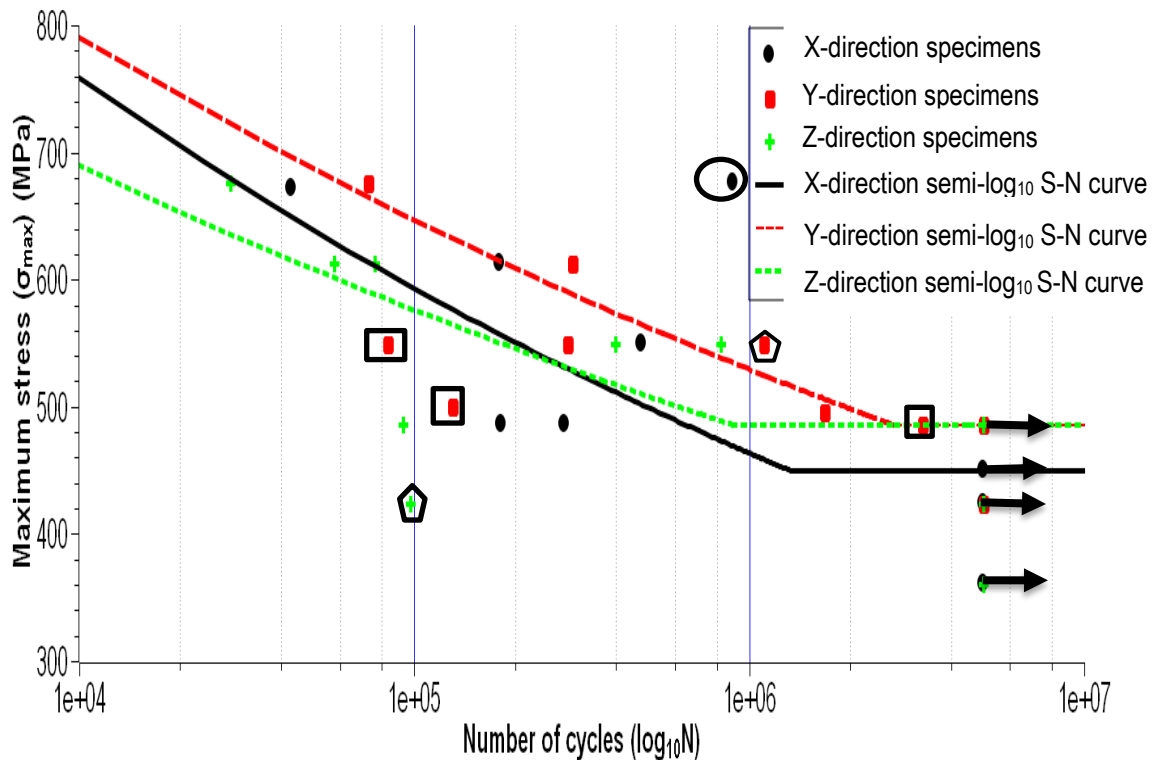


Figure 4.64: Semi- \log_{10} HCF S-N curves for as-built DMLS Ti6Al4V (ELI) specimens oriented in the X-Y- and Z-directions

In Figure 4.64, the fatigue strengths of the as-built DMLS Ti6Al4V (ELI) specimens at 10^4 load cycles is seen to increase in the order of Z-, X- and Y-direction specimens. The fact that the value of fatigue strength at 10^4 load cycles of the Z-direction specimens is the lowest is consistent with the report by Yadroitsev et al. [41] that the value of UTS of as-built DMLS Ti6Al4V (ELI) was lower for vertically oriented specimens than for horizontally oriented specimens [41]. Unlike the case for the fatigue strength at 10^4 load cycles, the Z- and Y- direction specimens have the same value of fatigue endurance limit that is higher than the value for the X-direction specimens. The coefficient of variance for the fatigue strengths at 10^4 load cycles for as-built specimens was found to be 7% and that of the endurance limits, 4.4%. The difference in the aforementioned coefficients of variance indicate as-built Ti6Al4V (ELI) specimens show a higher degree of anisotropy at fatigue strengths at 10^4 load cycles (high loads) than at the endurance limits, as seen in Figure 4.64. The coefficients of variance of 4.4% and 7% are, however, small and statistically insignificant given the spread of the

data points, which implies insignificant anisotropy of fatigue strength and endurance limit arising from the DMLS process.

The fatigue cracks of the fractured stress-relieved plus HTA DMLS Ti6Al4V (ELI) specimens initiated from surface and sub-surface DMLS process-related pores and from surface facets. The faceted crack initiation sites showed high numbers of load cycles to failure at high loads, made evident by specimens X-5, Y-8 and Z-3. Similar to the as-built specimens, a low ΔK resulting from either a low stress load or a low projected crack initiation pore in a specimen resulted in the fracture of the specimen after a high number of load cycles. This was made evident by specimens X-4 (high stress load, low crack initiation pore \sqrt{area} , and relatively high number of load cycles to failure) and specimen Z-7 (stress load below the fatigue endurance limit, high crack initiation pore \sqrt{area} and relatively low number of load cycles to failure).

Figure 4.65 shows the super-imposed semi- \log_{10} S-N curves for stress-relieved plus HTA DMLS Ti6Al4V (ELI) specimens built in the X-, Y- and Z-directions.

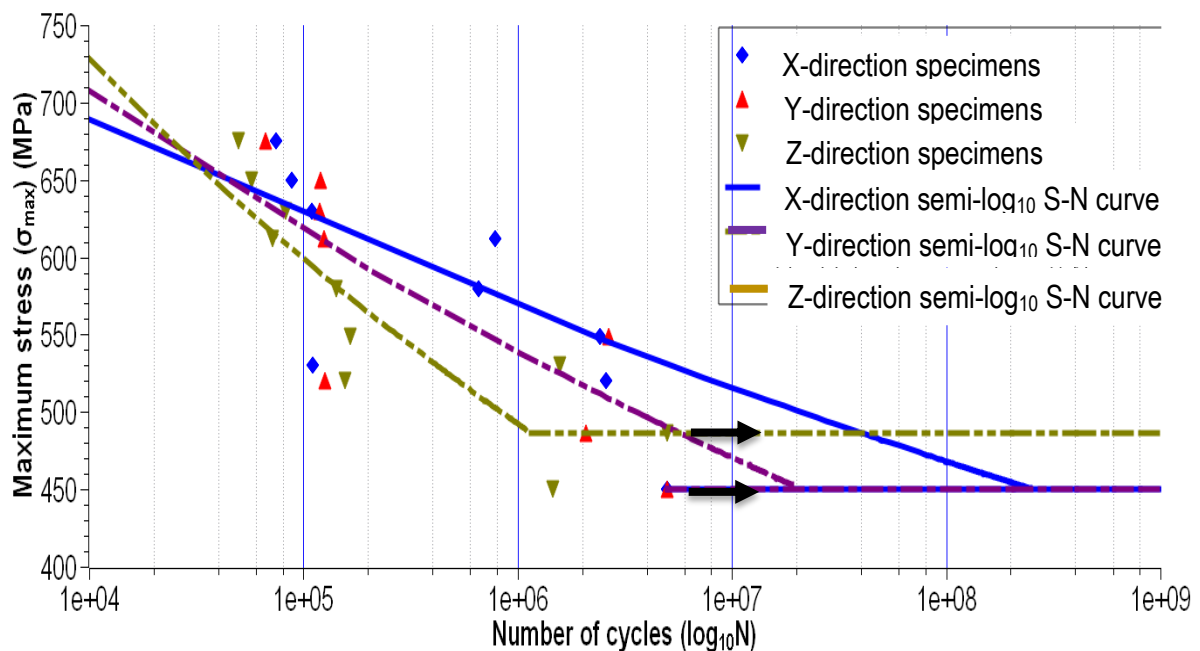


Figure 4.65: Semi- \log_{10} HCF S-N curves for stress-relieved plus HTA DMLS Ti6Al4V (ELI) specimens built in the X-Y- and Z-directions

The fatigue strengths of stress-relieved plus HTA Ti6Al4V (ELI) at 10^4 load cycles determined here, increase in the order of X-, Y- and Z-direction specimens. Whereas, their fatigue endurance limits

are the same for the X- and Y-directions, and slightly lower than the values determined for the Z-direction, these values of the fatigue strengths at 10^4 load cycles and the fatigue endurance limits are contrary to the values of the UTS of stress-relieved plus HTA DMLS Ti6Al4V (ELI) determined in this investigation in which the values in the Z-build direction was the lowest. The coefficient of variation for the fatigue strength at 10^4 load cycles is 2.2% and that of the fatigue endurance limits is 4.5%. These values of the coefficients of variance indicate a higher degree of anisotropy at the fatigue endurance limit loads than at the fatigue strengths at 10^4 load cycles, as seen in Figure 4.65. The coefficient of variance of 4.5% in the fatigue endurance limits of stress-relieved plus HTA Ti6Al4V (ELI) specimens is small and statistically insignificant, given the spread of the data points. Anisotropy that might result from the DMLS process does not reflect in the fatigue properties of parts.

Figure 4.66 shows the super-imposed semi- \log_{10} S-N curves for as-built and stress-relieved plus HTA DMLS Ti6Al4V (ELI) specimens built in the X-, Y- and Z-directions.

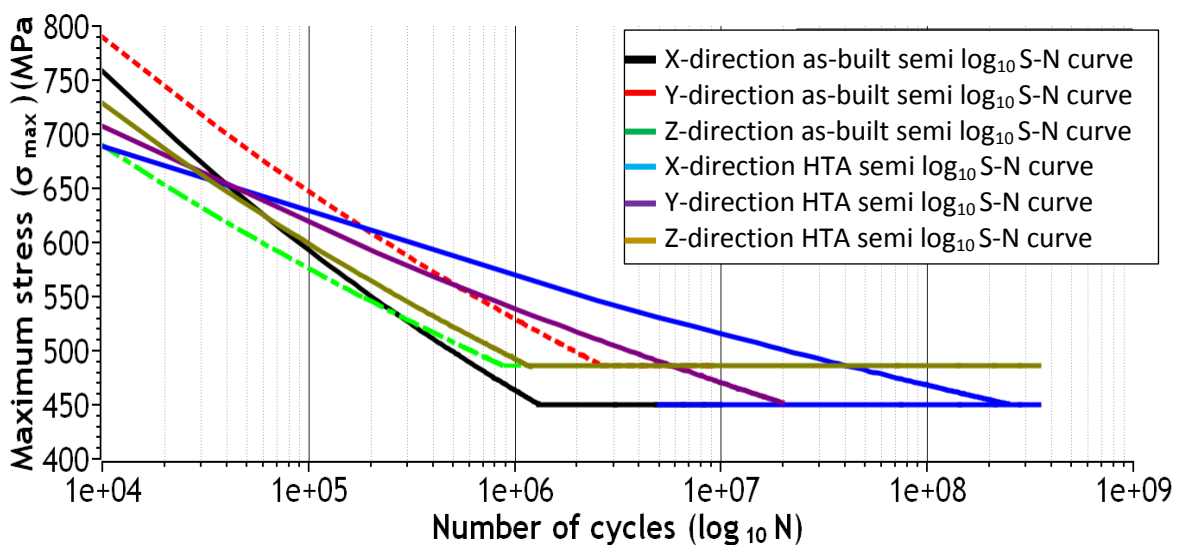


Figure 4.66: Semi- \log_{10} HCF S-N curves for as-built and stress-relieved plus HTA DMLS Ti6Al4V (ELI) specimens built in the X-Y- and Z-directions

Table 4.16 shows a summary of the fatigue strengths at 10^4 load cycles and the fatigue endurance limits for as-built and stress-relieved plus HTA DMLS Ti6Al4V (ELI) specimens for the X-, Y- and Z-built specimens.

Table 4.16: Comparison of the fatigue strengths at 10⁴ load cycles and the fatigue endurance limits between the as-built and stress-relieved plus HTA DMLS Ti6Al4V (ELI) specimens

DMLS build orientation	Fatigue endurance limits for as-built specimens (MPa)	Fatigue endurance limits for stress-relieved plus HTA specimens (MPa)	Fatigue strength at 10 ⁴ cycles for as-built specimens (MPa)	Fatigue strength at 10 ⁴ cycles for HTA specimens (MPa)
X	450	450	760	690
Y	486	450	790	706
Z	486	486	688	730
Mean	474	462	746	712
Standard deviation	20.78	20.78	52.17	15.68
Coefficient of variance	4.4%	4.5%	7.0%	2.2%

The fatigue endurance limits for the as-built and stress-relieved plus HTA DMLS Ti6Al4V (ELI) specimens are the same for the X- and Z-built specimens and the as-built Y-built specimens are slightly higher than the Y-built specimens of the stress-relieved plus HTA specimens as shown in Figure 4.66. However, this difference is also statistically insignificant. It can thus be concluded that stress-relieving plus HTA of DMLS Ti6Al4V (ELI) specimens does not influence the fatigue endurance limit of the specimens. The stress-relieved plus HTA specimens showed a higher percentage of their fatigue endurance limit to their UTS in their respective build orientations than the as-built specimens. The percentages are 48%, 48%, and 53% for HTA specimens and 36%, 38% and 39% for as-built specimens. These are for the X-, Y- and Z-built specimens, respectively. The stress-relieved plus HTA specimens also show higher percentages of the fatigue strengths at 10⁴ load cycles to their UTS than as-built specimens. The percentages are 75%, 75%, and 80% for stress-relieved plus HTA specimens and 60%, 62% and 55% for as-built specimens. These are for the X-, Y- and Z-built specimens, respectively. It can thus be concluded that stress-relieved plus HTA of DMLS Ti6Al4V (ELI) specimens lowers the UTS [41] but improve the fatigue properties in relation to the UTS. The gradients of the linearized semi-log₁₀ S-N curves for stress-relieved plus HTA specimens in the X- and Y-orientations are lower than those of the as-built in the same orientations leading to knee points above set number of run-out cycles. This is, however, not the case for Z-built orientation specimen whose gradients and knee points are similar. The gradients for the stress-relieved plus HTA specimens in the X- and Y-orientations are -0.052 and 0.054 and for as-built specimens in the X- and Y-built orientations are -0.107 and -0.087. This implies that the stress-relieved plus HTA of Ti6Al4V (ELI) specimens resulted in an increase in the number of load

cycles to failure below the stress load of 655 MPa for the specimens X-built orientation and 558 MPa in the Y-built orientation as seen in Figure 4.66. The degree of scatter of the fractured specimens on the semi-log₁₀ S-N curves is higher for the as-built specimens than the stress-relieved plus HTA specimens, which can be attributed to the presence of residual stresses in the as-built specimens. However, for all the curves, the scatter of the fractured specimens can be attributed to the different sizes of (\sqrt{area}) and locations of crack initiation pores in the specimens.

4.7 Comparison of the DMLS Ti6Al4V fatigue endurance limits

This section compares the tension–tension fatigue results for cylindrical SLM/DMLS Ti6Al4V found in literature with the ones tested here, all in accordance with ASTM E466. The fatigue endurance limits of these cylindrical DMLS Ti6Al4V specimens from literature and in the present work and their respective process parameters for production are shown in Table 4.17. The hatch spacing and the layer thickness for all the specimens referenced in this table were 100 μm and 30 μm , respectively. The specimens from all the references were also machined to negate the influence of the DMLS process-related surface finish on the properties of the specimens [108]. The specimens were cycled at a fatigue stress ratio $R = 0.1$.

Table 4.17: DMLS process parameters used in the production of specimens and the resulting material and fatigue features

References	Porosity (Vol %)	Laser power (W)	Scan speed (mm/s)	Post-heat treatment	Fatigue endurance limit (MPa)
Gong et al. [109]	0.45	120	960	none	350
Present study as built	<0.001	170	1200	none	474
Wycisk et al. [80]	0.4	170	1250	650 °C 3h	510
Wycisk et al. [79]	NR	200	NR	650 °C 3h	500
Wycisk et al. [110]	NR	200	NR	650 °C 3h	500
Rafi et al. [111]	NR	170	1,250	650 °C 4h	550
Rafi et al. [81]	NR	NR	NR	NR	550
Present study HTA	<0.001	170	1200	950 °C 2h	462

*NR – Not recorded

Gong et al. [109] published the HCF results of DMLS Ti6Al4V that were not subjected to post-stress-relieving heat treatment. In his work, cylindrical bars of 10 mm diameter were built in an EOS M270 machine in the Z-orientation, from which fatigue specimens were machined in accordance with ASTM E466. He reported a fatigue endurance limit of 350 MPa which was the lowest of all the

tabulated fatigue endurance limits in Table 4.17. The low endurance limit was attributed by the authors to the fact that the powder particle size used was different from that of the standard EOS Ti6Al4V powder and that the process parameters used were different from those recommended by EOS.

Wycisk et al. [80] (fourth row of Table 4.17), in their publication on the HCF properties of DMLS Ti6Al4V, reported an endurance limit of 510 MPa for specimens that were built with their longitudinal axis at 45° to the build plate. In their continued work (fifth row of Table 4.17) on the HCF properties of DMLS Ti6Al4V in a separate publication, they compared specimens built with their longitudinal axes at 45° and 90° to the base plate [79]. They reported the difference in the fatigue endurance limits to be insignificant with regard to specimens built with their longitudinal axes oriented in the Z-direction, having a higher fatigue endurance limit of 500 MPa. In the last study referenced in Table 4.17 by Wycisk et al [110] (sixth row of Table 4.17), a fatigue endurance limit of 500 MPa was reported from the specimens that were also built with their longitudinal axes oriented in the Z-direction. The specimens reported on in all three publications were built to the blank dimensions of fatigue specimens specified in ASTM E466. The specimens were then stress relieved in a vacuum at 650 C and soaked for 3 hours, followed by cooling in an environment of argon gas to room temperature. The specimens were then machined and polished to the net dimensions of fatigue specimens specified in ASTM E466.

Rafi et al [111][81], in both the publications referenced in Table 4.17, reported a fatigue endurance limit of 550 MPa, which is higher than all the endurance limits reported there. The specimens in this publication were also built with their longitudinal axes orientated in the Z-direction and machined down to the net shape specified in ASTM E466, as was the case with the other specimens in the table. The only difference between these specimens and the others in the table lies in the parameters of the stress-relieving heat treatment, whereby the specimens were heated in an argon atmosphere to 650 °C and soaked for 4 hours followed by furnace cooling to room temperature. The stress-relieving treatment by Wycisk was carried out at 650 °C but in vacuum with a soaking period of 3 hours, followed by cooling within an environment of argon gas. No stress-relieving heat treatment was employed in the publication by Gong.

Figure 4.67 shows the endurance limits of DMLS Ti6Al4V machined specimens cycled at a stress ratio of R=0.1 based on the data shown in Table 4.17.

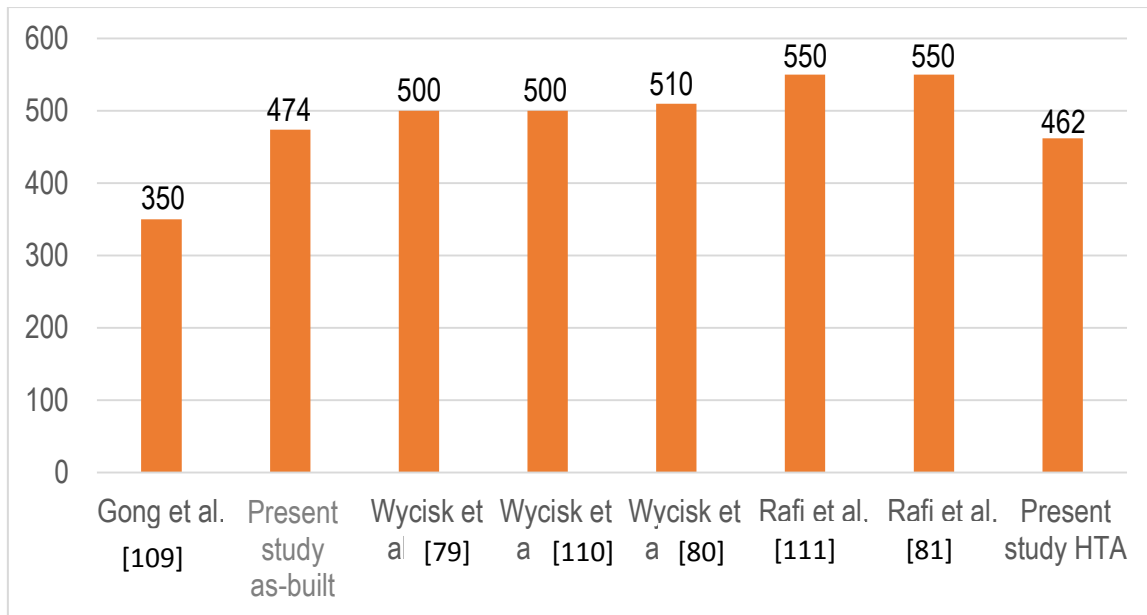


Figure 4.67: Comparison of the values of fatigue endurance limits presented in Table 4.17

The microstructure of the specimens from the referenced publications in Table 4.17 were reported to be of acicular α' martensite within the prior β grains. The references showed that the cracks of the fractured specimens all initiated from DMLS process-related pores. Wycisk et al. [79] reported that specimens that showed low fatigue life failed from cracks that initiated from internal DMLS pores and those that showed high fatigue life failed from cracks that initiated from surface DMLS process-related pores. It was concluded by the authors that for internally initiated cracks, the critical crack length is smaller than that of surface initiated cracks [79]. This is in agreement with the results from stress-relieved plus HTA DMLS Ti6Al4V (ELI) specimens in the current project where the one specimen with an internal crack initiation site, specimen Y-8, fractured after a low number of cycles. However, the crack initiated from internal facets. The specimens with surface sites of crack initiation that showed high numbers of cycles to failure were from faceted sites of initiation of surface cracks made evident by specimens X-5 and Z-8 of the stress-relieved plus HTA DMLS Ti6Al4V (ELI) specimens. The aforementioned results of Wycisk et al. [79] are also in contrast to the results of the as-built DMLS Ti6Al4V (ELI) specimens in the present work, because all their fractures originated from surface DMLS process-related pores. Rafi et al. [111] reported that failure of all the specimens in their work originated from the cracks that initiated from sub-surface DMLS process-related pores. A high degree of scatter of the fatigue data on the S-N curves was reported in all the references. This scatter may be attributed to the different geometry of the DMLS process-related pores at

random locations within the different specimens. The low fatigue endurance limit in the first referenced publication in Table 4.17 can be attributed to the high level of porosity in the specimens.

From Figure 4.67, it can be concluded that the stress relieving of DMLS Ti6Al4V specimens improves their fatigue endurance limits, which is consistent with the discussion in section 2.7.4 to the extent that the tensile residual stress inherent in DMLS parts promote crack initiation and propagation under tensile–tensile fatigue loading. HTA of DMLS Ti6Al4V (ELI) lowers the fatigue endurance limit, as shown in Figure 4.67. This is because the reduced tensile stress of DMLS Ti6Al4V (ELI) after HTA also reduces the localized stresses required for crack initiation and propagation. However, the percentage of the fatigue endurance limit to the UTS is increased because HTA of DMLS Ti6Al4V reduces the UTS further from that of stress-relieved specimens.

CHAPTER 5 CONCLUSIONS AND FUTURE WORK

5.1 Introduction

The aim of this study was to determine the fatigue properties of DMLS Ti6Al4V (ELI) specimens and their level of conformity to the internationally accepted specifications for such parts produced through conventional manufacturing routes. This was achieved through investigating the HCF properties of as-built and post-process stress-relieved plus HTA DMLS Ti6Al4V (ELI) specimens. Since the fatigue specimens tested were all machined and polished, reference to surface crack initiation pores in this document actually are internal pores with reference to the bulk specimens built on the DMLS machine.

5.2 Conclusions

- The as-built DMLS Ti6Al4V (ELI) specimens were both homogeneous and isotropic. HTA of DMLS Ti6Al4V (ELI) gave rise to tensile anisotropy in the three mutually orthogonal DMLS build orientations, with the Z-built specimens showing the lowest values of 0.2% proof stress, modulus of elasticity and UTS of the three DMLS specimen orientations. DMLS process-related pores had no influence on the anisotropy of the tensile properties of stress-relieved and HTA DMLS Ti6Al4V (ELI) specimens, or the location of the fracture planes.
- HTA of DMLS Ti6Al4V (ELI) completely transformed the acicular α' martensite microstructure to colonies of $\alpha + \beta$ phase with an uneven distribution of equiaxed α grains. At the annealing parameters used, grain boundary α grains began to nucleate and grow at the boundaries of the prior β grains.
- HTA of DMLS Ti6Al4V (ELI) lowered the values of the 0.2% proof stress and UTS, but increased the strain at fracture of the specimens from their as-built state. Moreover, HTA of DMLS Ti6Al4V (ELI) specimens improved the percentages of the HCF strength to the UTS. There was, however, no significant difference in the fatigue endurance limits of as-built and HTA DMLS Ti6Al4V (ELI) specimens. HTA of DMLS Ti6Al4V (ELI) specimens improved the number of cycles to failure in the specimens with their longitudinal axes oriented in the X- and Y-directions for maximum stress loads below 655 MPa and 558 MPa, respectively.
- The values of HCF endurance limits for the as-built, compared to stress-relieved followed by HTA, DMLS Ti6Al4V (ELI) specimens were the same for the specimens whose longitudinal

axes were oriented in the Y- and Z-directions and X and Y directions, respectively, and slightly higher and lower in each case, than the values determined for the X and Z-directions, respectively. Moreover, the values of HCF endurance limits for the as-built, compared to stress-relieved followed by HTA, DMLS Ti6Al4V (ELI) specimens were the same in the specimens whose longitudinal axes were oriented in the X- and Z-directions and the values in the Y-direction for the as-built specimens were slightly higher than those of the stress-relieved followed by HTA specimens. However, the differences observed were small and statistically insignificant, given the spread of the data points. Therefore, anisotropy that might have resulted from the DMLS process did not reflect in the fatigue endurance limits of the specimens, and stress-relieved followed by HTA DMLS Ti6Al4V (ELI) specimens had small but insignificant reduction in their fatigue endurance limit properties.

- The HCF fracture surfaces of both as-built and stress relieved followed by HTA DMLS Ti6Al4V (ELI) specimens displayed the four HCF fracture features i.e., crack initiation, slow- and fast crack propagation, and final fracture. It was further noted that the fatigue cracks in both as-built and stress relieved followed by HTA DMLS Ti6Al4V (ELI) initiated from surface and sub-surface DMLS process related micro-pores. The specimens with sub-surface crack initiation sites exhibited higher numbers of cycles to failure than those with surface crack initiation sites, despite in some cases having relatively larger crack initiation pores. The HCF life of the DMLS Ti6Al4V (ELI) specimens mainly depended on the area of the process-related crack initiation pores projected onto the fracture plane. Pores with large crack initiation areas led to lower numbers of cycles to failure than those with small crack initiation areas loaded at the same stress loads.
- Micro-CT scanning of DMLS Ti6Al4V (ELI) parts can be used to predict the life of the parts by identifying the DMLS process-related pores within them and using LEFM to determine the stress intensity factors of the pores and their deviations from a reference value of ΔK_{th} . Such micro-CT scanning showed that the inconsistencies in the behaviour of the tested specimens to uniaxial tensile and fatigue tension–tension tests could be traced to the size of crack initiation pores for all specimens with longitudinal axes oriented in the three mutually orthogonal X-, Y- and Z-directions. It was also evident from the micro-CT scans that the HCF strength of machined DMLS Ti6Al4V (ELI) specimens, as-built and as-built followed by stress relieving and HTA heat treatments, is dependent on the size, orientation, and distribution of the surface pores and, to a small extent, on internal pores.

5.3 Future Work

- The effect of the DMLS surface finish on the HCF properties of Ti6Al4V (ELI) should be investigated by testing specimens built to standard HCF specimens size (without post process machining and polishing).
- Further work on the influence of prior β grain boundaries on the HCF properties should be done.
- The radii of the DMLS process related pore tips have yet to be measured and incorporated into the Murakami equation in order to improve the accuracy of prediction arising from its use.
- The accuracy of the calculations of stress intensity change (ΔK) of the DMLS pores should be improved by defining the distance that distinguishes sub-surface and internal pores.
- The aerospace industry standards stipulate post process use of hot isostatic pressing (HIP) of DMLS Ti6Al4V (ELI) parts. Therefore, the HCF properties of HIPed DMLS Ti6Al4V (ELI) specimens should be investigated and compared with those recorded in this project.

REFERENCES

- [1] ASTM F2792-12a. "Standard Terminology for Additive Manufacturing Technologies, ASTM International," ASTM International, West Conshohocken, PA, 2012.
- [2] B. Dutta and F.H. Foes, "Additive Manufacturing of Titanium Alloys State of the Art, Challenges, and Opportunities," *Joe Hayton, Elsevier Inc*, 2016.
- [3] B. Johnston, "High-strength fully porous biomaterials for bone replacement and their application to a total hip replacement," Dissertation of Master of Engineering Degree, submitted at McGill University, Montreal on the month of April, 2016.
- [4] EOS GmbH - Electro Optical Systems "Material Data Sheet, EOS Titanium Ti6Al4V (ELI)," 2016.
- [5] EOS GmbH - Electro Optical Systems "Laser Sintering System EOSINT M 280 for the Production of Tooling Inserts, Prototype Parts and End Products Directly in Metal", 2013.
- [6] M.G. Moletsane, P. Krakhmalev, N.A. Kazantseva, A. du Plessis, I. Yadroitsava. and I. Yadroitsev, "Tensile properties and microstructure of direct metal laser sintered Ti6Al4V (ELI) alloy". *South African Journal of Industrial Engineering*, vol. 27(3) Spec. ed. pp. 110–121, 2016.
- [7] C. Leyens, and M. Peters, "*Titanium and titanium alloys*". Weinheim: Wiley-VCH Verlag, 2003.
- [8] E. Wycisk, C. Emmelmann, S. Siddique and F. Walther, "High Cycle Fatigue (HCF) Performance of Ti6Al4V Alloy Processed by Selective Laser Melting," *Advance Materials Research*, vol. 816–817, pp. 154–159, 2013.
- [9] S.S Muthu and M.M. Savalani, "*Handbook of Sustainability in Additive Manufacturing*," Sprengler Science+Business Media Singapore, vol. 2, 2016.
- [10] K. D. Rekedal, "Investigation of the High Cycle Fatigue Life of Selective Laser melted and Hot Isostatically Pressed Ti6Al4V," Dissertation of Master of Science in Aeronautical Engineering, submitted at the Air Force Institute of Technology, on the month of February, 2015.
- [11] Y. Tetsuya, T. Takayoshi. and U. Takashi. "New Photocurable Resin Compositions for Stereolithography with a New Photofabricator," SCS-300P, MY0001399. [Online]. Available: https://inis.iaea.org/collection/NCLCollectionStore/_Public/31/016/31016300.pdf, Referenced on 23-August-2018.
- [12] J. Ramkumar, "Additive Manufacturing," Lecture-5, Department of Mechanical Engineering, IIT Kanpur, 2017. Available: <http://home.iitk.ac.in/~jrkumar/download/Lecture-5.pdf>, Referenced on 05-February-2017.

- [13] O. Dandgaval and P. Bichkar, "Rapid Prototyping Technology-Study of Fused Deposition Modeling Technique," *International Journal of Mechanical Production Engineering*, vol. 4, Issue-4, ISSN; 2320-2092, 2016.
- [14] P. Deepa, "Fused Deposition Modeling – A Rapid Prototyping Technique for Product Cycle Time Reduction Cost Effectively in Aerospace Applications," *IOSR Journal of Mechanical and Civil Engineering (IOSR-JMCE)*, pp. 62–68, 2014.
- [15] A. Hehr and M. J. Dapino, "Dynamics of ultrasonic additive manufacturing," *Elsevier B.V., Ultrasonics*, vol. 73, pp. 49–66, 2017.
- [16] I. Gibson, D. Rosen and B. Stucker, "*Development of Additive Manufacturing Technology*," Sprengler Science+Business Media New York, ISBN: 978-1-4939-2112-6, 2015.
- [17] V. Bhavar, P. Kattire, V. Patil, S. Khot, K. Gujar, and R. Singh, "A Review on Powder Bed Fusion Technology of Metal Additive Manufacturing," Proceedings of the 4th International conference and exhibition on Additive Manufacturing Technologies-AM-2014, Bangalore, India, 2014.
- [18] S. Farid, S. Shirazi, S. Gharekhani, M. Mehrali, H. Yarmand, H. Simon, C. Metselaar, N. A. Kadri, N. Azuan, and A. Osman, "A review on powder-based additive manufacturing for tissue engineering : selective laser sintering and inkjet 3D printing," *Science and Technology of Advanced Materials*, vol 16, pp. 20, 2015.
- [19] S.O. Onuh, and Y.Y. Yusuf, "Rapid Prototyping Technology : Applications and Benefits for Rapid Product Development," *Journal of Intelligent Manufacturing*, vol. 10, pp. 301–311, 1999.
- [20] O. Nyrhila, A. Danzig. and M. Frey. "Direct Metal Laser Sintering (DMLS) of Titanium alloys," EOS GmbH - Electro Optical Systems, 2007.
- [21] M.K.E. Ramosoou, "Characterisation and Static Behaviour of the DMLS Ti6Al4V for Bio-medical Applications." Dissertation for Magister Technology: Mechanical Engineering, submitted at Central University of Technology, Free State, Bloemfontein in the month of February, 2012.
- [22] Y. M. Ahmed, K. Salleh, M. Sahari, M. Ishak, and B. A. Khidhir, "Titanium and its Alloy," *International Journal of Science and Research*, vol. 3, ISSN: 2319-7064, 2012
- [23] A. T. Sidambe, "Biocompatibility of advanced manufactured titanium implants-A review," *Materials*, vol. 7, pp. 8168–8188, 2014.
- [24] P. Pederson. "Microstructure and Phase Transformation of Ti-6Al-4V," Licentiate Thesis, Department of Applied Physics and Mechanical Engineering Division of Engineering Materials, submitted at Lulea University of Technology, in the year 2002.

- [25] J.M.A. Donachie. "Titanium a Technical Guide" 2nd ed., ASM International, 2000.
- [26] S.K. Kar, "Modeling of mechanical properties in Alpha/Beta-Titanium Alloys," Dissertation of Doctor of Philosophy Degree, submitted at Ohio State University, Ohio in the year 2005.
- [27] EOS GmbH - Electro Optical Systems "Material data sheet (provisional data) EOS Titanium Ti64 and EOS Titanium Ti6A4V ELI for EOSINT M 270 Systems (Titanium Version),", 2007.
- [28] ASTM B348-13. "Standard Specifications for Titanium and Titanium Alloy Bars and Billets," ASTM International, West Conshohocken, PA, 2013.
- [29] B. Moorhouse, "Controlling the interstitial element concentration in Ti-6Al-4V using Calciothermic Reduction," Dissertation for Doctor of Philosophy, submitted at the Imperial College London, 2013.
- [30] ASTM F1472-08. "Standard Specification for Wrought Titanium-6Aluminium-4Vanadium Alloy for Surgical Implant Applications (UNS R56400)" ASTM International, West Conshohocken, PA, 2008.
- [31] C. Veiga, J.P. Davim and A.J.R. Loureiro, "Properties and Applications of Titanium Alloys: A Brief Review," *Rev. Adv Mater. Sci.*, vol. 32, pp 133-148, 2012.
- [32] C. R. Knowles, T. H. Becker, and R. B. Tait, "The Effect of Heat Treatment on the Residual Stress Levels within Direct Metal Laser Sintered Ti6Al4V as Measured using the Hole-Drilling Strain Gauge Method," Proceedings of the 12th international RAPDASA Conference, North West South Africa, 2012.
- [33] R. Wanhill and S. Barter, "Fatigue of Beta Processed and Beta Heat-treated Titanium Alloys," *Springerbrief in Applied Sciences and Technology*, DOI: 10.1007/978-94-007-2524-9_1, , 2012.
- [34] A.A. Antonysamy, "Microstructure, Texture and Mechanical Property Evolution during Additive Manufacturing of Ti6Al4V Alloy for Aerospace Applications," Dissertation for Doctor of Philosophy in the Faculty of Engineering and Physical Sciences, submitted at the University of Manchester in the year 2012.
- [35] G.Lütjering, "Influence of Processing on Microstructure and Mechanical Properties of (α + β) Titanium Alloys," *Materials Science Engineering A243*, pp. 32–45, 1988.
- [36] Y. Fan, W. Tian, Y. Guo, Z. Sun, and J. Xu, "Relationships Among the Microstructure , Mechanical Properties, and Fatigue Behavior in Thin Ti6Al4V," *Advances in Materials Science and Engineering*, Article ID7278267, 2016.
- [37] G. Q. Wu, C. L. Shi, W. Sha, A. X. Sha, and H. R. Jiang, "Effect of Microstructure on the Fatigue Properties of Ti6Al4V Titanium Alloys," *Materials and Design*, vol. 46, pp. 668–674, 2013.

- [38] H. J. Rack and J. I. Qazi, "Titanium Alloys for Biomedical Applications," *Materials Science and Engineering*, vol. 26, issue 8, pp. 1269–1277, 2006.
- [39] X. Tan, Y. Kok, Y. Jun, M. Descoins, D. Mangelinck, S. Tor, K. Fai, and C. Kai, "Acta Materialia Graded Microstructure and Mechanical Properties of Additive Manufactured Ti6Al4V via Electron Beam Melting," *Acta Mater*, vol. 97, pp. 1–16, 2015.
- [40] Y. Ming and Y. Peng, "Overview of Densification, Microstructure and Mechanical Property of Additively Manufactured Ti-6Al-4V — Comparison among Selective Laser Melting, Electron Beam Melting, Laser Metal Deposition and Selective Laser Sintering, and with Conventional Powder Metallurgy." *InTech*, DOI:10.5772/59275, 2015, <https://www.intechopen.com/books/sintering-techniques-of-materials/an-overview-of-densification-microstructure-and-mechanical-property-of-additively-manufactured-ti-6a>, Chapter 5 of *Techniques of Materials*, Publisher: InTech, Editor: A. Lakshmana. Referenced on 01-November-2017.
- [41] I. Yadroitsev, P. Krakhmalev, I. Yadroitsava and A. du Plessis, "Qualification of Ti6Al4V ELI Alloy Produced by Laser Powder Bed Fusion for Biomedical Applications," *The Minerals, Metals and Materials Society*, DOI:10.1007/s11837-017-2655-5, 2017.
- [42] F. Yan, W. Xiong, and E. J. Faierson, "Grain Structure Control of Additively Manufactured Metallic Materials," *Materials*, vol. 10, 1260;doi:10.3390/ma10111260, 2017.
- [43] A. E. Patterson, S. L. Messimer, and P. A. Farrington, "Overhanging Features and the SLM/DMLS Residual Stresses Problem : Review and Future Research Need," *Technologies*, vol. 5, 15:DOI:10.3390/technologies5020015, 2017.
- [44] C.R. Knowles, T.H. Becker and R.B. Tait, "Residual Stress Measurements and Structural Integrity Implications for Selective Laser Melted Ti6Al4V," *South African Journal of Industrial Engineering*, vol. 23 (3), pp. 119–129, 2012.
- [45] S.L. Pityana, M. Tlotleng, L.C. Tshabalala, N.W. Makoana, A. Botes and E.L. Hachemi Amara, "Multiphysics Simulation of Thermal Phenomena in Direct Laser Metal Powder Deposition," Proceedings of the 17th international RAPDASA Conference, Vaal University of Technology, 2016.
- [46] P. Mercelis and J.P. Kruth, "Residual Stresses in Selective Laser Sintering and Selective Laser Melting," *Rapid Prototyping Journal*, vol. 12/5, pp. 254–265, 2006.
- [47] L. Mugwagwa, D. Dimitrov, S. Matope, and A.M. Venter, "Residual Stress Distribution within Components Manufactured using Selective Laser Melting," Proceedings of the 18th international RAPDASA Conference, International Conference Centre, Durban, 2017.
- [48] I. Van Zyl, I. Yadroitsava and I. Yadroistev, "Residual Stress in Ti6Al4V Objects Produced by Direct Metal Laser Sintering," *South African Journal of Engineering*, vol 27(4), pp. 134–141, 2016.

- [49] M. Qian, W. Xu, M. Brandt, and H. P. Tang, "Additive manufacturing and postprocessing of Ti6Al4V for superior mechanical properties," *Metallic Material for 3D Printing*, vol. 41(10), pp. 775–784, 2016.
- [50] A. Yadollahi, N. Shamsaei, S. M. Thompson, A. Elwany, and L. Bian, "Effects of building orientation and heat treatment on fatigue behavior of selective laser melted 17-4 PH stainless steel," *International Journal of Fatigue*, vol. 94, pp. 218–235, 2017.
- [51] C. Leyens and M. Peters, "Titanium and Titanium Alloys," Weinheim: Wiley-VCH Verlag, 2003.
- [52] J. Everaerts, B. Verlinden and M. Wevers, "The Influence of the Alpha Grain size on the Internal Fatigue Crack Initiation in Drawn Ti6Al4V wires," *Procedia Structural Integrity*, vol. 2, pp. 1055-1062, 2016.
- [53] D.D. Malka-Markovitz, A. Katsman, A Shirizly and M. Bamberger, "Microstructure and Mechanical Properties of Laser Melting and Manufactured Ti6Al4V," Proceedingng of the International Conference and Exhibition on advanced and Namo Materials, held at Ottawa, Canada, 2015.
- [54] B. Vrancken, L. Thijs, J.P. Kruth, and J. Van Humbeeck, "Heat Treatment of Ti6Al4V Produced by Selective Laser Melting: Microstructure and Mechanical Properties," *Journal of Alloys and Compounds*, vol. 541, pp. 177–185, 2012.
- [55] R. Sabban, S. Bahl, K. Chatterjee and S. Suwas, "Globularization using heat Treatment in Additively manufactured Ti6Al4V for High Strength and Toughness," *Acta materialia*, vol. 162, pp. 239-254, 2018.
- [56] E.L. Sallica, R. Caram, A. L. Jardini, and J. B. Fogagnolo, "Ductility Improvement due to Martensite α' Decomposition in Porous Ti6Al4V Parts Produced by Selective Laser Melting for Orthopedic Implants," *Journal of Mechanical Behavior of Biomedical Material*, vol. 54, pp. 149–158, 2016.
- [57] C.R. Knowles, "Residual Stress Measurement and Structural Integrity Evaluation of SLM Ti6Al4V," Dissertation for Master of Science Degree, submitted at the University of Cape Town, Cape Town in the month of July, 2012.
- [58] ASM Handbook, "Fatigue and Fracture," ASM International, 1996.
- [59] E. Ghafoori, M. Motavalli, A. Nussbaumer, A. Herwig, G.S. Prinz and M. Fontana, "Determination of minimum CFRP Pre-stress levels for Fatigue Crack prevention in Retrofitted Metallic Beams," *Engineering Structures*, vol. 84, pp. 29–41, 2015.
- [60] J. Schijve, "Fatigue of Structures and Materials," 2009. Available: <http://www.springer.com/978-1-4020-6807-2>, Referenced on 02 March 2018.

- [61] A. A. Azeez, "Fatigue Failure and Testing Methods," Bachelor's Thesis submitted at the Hamk University of Applied Sciences on the month of May, 2013.
- [62] H. E. Boyer, "*Atlas of Fatigue Curves*," ASM International, ISBN: 978-0-87170-214-2, 1986.
- [63] R. K. Nalla, B. L. Boyce, J. P. Campbell, J. O. Peters, and R. O. Ritchie, "Influence of microstructure on high-cycle fatigue of Ti-6Al-4V: Bimodal vs. lamellar structures," *Metallurgical Materials Transactions A*, vol. 33(13), pp. 899–918, 2002.
- [64] J.K. Sushant, S.J. Christopher, G.J. Patrick, P.J. William and J. Reji, "Characterization of Fatigue Crack Initiation Facets in Relation to Lifetime Variability in Ti6Al4V," *International Journal of Fatigue*, vol. 42, pp. 248–257, 2012.
- [65] P.P. Benham and R.J. Crawford, "*Mechanics of Engineering Materials*." Second Edition, Longman Group Limited, 1996.
- [66] S.Suresh, "*Fatigue of Materials*," Cambridge University Press, 2nd ed. 2004.
- [67] P. P. Milella, "*Fatigue and Corrosion in Metals*," Springer-Verlag, DOI:10.1007/978-88-470-2336-9_2, 2013.
- [68] J. Man, K. Obrtlík, and J. Polák, "Extrusions and Intrusions in Fatigued Metals. Part 1. State of the art and history," *Philosophical Magazine*, vol. 89(16), pp. 1295–1336, 2009.
- [69] W.W. Feng, R.G. Scott, R.D. Streit and A. Goldberg, "*Mechanical properties and science of engineering materials*," John Wiley and Sons, 2002.
- [70] ASM Handbook, "*Fractography*," ASM International, 1987.
- [71] A. Fatemi, "Chapter 3: Macro/Micro Aspects of Fatigue of Metals," Available: https://www.efatigue.com/training/chapter_3.pdf. Referenced on 09-October-2017.
- [72] M.F. Ashby and D.R.H. Jones, "*Engineering Materials*," Pergamon Press, 1980.
- [73] International Standard ISO 12106, "Metallic Materials Fatigue Testing Axial-Strain-Controlled Method," International Organization for Standardization, 1st Edition, 2003.
- [74] International Standard ISO 1099, "Metallic Materials Fatigue Testing Axial Force-Controlled Method," International Organization for Standardization, 2nd ed. 2006.
- [75] F.C. Campbell, "*Elements of Metallurgy and Engineering Alloys*," ASM International, 2008.
- [76] G. E. Dieter, "*Metallurgical and Metallurgical Engineering*," 3rd ed. New York: McGraw Book Company, 2013.

- [77] Materion Brush Performance Alloys, "Fatigue and Stress Ratio," Technical Tidbits, Issue No.53-May 2013. Available :<http://materion.com/-/media/files/alloy/newsletters/technical-tidbits/issue-no-53-fatigue-and-stress-ratio.pdf>. Referenced on 09 August 2018.
- [78] B. Vayssette, N. Saintier, C. Brugger, M. Elmay and E. Pessard, "Surface Roughness of Ti6Al4V parts obtained by SLM and EMB: Effect on the High Cycle Fatigue Life," *Procedia Engineering.*, vol. 213, pp. 89–97, 2018.
- [79] E. Wycisk, A. Solbach, S. Siddique, D. Herzog, and F. Walther, "Effects of Defects in Laser Additive Manufactured Ti-6Al-4V on Fatigue Properties," *Phys. Procedia*, vol. 56, pp. 371–378, 2014.
- [80] E. Wycisk, C. Emmelmann, S. Siddique, and F. Walther, "High Cycle Fatigue (HCF) Performance of Ti-6Al-4V Alloy Processed by Selective Laser Melting," *Advanced Materials Research*, vol. 817, pp. 134–139, 2013.
- [81] H. K. Rafi, N. V Karthik, H. Gong, T. L. Starr, and B. E. Stucker, "Microstructures and Mechanical Properties of Ti6Al4V Parts Fabricated by Selective Laser Melting and Electron Beam Melting," *Journal of Materials Engineering and Performance*, vol. 22(12), pp. 3872–3883, 2013.
- [82] Y. Murakami, *"Metal Fatigue: Effects of Small Defects and Non-metallic Inclusions,"* Elsevier Science Ltd, 2002.
- [83] P. J. Withers, I. Todd, and P. B. Prangnell, "The Influence of Porosity on Fatigue Crack Initiation in Additively Manufactured Titanium Components," *Science. Report*, DOI:10.1038/s41598-017-5, pp. 1–13, 2017.
- [84] J. Günther, D. Krewerth, T. Lippmann, S. Leuders, T. Tröster, A. Weidner, and H. Biermann, "Fatigue Life of Additively Manufactured Ti6Al4V in the Very High Cycle Fatigue Regime," *International Journal of Fatigue*, vol. 94, pp. 236–245, 2017.
- [85] ASTM E 494-95. "Standard Practice for Measuring Ultrasonic Velocity in Materials, ASTM International," ASTM International, West Conshohocken, PA, 1995.
- [86] J. Sieniawski, W. Ziaja, K. Kubiak and M Motyka, "Microstructure and Mechanical Properties of High Strength Two-Phase Titanium Alloys." *Intech*, DOI: 10.5772/56197, 2013. Available: https://www.researchgate.net/publication/260276611_Microstructure_and_mechanical_properties_of_high_strength_two-phase_titanium_alloys, In book: Titanium alloys - Advances in Properties Control, Publisher: InTech, Editors: Jan Sieniawski, Waldemar Ziaja. Referenced on 11-July-2018
- [87] A. du Plessis, S.G. le Roux and A. Guelpa, "The CT Scanner Facility at Stellenbosch University : An open access X-ray computed tomography laboratory," *Nuclear Instruments and Methods in Physics Research B*, vol. 384, pp. 42–49, 2016.
- [88] A. du Plessis, C. Broeckhoven, A. Guelpa, and S.G. le Roux, "Laboratory X-ray Micro-

- computed Tomography: a user guideline for biological samples,” *Giga Science*, vol. 6(6), pp. 1–11, 2017.
- [89] A. Blake, “*Handbook of Mechanics, Materials, and Structures*,” Winley Series in Mechanical Engineering Practice, 1985.
- [90] TITANEX GmBH, “Titanium Grade 5/23/ELI”, http://www.titanex.com/images/Grade_5_23_ELI.pdf. Referenced on 26-July-2018.
- [91] J. Sieniawski, W. Ziaja, K. Kubiak, and M. Motyka, “Microstructure and Mechanical Properties of High Strength Two-Phase Titanium Alloys”, <http://dx.doi.org/10.5772/56197>, 2013.
- [92] G.M. Ter Haar and T. H. Becker, “Selective Laser Melting Produced Ti6Al4V: Post-Process Heat Treatments to Achieve Superior Tensile Properties,” *Materials*, vol. 11(146), DOI:10.3390/ma11010146, 2018.
- [93] P. Krakhmalev, G. Fredriksson, I. Yadroitsava, N. Kazantseva, A. du Plessis and I. Yadroitsev, “Deformation Behavior and Microstructure of Ti6Al4V manufactured by SLM,” *Physics Procedia*, vol. 83, pp. 778–788, 2016.
- [94] W. T. Becker, “*Principle of Failure Analysis, Ductile and Brittle*,” ASM International, 2002, <http://faculty.up.edu/lulay/failure/Lesson3.pdf>. Referenced on 20-August-2018.
- [95] W. T. Becker, “*Fracture Appearance and Mechanisms of Deformation and Fracture*” ASM International, 2002, http://fdjpkc.fudan.edu.cn/_upload/article/files/1f/12/b8b8c0704926994e368a107893d4/6ad0c8ee-53c3-4790-a931-211df202df69.pdf. Referenced on 20-August-2018.
- [96] S. Leuders, M. Thöne, A. Riemer, T. Niendorf, T. Tröster, H. A. Richard, and H. J. Maier, “On the mechanical behaviour of titanium alloy TiAl6V4 manufactured by selective laser melting : Fatigue resistance and crack growth performance,” *International Journal of Fatigue*, vol. 48, pp. 300–307, 2013.
- [97] R. Konecna, L. Kunz, A. Baca, and G. Nicoletto, “Long Fatigue Crack Growth in Ti6Al4V Produced by Direct Metal Laser Sintering,” *Procedia Engineering*, vol. 160, pp. 69–76, 2016.
- [98] R. Konecna, L. Kunz, A. Baca, and G. Nicoletto, “Resistance of Direct Metal Laser Sintered Ti6Al4V Alloy Against Growth of Fatigue Crack,” *Engineering Fracture Mechanics*, vol. 185, pp. 82–91, 2017.
- [99] T.H. Becker, M. Beck and C.Scheffer, “Microstructure and Mechanical Properties of Direct Metal Laser Sintered Ti-6Al-V,” *South African Journal of Industrial Engineering*, vol 26(1), pp. 1-10, 2015.
- [100] Z. Sun and M. Huang, “Fatigue Crack Propagation of New Aluminum Lithium Alloy Bonded

- with Titanium Alloy Strap,” *Chinese Journal of Aeronautics*, vol. 26(3), pp. 601–605, 2013.
- [101] G.E. Dieter, “*Mechanical Metallurgy SI metric Edition*,” McGraw-Hill, UK, 1989.
- [102] P. Grad, B. Reuscher, A. Brodyanski, M. Kopnarski, and E. Kerscher, “Mechanism of Fatigue Crack Initiation and Propagation in the Very High Cycle Fatigue Regime of High-Strength Steels,” *Scripta Materialia*, vol. 67(10), pp. 838–841, 2012.
- [103] X. Liu, C. Sun, and Y. Hong, “Faceted Crack Initiation Characteristics for High-Cycle and Very-High-Cycle Fatigue of a Titanium Alloy Under Different Stress Ratios,” *International Journal of Fatigue*, vol. 92, pp. 434–441, 2016.
- [104] M. Janecek, F. Novy, P. Harcuba, J. Strasky, L. Trsko, M. Mhaede and L. Wagner, “The Very High Cycle Fatigue Behaviour of Ti 6Al 4V Alloy,” *Acta Physica Polonica A*, vol. 128(4), pp. 497–502, 2015.
- [105] S.G. Ivanova, R. R. Biederman and R. D. Sisson Jr, “Investigation of Fatigue Crack Initiation in Ti-6Al-4V During Tensile-Tensile Fatigue Investigation of Fatigue Crack Initiation in Ti-6Al-4V During Tensile-Tensile Fatigue,” *Journal of Materials Engineering and Performance*, vol. 11(2), pp. 226–231, 2002.
- [106] A.L. Pilchak, R.E.A. Williams and J.C. Williams, “Crystallography of Fatigue Crack Initiation and Growth in Fully lamellar Ti6Al4V,” *Metallurgical and Materials Transactions A*, vol. 41A, DOI: 10.1007/s11661-009-0064-2, 2010.
- [107] S.T. Tu and X.C. Zhang, “Fatigue Crack Initiation Mechanisms,” *Elsevier Inc*, DOI:1016/B978-D-12-803581-802852-6, 2016.
- [108] D. Agius, K. I. Kourousis, and C. Wallbrink, “A Review of the As-Built SLM Ti6Al4V Mechanical Properties Towards Achieving Fatigue Resistant Designs,” *Metals*, vol. 8(75), doi:10.3390/met8010075, 2018.
- [109] H. Gong, K. Rafi, H. Gu, G.D.J. Ram, T. Starr, and B. Stucker, “Influence of Defects on Mechanical Properties of Ti6Al4V Components Produced by Selective Laser Melting and Electron Beam Melting,” *Materials and Design*, vol. 86, pp. 545–554, 2015.
- [110] Wycisk, S. Siddique, D Herzog F. Walther and C Emmelmann, “Fatigue Performance of Laser Additive Manufactured Ti6Al4V in Very High Cycle Fatigue Regime up to 10⁹ Cycles,” *Frontiers in Materials*, vol. 2, article 72, 2015.
- [111] H. K. Rafi, T. L. Starr, and B. E. Stucker, “A Comparison of the Tensile, Fatigue, and Fracture Behavior of Ti6Al4V and 15-5 PH Stainless Steel Parts made by Selective Laser Melting,” *Int J Adv Manuf Technol*, vol 69, pp. 1299–1309, 2013.

APPENDIX A- TENSILE AND FATIGUE TEST SPECIMEN

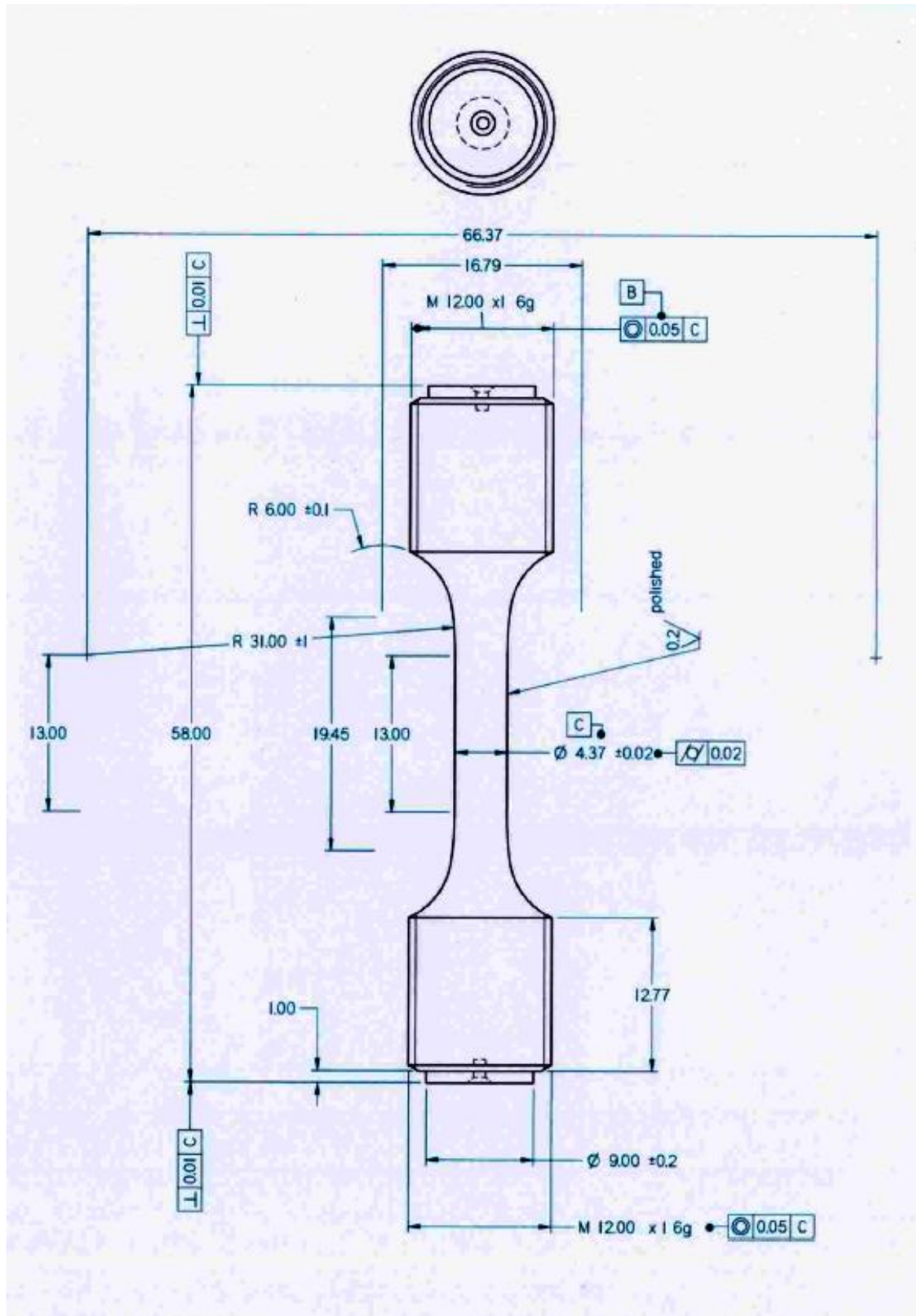


Figure A.1: Tensile and fatigue specimen dimensions

APPENDIX B– CRACK INITIATION SITES

Figure B.1 shows the crack initiation sites of the fractured as-built DMLS Ti6Al4V (ELI) specimens built in the X-build direction.

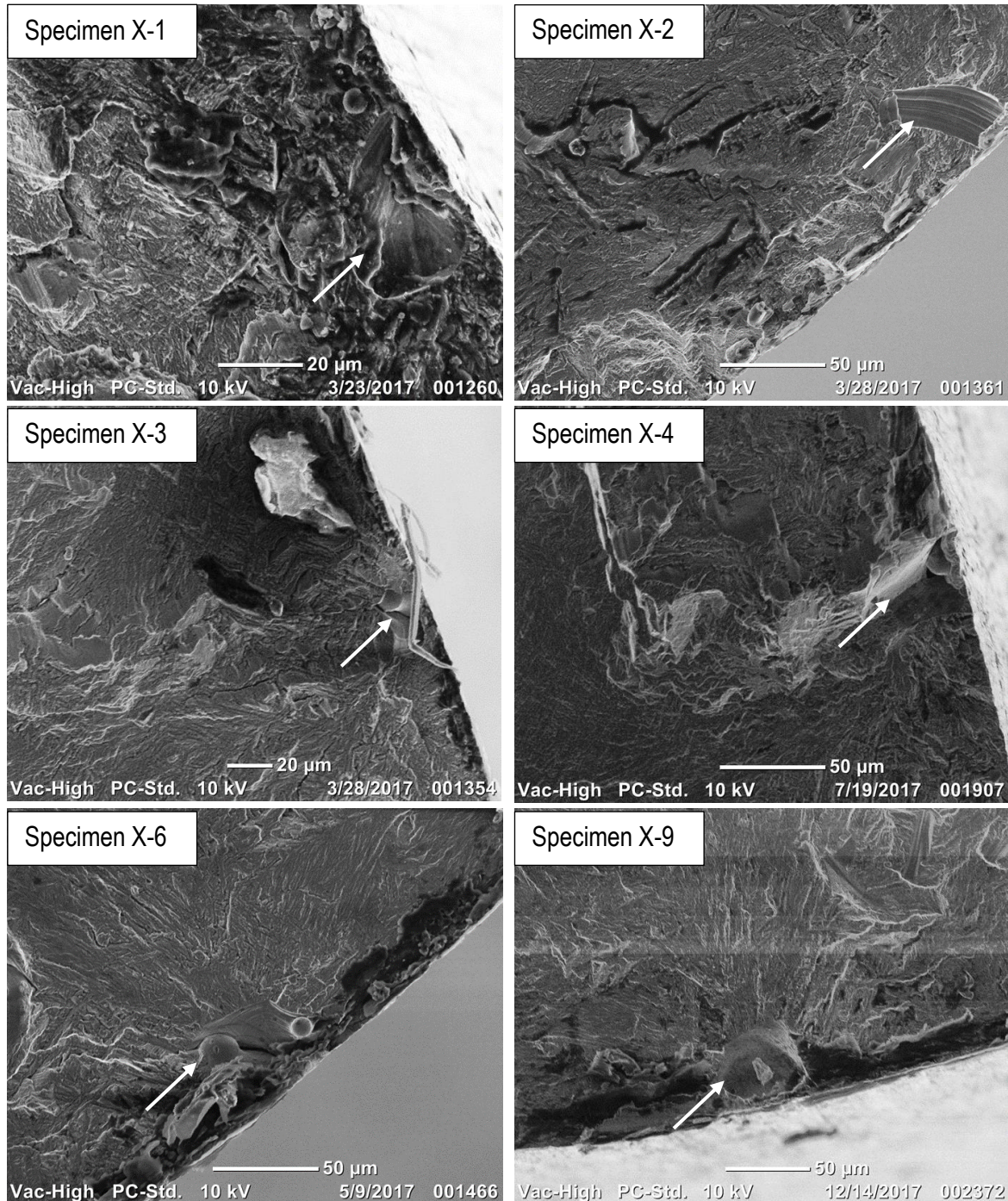


Figure B.1: Crack initiation sites of as-built X-build direction specimens indicated by arrows

Figure B.2 shows the crack initiation sites of the fractured as-built DMLS Ti6Al4V (ELI) specimens built in the Y-build direction.

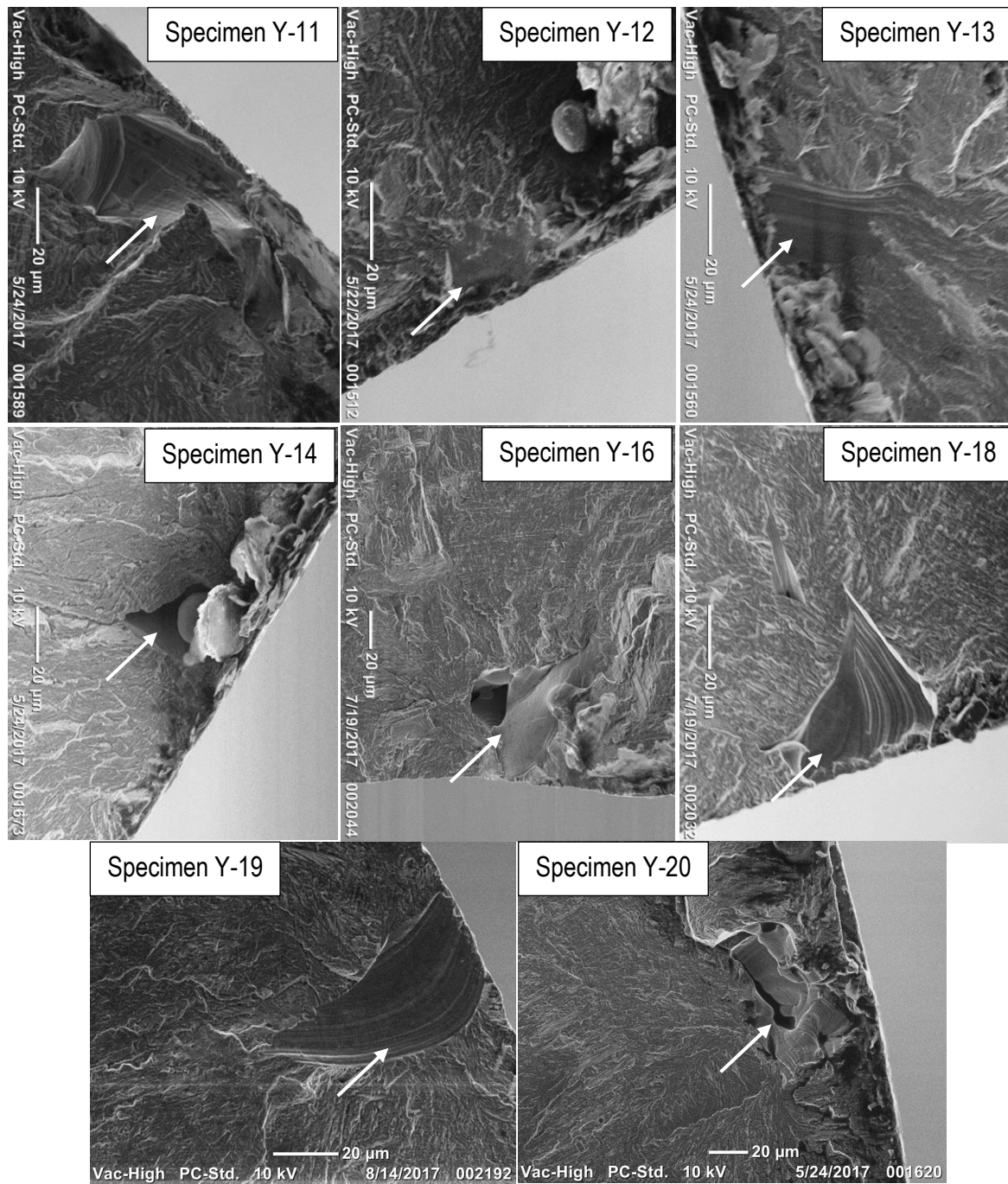


Figure B.2: Crack initiation sites of as-built Y-build direction specimens indicated by arrows

Figure B.3 shows the crack initiation sites of the fractured as-built DMLS Ti6Al4V (ELI) specimens built in the Z-build direction.

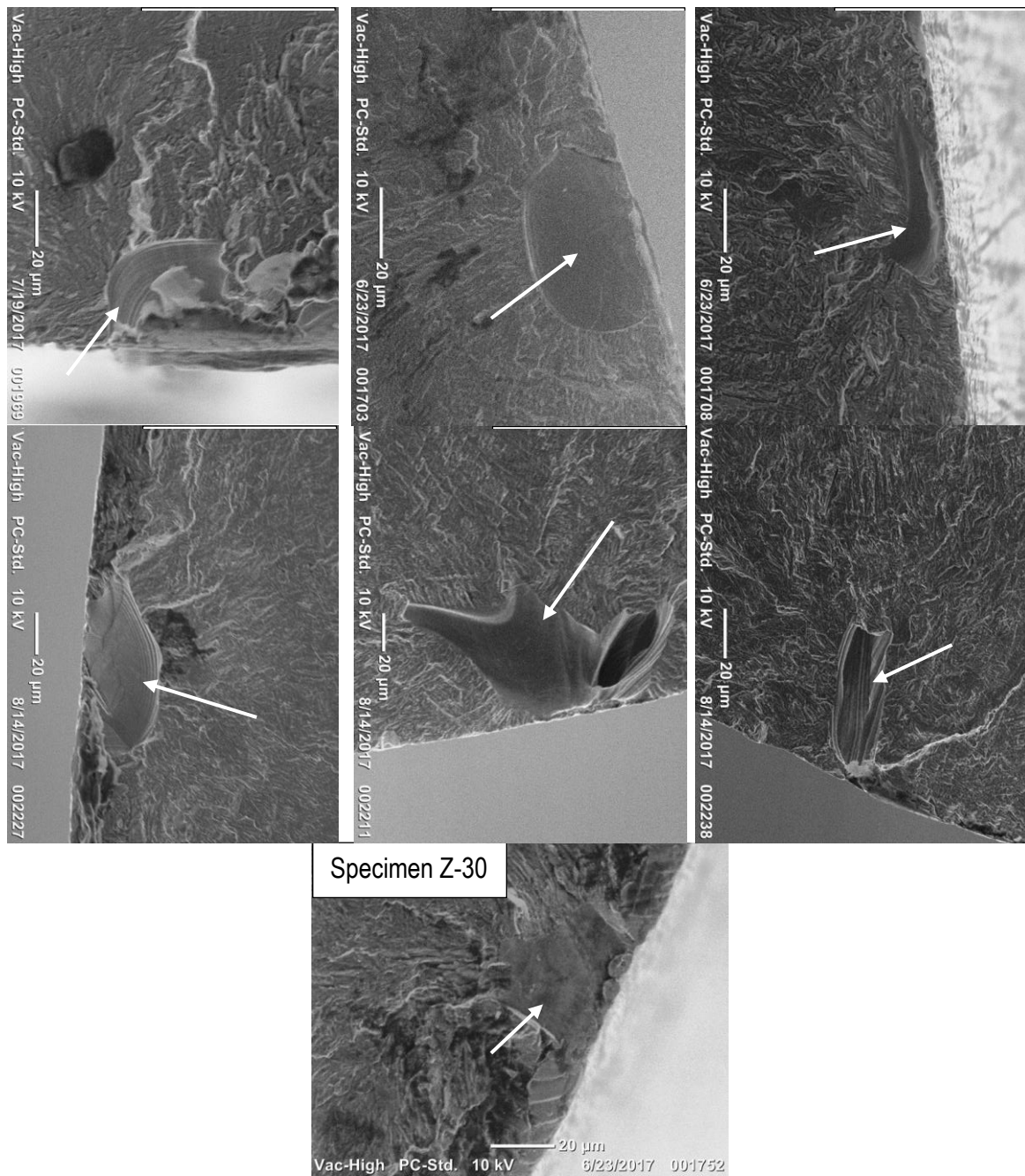


Figure B.3: Crack initiation sites of as-built Z-build direction specimens indicated by arrows

Figure B.4 shows the crack initiation sites of the fractured HTA DMLS Ti6Al4V (ELI) specimens built in the X-build direction.

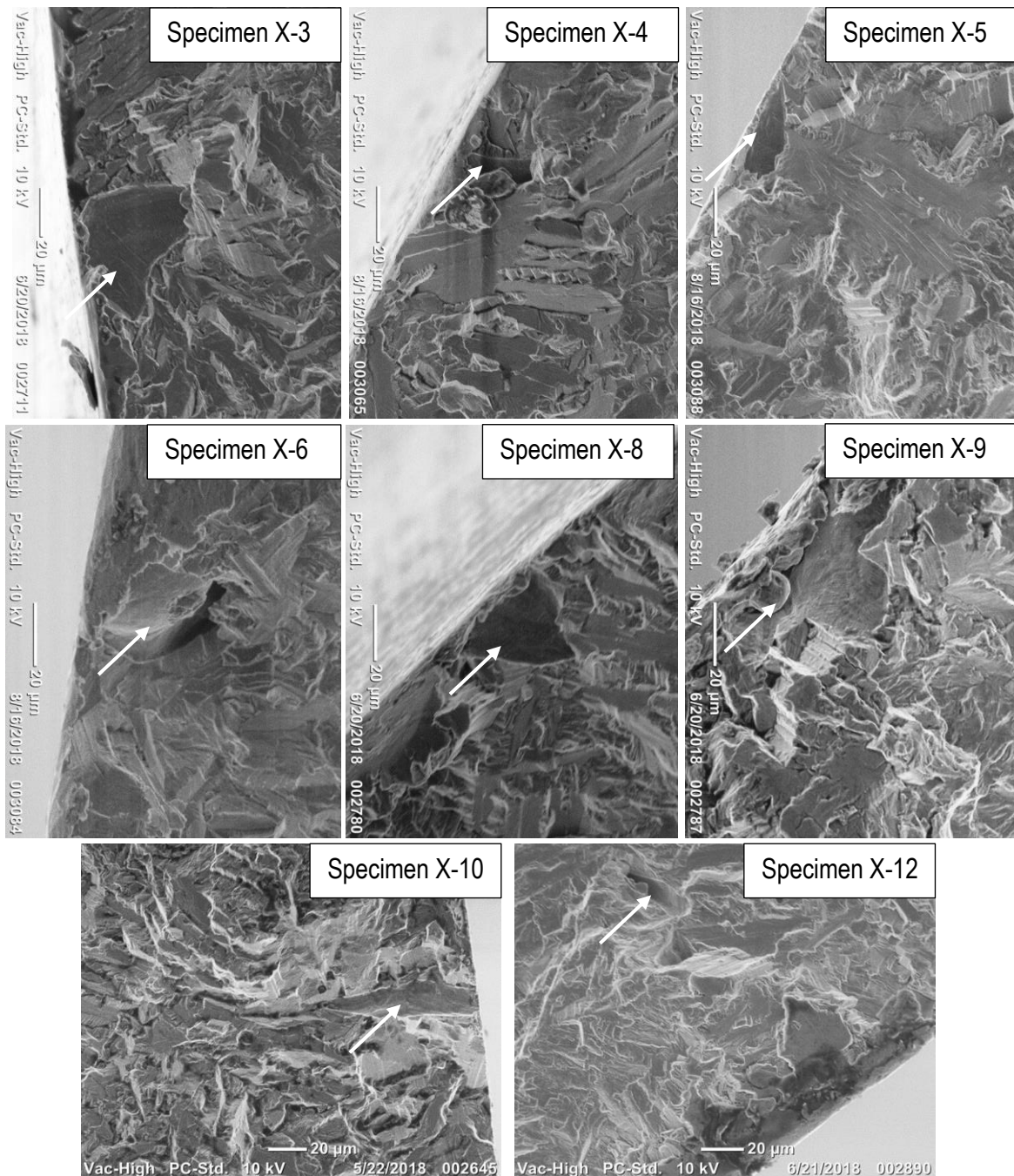


Figure B.4: Crack initiation sites of HTA X-build direction specimens indicated by arrows

Figure B.5 shows the crack initiation sites of the fractured HTA DMLS Ti6Al4V (ELI) specimens built in the Y-build direction.

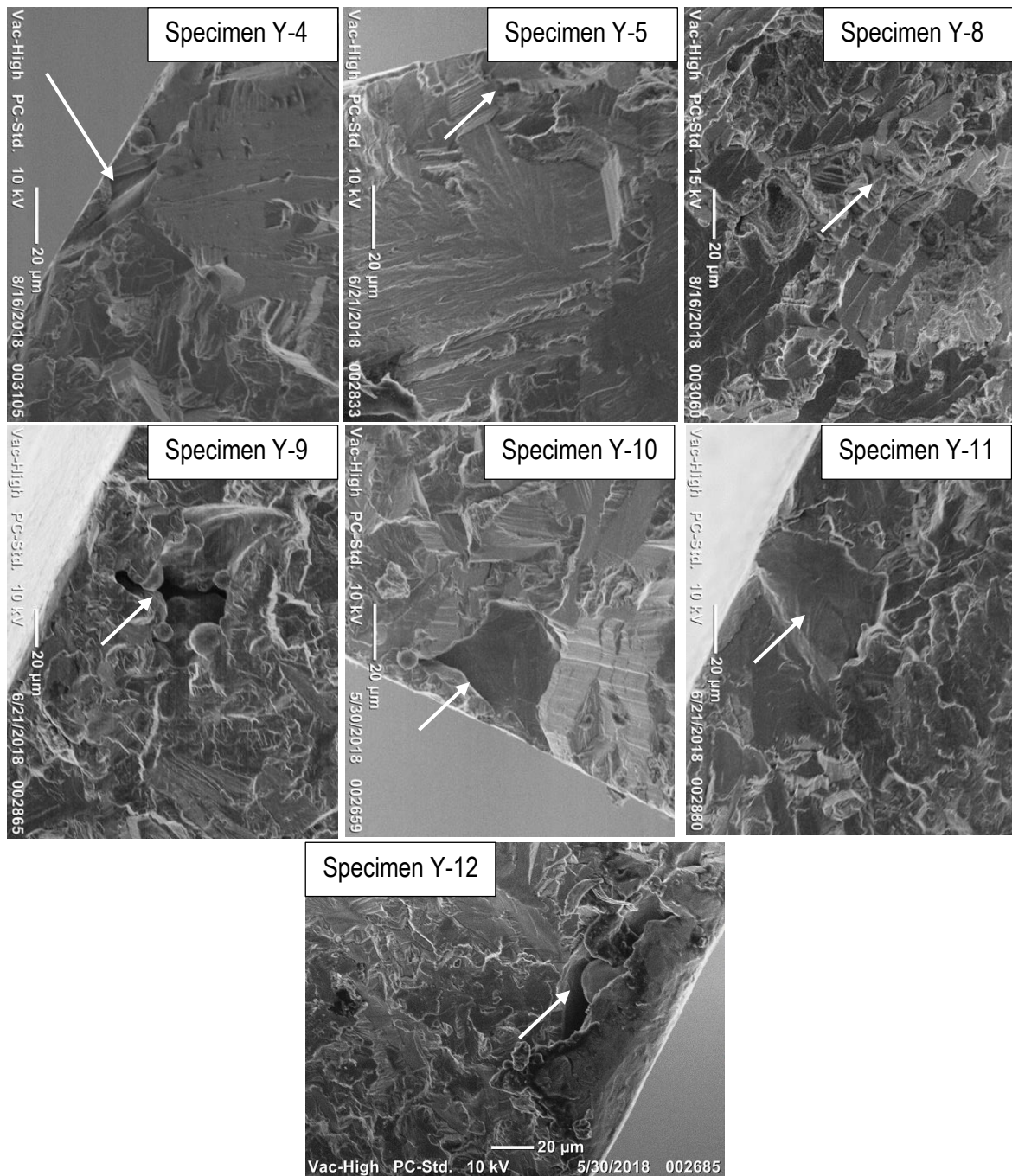


Figure B.5: Crack initiation sites of HTA Y-build direction specimens indicated by arrows

Figure B.6 shows the crack initiation sites of the fractured HTA DMLS Ti6Al4V (ELI) specimens built in the Z-build direction.

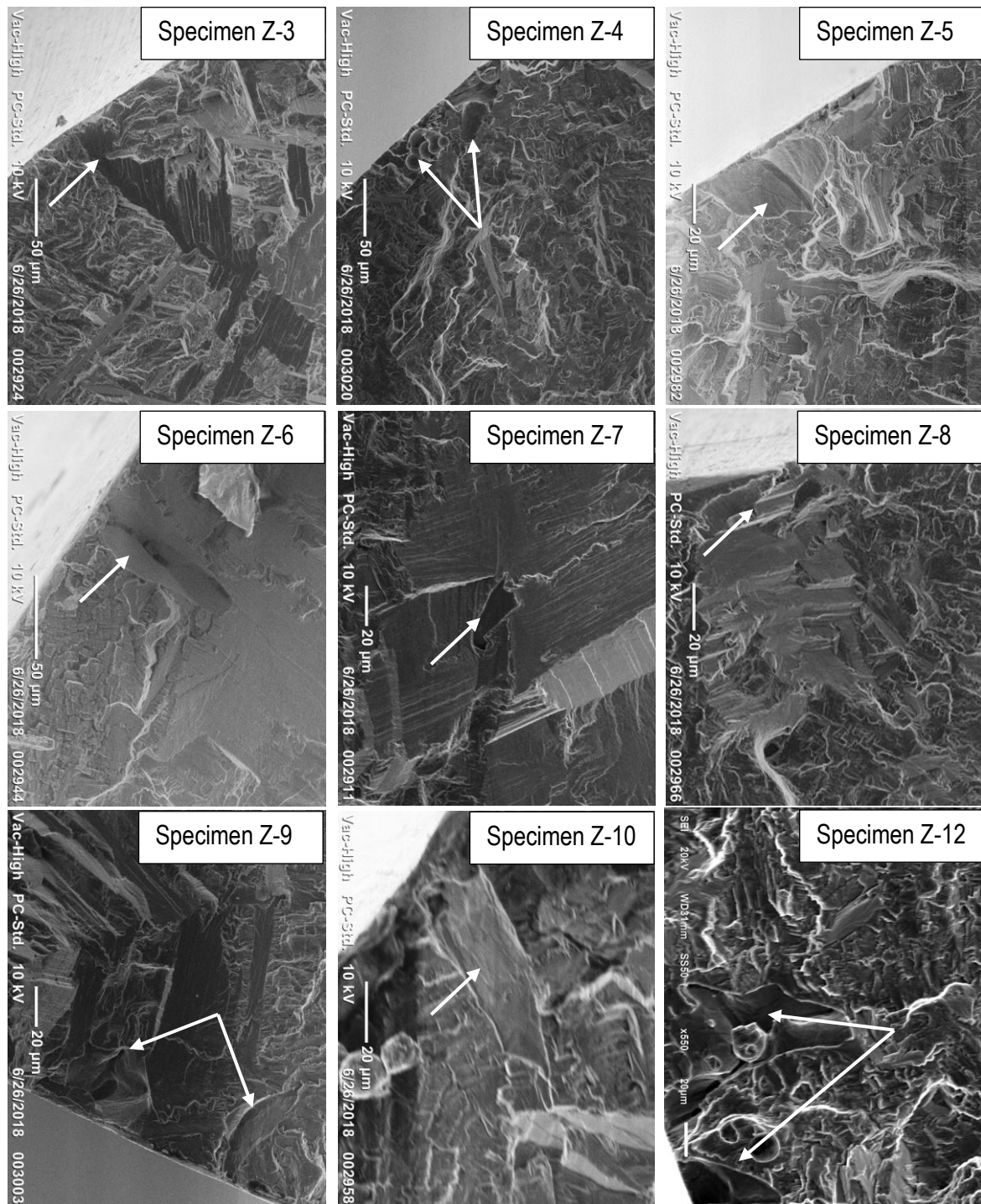


Figure B.6: Crack initiation sites of HTA Z-build direction specimens indicated by arrows